On the Insulator-Conductor Transition in Polymer Nanocomposites

THÈSE N^{O} 4612 (2010)

PRÉSENTÉE LE 19 MARS 2010
À LA FACULTÉ SCIENCES ET TECHNIQUES DE L'INGÉNIEUR
LABORATOIRE DE PRODUCTION MICROTECHNIQUE 2
PROGRAMME DOCTORAL EN SYSTÈMES DE PRODUCTION ET ROBOTIQUE

ÉCOLE POLYTECHNIQUE FÉDÉRALE DE LAUSANNE

POUR L'OBTENTION DU GRADE DE DOCTEUR ÈS SCIENCES

PAR

Gianluca AMBROSETTI

acceptée sur proposition du jury:

Prof. M.-O. Hongler, président du jury
Prof. P. Ryser, Dr C. Grimaldi, directeurs de thèse
Dr A. Danani, rapporteur
Prof. G. Foffi, rapporteur
Dr E. Grivei, rapporteur

ÉCOLE POLYTECHNIQUE
FÉDÉRALE DE LAUSANNE
Suisse
2010

To Michael Brecker (1949-2007)

My childhood hero

Abstract

This thesis presents an investigation of the models describing electrical conductivity in polymer nanocomposites, which consist in more or less random dispersions of nanometric conductive fillers like carbon nanotubes, nanofibers or graphene sheets in a polymer matrix. The investigation is carried out mainly through simulations with *ad-hoc* developed algorithms coupled with analytical studies of both the global system connectivity and the details of a realistic electron tunneling inter-particle conduction mechanism.

Conductive polymer nanocomposites manifest a sudden increase of the bulk conductivity when the content of the conductive species exceeds a certain threshold, a behavior shared with many other insulator-conductor biphasic systems. Percolation theory remains the most widely used theoretical formulation to describe for such transition. Its embodiment which most faithfully takes into account the microscopic features of the composite is the hard-core-penetrable-shell model, and in the present work has been extended to a wide range of anisotropic filler particle shapes modeled as hard ellipsoids-of-revolution. However, such connectivity-based description of the insulator transition manifests some fundamental incompatibilities when applied to the specific case of nanocomposites. Indeed, the percolation formulation requires the connections between the filler particles to be of the “on-off” binary sort, but this is in contrast with a microscopically justified electron tunneling inter-particle conduction mechanism, which entails no sharp cutoff of the connectivity. Since the tunneling conductance decays exponentially over the distance with a characteristic decay length in the order of a few nanometers, for macroscopic fillers an abrupt cutoff description of inter-particle connectivity may still be suitable. This ceases to be valid for nanometric fillers, which have one or more characteristic dimensions that are comparable with the distances of tunneling.

The solution of the tunneling-percolation problem in the nanocomposite regime is the main focus of this thesis. We present a model of conductivity where the filler particles form a network of globally connected objects via tunneling. Such a model does not need any abrupt interruption to induce the insulator-conductor transition and is able to reproduce the typical conductivity versus nanofiller volume fraction curves found experimentally. In this description, the transition is interpreted as the crossover region where the conductivity contribution due to the tunneling network overtakes the intrinsic one of the polymer matrix. Furthermore, we introduce an approximation route and explicit formulas based on the critical path method, which allow a quick and precise estimation of the overall system conductivity for various commonly employed nanocomposites. The validity of our formulation is verified by extracting from a large number of experimental results the characteristic tunneling length, which is found to be within the expected range of its values.

Finally, we consider the case of graphite polymer composites in more detail, and we introduce a simple model of conductivity, which is able to account for some of the features of these materials.

Keywords: Conductive polymer composites, nanocomposites, graphite polymer composites, transport properties, DC conductivity, percolation, electron tunneling, hard ellipsoid fluid, excluded volume.

Riassunto

In questa tesi viene presentata un'investigazione dei modelli atti a descrivere la conducibilità elettrica nei nanocompositi a base polimerica, che consistono in dispersioni più o meno disordinate di nanoparticelle quali nanotubi e nanofibre di carbonio o fogli di grafene in una matrice polimerica. L'investigazione è eseguita principalmente mediante simulazioni con algoritmi sviluppati *ad hoc* e mediante studi analitici sia della connettività del sistema che dei meccanismi di conduzione interparticellare basati sulla conduzione elettronica tramite effetto tunnel (o tunneling).

I nanocompositi conduttori a matrice polimerica manifestano un drastico aumento della conduttività globale una volta superata una certa concentrazione della specie conduttiva, un comportamento condiviso con molti altri sistemi bifasici isolante-conduttore. La formulazione teorica più sovente utilizzata per rendere conto di tale transizione rimane la teoria della percolazione e la sua incarnazione più fedele alle caratteristiche microscopiche dei compositi è rappresentata dal cosiddetto modello a nucleo duro con guscio penetrabile, che nel presente lavoro viene esteso ad un largo spettro di particelle anisotropiche modellate come ellissoidi di rotazione. Tuttavia, tali descrizioni della transizione isolante-conduttore basate sulla connettività vanno incontro ad incompatibilità fondamentali quando applicate al caso specifico dei nanocompositi. Infatti, la formulazione della percolazione richiede che le connessioni tra le particelle conduttive sia di tipo binario (cioè o connesso o disconnesso), ma ciò è in contrasto con un meccanismo di conduzione interparticellare basato sul tunneling che invece non implica nessuna interruzione netta della connettività. Poiché la conduttanza di tunneling decade esponenzialmente con una lunghezza caratteristica di decadimento dell'ordine di qualche nanometro, per dispersioni con particelle macroscopiche una descrizione della connettività interparticellare a interruzione netta può ancora essere adeguata. Ciò cessa di essere valido per particelle nanometriche, poiché esse hanno una o più dimensioni caratteristiche comparabili con le distanze di tunneling.

La risoluzione dell'incompatibilità tra tunneling e percolazione nel regime di validità dei nanocompositi è lo scopo principale di questa tesi. Presentiamo un modello della conducibilità dove le particelle della dispersione formano una rete di oggetti globalmente interconnessi tramite tunneling. Questo modello non richiede nessuna interruzione drastica della connettività per indurre la transizione isolante-conduttore ed è capace di riprodurre la tipiche curve di conduttività in funzione del contenuto di nanodispersione trovate sperimentalmente. In tale descrizione, la transizione viene interpretata come la regione di crossover dove il contributo alla conduttività dovuto al rete di particelle interconnesse mediante tunneling supera quello intrinseco della matrice polimerica. Introduciamo poi una procedura di approssimazione nonché formule esplicite basate sul metodo di cammino critico che permettono una stima rapida e precisa della conduttività globale per molti nanocompositi abitualmente utilizzati. La validità della formulazione è verificata tramite l'estrazione da un grande numero di risultati esperimentali la distanza caratteristica di tunneling, che risulta sempre nella fascia di valori attesa.

Consideriamo infine in maggiore dettaglio il caso dei compositi grafite polimero e introduciamo un semplice modello della conduttività capace di rendere conto di alcune caratteristiche di tali materiali.

Parole chiave: Compositi polimerici conduttivi, nanocompositi, compositi grafite polimero, proprietà di trasporto, conduttività in corrente continua, percolazione, effetto tunnel, fluido di ellissoidi duri, volume escluso.

Acknowledgements

When I decided to start a PhD three years ago, I got exposed to a number of considerations by a number of people, saying that it was both a hardship and the deepest experience of a lifetime, a selfish introspective journey, and the result of synergistic team work with extraordinary mentors, a period ridden with frustrating standstill and ecstatic moments of discovery. At the time, I honestly thought these were mere exaggerations and never even considered they could all be simultaneously true. Well, I was wrong. It was all that.

Although a thesis bears the name of one person only, every fragment of it owes something to a large number of people who, in a more or less direct way, made it possible. These very same persons are also accountable for another essential component of these last three years: lots of fun. The journey was not made alone.

For a start, I would like to thank Prof. Peter Ryser, for allowing me to carry out the research for my PhD at the Laboratoire de Production Microtechnique (LPM) of EPFL, and for letting me grow into it without boundaries, in a stimulating and inspiring environment. My deepest gratitude also goes to the co-director of my thesis, Dr. Claudio Grimaldi, for his skilful and patient supervision, his clear visions and restless creativity. With him I learned how deep a synergy between two human beings can push a research, and also how inspiring guidance can be. I couldn't have hoped for anyone better, nor could I imagine it. Countless pleasant evenings were spent together, sharing more than just work, most of the time brightened up by the presence of Claudio's wife Claudia and their wonderful little son Marco, to whom I extend my innermost gratitude.

Two fellow PhD students at LPM played an important role in the outcome of the present research: Niklaus (Niki) Johner, who gave me invaluable support in sharing his simulation programs and in helping me get mine straight, and Nathalie Serra, who carried out several experiments on graphite-polymer composites. They also made sure I would visit as many restaurants and bars in Lausanne as my stays would allow.

I would also like to thank the members of the jury for the time they dedicated to the reading of my thesis, and for the stimulating and constructive atmosphere they were able to create during the oral exam: Dr. Andrea Danani, whom I also thank for giving me the opportunity to start my PhD in the first place, Prof. Giuseppe Foffi, Dr. Eusebiu Grivei and the president of the jury, Prof. Max-Olivier Hongler.

As researchers for TIMCAL Graphite & Carbon SA, Dr. Eusebiu Grivei, Dr. Nicolas Probst and Carmine Ciallella had a fundamental role in the CTI-funded project GraPoly, in the frame of which my thesis took place. I shall never forget their positive and playful attitude in the most difficult moments.

LPM's Dr. Thomas Maeder was another great source of inspiration and ideas all along, he never stopped amazing me with his vast and, apparently, inexhaustible knowledge.

Thank you also to Isaac Balberg, for supporting the global tunnelling model featured in the thesis and for joining us in the odyssey towards its publication.

My gratitude also goes to Elodie Boller of the European Synchrotron Radiation Facility of Grenoble (France), for the tomographies illustrated in Figures 7.8-7.10.

A great share of the present acknowledgments goes to my colleagues of the TMM group at ICIMSI-SUPSI, with whom I spent most of my time. In particular, I would like to thank Walter Amaro, the group responsible, for helping me prepare the funding request for the GrayPoly project. My gratitude goes to him and Andrea Danani for generously financing my Lausanne-Lugano trips. Thank you also to Giulio Scocchi, who helped me with many practical issues, such as bibliographic research, and who patiently allowed me to use his computer's software to visualize my simulated systems. Raffaele Ponti (RP) is the creator behind the beautiful images of Figures 3.1, A.1 and A.2 and was a great companion of many saxophone blowing sessions. Matteo Dotta was the helpful teacher who taught me how to produce good micrographs, whereas Simone Pusterla kindly performed the 3D reconstruction of Figures 7.8-7.10 tomographies. Essential to the present thesis were the endless simulation runs I could freely perform on the ARES Cluster, for which I have to thank Maurizio Barbato, Eric Jaminet and Roberto Nunnari. Data analysis can enormously slow down a novice, and if I was almost entirely spared I have to thank the vast experience of Ermanno Oberrauch. The variety of personalities I got to mix with, the endless discussions we had on about anything and everything, the constant complaints (mostly by the author) about the horrible cream-loaded food of the nearby restaurants, as well as the hilarious coffee breaks and aperitifs, made my stay at ICIMSI an unforgettable experience, for which I also have to thank the other TMM members (Alberto, the Andreas, Claudio, Dany, Davide, Emanuele, Ettore, Giovanni and Luca) and some ICIMSI colleagues, namely Cinzia, Franco, Michele and Tiziano.

A warm thank you goes to all the people who made me feel at home during my stays in Lausanne. Besides Claudio, Niki, and Nathalie, the presence of Daniel, Christine, Giuseppe and Nao has also been vital.

Grazie mille to my Lugano friends, the "usual suspects" (i.e. Ada and Dado, Alessia, Pietro and their son Giacomo, Anne, Francisca, Johnny and

the Aus der Beek, Giosé, Ivo, Maca, Christian and baby Martina, Marco, Mitch, Sandra and Andy, Stefi, Sergio and little Amélie), for the conspicuous quantities of laughs, food and drinks we fondly shared over the years.

Thank you also to Fusillo della Bonarda, who quietly (and unavoidably) listened to all my oral exam rehearsals.

Arigato gozaimasu to Fatiah, for sharing so many of the bright and dark moments of my PhD. Without her I would never have made it.

Again and again, my gratitude goes to John Coltrane, for being such and outstanding and everlasting example of absolute research.

Finally, *ça va sans dire*, I would like to express the deepest gratitude to my family, especially to my "extended" parents, Franco and Silli, Ursula and Leonardo, and my sister Flavia. They are the backbone of my life.

Contents

Chapter 1

Introduction

The rise of nanotechnology from laboratory curiosity to a multibillion dollar business, has been one of the most remarkable transformations seen by the high technology industry in years, and by now nanotechnology has become a street word. As usual in these situations, many preexisting techniques and products containing at least some part in the nanometer range were re-branded as “nano”, although they didn’t exploit any particular property arising by working at the nanoscale. This brings us to the following question: What pre-requisite does a substance or device need to satisfy in order to qualify as nanotechnology? There is a general agreement in the field of materials science that nanomaterials are defined as such when they exploit characteristics which become manifest only at the nanometric scale and that are not present in the bulk material. Since at this small scale the laws of physics are those of quantum mechanics, most of the peculiar behaviors of nanostructures originate from quantum phenomena.

One important class of nanomaterials is that of nanocomposites, which consist in a large number of nanometric particles, like nanotubes or graphene sheets (the filler), dispersed in a more or less ordered fashion in some sort of matrix, most commonly constituted by a polymer. The reasons behind these materials may be the obtention of improved mechanical properties or, as will be considered in the present thesis, the obtention of improved electrical properties with respect to the insulating matrix. This modus operandi is in reality not new, and man-made composite materials have a long history and range from concrete to fancy ceramic-ceramic composites for hypersonic planes, passing through carbon fiber-epoxy racing car parts.

At this point, one could legitimately ask if nanocomposites qualify as nanomaterials. For sure, some of them really do, but many others resemble their macroscopic counterparts, only with smaller fillers. In the case of conductive polymer nanocomposites, the description of their electrical properties has in fact exploited the same formulations used for macroscopic filler composites with generally no inclusion of quantum effects. This may be motivated by the observation that the conductivity as a function of the nanoparticle content does not show a behavior significantly different from the one obtained with micrometric particles: both manifest a sharp increase of the overall conductivity once a certain filling fraction is reached, a common feature of random insulator-conductor mixtures. The mainstream theory used to account for such behavior is percolation theory [1, 2] and identifies the insulator-to-conductor transition with the formation of a network of electrically connected conductive particles, which extends through the material. However, percolation formulations generally require a sharp cutoff of the connectivity between the particles of the system in order to be applicable. Yet, there is general agreement that, at least near the transition region, the main conduction mechanism between the conductive particles of the composite is quantum mechanical electron tunneling, and tunneling implies no abrupt interruption of the connectivity. This may result particularly relevant for nanocomposites, as in their case the dispersed conductive particles have at least one characteristic dimension, which is in the same scale of the typical distances of tunneling. Thus, it is sensible to expect that in these materials the detailed behavior of tunneling has to be taken into account, although this conflicts with a percolation description. Hence, the main focus of this thesis is the investigation of a tunneling-based model of conductivity in nanocomposites which does not rely on any sharp cutoff of the interactions between the filler particles to obtain the insulator-conductor transition found experimentally. Such a formulation may cease to be valid for macroscopic filler composites, but that would show that conductive nanocomposites do indeed behave differently than their larger scale counterparts, and that they eventually qualify as true nanomaterials.

1.1 Thesis overview

In the next chapter, an introduction to conductive polymer composites from a phenomenological point of view will be first given. Then, we will focus on the current models used to account for the electrical properties of these materials.

In Chapter 3, we are going to describe the simulation algorithms we developed to numerically replicate the microscopic morphology of composite materials with fillers of a variety of shapes. Filler particles are modeled as impenetrable ellipsoids of revolution (spheroids) and some considerations on random assemblies of hard spheroids are made.

Chapter 4 will be concerned with the investigation of connectivity-based geometrical percolation models. A strong emphasis will be put on the influence of the particle shape-anisotropy as well as on the identification of simple equations which allow to estimate relevant characteristic quantities of these systems.

Quantum mechanical electron tunneling plays a major role in the present thesis and Chapter 5 will be devoted to a more formal treatment of the filler-filler tunneling problem.

A model of conductivity in nanocomposites where the filler particles form a network of globally connected objects via tunneling will then be introduced in Chapter 6. Numerical investigations will be presented first and an effective formulation based on the critical path method allowing to obtain precise estimations of the overall conductivity will be presented afterwards. By extracting from a large number of experimental results on nanocomposites characteristic tunneling distances which are fully compatible with their expected values, we will show that the proposed model is reliable and robust.

The special case of graphite-polymer composites will be considered in Chapter 7, where a simple model able to account for some of the electric properties of these composite is introduced and where several 2D micrographs and 3D tomographic reconstructions will show how complex the microscopic morphology of real composites can get.

Finally, in the conclusion Chapter 8, some open questions which remain unanswered will be raised.

1.2 List of symbols

We present in Tables 1.1 and 1.2 a list of the most important symbols used in the present thesis.

Symbol	Definition
a	Spheroid polar semi-axis
b	Spheroid equatorial semi-axis
a/b	Spheroid aspect-ratio
B_c	Average bond connectivity
d	Cutoff shell thickness ($d = \delta/2$)
D	Spheroid major axis ($D = 2\max(a, b)$)
$\mathfrak{d}$	Inter-particle distance (Chapter 5)
e	Electron charge
E	Electron energy
g	Radial distribution function
G	System conductance
$\hbar$	Plank's constant h divided by 2π
k	$\sqrt{2mE}/\hbar$
L	Simulation cell size
m	Electron mass
S	Nematic order parameter
t	DC transport critical exponent
t	Time (Chapter 5)
V	Volume
V	Potential (Chapter 5)
w	Tunneling barrier width

Table 1.1: Frequently used Latin symbols and disambiguation.

Symbol	Definition
γ	$\gamma = 0.4$ for prolate spheroids and $\gamma = 0.6$ for spherocylinders
δ	Inter-particle cutoff distance
δ^{ij}	Inter-particle distance (except Chapter 5)
δ_{ij}	Kronecker delta
$\delta(x)$	Dirac delta function
Δ	Percolation transition width
κ	$\kappa = \sqrt{2m(V_0 - E)}/\hbar$
$\theta(x)$	Heaviside step function
θ, φ	Spheroid mutual orientation angles (See below for φ)
θ, φ	Spherical coordinates (Chapter 5)
Θ, Φ	Spherical coordinates (Chapter 3)
ν	Correlation length exponent
ξ	Characteristic tunneling length
ρ	Particle number density
$\rho(E)$	Electron state density (Chapter 5)
$\boldsymbol{\rho}$, ρ	Position vector inside integration surface (Section 5.3)
ϱ	Inter-particle conductance
σ	System conductivity
υ	Inter-particle conduction channel radius (Chapter 7)
ϕ	Volume fraction
ϕ	Electron wavefunction (Chapter 5)
φ	Angle between two spheroid polar (symmetry) axes
$\Phi(\varphi)$	Spheroid orientation distribution function
χ	Shape-anisotropy ($\chi = \max(a,b)/\min(a,b)$)
ψ	Electron wavefunction (Chapter 5)

Table 1.2: Frequently used Greek symbols and disambiguation.

Chapter 2

Electrically conductive polymers and the models describing their transport properties

In this chapter, aimed at giving the background notions on which the work of the present thesis develops, we will first briefly introduce conductive polymer composites and their direct current (DC) transport properties from a phenomenological point of view. Then, we will overview the existing models which are used to describe the quite singular electrical behavior of this important class of materials, and, finally, raise some key open questions which this work will try to answer.

2.1 Electrically conductive polymer composites

Polymeric organic materials, more commonly called plastics, are well known for their generally excellent behavior as electric insulators. The insulating properties of polymers are extensively exploited for countless industrial and consumer applications, ranging from power cables to printed circuit boards. The conductivities of such materials are between the lowest reported, and are typically in the $10^{-13} \div 10^{-18}$ S/cm range [3]. Less known is the fact that polymers, alone or in combination with additives, can offer conductivities which come close to that of metals [3, 4]. Conductive polymers can be divided in two main categories, and namely that of intrinsically conductive polymers (ICPs), where conductivity originates from the electronic structure of the polymer itself, and that of conductive polymer composites (CPCs), where conductivity is achieved by means of conductive additives dispersed in sufficient quantity in the polymer. These latter offer generally a better stability, and are more economic, and will be the subject of the analysis of this thesis.

Conductive polymer composites have a broad application spectrum and, before continuing, we will briefly outline some of these applications [3, 5]:

CPC-based *electromagnetic interference (EMI) shielding* enclosures, which are conductive enough to shield against (typically high frequency) electromagnetic radiation, allow cost reductions with respect to conventional metallic enclosures since they can be formed easily e.g. by injection molding. Examples include electronic equipment housings like mobile phone or laptop bodies.

Antistatic materials, also called electrostatic dissipation (ESD) materials, have conductivities (in the $10^{-6} \div 10^{-2}$ S/cm range) adequate to dissipate charge accumulations and prevent arching discharges. They are used for instance for sensible electronic component packaging, conveyor belts, airplane tires, and special flooring.

Plastics allowing direct plating/painting are materials that are conductive enough to be either directly electroplated or directly painted by electrophoresis and are used for car body and interior parts.

Medium/high voltage cable shielding, where semiconducting layers are used near the conductor to avoid corona discharge.

Resistor materials. CPCs are used both for low-noise variable resistors and, owing to their strong positive temperature coefficient of resistance (PTC), as current-limiting resistors.

Printable electronics is another field where CPCs are crucial, and applications range from industrial conductive inks for e.g. printed radio frequency identification (RFID) transponder antennas, to novel light-emitting elastic conductors [6].

Conductive pastes/adhesives are widely used in the electronic industry as alternative to soldering for joint bonding of electronic components.

Other applications include current collectors, bipolar plates for fuel cells, transparent conductive coatings as electrodes for solar photovoltaic cells, lighting protection in composite material aircraft structural parts, and thin film transistors [7].

As it is natural, different uses have different requirements, and the satisfaction of these requirements is often an engineering challenge.

Conductive polymer composites exhibit a feature common to most random insulator-conductor mixtures mixtures and namely that, once a certain filling fraction of the conductive phase is reached, a sharp increase of the conductivity σ is observed. This transition is associated with the formation of a network of electrically connected filler particles which spans the entire sample. One of the first investigations into the filler concentration dependence of the overall composite conductivity was carried out in the sixties by Gurland [8] and considered bakelite (a thermosetting phenol formaldehyde

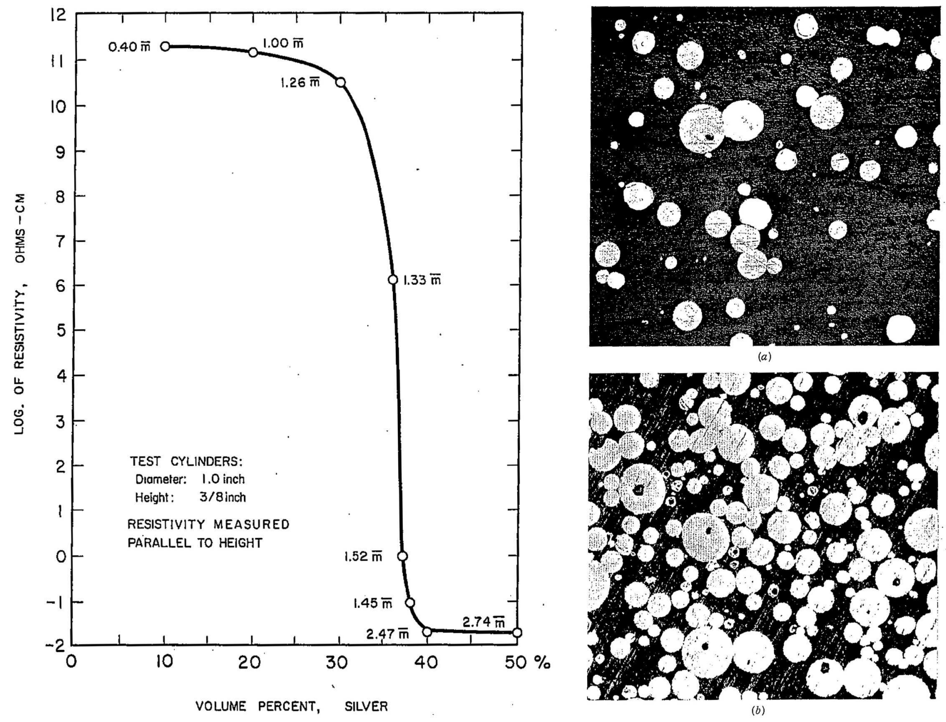

Figure 2.1: The silver-bakelite conductive composites of Gurland [8]. *Left*: Resistivity (inverse of conductivity) as a function of the filler volume fraction ϕ (expressed in percent). *Right*: Micrographs of the composites. (a) $\phi = 0.1$, (b) $\phi = 0.4$. For the scale, the real length of the micrograph side is ~ 1.45 mm.

resin) compounded with spherical silver particles. Figure 2.1 shows extracts of that article, most notably the resistivity as a function of the filler volume fraction, defined as the ratio between the filler volume and the total composite volume and which we label as ϕ. It can be seen how, at low silver volume fractions, the resistivity is roughly that of pristine bakelite, while between $\phi = 0.3$ and $\phi = 0.4$ the resistivity drops abruptly by more than twelve orders of magnitude to settle at around 0.2 Ω·cm (5 S/cm). This sigmoidal-shaped curve is the fingerprint of conductive polymer composites and is constantly recurring in the publications on the subject.

Since the sixties, a large number of polymers has been loaded with almost any possible conductive additive, with the most disparate particle shapes, and with characteristic sizes varying from sub-millimetric down to few nanometers. These include most metals (e.g. gold [10,11], silver [8,10], platinum [12], palladium [10], cobalt [13], copper [14,15], zinc [16], nickel [13,17,18], cupronickel [19], aluminium [20], and iron [20, 21]), carbonaceous fillers (carbon black [22], graphite [23, 24], carbon fibers [25], carbon nanofibers [26], carbon nanotubes [27], graphite nanosheets [28], and graphene [29]), metal

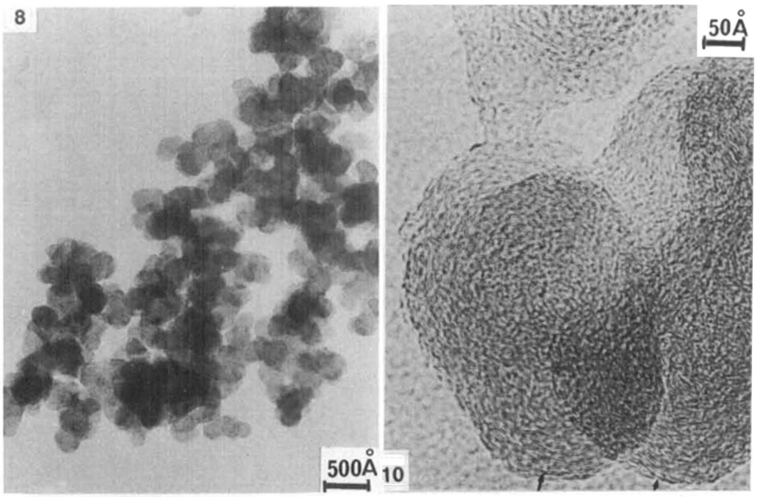

Figure 2.2: *Left*: Morphology of a carbon black cluster. *Right*: Detail of a carbon black particle. Adapted from Reference [9].

fibers [30], metal nanofibers [31], silver-coated glass spheres [32], nickel-coated carbon fibers [30,33], nickel-coated mica [34], silver-coated basalt [35], and intrinsically conductive polymers [36].

From an industrial point of view, the most extensively used additives for conductive plastics remain carbonaceous fillers, especially carbon black (CB) [37]. Carbon black is generally composed of more or less structured assemblies of nanometric spheroidal or spherical particles formed by onion-like concentric graphitic shells [9]. Figure 2.2 shows an example.

The degree of structure of the CB has profound consequences on the electrical properties of the composite, with high structure blacks (HSCB) offering good conductivities at lower volume fractions compared to less structured ones [38]. A the opposite end there are the low structure CBs (LSCB), which are basically loose (generally spherical) CB particles. We also note that LSCBs have larger average particle sizes (in the order of hundreds of nanometers), as can be appreciated from the example of Figure 2.3. The influence of the CB type on the composite conductivity is shown in Figure 2.4.

The case of carbon black shows us how the morphological aspects of the filler can have a strong impact on the composite conductivity. Many other factors are at play, and we will consider them in more detail in a few pages, but the influence of the filler geometries remains one of the most controllable aspects of CPCs and, therefore, one of the most important. A large part of this thesis will be devoted to the parameterizations of these influences, and, before continuing, we will illustrate some of their experimental aspects.

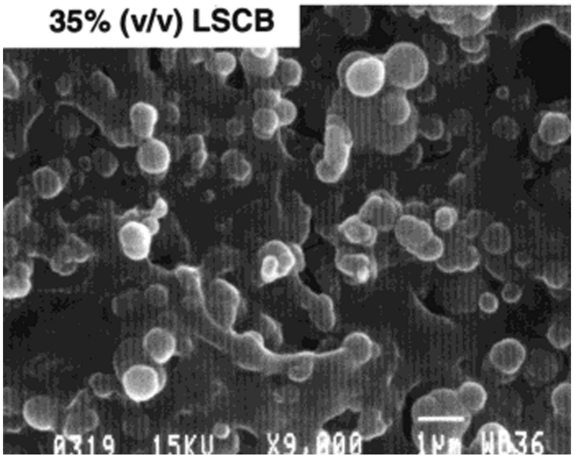

Figure 2.3: Low structure carbon black in an polyethylene-octene elastomer matrix. Adapted from Reference [39].

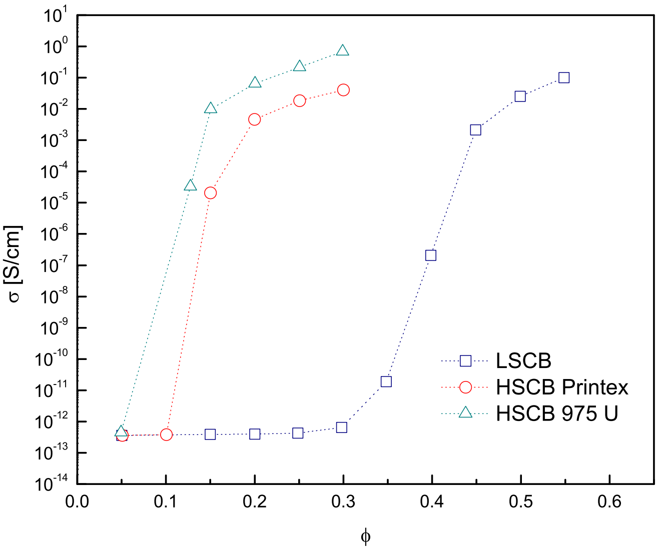

Figure 2.4: Conductivity σ as a function of the volume fraction ϕ for different carbon blacks in an ethylene-octene elastomer matrix. Adapted from Reference [39].

2.1.1 Influence of the filler geometry

With carbon black, we saw that more structured particle assemblies give rise to higher conductivities at a given volume fraction. This is not surprising if we consider that more structured fillers will have large electrically connected networks already in place and, as a consequence, will more easily originate globally connected networks. However, filler particle clustering is

not the only possibility to enhance the conductivity of a composite. It was soon realized that when the fillers had shapes deviating consistently from the sphere (like e.g. for fibers or plates), high conductivity levels could be obtained already at very low volume fractions also with systems composed of well dispersed particles. At this point, it must be noted that the pursuance of good conductivity at lower filler fractions is strongly motivated by the fact that high loadings lead to a consistent degradation of both the ease of processing and of the mechanical properties of the resulting composite [3], which tends to become brittle. Another motivation is then cost reduction. Therefore, a large number of works dealt with the lowering of the additive volume fraction through aspherical particles, some of which we will now briefly review.
To quantify the deviation of the particle shape from that of a sphere, the concept of *shape-anisotropy* is introduced, which defined as the ratio between the major particle dimension to its minor dimension and which we label as χ. This is closely related to the concept of *aspect-ratio*, which we will define more precisely in the next chapter. In the remaining of this chapter we will consider the two quantities as identical.

Good conductivity at very low concentrations is the rationale behind basically all the works dealing with carbon nanotubes and carbon (or metal) nanofibers. A comprehensive list of these can be found in the reviews of Refs. [26, 27]. For other filler types, researches which compared different particle shape-anisotropies considered for instance carbon black and carbon fibers [25, 39, 43], different graphite types [24], graphite and graphite nanosheets [41], graphene and graphite nanosheets [29, 44], copper spheres and fibers [15], and nickel flakes, fibers and powders [45]. To illustrate quantitatively the conductivity enhancement achievable by means of high aspect-ratios we display in Figure 2.5 four examples of composites filled with different spherical, fibrous and plate-like particles. To familiarize with the morphology of such composites, we then show four examples in Figure 2.6. We note that more specific aspects of the geometry of the filler particles (like e.g. their detailed shape or the presence of bending/coiling for fibers) will also have a role in the overall composite properties, but a generally minor one when compared to effect of shape-anisotropy and the correlated distinction between elongated and flattened objects.

We conclude this section by observing that another important filler particle characteristic is naturally its size. There is a general agreement that smaller average sizes lead to an enhancement of the conductivity. However, we defer a more detailed discussion about the size effects to Section 8.1.2.

2.1.2 Filler ensemble effects

In the previous section, we considered the effect of the single filler particle shape on the composite conductivity. In this section we are going to overview

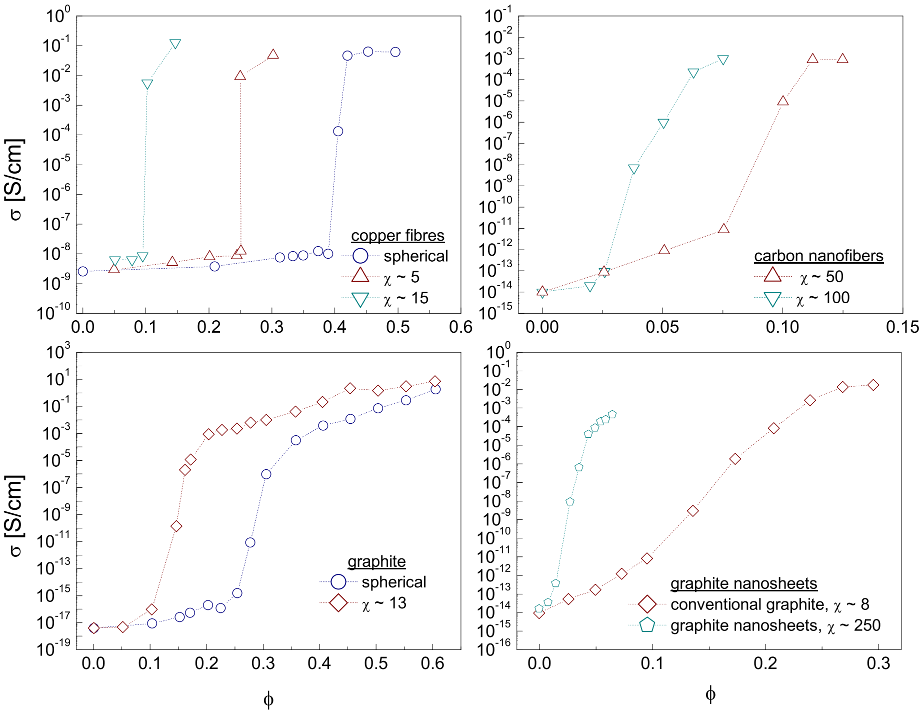

Figure 2.5: Four examples of the effect of the filler particle shape-anisotropy χ on the composite conductivity. *Top left*: Copper fibers (and spheres) in a styrene-butadiene rubber matrix, from Ref. [15]. *Top right*: Carbon nanofibers in a polypropylene matrix, from Ref. [40]. *Bottom left*: Graphite in a low density polyethylene matrix, from Ref. [24]. *Bottom right*: Graphite and graphite nanosheets in an epoxy matrix, from Ref. [41]. Systems with comparable particle sizes were considered.

the numerous effects and deviations which involve the filler particles as an ensemble. These can have a huge impact on the composite conductivity, and, unfortunately, can be quite difficult to control. Let us start with aspects of the filler ensemble itself. Perhaps the most important one is that fillers can have a *non-uniform particle size*. This is basically always the case, and fillers are characterized by particle size distributions (PSD) [46]. PSDs can be approximated by mathematical distributions like the log-normal one, but their exact form is often unknown. Moreover, the determination of the PSD for non-spherical fillers can be quite challenging. Since polydisperse systems can be packed more densely (this can be easily visualized if we think that the smaller particles can occupy the interstices left by the larger ones) we may expect that their composites will imply, at a given volume fraction, a

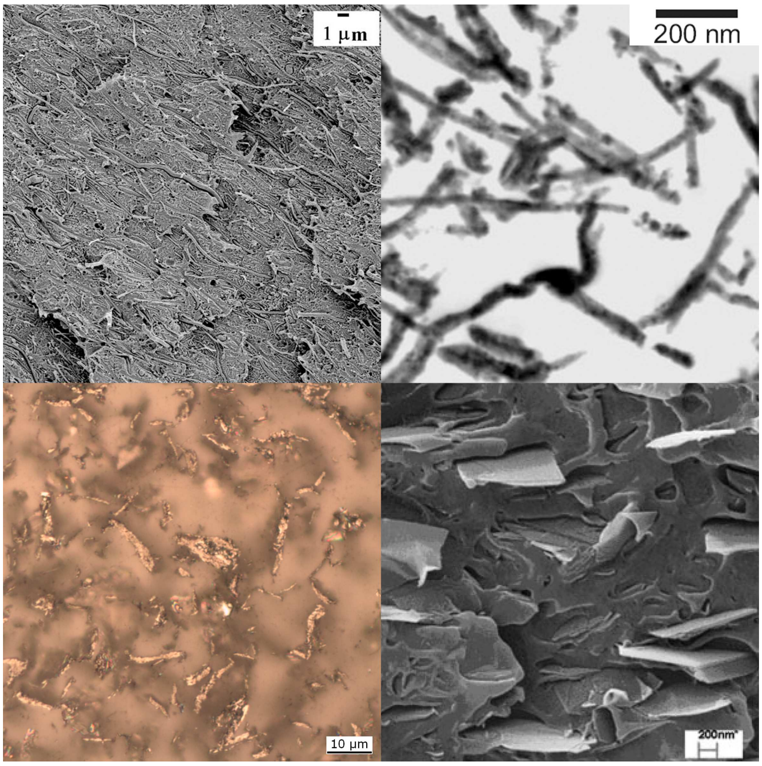

Figure 2.6: Four micrographs of aspherical filler conductive polymer composites. *Top left*: Carbon nanofibers in a high density polyethylene matrix, from Ref. [26]. *Top right*: Copper nanofibers in a polystyrene matrix, from Ref. [31]. *Bottom left*: Graphite in an epoxy matrix, present work. *Bottom right*: Graphite nanosheets in a acrylonitrile-styrene copolymer, from Ref. [42].

lower conductivity. This is indeed the case [18, 20], but the outcome will also depend on the specific form of the PSD. For example, as we will see in Chapter 7, strongly bi-disperse systems can lead to different effects. An aspect directly related to non-uniform particle sizes is *non-uniform particle aspect-ratio*. Being quite difficult to characterize, its effect on the composite conductivity is hard to evaluate experimentally. Fillers can also possess a *non-uniform particle geometry*, and have different forms or be bent, coiled or crumbled to different extents.

We have then a series of effects which come from the interaction of the filler particles with themselves and the polymer matrix, especially during the processing phase. These include, for instance, *particle orientation*, which is common with injection and compression molded composites containing aspherical fillers. Orientation leads to anisotropic conductivities [48] and to reduced conductivities with respect to a same volume fraction isotropic system [30]. Significative are also non-uniform filler dispersion effects. One

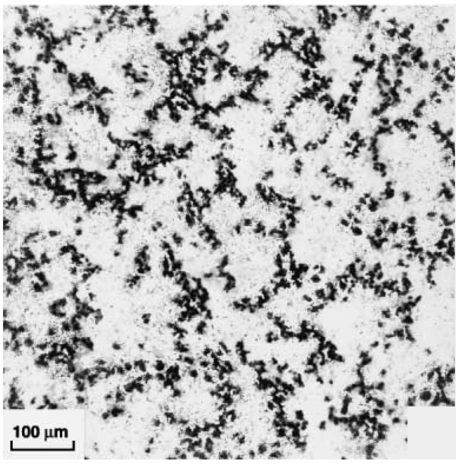

Figure 2.7: Micrograph of a segregated polyvinylchloride-nickel composite. Adapted from Reference [47].

is *particle agglomeration*, which is detrimental to the composite conductivity [49]. Another one is *particle segregation*. Segregation, which originates when connected filler-depleted and filler-enriched regions are formed, is a very important effect and, for a given filler volume fraction, enhances the composite conductivity. This condition may be generated on purpose by mixing in solid phase a conductive filler with significantly larger polymer particles and by molding the resulting compound [50]. An example is shown in Figure 2.7. There is then *particle sedimentation*, which originates typically from gravitational effects. Finally, *processing filler alterations* like e.g. fiber breaking can have relevant consequences on the composite conductivity.

2.2 Models of electrical conductivity in polymer composites

Since the earliest works of Gurland [8], it has been customary to associate the insulator-to-conductor transition of conductive polymer composites with the formation of a cluster of electrically connected filler particles which extends through the whole sample. The transport properties of such cluster will be defined by the conductances of the contacts between the particles (which are generally considerably smaller than the internal conductance of the particles themselves) and it is a natural step to map this system onto an equivalent resistor network. The resistor network will then share the same connection topology, the same conductances and thus the same (DC) electrical properties of the filler particles cluster. As the filler fraction is decreased, the globally connected network will shrink and eventually disappear (with

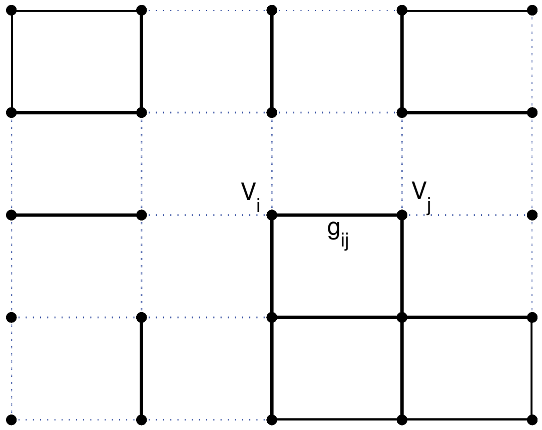

Figure 2.8: Example of a simple random resistor network. The empty bonds are shown as dashed lines while the occupied ones as solid lines. This figure is taken from Ref. [51].

the overall conductivity of the composite dropping abruptly to that of the polymer matrix). The increase of the conductivity for higher volume fractions (above the transition) is likewise interpreted as the growth of the global cluster. The mapping of the system on a resistor network reduces the study of the system to that of the network, which allows further simplifications by still retaining the essence of the problem. The first theoretical and numerical investigations of resistor networks were carried out by Kirkpatrick [1] and involved 2D and 3D cubic lattices, with the lattice sites representing the filler particles, where the sites were randomly occupied and nearest neighbors considered interconnected (site percolation model) or, similarly, where nearest neighbors were randomly interconnected by bonds of given conductance (bond percolation model). To illustrate this in further detail, let us consider a (two-dimensional) square lattice where the probability of having a bond of conductance $\varrho_{ij} = 1$ between, say, site i and (nearest neighbor) site j, is p and where, consequently, the probability of having that bond empty is $(1-p)$ [51]. The resulting system, called a random resistor network (RRN), is shown schematically in Figure 2.8.

Now, for such a system, as p is increased, the likelihood to have large connected clusters of sites spanning the lattice also increases, and, if we measure the conductance G by applying a unit voltage drop between two opposite edges of the lattice and measuring the current flowing through the network, G will also increase. In the same way, as p is decreased, the large clusters will disappear and the conductance will drop to zero. Comparing this with the interpretation of the insulator-to-conductor transition in composite ma-

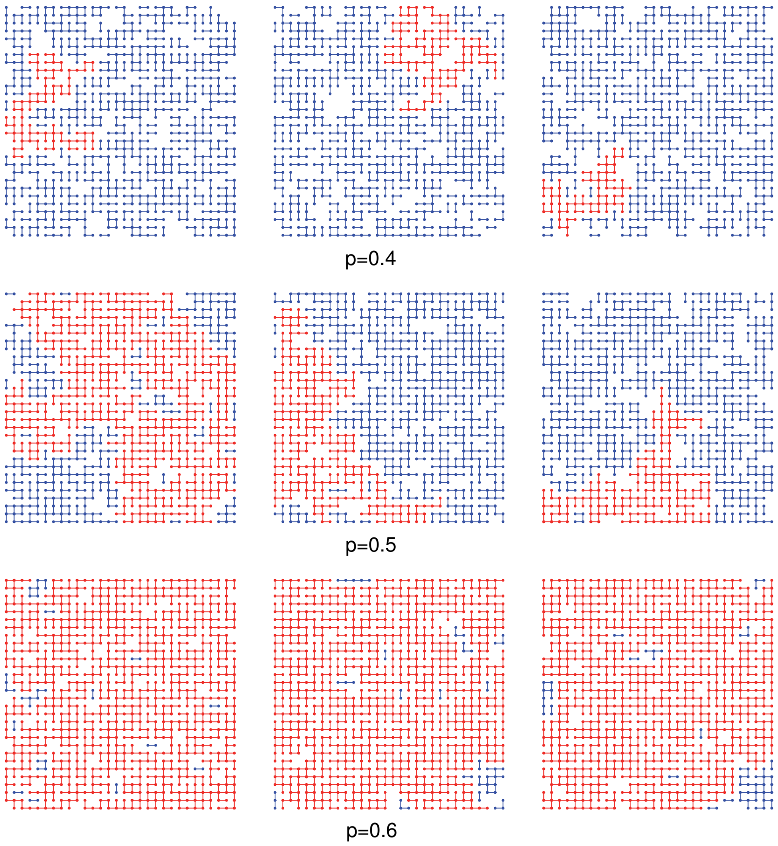

Figure 2.9: Three realizations of random resistor networks for three different bond occupation probabilities p. The largest cluster in the system is shown in red. This figure is taken from Ref. [51].

terials, we can grasp a certain correspondence between the bond occupation probability p and the filler volume fraction ϕ.

It is then a straightforward next step to study the effect of p on the RRN conductance by numerically replicating a large number of configurations with the same p and by recording the resulting conductance (if any). This is illustrated for three realizations and for three different values of p in Figure 2.9, with the largest connected cluster shown in red.

By observing Figure 2.9, we may get the idea that there will be values of p for which the system will almost never have a connected cluster spanning the lattice and, similarly, that there will be (larger) values of p for which there will be almost always such a cluster. It is also intuitive to realize that, the smaller our square lattice is, the more prone to local effects it will be, which implies in turn a less defined divide between the concentrations giving rise to always disconnected systems and the ones giving rise to always connected systems. This intuition is indeed correct, and for very large (eventually infinite) lattices the transition takes place at a well defined critical value of p, which we label p_c. The study of such connectivity problems and the investigation of the behavior of the system near the critical probability p_c is the subject of percolation theory [2], and it is customary to call p_c the percolation threshold. For the random bond resistor network on a square lattice, we have $p_c = 0.5$.

Percolation theory, which is a broad subject with applications ranging from forest fires to fluid flow in porous media [2], investigated such systems by and large, and tells us that the conductivity of an (infinite) RRNs above but near p_c will behave as a power law of the form [1, 2]

$$\sigma = \sigma_0 \left(p - p_c\right)^t . \tag{2.1}$$

In this equation, σ_0 is a pre-factor and t is the DC transport critical exponent. We note that, to avoid the geometrical dependence of the conductance G, we used here, as we will in the following, the conductivity σ of the system, which in the case of a square or cubic lattice is related to G by the relation $\sigma = GL^{\mathrm{D}-2}$, where L is the lattice size and D the system dimensionality. The transport exponent t, as any critical exponent, is expected to depend only on the dimensionality of the system, and not on its structural details like e.g. the lattice type (square, triangular, honeycomb), and its value is currently estimated at $t \simeq 1.3$ in two dimensions and at $t \simeq 2$ in three dimensions. However, like in the case where the bond conductances ϱ do not have anymore a fixed value but follow a singular conductance distribution, t can take different (larger) values. The so-called transport non-universality is also found experimentally and several works have been devoted to it. A comprehensive account can be found in Ref. [51]. We finally note that the above described random resistor networks involved bond occupation probabilities and thus fall in the category of bond percolation systems. Similarly, it is possible to construct site percolation systems, where a site has a certain probability p^s to be occupied and where two neighboring sites which happen to be occupied are considered as connected. However, near the percolation threshold this system is still described by the power law (2.1) (with p^s instead of p). The site percolation model has the advantage of displaying a more clear correspondence between p^s and the volume fraction ϕ of a composite.

2.2.1 Continuum percolation models

The lattice representation of the connected networks of conductor-insulator composites is somehow restrictive, and, as a consequence, off-lattice or continuum models have been introduced, where the constituents of the system are now free to randomly occupy the space and assume anisotropic configurations. One of the first continuum models was the “swiss cheese” model

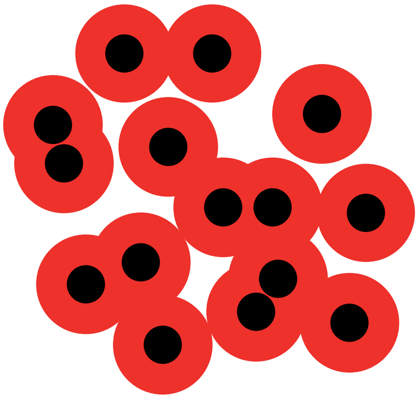

Figure 2.10: Schematic illustration of the hard-core-penetrable-shell model with the hard particles shown in black and the penetrable shells shown in red. This figure is taken from Ref. [60].

of Feng, Halperin and Sen [52], which is constructed by randomly placing (mono-sized) spherical insulating voids in an uniform conductive medium. A strictly correlated system introduced by the same authors is the inverted swiss cheese or inverted random void model, which exchanges the insulating and conducting phases, i.e. considers random distributions of overlapping conductive spheres in an insulating matrix. Clearly, this latter systems starts to be a quite good representation of a real conductive polymer composite. However, real spherical filler are generally constituted of solid particles, and a model more representative of the composite microstructure would be one where the spheres are not allowed to overlap. The problem of such a system is that equally-sized hard spheres randomly dispersed in the continuum originate contacts and global connectivity only at the close packing limit, at a volume fraction of $\phi \simeq 0.64$ [53], way higher than the filling fractions at which the insulator-to-conductor transition is experimentally observed. To counter this issue and to introduce a more versatile connectivity criterion between the particles, it became customary to coat the hard spheres by a penetrable shell of constant thickness and to consider them as connected if their shells overlap. In other words, a cutoff on the minimal distance between two spheres is introduced below which these are considered connected and beyond which these are considered disconnected. This formulation is called hard-core-penetrable-shell model or cherry-pit model [11, 18, 54–60] and a schematic illustration is shown in Figure 2.10.

The hard-core-penetrable-shell model has also been extended to non-spherical particle shapes, especially for elongated objects like e.g. sticks [55, 61–63] or ellipsoids of revolution [64], while general triaxial ellipsoids were considered in Ref. [65].

Also for these continuum systems, if we associate to every connected particle couple a bond of a certain conductance, near the critical concentration, the bulk conductivity will again follow a power law of the form of (2.1), which we can rewrite in terms of the filler volume fraction ϕ as

$$\sigma = \sigma_0 \left(\phi - \phi_c\right)^t \tag{2.2}$$

and, if the bond conductances distribution is not singular, the critical exponent t will be again $t \simeq 2$ [51]. However, if t is (under these conditions) universal, the percolation critical concentration ϕ_c is system-dependent and will vary for different particle morphologies. The percolation critical concentration is for many real cases the most important quantity, and of the above quoted studies of the hard-core-penetrable-shell model most dealt with the exploration of the system configuration influences on ϕ_c, with the exception of Refs. [11, 60], which also considered conductivity.

2.2.2 Inter-particle conduction mechanisms

So far, we have described the insulator-to-conductor transition in composite materials in the framework of percolation theory, and considered the conductive networks which are formed as originating from the contacts between the microscopic filler particles. However, when dealing with such microscopic systems, some care must be taken with the concept of contact. The considerations which led to the introduction of the hard-core-penetrable-shell model have already shown how a pure contact model can lead to difficulties. Moreover, electrons can flow also through a sufficiently small insulating barrier owing to quantum mechanical tunneling [66], and tunneling is considered as the main transport mechanism in composite materials near the transition region [67–71]. By studying the temperature and high field behavior [72, 73] as well as the alternating current (AC) stress behavior [74] of carbon black-polyvinylchloride composites, Sheng and co-workers showed in their pioneering works of the late seventies how the results could be optimally interpreted in terms of fluctuation-induced tunneling. Tunneling was again identified as the dominating contribution to conduction by measuring field, temperature and pressure dependencies of graphite nanosheet-epoxy and polyurethane composites [75, 76], and the same conclusion was drawn for a conductive polymer filler in a polycarbonate matrix [77]. By using an approach which shares some similarities with the rationale of the experimental results interpretation of Chapter 6, tunneling was once more held responsible for the transport properties of a graphite-polyethylene composite by the authors of Ref. [23]. Finally, direct measurements of the conductances between two isolated filler particles in air and in an insulating liquid as a function of the particles inter-distance have clearly evidenced a tunneling region before the origination of true contact [11, 71]. An example for gold particles in air is shown in Figure 2.11.

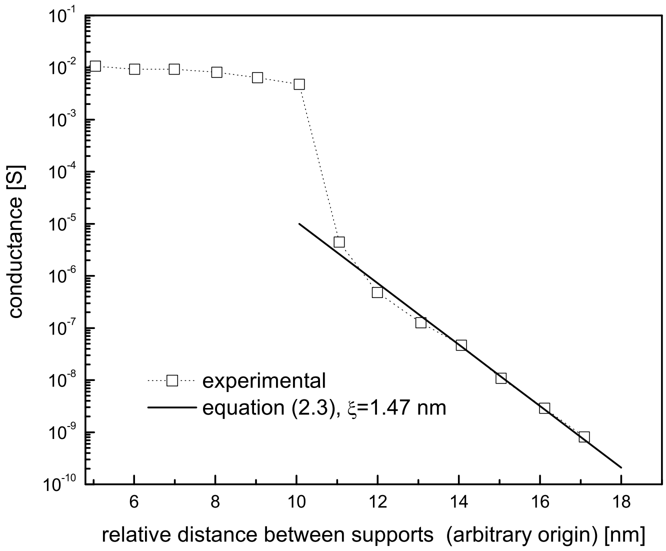

Figure 2.11: Electrical conductance between two (roughly) spherical gold particles with a diameter of $\sim$ 10 μm brought together at a speed of 1 nm/s. The large jump near 10 nm is attributed to the formation of physical contact. The tunneling region results have been fitted with Equation (2.3). Adapted from Ref. [11].

Now, the tunneling conductance between a filler particle pair i, j can be written in the simplified form [69]:

$$\varrho^{ij} = \varrho_0 \exp\left(-\frac{2\delta^{ij}}{\xi}\right) \tag{2.3}$$

where ξ is the characteristic tunneling length, which measures the electron wave function decay within the polymer, δ^{ij} is the minimal distance between the two particles surfaces, and ϱ_0 a pre-factor which for the time being we consider as constant. Further details about the form of the tunneling conductance ϱ^{ij} will be given in Chapter 5. We applied Equation (2.3) to the results of Figure 2.11, extracting $\xi \simeq 1.47$ nm, within its expected value range [69] (a more thorough overview of the values of ξ can be found in Chapter 6). So, tunneling conductances show a typical exponential decay with the increase of the separation between the particles, and tunneling gives a significative contribution to the inter-particle transport when these are closer than a few tens of nanometers. However, it is also clear that tunneling conduction, albeit decaying fast, does not imply a sharp cutoff of the connectivity between the particles as these are brought further apart. For large fillers, with average sizes of several microns, the characteristic dimensions of the system are considerably larger that ξ and a sharp cutoff “on-off” description of the contacts can be adequate. Nevertheless, this ceases to hold for fillers such as nanotubes, nanofibers, nanosheets and nanospheres, which have one or more characteristic dimensions that are comparable with the typical distances of tunneling. In these cases, the detailed behavior of tunneling has to be taken into account, including the absence of a cutoff. There is thus a dichotomy between a percolation description, requiring a well defined distinction between connected and disconnected objects, and one involving tunneling. To show how a global tunneling network description of polymer composites containing nanometric fillers can account for the experimentally observed conductivity versus volume fraction results is one of the main aims of the present thesis.

We conclude this section by observing that tunneling and percolation have been combined to explain the non-universality of the critical transport exponent t [51, 60, 69, 78], but all these descriptions involved an interaction cutoff to induce percolation.

2.3 Towards a microscopically-based model of conductivity in nanocomposites

The overview of the last section focused on models of conductivity in composite materials which where based on a more or less faithful reproduction of their microscopic structure. It should be noted that there is also a certain number of percolation-based models which try to obviate to the predictive shortcomings of the original formulation by including phenomenologically justified correction terms, and further details can be found in Refs. [71,79,80]. However, we believe that with the nowadays computing power, a direct bottom-up investigation carried out with numerical simulation techniques enables to gain unprecedented insights into the true transport phenomena which are at the origin of the electric properties of conductive polymer composites. This thesis will thus focus on the construction of improved microscopically-based models which explicitly take into account aspects such as the filler particle shape and the inter-particle conduction mechanism and which try to explain and reproduce the experimentally observed filler volume fraction dependence of the composite conductivity. These models will be geared towards nanocomposites, and electron tunneling conduction will play a major role.

Chapter 3

Numerical replications of the composite morphology

A fundamental aspect of the numerical investigation of the physical properties of particle-loaded composite materials is the re-creation of their relevant microscopic features with computer simulation routines. In this chapter, we give the details of the procedures used in the present thesis and describe an algorithm which generates random distributions of non-overlapping ellipsoids of revolution and that calculates their inter-distance (meant as the minimal distance between two ellipsoid surfaces), this latter being an important quantity for the analysis of the next chapters.

3.1 Modeling filler particles with ellipsoids of revolution

In the numerical replications of our composites, we want to describe filler particle shapes which can vary from rod-like to plate-like. For that purpose, the most versatile geometrical form defined by simple surface equations is perhaps the ellipsoid of revolution, also called spheroid. A spheroid is an ellipsoids with two equal axes and may be obtained by rotation of a 2D ellipse around one of its symmetry axes. The reasons for preferring spheroids to more general triaxial ellipsoids are twofold: firstly, spheroids are characterized by a smaller number of parameters (7 against 9 of the general ellipsoid); secondly, experimental measurement techniques of the filler particle size distributions are generally able to extract only major and minor dimensions, making it difficult to quantitatively define a size distribution for the third axis.

Spheroids will have a polar axis (the one around which the 2D ellipse was rotated) and an equatorial axis (corresponding to the other symmetry axis of the 2D ellipse). If we label a and b the polar and the equatorial

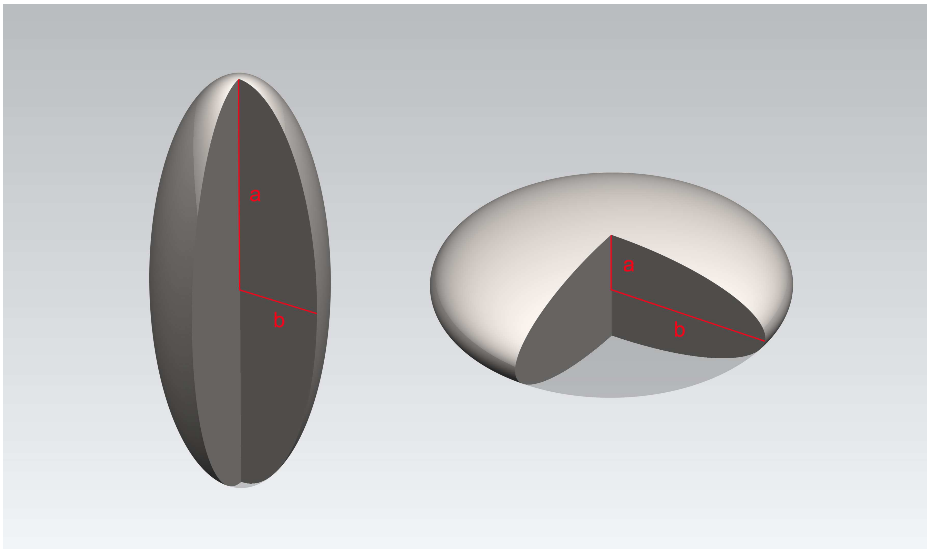

Figure 3.1: Illustration of a prolate (left) and an oblate (right) ellipsoid of revolution (spheroid).

semi-axes respectively, we can identify two main spheroid families: those with $a > b$, which are called prolate, and those with $a < b$, which are called oblate. A special case is that of the sphere, with $a = b$. The volume of a spheroid is $V = 4\pi ab^2/3$. An example of a prolate and an oblate spheroid is shown in Figure 3.1. The shapes of ellipsoids of revolution are completely defined by their polar-to-equatorial semi-axes ratio a/b, which is customarily called aspect-ratio. A related quantity introduced in the last chapter is the shape-anisotropy χ, which in the case of spheroids will have the form $\chi = \max(a,b)/\min(a,b)$. Obviously, χ will always take values which are equal or greater than 1, while a/b will be larger than 1 in the prolate case and comprised between 0 and 1 for the oblate case. However, it is common usage to refer to both the extreme prolate ($a/b \gg 1$) and the extreme oblate ($a/b \ll 1$) limits as high aspect-ratio, although it would be correct to say high shape-anisotropy.

To build an algorithm which generates distributions of non-overlapping spheroids and that can evaluate the minimal distance between two spheroid surfaces we may require two functions, an ellipsoid overlap criterion and the distance between two ellipsoids, the first being needed of course only if it can be computed in a time consistently shorter than the second. For $a \neq b$, none of these functions allows simple closed form solutions, but some evaluation techniques are nevertheless available [81–83]. We have chosen the approach proposed by Rimon and Boyd (R&B) [84, 85] which was used for an obstacle collision detection procedure for robots, where short computational times are essential. The R&B technique allows two key benefits: 1) A quick estimation procedure of the distance between two ellipsoids that uses standard computation routines and that can be made sufficiently precise. 2) An overlap criterion between two ellipsoids as an intermediate result to the inter-distance computation that can be calculated in about half the time needed for the complete calculation. The computation is based on a formula for the distance of a point from an ellipsoid which reduces the problem to the calculation of the minimal eigenvalue of an auxiliary matrix constructed from the geometrical data. In more detail, given two ellipsoids ε_A and ε_B identified by their 3x3 form matrices $\hat{A}$ and $\hat{B}$ and centered in $\mathbf{c}_A$ and $\mathbf{c}_B$ respectively,

$$\varepsilon_A \quad : \quad (\mathbf{x}-\mathbf{c}_A)^T \hat{A}\,(\mathbf{x}-\mathbf{c}_A) = 0 \tag{3.1}$$

$$\varepsilon_B \quad : \quad (\mathbf{x}-\mathbf{c}_B)^T \hat{B}\,(\mathbf{x}-\mathbf{c}_B) = 0 \tag{3.2}$$

where $\mathbf{x}$ is the position vector defining the ellipsoidal surfaces, we have that the minimal distance δ between the ellipsoids can be estimated as:

$$\delta(\varepsilon_A, \varepsilon_B) = \|\mathbf{x}^* - \mathbf{y}^*\| \tag{3.3}$$

where

$$\mathbf{x}^* = \mathbf{c}_A + \lambda \hat{A}^{-\frac{1}{2}} \left[\lambda\, \mathbf{I}_{3x3} - \widehat{ABA}^{-1} \right]^{-1} \hat{A}^{\frac{1}{2}} (\mathbf{c}_B - \mathbf{c}_A) \tag{3.4}$$

and where we have introduced

$$\widehat{ABA} \equiv \hat{A}^{-\frac{1}{2}} \hat{B} \hat{A}^{-\frac{1}{2}}. \tag{3.5}$$

λ is the minimal eigenvalue of the 6x6 matrix

$$\begin{pmatrix} \widehat{ABA}^{-1} & -\mathbf{I}_{3x3} \\ -\left[\widehat{ABA}^{-\frac{1}{2}} \hat{A}^{\frac{1}{2}} (\mathbf{c}_B - \mathbf{c}_A)\right] \left[\widehat{ABA}^{-\frac{1}{2}} \hat{A}^{\frac{1}{2}} (\mathbf{c}_B - \mathbf{c}_A)\right]^T & \widehat{ABA}^{-1} \end{pmatrix} \tag{3.6}$$

while

$$\mathbf{y}^* = \mathbf{x}^* + \mu \left[\mu\, \mathbf{I}_{3x3} - \hat{A}^{-1} \right] (\mathbf{c}_A - \mathbf{x}^*) \tag{3.7}$$

and μ is the minimal eigenvalue of the 6x6 matrix

$$\begin{pmatrix} \hat{A}^{-1} & -\mathbf{I}_{3x3} \\ -\left[\hat{A}^{-\frac{1}{2}} (\mathbf{c}_A - \mathbf{x}^*)\right] \left[\hat{A}^{-\frac{1}{2}} (\mathbf{c}_A - \mathbf{x}^*)\right]^T & \hat{A}^{-1} \end{pmatrix} \tag{3.8}$$

$\mathbf{I}_{3x3}$ is naturally the 3x3 identity matrix.

The overlap criterion spurs from $\mathbf{x}^*$ alone. If we construct the quantity

$$m(\varepsilon_A, \varepsilon_B) \equiv (\mathbf{x}^* - \mathbf{c}_A)^T \hat{A} (\mathbf{x}^* - \mathbf{c}_A) - 1 \tag{3.9}$$

we will have that

$$\begin{cases} m < 0 & \varepsilon_A, \varepsilon_B \text{ overlap} \\ m = 0 & \varepsilon_A, \varepsilon_B \text{ touch} \\ m > 0 & \text{otherwise} \end{cases} \tag{3.10}$$

The algorithm implementation followed then the route outlined by R&B [84, 85] although in the present case we have used FORTRAN 90 instead of C as programming language.

3.2 Distribution generation procedure

We are now going to outline how the distribution generation algorithm is constructed. Its architecture is based on a program for spherical particles written by Niklaus Johner, a description of which can be found in Ref. [51]. The present version is extended to equally-sized non-spherical particles and to include a high density generation routine. Figure 3.2 shows examples of the generated distributions for spheroids with different aspect-ratios a/b and volume fractions ϕ obtained by loading the configuration output files into the software [86] used as a viewer.

3.2.1 Random sequential addition

In the first step of the generation procedure, a spheroid distribution is created inside a cubic cell of volume L^3 with periodic boundary conditions via random sequential addition (RSA): for every new particle, random placing is attempted and accepted as valid only if there is no overlap with any neighboring particle. The spheroid angles are generated as to assure an isotropic distribution of orientations [87, 88]. For that purpose, if $\bar{r}_1 \cdots \bar{r}_n$ is the outcome of a random number generator with uniform distribution over the [0,1] interval, and Θ, Φ the azimuthal and polar angles respectively of the spheroid symmetry axis, then we may obtain an isotropic orientation distribution by generating the angles as $\Phi = 2\pi\bar{r}_i$ and $\Theta = \arccos(1 - 2\bar{r}_{i+1})$. The absence of global orientation was verified by monitoring the nematic order parameter S [63, 89], which is the largest eigenvalue of the tensor

$$Q_{ij} = \frac{1}{2N} \sum_{\mu=1}^{N} \left(3u_i^\mu u_j^\mu - \delta_{ij} \right), \tag{3.11}$$

where $i, j = x, y, z$, u_i^μ is the i component of the unit vector defining the orientation of particle μ, δ_{ij} the Kronecker delta, and N the total particle number. S is zero for a perfectly isotropic configuration while it is unity for fully aligned configurations.

To speed up the search for neighbors, the main cubic cell is subdivided in discrete (cubic) binning cells of size comparable to the major dimension of

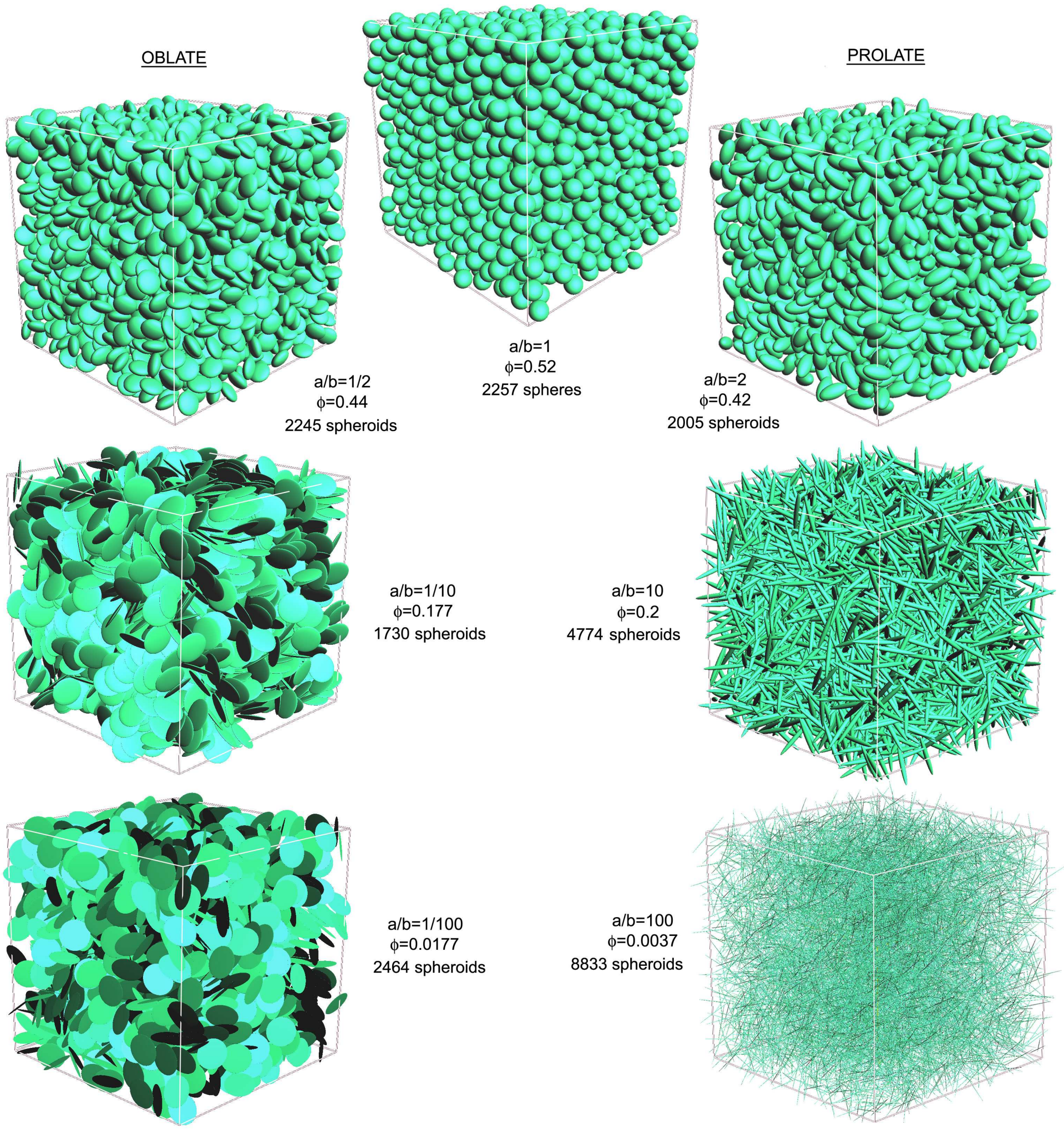

Figure 3.2: Examples of distributions of impenetrable spheres and spheroids of different aspect-ratios a/b and volume fraction ϕ generated by the algorithms used in the present work.

the spheroids, so that potential overlapping neighbors can be only either in the cell where the trial spheroid landed in or in the 26 adjacent cells. Then, when checking for overlap, simple geometrical criteria to identify neighbors which are distant enough as not to be able to lead to an overlap in any case are used to avoid unnecessary computations of the time-consuming R&B

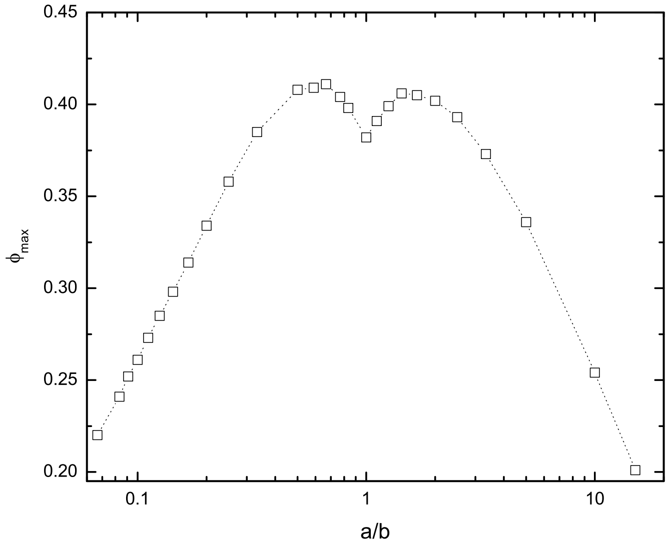

Figure 3.3: Maximum volume fraction ϕ_{max} achievable with random sequential addition as a function of the spheroid aspect-ratio a/b. Adapted from Ref. [90].

function.

The generation of particle distributions with random sequential addition has the advantages of being quick and that the obtained particle ensemble has an isotropic orientation distribution. However, it has also has two drawbacks. The first one is that RSA dispersions are non-equilibrium configurations [57]. The second one is that RSA has an upper limit in the volume fractions that can be achieved [90], and, near that limit, slows down enormously. The maximum volume fractions obtainable with RSA for different aspect-ratio spheroids are reported in Figure 3.3, and we may note that these are significantly lower than the random close packing limit [53, 91].

3.2.2 System relaxation

To allow the generated configurations to attain equilibrium, the systems are relaxed via Monte Carlo (MC) runs [92, 93]: For each spheroid, random displacement of its center and random rotation of its axes is attempted and accepted if it does not give rise to an overlap with any of its neighbors. After having attempted to move once every particle of the distribution, i.e. after the so-called sweep, the process is reiterated. The random rotations are generated by adding to the (unit) vector specifying the orientation of a given particle a vector of fixed length but with an orientation chosen at random and by using the resulting vector as the new spheroid orientation [93]. The magnitudes of the random displacement and rotation are chosen as to lead to an average acceptance of 20-30 per cent. To verify that equilibrium is attained, for the special case of spheres the radial distribution function is sampled and confronted with known results [57,94]. For the case of spheroids, equilibrium is considered attained when the ratio between the number of accepted trial moves versus the number of rejected ones has stabilized around a certain value, and needs typically some thousand MC sweeps for high density configurations.

3.2.3 Generation of high-density distributions

To investigate densities above the ones obtainable through RSA, we implemented a high density generation procedure which is somehow similar to that of Ref. [94]. After having generated a spheroids distribution close to the RSA limit, these are moved with MC sweeps, where, in contemporary with the trial move, it is attempted to inflate the spheroids by increasing their axes by a small amount. Again, the trial moves/inflations are accepted only if no overlap with neighboring particles is originating. Once the desired volume fraction is reached, the system is relaxed with several “regular” MC sweeps.

3.2.4 Inter-particle distance computation

As a last step, the inter-particle distance is computed. To do this, a first R&B calculation is executed, then the computation is continued by performing the R&B calculation with exchanged spheroids, since the R&B procedure does not treat the spheroid couple in a symmetrical fashion. Successively, the outcomes of the two calculations are compared and the shortest one is retained. Finally, a part of the R&B computation is reiterated to obtain a further correction. When comparing the results with a more accurate but much slower distance evaluation routine, this procedure leads to a distance estimate that has an average error of about $+1$ % on a wide range of distance to major spheroid dimension ratios (from 10^{-4} to 10).

3.3 Some observations on the phase diagram of the hard ellipsoid fluid

When modeling a composite with equilibrium hard spheroid distributions, it is important to consider some aspects of the phase diagram of these systems. The first numerical investigations of the phases of the hard ellipsoid of revolution fluid go back to the classic work of Frenkel and Mulder [93], where four distinct phases were identified i.e. isotropic fluid, nematic fluid, plastic solid, and ordered solid. The authors also drew a phase diagram, which is

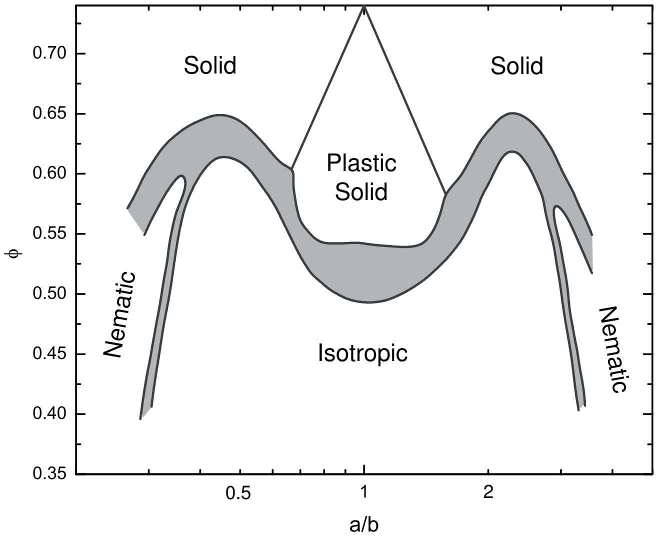

Figure 3.4: The Frenkel and Mulder hard spheroid fluid phase diagram [93]. The gray areas are coexistence regions. Adapted from Ref. [95].

reported in Figure 3.4. For our purposes, the most important aspect is the presence of the nematic fluid phase, where the equilibrium configurations have a high orientational order. This is because for high shape-anisotropy particles the isotropic-nematic (I-N) transition is located at quite low volume fractions. On the other side, we may want to generate configurations with volume fractions above the transition and still retain the isotropy of the spheroid orientation, since in real composites the transition to the nematic phase is hampered by the viscosity of the polymer matrix and these systems are inherently out of equilibrium [96]. When this situation occurred, we generated the distribution with random sequential addition alone, without successive Monte Carlo relaxation.

Now, to estimate the I-N transition for spheroids with higher shape-anisotropy than those considered in the Frenkel and Mulder phase diagram, we can use directly available results [97], or extrapolate from the results for zero thickness hard disks [98, 99] for sufficiently thin oblate spheroids, or use the Onsager model [100] for sufficiently high aspect-ratio prolate spheroids. In more detail, for the case of thin oblate spheroids, we have that the lowest limit of the I-N coexistence area may be estimated as $\phi_I \simeq \rho_I \pi(a/b)/6$ and the highest limit as $\phi_N \simeq \rho_N \pi(a/b)/6$, where $\rho_I = 3.68$ and $\rho_N = 3.98$ are the coexistence particle number densities for unitary diameter infinitely thin hard disks [99]. For high aspect-ratio prolate spheroids, from the Onsager theory for slender rods we can estimate $\phi_I \simeq (2/3)c_I/(a/b)$ and $\phi_N \simeq (2/3)c_N/(a/b)$ with $c_I = 2\pi a^2 b \rho_I \simeq 3.29$ and $c_N = 2\pi a^2 b \rho_N \simeq 4.19$ [101, 102].

Prolate			Oblate		
a/b	ϕ_I	ϕ_N	a/b	ϕ_I	ϕ_N
10	$0.207^\dagger$		$1/10$	$0.185^\dagger$	
10	0.219	0.279	$1/10$	0.193	0.208
50	0.0439	0.0559	$1/50$	0.0385	0.0417
100	0.0219	0.0279	$1/100$	0.0193	0.0208
200	0.0110	0.0140	$1/200$	0.0096	0.0104
300	0.0073	0.0093	$1/300$	0.0064	0.0070
500	0.00439	0.00559	$1/500$	0.00385	0.00417
1000	0.00219	0.00279	$1/1000$	0.00193	0.00208
2000	0.00110	0.00140	$1/2000$	0.00096	0.00104
3000	0.00073	0.00093	$1/3000$	0.00064	0.00069

† simulation results from Ref. [97]

Table 3.1: Isotropic and nematic coexistence volume fractions ϕ_I and ϕ_N for high shape-anisotropy prolate and oblate spheroids as extrapolated from the results for infinitely thin hard disks [98, 99] and from the Onsager theory [101, 102].

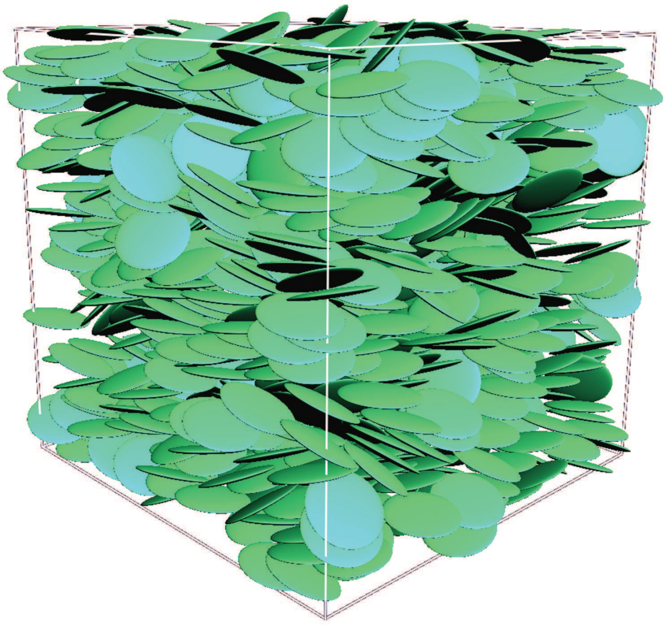

Figure 3.5: Example of a nematic distribution of oblate spheroids with $a/b = 1/10$ at $\phi = 0.23$. The system was relaxed from the original RSA configuration with 10^5 MC sweeps. The nematic order parameter is $S = 0.755$.

The estimates of ϕ_I and ϕ_N for prolate and oblate spheroids with selected values of aspect-ratio can be found in Table 3.1. An example of a nematic distribution of oblate spheroids with $a/b = 1/10$ at $\phi = 0.23$ is displayed in Figure 3.5. The nematic order parameter is $S = 0.755$. The system was relaxed from the original random sequential addition configuration with 10^5 Monte Carlo sweeps, and it is interesting to observe that the same number of sweeps was used for the $a/b = 1/10$ and $\phi = 0.177$ configuration of Figure 3.2 (the distribution is the left middle one), which has clearly no global preferred orientation (the nematic order parameter is $S = 0.046$).

It is finally interesting to make some considerations about the random close packing limit of spheroid distributions [53, 91]. This is taking place at higher densities than the isotropic-nematic transition and is most of the times outside our region of interest, especially for non extreme shape-anisotropy values. However, for high aspect-ratio prolate systems, this limit can go quite low, as can be evaluated by means of the asymptotic scaling relation of Ref. [103]

$$\phi_{RCP} \simeq \frac{2}{3}\frac{5.4}{a/b}, \tag{3.12}$$

which is valid for $a/b > 10$. The 2/3 factor comes from the fact that the original result was for spherocylinders (which are cylinders capped with semi-spheres of the same diameter as the cylinder).

Chapter 4

Connectivity-based models

Connectivity-based geometrical percolation models have occupied a large part of the literature aimed at explaining the insulator-conductor transition of conductive polymer composites. The hard-core-penetrable-shell formulation is perhaps the most faithful to the microscopic morphology of the composites, and in the present chapter we are going to present the results that were obtained for hard prolate and oblate spheroids surrounded with a penetrable shell with an unprecedented broad range of aspect-ratios and shell thicknesses. It is important to note that these results are not an end in themselves but will have a crucial role in the conductivity evaluation procedures of Chapter 6. Successively, we will introduce some techniques which allow to estimate fundamental quantities like the critical volume fraction (or, equivalently, the critical shell thickness) starting from few parameters like the spheroid aspect-ratio and the shell thickness (or the system volume fraction). Finally, we will briefly consider some results of the hard-core-penetrable-shell model with conductivity.

4.1 Percolation properties of hard ellipsoids of revolution with a penetrable shell

As we saw in Section 2, a large part of the continuum geometrical percolation studies dealt with spherical inclusions. However, a broad range of fillers in real composites have forms which deviate consistently from the sphere. Previous investigations have considered different particle shapes like e.g. sticks [54, 87, 104–106],wavy sticks [107], plates [28, 108, 109], ellipsoids [88, 110–112] or soft-core prisms [113] in the fully penetrable case, where the particles are allowed to freely overlap. Only a few works dealt with non-spherical hard objects surrounded with a penetrable shell like hard sticks [55, 61–63] or triaxial polydisperse ellipsoids [65], while a recent paper [64] contemplated, as in the present work, the case of hard ellipsoids of revolution but only in the prolate domain. The widespread use of composites containing fibrous fillers has made the stick, or other elongated objects, the favorite non-spherical shape in many studies. Nevertheless, some other fillers, notably graphite and graphene sheets, have shapes which are better assimilable to flattened ellipsoids or platelets, and over a broad range of aspect-ratios. Therefore, the exploration of the relatively uncharted terrain of the percolative properties of oblate objects as a function of their aspect-ratio is one of the aims of this chapter.

Our model is defined by a dispersion of impenetrable spheroids of identical dimensions with isotropic distribution of the symmetry axis orientation. Following the hard-core-penetrable-shell model, given any two spheroids, a connectivity criterion is introduced by allowing an upper cutoff distance, δ, beyond which the two spheroids are considered disconnected. More precisely, each spheroid is coated with a penetrable shell of constant thickness d, and two particles are connected if their shells overlap. Obviously, we have $\delta = 2d$. Note that the inclusion of a constant thickness shell leads to a shape of the total object which is not anymore that of a spheroid. On the other side, a penetrable shell consisting of an enlarged spheroid, as done in Ref. [64] for the case of prolate ellipsoids, implies increasingly non-uniform shell thicknesses as the aspect-ratio gets higher.

To carry out the numerical investigation we exploited the algorithm described in the last chapter to generate random distribution of impenetrable spheroids inside a cubic cell with periodic boundary conditions. Then, once the desired distribution had been created and the neighboring particles inter-distances computed, the distribution algorithm output data were fed into a program described in Ref. [51] which isolates the connected particle cluster using a modified version of the classic Hoshen-Kopelman algorithm [2, 114, 115]. Finally, it was verified if the connected cluster spanned two specific opposite sides of the simulation cell, the necessary condition to consider the system as percolating.

4.1.1 Random sequential addition results with finite size scaling

To explore the percolation properties of hard spheroids surrounded with a penetrable shell of constant thickness, let us start with an investigation of the effect of the system size. It is intuitive that larger systems will be more representative of the bulk material and, to get a feeling of how quickly the bulk regime is reached, it is sufficient to consider that one cubic centimeter of a composite loaded at $\phi = 0.4$ with 5 μm diameter spherical particles contains more than six billion of them [71]. Furthermore, we already encountered some aspects of the system size dependence when we considered random resistor networks in Chapter 2. Percolation theory is well equipped to deal with size effects and we are now going to apply some of its results to our case. For that purpose, we considered oblate spheroids with an aspect-ratio between 1 (spheres) and 1/100. The ratio of the cutoff distance δ to twice the spheroid major axis, $\delta/2b$, was chosen to variate between 0.05 and 4.0. Introducing $D \equiv 2\max(a,b) = 2b$, we rewrite this ratio as δ/D.

Since the investigation of size scaling requires large systems, we limited the distribution generation procedure to pure random sequential addition, because Monte Carlo relaxation would have been too time consuming. The thinnest shell limit was then bounded to the maximum volume fraction which can be achieved through random sequential addition (see previous chapter) for the $a/b = 1$ (spheres) case.

To extrapolate the infinite system percolation threshold from the simulation results we followed finite-size scaling arguments as described in Ref. [116] and briefly outlined below. For a given size L of the cube, we obtained the spanning probability as a function of the spheroid volume fraction by recording the number of times a percolating cluster appeared over a given number of realizations. The resulting spanning probabilities were then plotted against the volume fraction and fitted with the sigmoidal function

$$f = \frac{1}{2}\left[1 + \tanh\left(\frac{\phi - \phi_c^{\text{eff}}}{\Delta}\right)\right] \quad , \tag{4.1}$$

where ϕ_c^{eff} for a given value of L corresponds to the hard particle volume fraction at which the spanning probability is equal to 1/2, while Δ represents the width of the percolation transition. In Fig. 4.1 we report the obtained spanning probability as a function of ϕ for $a/b = 1$ and $a/b = 1/2$ and for selected values of the cell size L. The cutoff distance was set equal to $\delta/D = 0.1111$. One can appreciate how larger systems imply a more defined transition. Now, both ϕ_c^{eff} and Δ depend on the size L of the system and, by following the scaling arguments of [116], allow us to deduce the percolation threshold ϕ_c for the infinite system through the following scaling relations:

$$\Delta(L) \propto L^{-\frac{1}{\nu}}, \tag{4.2}$$

$$\phi_c^{\text{eff}}(L) - \phi_c \propto L^{-\frac{1}{\nu}}, \tag{4.3}$$

where ν is the correlation length exponent. By repeating the simulation procedure for different cell sizes it is possible, via the percolation transition widths Δ and the inversion of Eq. (4.2), to extract ν and consequently, from Eq. (4.3), the percolation threshold ϕ_c for $L = \infty$. We choose to simulate ten different cell sizes, $L = 10$, 13, 15, 17, 20, 23, 25, 27, 30 and 35 times the major spheroid dimension D. For thick shells ($\delta/D \geq 1.0$) the cell sizes were increased further. The spheroid number was in the order of thousands for the smallest cells up to about $70'000$ for the largest. The number of realizations per volume fraction step varied from 50 for the smallest shell thickness up to 400 for the thicker ones. Higher realization numbers did not show appreciable

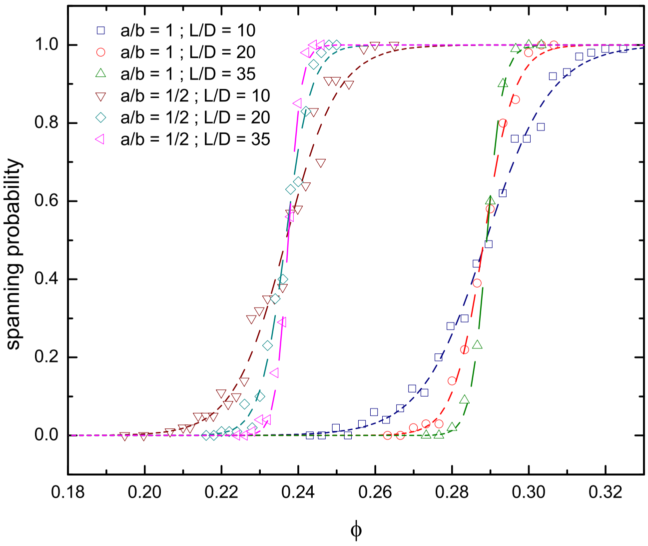

Figure 4.1: Percolation width variation with the increase of the simulation cell size for the aspect-ratio a/b=1 and a/b=1/2 cases. $\delta/D = 0.1111$.

improvements. This may be illustrated more concretely by considering one specific example: for the aspect-ratio $a/b = 3$ and cutoff distance $\delta/D = 0.1111$ case, 30 realizations per cell size led to a percolation threshold for the infinite system of $\phi_c = 0.2612 \pm 0.0008$, while 100 realizations led to $\phi_c = 0.2613 \pm 0.0003$ and 200 realizations led to $\phi_c = 0.26125 \pm 0.00025$. It can be seen that even with 30 realizations the error bar was of only $\pm 0.4\%$ and that 100 realizations, as used for all the $\delta/D = 0.1111$ cases did not lead to significant lesser precision when compared to 200 realizations. In all cases, the correlation length exponent ν had a value around 0.9, in good agreement with previous results on spheres [56, 60, 116]. An example of such a finite size analysis is shown in Figure 4.2 for the $a/b = 1/10$ and $\delta/D = 0.1111$ case, obtaining $\phi_c = 0.07349 \pm 0.00025$. However, there were quite a few cases where the fluctuations of ϕ_c^{eff} were too large and a simple average of the results provided a more significative result than the one obtained from the finite size analysis. Considering again Figure 4.2, it is also clear that also when the finite size analysis can be performed, the average can provide already a quite good estimate of ϕ_c, at least on the system size range considered here. Moreover, if one is not interested in an extremely precise evaluation of the percolation threshold, a (large enough) single cell size simulation can be sufficient.

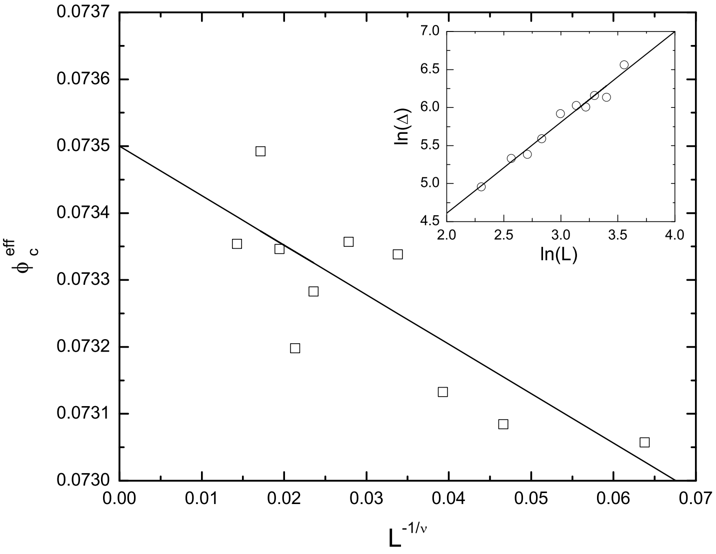

Figure 4.2: Percolation threshold ϕ_c^{eff} as a function of $L^{1/\nu}$ for the $a/b = 1/10$ and $\delta/D = 0.1111$ case. Extrapolated infinite system percolation threshold $\phi_c = 0.07349 \pm 0.00025$. *Inset*: Percolation width Δ as a function of the simulation cell size L. Extrapolated correlation length exponent $\nu = 0.837 \pm 0.026$.

Going back to Figure 4.1 it is clear that decreasing the aspect-ratio from $a/b = 1$ (spheres) to $a/b = 1/2$ (i.e. raising the shape-anisotropy from $\chi = 1$ to $\chi = 2$) leads to a lowering of the percolating volume fraction. This trend is confirmed by the full results for the critical hard particle volume fraction ϕ_c as a function of the cutoff distance δ/D for several values of the aspect-ratio a/b, which are plotted in the left panel of Figure 4.3. For the thinnest shells we find that ϕ_c can be reduced by about one order of magnitude in going from $a/b = 1$ down to $a/b = 1/100$. This result is fully consistent with the frequently reported trend that assemblies of oblate objects with more extreme aspect-ratios entail a lower percolation threshold which we reviewed in Chapter 2. As another way to display the results which emphasizes the high shape-anisotropy results, we plot on the right panel of Figure 4.3 the critical volume fractions re-scaled by multiplying them by the ratio of the volume of the spheroid enclosing sphere (i.e. a sphere with diameter equal to the spheroid major axis) with the volume of the spheroid itself, which in the oblate case is $V_{sphere}/V_{spheroid} = b/a$.

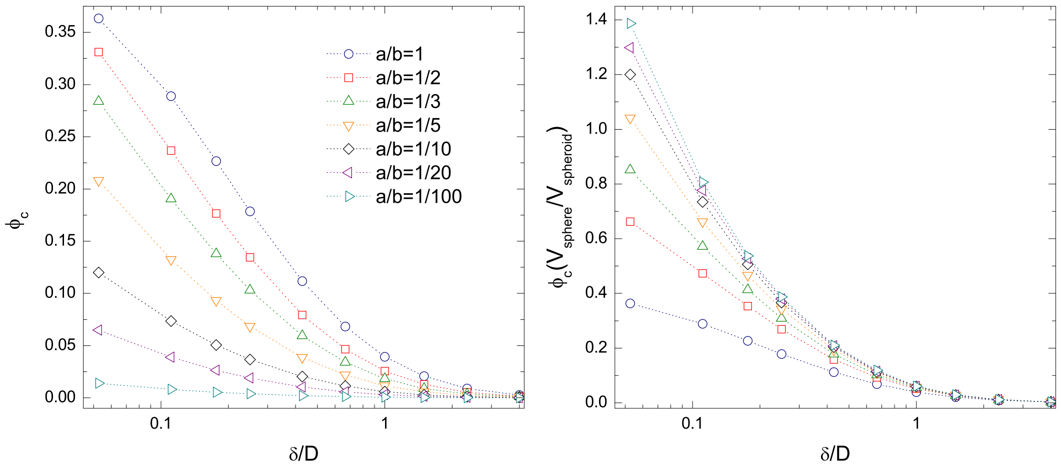

Figure 4.3: *Left*: Critical volume fraction (percolation threshold) ϕ_c as a function of the cutoff distance δ/D for oblate spheroids with different aspect-ratios a/b and distributions generated with random sequential addition. *Right*: Re-scaled critical volume fraction as a function of the cutoff distance δ/D for the same system.

4.2 Equilibrium and high density results

Let us now consider the results which were obtained for Monte Carlo equilibrated distributions which include also high density configurations beyond the reach of random sequential addition. Since we are not interested in overly precise estimation of the percolation threshold, the analysis was carried out in a similar fashion to what was done for the RSA case, but without finite size analysis and with single system sizes of around 2000 particles. For high aspect-ratio prolate spheroids the particle number was increased up to ~ 8000 in order to be able to maintain the periodic boundary condition on the simulation cell. The realization number varied typically from 40 for the highest densities up to 500 for the lowest ones. The sigmoidal fit (4.1) was usually performed with 10-20 spanning probability results.

As a first validation of our procedures, we confronted the results for the special case of spheres ($a/b = 1$) with available results of the literature [56, 59, 60]. The outcome is displayed in Figure 4.4. We can appreciate how there is excellent agreement with the equilibrium results, while the RSA data shows a certain degree of deviation. It is also interesting to observe that the results of Refs. [56, 60] are obtained from finite size analysis.

4.2.1 Prolate systems results

We present first the case of prolate ($a/b > 1$) spheroids. In Figure 4.5 we report the calculated values of the critical volume fraction ϕ_c as a function of the cutoff distance δ/D (with $D = 2\max(a,b)$) for spheres ($a/b = 1$, together with the results of Ref. [59]) and for $a/b = 2$, 10, 20, and 100. For a given δ/D, the consistent reduction of ϕ_c with the increase of the aspect-ratio (shape-anisotropy) is again manifest. In the plot of Figure 4.6 the same data are displayed with δ/D multiplied by the ratio $V_{sphere}/V_{object} = (a/b)^2$, where $V_{sphere} = \pi D^3/6$ is the volume of a sphere with diameter equal to the major axis of the prolate spheroid and V_{object} is the volume of the spheroid itself. For comparison, we plot in Figure 4.6 also the results for impenetrable spherocylinders of Refs. [62, 63]. These are formed by cylinders of radius R and length H, capped by hemispheres of radius R, so that $a = R + H/2$ and $b = R$, and $V_{sphere}/V_{object} = (a/b)^3/[(3/2)(a/b) - 2] \simeq (2/3)(a/b)^2$ for $a/b \gg 1$. As it is apparent, for sufficiently large values of a/b this simple transformation collapses both spheroids and spherocylinders data into a single curve. This holds true as long as the aspect-ratio of the spheroid plus the penetrable shell $(a+\delta/2)/(b+\delta/2)$ is larger than about 5. In addition, for $\phi \lesssim 0.03$ the collapsed data are well approximated by $\phi_c(V_{sphere}/V_{object}) = 0.4/(\delta/D)$ (solid line), leading to the following asymptotic formula:

$$\phi_c \simeq \frac{\gamma(b/a)^2}{\delta/D}, \tag{4.4}$$

where $\gamma = 0.4$ for spheroids and $\gamma = 0.6$ for spherocylinders. Equation (4.4) is fully consistent with the scaling law of Ref. [117] based on the second-virial approximation for semi-penetrable spherocylinders (see also Section 4.3.1).

4.2.2 Oblate systems results

Let us now turn to the case of oblate ($a/b < 1$) spheroids. The simulation results for ϕ_c as a function of δ/D are displayed in Figure 4.7 for $a/b = 1$, 1/2, 1/10, 1/100, and 1/200. Now, as opposed to prolate fillers, almost all of the experimental results on nanocomposites containing oblate filler with high shape anisotropy like graphene [29] are at volume fractions for which a corresponding hard spheroid fluid at equilibrium would already be in the nematic phase. From Table 3.1 we know that for oblate spheroids with $a/b = 1/10$ the isotropic-nematic (I-N) transition is at $\phi_{I-N} \sim 0.185$, while for $a/b = 1/100$ it is $\phi_{I-N} \sim 0.0193$, and for $a/b = 1/200$ $\phi_{I-N} \sim 0.0096$. However, we also saw that in real nanocomposites the transition to the nematic phase is prevented by the viscosity of the polymer matrix. Then, in order to maintain global isotropy also for $\phi > \phi_{I-N}$, we generated oblate spheroid distributions with random sequential addition (RSA) alone. The outcomes are again displayed in Figure 4.7 and one can appreciate that

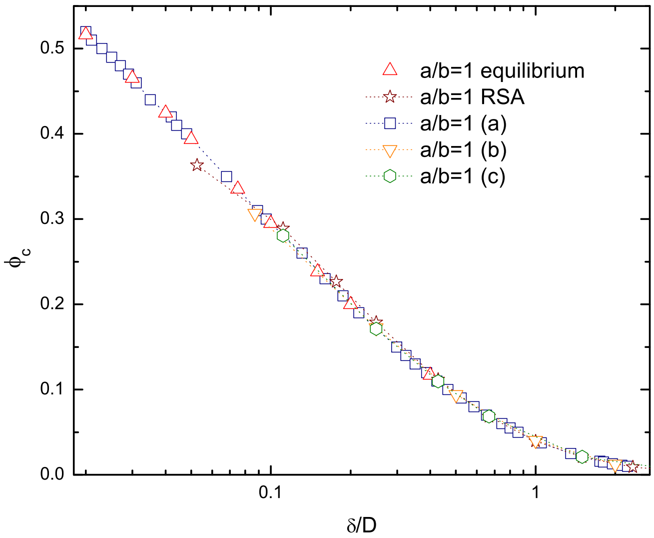

Figure 4.4: Critical volume fraction (percolation threshold) ϕ_c as a function of the cutoff distance δ/D for the case of spheres ($a/b = 1$). (a) results from Ref. [59]. (b) results from Ref. [60]. (c) results from Ref. [56].

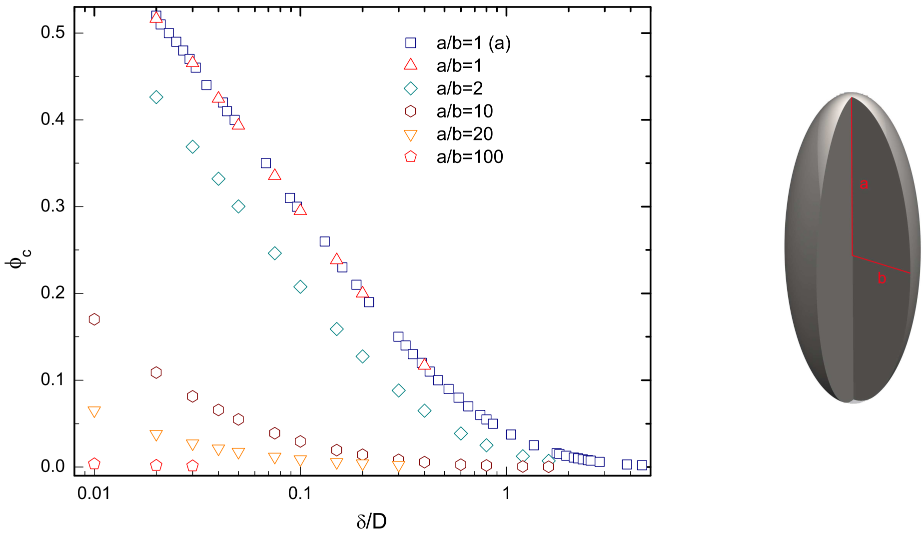

Figure 4.5: Dependence of the critical volume fraction ϕ_c upon the cutoff distance δ/D for impenetrable prolate spheroids with $a/b = 1$, 2, 10, 20, and 100. (a) results from [59].

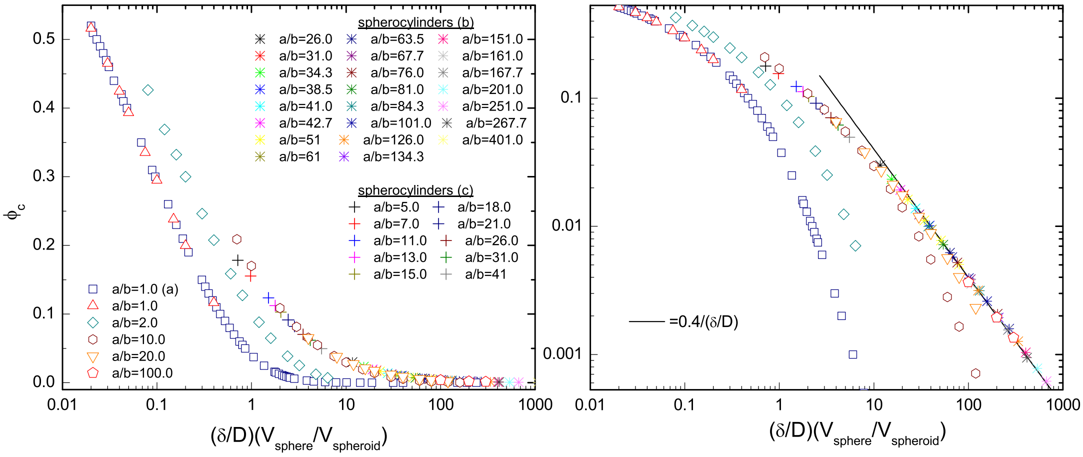

Figure 4.6: Critical volume fraction ϕ_c versus re-scaled cutoff distances for prolate spheroids, for spheres (together with (a) Ref. [59]), and for the impenetrable spherocylinders of: (b) Ref. [62], and (c) Ref. [63]. We note that for spherocylinders, $a/b = (R + H/2)/R$. The solid line is the asymptotic behavior for $a/b \gg 1$ (see Equation (4.4)).

the difference with the equilibrium results for $\phi < \phi_{I-N}$ is quite small and negligible for the present aims. Proceeding further, for oblate spheroids a fruitful way of re-scaling the data is, as we saw for the RSA case, the multiplication by $V_{sphere}/V_{spheroid} = b/a$ of the critical volume fractions ϕ_c (instead of δ/D). Indeed, as shown in Figure 4.8, for sufficiently high shape anisotropy the re-scaled results collapse into a single curve (the results for $a/b = 1/100$ and $a/b = 1/200$ are completely superposed).

We finally display in the left panel Figure 4.9 a comparison between the critical volume fractions ϕ_c of prolate and oblate spheroids with the same shape-anisotropy χ, which shows how prolate systems enhance the lowering of the percolation threshold, a fact also observed in real composites. The right panel of Figure 4.9 shows instead the spheroid aspect-ratio dependence of the critical volume fraction for one of the shortest investigated cutoff distances ($\delta/D = 0.02$). It is interesting to observe that, although the ϕ_c for spheres is close to the meta-stable region of the hard sphere fluid, there is no sign of the dip near $a/b = 1$ which appears for instance in the maximum achievable density with random sequential addition (see Figure 3.3), in the hard spheroid phase diagram (see Figure 3.4) and in the spheroid maximum random close packing density (see e.g. Refs. [53, 91]).

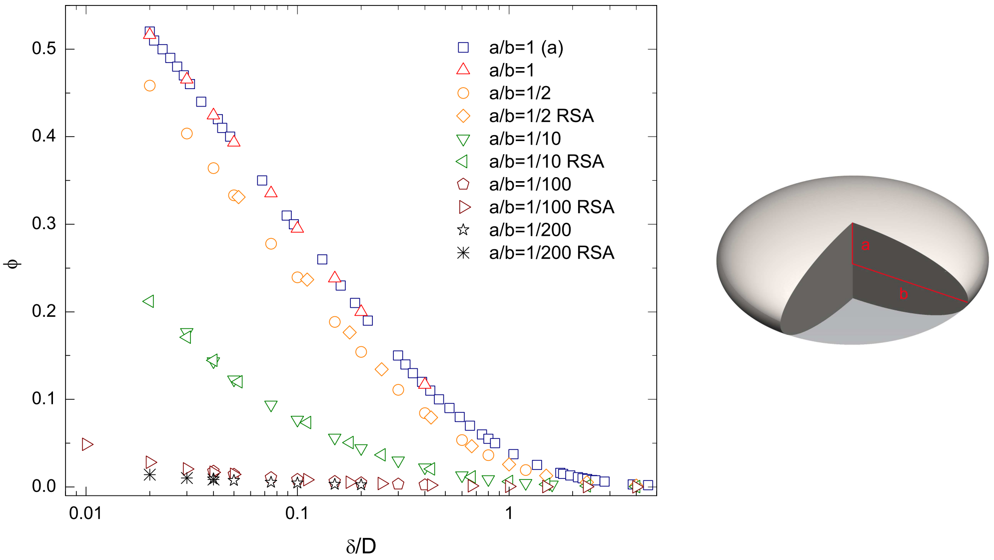

Figure 4.7: Dependence of the critical volume fraction ϕ_c upon the cutoff distance δ/D for impenetrable oblate spheroids with $a/b = 1$, $1/2$, $1/10$, $1/100$, and $1/200$. Results obtained by RSA alone are also reported. (a) results from Ref. [59].

4.2.3 Bond connectivity at the percolation threshold

In continuum percolation, an important quantity providing information on the local topology of the percolating cluster is the average number B_c of objects connected to a given particle. For fully penetrable spheres the evaluation of B_c from a direct enumeration of connections in their assemblies at percolation [55, 59] gives $B_c \simeq 2.74$. However, for semi-penetrable spheres, the presence of hard-core introduces a spatial correlation so that B_c is expected to deviate from the uncorrelated case. In particular, B_c is found to decrease as the hard-core portion of the sphere increases, reaching $B_c \simeq 1.5$ for very thin penetrable shells [55, 59], as a result of the repulsion of the impenetrable hard-cores.

Let us now consider the case of assemblies of prolate ellipsoids. In the left panel of Figure 4.10 we plot the computed values of B_c as a function of the cutoff distance δ/D and for selected values of the aspect-ratio a/b. Results of Ref. [59] are also plotted for comparison. For $a/b = 1$ we recover the results for the spheres: $B_c \simeq 2.7$ for large values of δ/D while $B_c \simeq 1.5$ for small values δ/D. For $a/b > 1$ and thick penetrable shells ($\delta/D > 1$), B_c remains close to the spherical case also for larger aspect-ratios because, for large δ/D values the entire object (hard-core plus penetrable shell) is basically a semi-penetrable sphere with a small hard-core spheroid. This ceases to be true for smaller cutoff distances, for which B_c decreases further and the

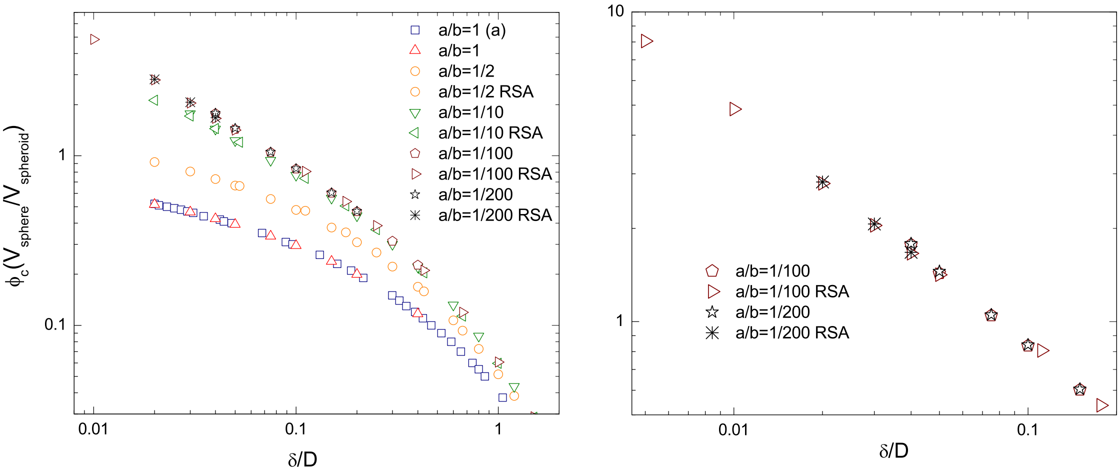

Figure 4.8: *Left*: Re-scaled critical volume fraction $\phi V_{sphere}/V_{spheroid} = \phi(b/a)$ plotted versus the cutoff distance δ/D. *Right*: Asymptotic behavior for $\delta/D < 0.1$. (a) results from Ref. [59].

particle connectivity distribution (right panel of Figure 4.10) becomes more peaked. This is in agreement with what is found by numerical evaluation for other prolate hard objects such as spherocylinders [55, 63]. For example, for spherocylinders (composed again of hard cylinders of length H and radius R capped by hemispheres) and with penetrable shells of thickness $0.2R$, B_c is found to decreases from $B_c = 1.61$ for $H/R = 8$ down to $B_c = 1.29$ at $H/R = 50$ [63], consistently deviating therefore from $B_c \simeq 1.76$ obtained for spheres of radius R and the same penetrable shell thickness [59]. We now turn to the case of oblate spheroids, which is displayed in the left panel of Figure 4.11. Interestingly, by decreasing δ/D, we find that B_c continues to remain very close to the $a/b = 1$ case also for the thinnest penetrable shells, irrespectively of the aspect-ratio, in contrast to what is found for prolate hard objects. This is also supported by the aspect-ratio independence of the particle connectivity distribution, shown in the right panel of Figure 4.11. However, we note that different behaviors of quasi-impenetrable oblate and prolate objects noted here are also found in the fully penetrable case. Indeed, B_c of prolate objects decreases as the aspect-ratio is increased and expected to approach unity in the extreme prolate limit [54], while B_c of oblate objects remains close to $B_c \simeq 3$ all the way from the moderate- to extreme-oblate regimes [112].

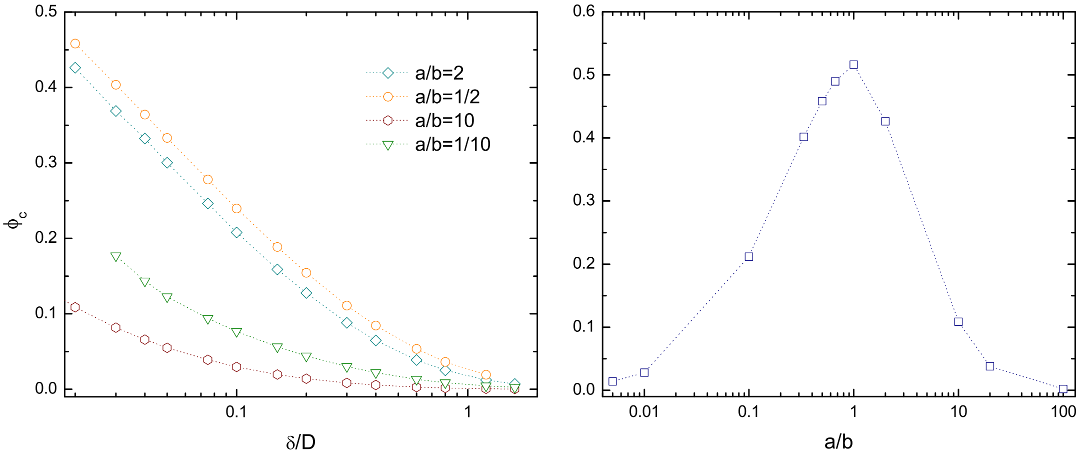

Figure 4.9: *Left*: comparison between the critical volume fractions ϕ_c of prolate and oblate spheroids with the same shape-anisotropy $\chi = \max(a,b)/\min(a,b)$. *Right*: Critical volume fractions ϕ_c of prolate and oblate spheroids as a function of the aspect-ratio a/b for $\delta/D = 0.02$. For $a/b = 1/10$, $1/100$, and $1/200$ the results come from random sequential addition alone.

4.3 Relations for the estimation of percolation critical quantities

We are now going to introduce some relations which, for a given particle aspect-ratio, allow to estimate critical quantities such as the percolation critical volume fraction ϕ_c as a function of the cutoff distance δ, or inversely (and more importantly for the following of the present work) the critical cutoff distance δ_c as a function of the system volume fraction ϕ.

4.3.1 Excluded volume relations

Since their introduction in the field of percolation theory [104,105], excluded volume quantities have been used frequently to obtain expressions for the estimation of the percolation threshold. Given two objects, the excluded volume V_{ex} is the volume around an object where the center of the other object cannot penetrate if overlap is to be avoided and while the respective orientations are maintained. In other words, it is the surface swept by the center of an object as it is displaced parallel to itself around another object while being kept in contact with it. For fully penetrable objects, there is a simple relation between the average bond connectivity B_c, critical particle

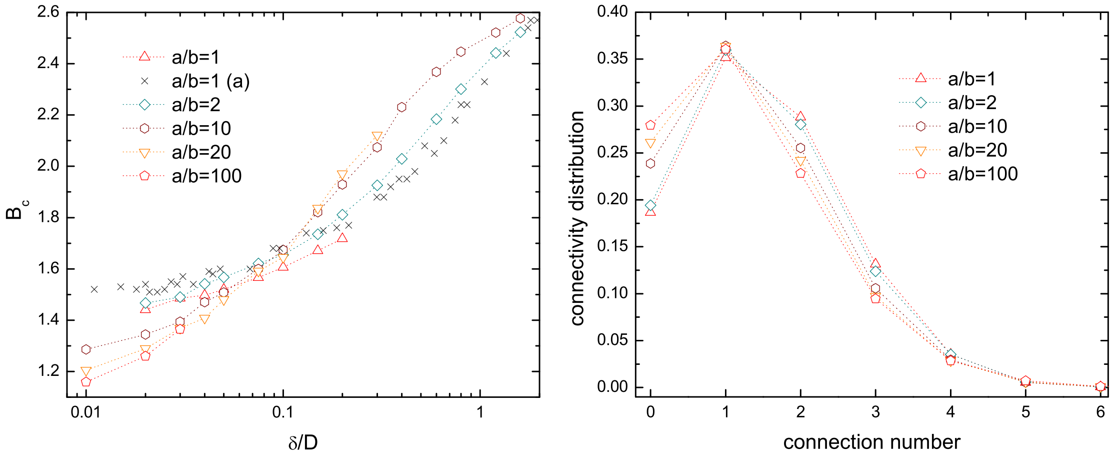

Figure 4.10: *Left*: B_c as a function of the cutoff distance from simulation for different aspect-ratio prolate ($a/b > 1$) spheroids. The results are obtained from the simulations by counting the connections number of each spheroid with its neighbors and averaging. *Right*: distribution of the particle connectivity for a cutoff distance $\delta/D = 0.02$. (a) results from Ref. [59].

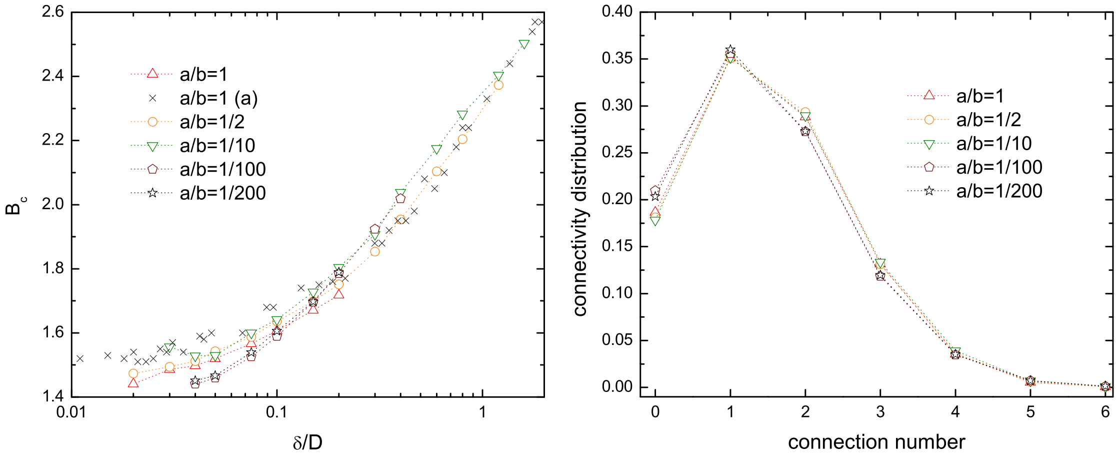

Figure 4.11: As above, for oblate (a/b<1) spheroids. For the particle connectivity it is $\delta/D = 0.04$.

number density and particle excluded volume [104]:

$$B_c = \rho_c V_{ex}, \tag{4.5}$$

where ρ_c is the particle number density at percolation. For penetrable spheres each of volume V, the excluded volume is $V_{ex} = 8V$ and, by using $\rho_c = 0.34/V$, the resulting connectivity number is $B_c \simeq 2.8$, which agrees well with the numerical evaluations of B_c [55, 59]. Indeed, for fully penetrable spheres, for which the sphere centers are distributed randomly, Eq. (4.5) simply states that B_c is equivalent to the average number of centers found within an excluded volume, irrespectively of the spatial configuration of the percolating objects. Now, starting from a more formal point of view, we can write a general relation between the average connection number B_c at percolation and the critical number density ρ_c. If we consider the case of hard spheroids with penetrable shell and with an isotropic distribution of orientations, then B_c reduces to:

$$B_c = \rho_c \int_0^{2\pi} \mathrm{d}\theta \int_0^{\pi} \mathrm{d}\varphi \, \Phi(\theta, \varphi) \int_{V_{exd}(\theta,\varphi)} \mathrm{d}^3\mathbf{r} \, g(\mathbf{r}, \theta, \varphi), \tag{4.6}$$

where θ and φ are the angles between the major axes of two spheroids separated by $\mathbf{r}$, $\Phi(\theta, \varphi)$ the angle distribution function and $g(\mathbf{r}, \theta, \varphi)$ is the radial distribution function: given a particle centered in the origin, $\rho_c \, g(\mathbf{r}, \theta, \varphi)$ represents the mean particle number density at position $\mathbf{r}$ with an orientation θ, φ. The integration in $\mathbf{r}$ is performed over the total excluded volume $V_{exd}(\theta, \varphi)$ (hard-core plus penetrable shell) centered at the origin and having orientation θ, φ.

We observe that all the information about the presence of a hard core inside the particles is included in the radial distribution function, which will be zero in the volume occupied by the hard core of the particle centered at the origin. However, $g(\mathbf{r}, \theta, \varphi)$ is a rather complex function and even for the case of spheres there are only approximate theoretical expressions [118]. Also, the construction of a fitted expression to simulation data may result to be excessively complicated when the respective orientation of the particles has to be taken into account.

Proceeding further, the lowest order approximation which we can consider, and which is exact in the case of fully penetrable particles (reducing to (4.5)), is the one where $g(\mathbf{r}, \theta, \varphi) \equiv g^0(\mathbf{r}, \theta, \varphi) = 1$. This is equivalent to neglect all contributions of the radial distribution function which spur from the presence of the hard core. The resulting quantity, which we denote by B_c^0, is then given by:

$$B_c^0 = \rho_c \int_0^{2\pi} \mathrm{d}\theta \int_0^{\pi} \mathrm{d}\varphi \, \Phi(\theta, \varphi) \int_{V_{exd}(\theta,\varphi)} \mathrm{d}\mathbf{r} = \rho_c \langle V_{exd} \rangle, \tag{4.7}$$

where $\langle V_{exd} \rangle$ is the orientation averaged total excluded volume. Given the averaged excluded volume of spheroids surrounded with a shell of constant

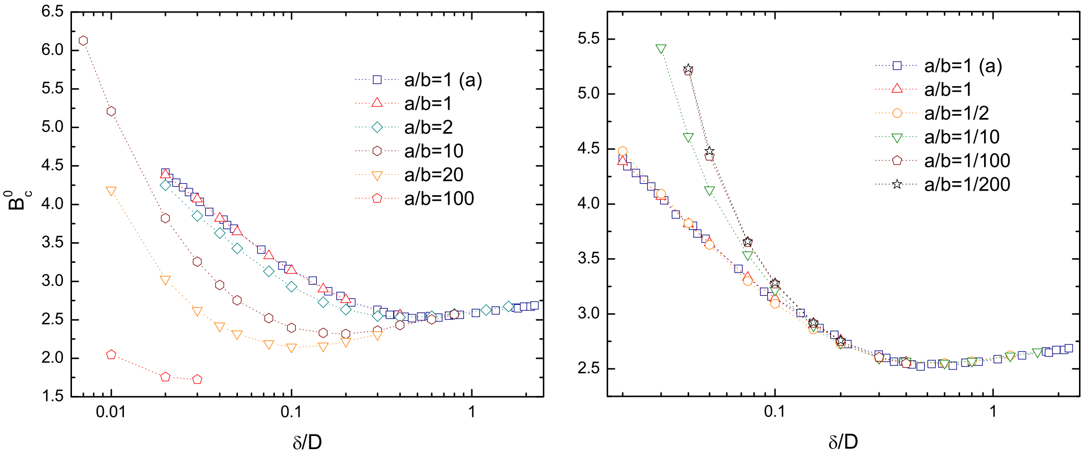

Figure 4.12: *Left*: B_c^0 as a function of the shell thickness for different aspect-ratio prolate spheroids. *Right*: The same for oblate spheroids. (a) results from Ref. [59].

thickness $\langle V_{exd}\rangle$ (A.29) or (A.36), together with the hard spheroid excluded volume expression (A.28) or (A.30), we can calculate B_c^0 from the percolation threshold results obtained from the simulations:

$$B_c^0 = \rho_c \langle V_{exd}\rangle = \phi_c \frac{\langle V_{exd}\rangle}{V} \quad , \tag{4.8}$$

where we have used the hard core volume fraction ϕ_c. The full details of the calculation of the excluded volume quantities can be found in Appendix A. The resulting values of B_c^0 are plotted in Figure 4.12 as a function of the penetrable shell thickness for several aspect-ratio prolate and oblate spheroids. B_c^0, which can be interpreted as the average number of particles centers per averaged excluded volume, is a different quantity than B_c and a correspondence between the two appears only in the thick shell limit, where the system is more similar to a fully penetrable one. This can be appreciated by comparing Figure 4.12 with Figures 4.10 and 4.11. The increasing discrepancy for thinner shells is due to stronger correlation effects spurring from the presence of the hard-core. Nevertheless, the behavior of B_c^0 for the case of oblate spheroids is still rather intriguing. Indeed, the dependence of B_c^0 on the penetrable shell thickness δ/D appears to be universal with respect to the aspect-ratio, for all δ/D values larger than $\delta/D > 0.1$. Furthermore, in this region of δ/D, B_c^0 has a rather weak dependence on the shell thickness, not deviating much from $B_c^0 \simeq 2.8$.

The quasi-invariance of B_c^0 for oblate spheroids may be a results of practical utility since, by using Eq. (4.8), the percolation threshold ϕ_c can be

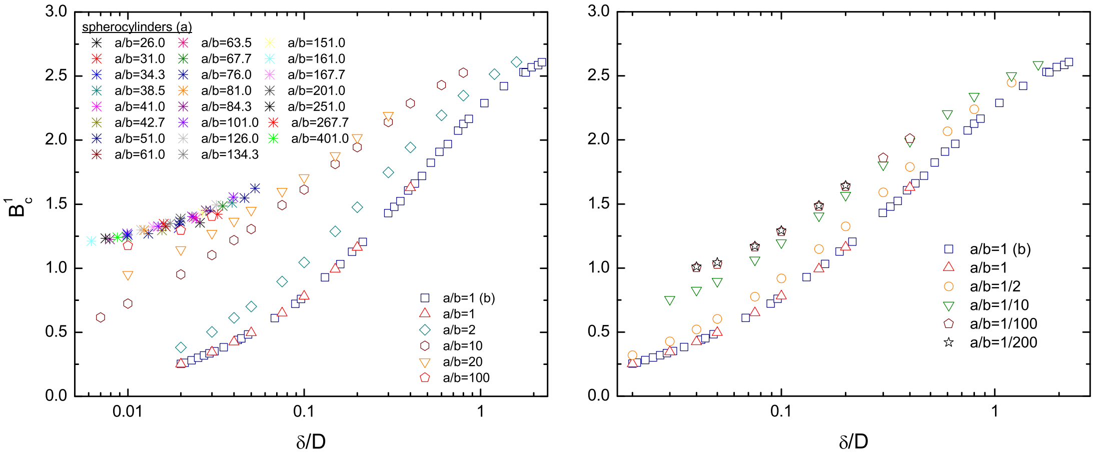

Figure 4.13: *Left*: B_c^1 as a function of the shell thickness for different aspect-ratio prolate spheroids. Results (a) for spherocylinders from Ref. [62] are also shown (in the case of spherocylinders, $a/b = (R + H/2)/R$). *Right*: The same for oblate spheroids. (b) results from Ref. [59].

estimated precisely from $\langle V_{exd} \rangle$ and B_c^0 data for a known case like e.g. spheres in a wide interval of δ/D and aspect-ratio values. The direct determination of the percolation threshold of hard oblate spheroids via simulations is a time consuming procedure. Thus, a relation which allows to quickly evaluate such a quantity as a function of the dispersion geometric parameters offers some advantage.

We now turn to another approximation of (4.6) which now includes the presence of the hard particle in $g(\mathbf{r}, \theta, \varphi)$ but neglects all other correlation effects. This is equivalent to the second-virial approximation [117]. For the case of spheres, this would lead to a radial distribution function of the form $g(\mathbf{r}) \equiv g^1(\mathbf{r}) = \theta(r - D)$, where θ is the Heaviside step function. For the general spheroid case $g^1(\mathbf{r}, \theta, \varphi)$ will depend on the orientation. However, the resulting quantity, B_c^1, is quite simple:

$$B_c^1 = \rho_c \int_0^{2\pi} \mathrm{d}\theta \int_0^{\pi} \mathrm{d}\varphi \, \Phi(\theta, \varphi) \int_{V_{exd}(\theta,\varphi)} g^1(\mathbf{r}, \theta, \varphi) \mathrm{d}\mathbf{r} =$$

$$= \rho_c \left(\langle V_{exd} \rangle - \langle V_{ex} \rangle \right) \equiv \rho_c \langle V_{exs} \rangle, \qquad (4.9)$$

where we have introduced the excluded volume contribution of the penetrable shell $\langle V_{exs} \rangle = \langle V_{exd} \rangle - \langle V_{ex} \rangle$, which can be easily calculated (for isotropic distributions) from (A.36). Figure 4.13 shows the values of B_c^1 obtained from the prolate and oblate spheroids critical volume fractions of the present work (via the usual relation $B_c^1 = \phi_c \langle V_{exs} \rangle / V$). For the prolate case, the results for spherocylinders of Ref. [62] are also shown (calculated with the spherocylinder excluded volume quantities of Equations (A.40) and (A.41)). Observing Figure 4.13, we note that for high aspect-ratio prolate objects there seems to be a region of sufficiently small δ/D where all the results have a value of B_c^1 comprised between 1.25 and 1.5. Now, in this regime ($a/b \gg 1$ and $\delta/D \ll 1$), we can use the corresponding simplified excluded volume quantities (A.39) and (A.42) in (4.9), obtaining

$$B_c^1 = \phi_c \frac{\langle V_{exs} \rangle}{V} = 3\phi_c \left(\frac{a}{b}\right)^2 \frac{\delta}{D} \quad , \quad \text{Prolate spheroids}$$

$$B_c^1 = \phi_c \frac{\langle V_{exs} \rangle}{V} = \phi_c \left(\frac{H}{R}\right)^2 \frac{\delta}{2H} \simeq 2\phi_c \left(\frac{a}{b}\right)^2 \frac{\delta}{H} \quad , \quad \text{Spherocylinders.} \tag{4.10}$$

If we confront these results with the asymptotic formula (4.4) and its plot in the right panel of Figure 4.6 we see that there is indeed full agreement when $B_c^1 \simeq 1.2$, showing that the expressions of (4.10) together with a constant value of B_c^1 capture well the behavior of high aspect-ratio prolate hard objects with a sufficiently thin shell. This is also consistent with the Onsager theory of the high aspect-ratio rods fluid [100] which states that the second-virial coefficient is sufficient to account for the properties of the system.

4.3.2 Relations for the critical cutoff distance

In the following of the present thesis, we will often need the critical cutoff distance δ_c for a given volume fraction ϕ instead of the inverse (i.e. the critical volume fraction ϕ_c for a given cutoff distance δ). We shall now illustrate that for sufficiently elongated prolate and for sufficiently flat oblate spheroids, as well as for spheres, simple relations exist that allow to estimate δ_c with good accuracy. For prolate systems, we already have the asymptotic formulas of Equations (4.4) and (4.10), which immediately allow to write

$$\delta_c/D \simeq \frac{\gamma (b/a)^2}{\phi}, \tag{4.11}$$

where, again, we have $\gamma = 0.4$ for spheroids and $\gamma = 0.6$ for spherocylinders. The results for prolate systems of Figure 4.6 plotted as the re-scaled δ_c as a function of ϕ are shown in Figure 4.14, together with Equation (4.11) (dashed line).

It is interesting to notice that in Figure 4.14 the re-scaled data for $\phi \gtrsim 0.03$ deviate from Equation (4.11) but still follow a common curve. We have found that this common trend is well fitted by an empirical generalization of Equation (4.11):

$$\delta_c/D \simeq \frac{\gamma(b/a)^2}{\phi(1+8\phi)}, \tag{4.12}$$

which applies to all values of ϕ provided that $(a+\delta_c/2)/(b+\delta_c/2) \gtrsim 5$ (solid line in Figure 4.14).

Turning to oblate spheroids, it is instructive to consider the case of perfectly parallel spheroids that can be easily obtained from general excluded volume result for aligned penetrable objects [119], which has the same form of (4.5) and where $B_c = 2.8$, like for the case of spheres. For infinitely thin parallel hard disks of radius b one therefore has $V_{exd} = 2.8/\rho$, where ρ is the number density and $V_{exd} = (4/3)\pi b^3[12(\delta_c/D)+6\pi(\delta_c/D)^2+8(\delta_c/D)^3]$ is the excluded volume of the plate plus the penetrable shell of critical thickness $d_c = \delta_c/2$. Assuming that this holds true also for hard-core-penetrable-shell oblate spheroids with a sufficiently thin hard core, we can then write

$$12(\delta_c/D) + 6\pi(\delta_c/D)^2 + 8(\delta_c/D)^3 \simeq \frac{2.8}{\phi(b/a)} \tag{4.13}$$

Equation (4.13) implies that δ_c/D depends solely on $\phi(b/a)$, suggesting that its aspect-ratio dependence will be reabsorbed by the volume fraction rescaling we performed in Figure 4.8. Figure 4.15 shows the results of that figure re-plotted as (re-scaled) δ_c as a function of ϕ, and we can appreciate how the aspect-ratio dependence of Equation (4.13) is indeed reabsorbed. Furthermore, with the introduction of two auxiliary parameters, equation (4.13) can be made to reproduce the $a/b \ll 1$ asymptotic behavior:

$$12\alpha(\delta_c/D)^\beta + 6\pi(\delta_c/D)^2 + 8(\delta_c/D)^3 \simeq \frac{2.8}{\phi(b/a)} \tag{4.14}$$

where $\alpha = 1.54$ and $\beta = 3/4$. The outcome of equation (4.14) is again displayed on Figure 4.15. Moreover, by retaining the dominant contribution of equation (4.14) for $\delta_c/D < 0.1$, we arrive at (inset of Figure 4.15):

$$\delta_c/D \simeq \left[\frac{0.15(a/b)}{\phi}\right]^{4/3}. \tag{4.15}$$

Finally, we show that also for a system of spheres it is possible to formulate the ϕ dependence of δ_c with high accuracy. Indeed, as discussed in Ref. [60], the ratio $\delta_c/\langle\delta_{NN}\rangle$, where $\langle\delta_{NN}\rangle$ is the mean minimal distance between nearest-neighbors spheres, has a rather weak dependence on ϕ. In particular, $\delta_c \simeq 1.65\langle\delta_{NN}\rangle$ for $\phi > 0.1$. Then, by using the asymptotic formula for $\langle\delta_{NN}\rangle$ of Ref. [57] valid in the high density regime we find that

$$\delta_c/D \simeq \frac{1.65(1-\phi)^3}{12\phi(2-\phi)}, \tag{4.16}$$

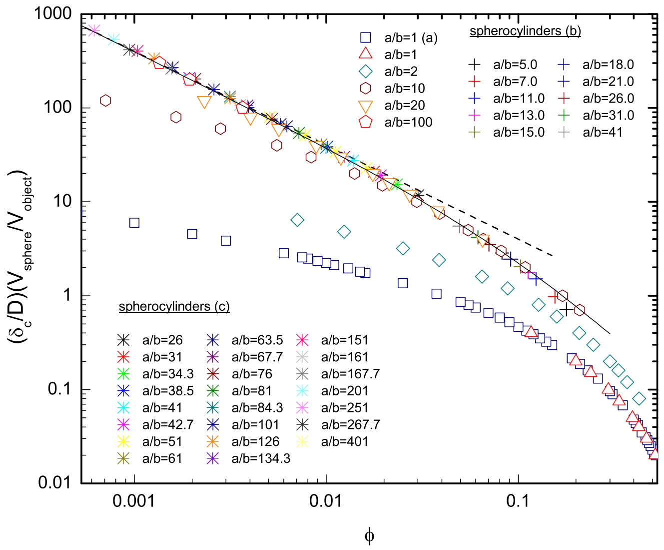

Figure 4.14: Re-scaled critical distances $(\delta_c/D)(V_{sphere}/V_{object})$ versus ϕ for the prolate spheroids and for the impenetrable spherocylinders of (b) Ref. [63] and (c) Ref. [62]. The dashed line is the asymptotic behavior for $a/b \gg 1$ of Equation (4.11). The solid line is Equation (4.12). (a) data from Ref. [59].

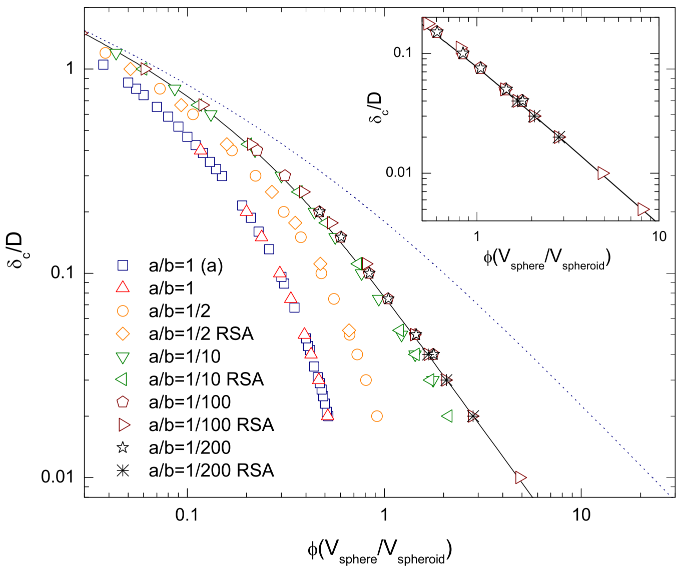

Figure 4.15: δ_c/D plotted versus the re-scaled volume fraction $\phi(V_{sphere}/V_{spheroid}) = \phi(b/a)$ for oblate spheroids. The dashed line is Equation (4.13) and the solid line is Equation (4.14). Inset: asymptotic behavior for $\delta_c/D < 0.1$. (a) data from Ref. [59].

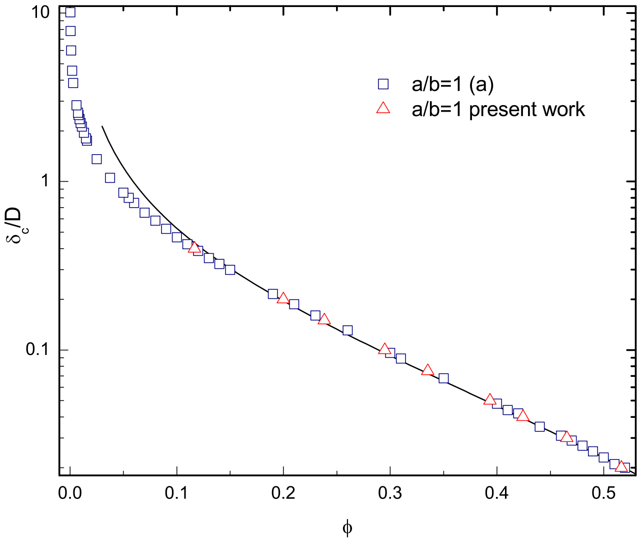

Figure 4.16: δ_c/D as a function of the volume fraction ϕ for spheres, together with the predictions of Equation (4.16) (solid line). (a) results from Ref. [59].

which is plotted by the solid line in Figure 4.16.

Recapitulating, we have that for sufficiently high-aspect ratio prolate objects, for sufficiently high shape-anisotropy oblate spheroids and for spheres, we can estimate the critical cutoff distance δ_c as a function of the system volume fraction ϕ and the object aspect-ratio by means of Equations (4.11), (4.15) and (4.16):

$$\delta_c/D \simeq \frac{\gamma(b/a)^2}{\phi} \qquad \text{for prolates,} \tag{4.17}$$

$$\delta_c/D \simeq \left[\frac{0.15(a/b)}{\phi}\right]^{4/3} \qquad \text{for oblates,} \tag{4.18}$$

$$\delta_c/D \simeq \frac{1.65(1-\phi)^3}{12\phi(2-\phi)} \qquad \text{for spheres.} \tag{4.19}$$

From the previously discussed conditions on the validity of these asymptotic formulas, it follows that they will hold when $(b/a)^2 \lesssim \phi \lesssim 0.03$ for prolates, $\phi \gtrsim a/b$ and $a/b < 0.1$ for oblates, and $\phi \gtrsim 0.1$ for spheres. If these conditions are not met, values of δ_c can be anyway extrapolated from the data of Figures 4.14, 4.15. For prolate systems one can also use the more precise Equation (4.12).

Finally, a remaining important case is that of the large cutoff distance limit ($\delta/D \gg 1$). In this regime, the penetrable shell is consistently larger than the hard core and is roughly of spherical shape, so that $\langle V_{exd}\rangle \simeq \langle V_{exs}\rangle \simeq (\pi/6)\delta^3$. Then, from e.g. (4.8) and the large cutoff distance limit value of B_c^0 i.e. $B_c^0 \simeq B_0 \simeq 2.8$, we have

$$\delta_c/D \simeq \left[\frac{2.8(b/a)^2}{\phi}\right]^{1/3} \qquad \text{for prolates, } \delta/D \gg 1, \tag{4.20}$$

$$\delta_c/D \simeq \left[\frac{2.8(a/b)}{\phi}\right]^{1/3} \qquad \text{for oblates, } \delta/D \gg 1, \tag{4.21}$$

$$\delta_c/D \simeq \left(\frac{2.8}{\phi}\right)^{1/3} \qquad \text{for spheres, } \delta/D \gg 1. \tag{4.22}$$

In all these expression we can observe a $\phi^{-1/3}$ dependence. This is easily understood if we consider that in the large cutoff distance limit we have $\delta + D \simeq \delta$, so that a variation of D has a negligible effect on the critical number density ρ_c while it has a cubic effect on the volume fraction. At the extreme of the large shell limit lies the point-particle case, for which from (4.5) it follows immediately

$$\delta_c \simeq \left(2.8\frac{6}{\pi\rho}\right)^{1/3} \simeq 1.75\rho^{-1/3} \qquad \text{for point particles.} \tag{4.23}$$

4.4 Connectivity-based models with conductivity

The final part of the present analysis of connectivity-based models will be devoted to the investigation of what behavior would the hard-core-penetrable-shell model show if, besides the connectivity between the particles one would also associate a conductance ϱ to the connected pairs and study the resulting global conductivity σ. For an infinite size system, below the percolation threshold ϕ_c, σ will be zero while above but close to ϕ_c it will grow from zero with the power law (2.2) $\sigma = \sigma_0(\phi - \phi_c)^t$ with $t = 2$. Then, away from the critical region, the conductivity will be enhanced further by the continuing growth of the bonds of the connected network. To substantiate these considerations, we performed numerical simulations with hard spheres surrounded with a penetrable shell where for each connected pair it was associated a unitary bond conductance $\varrho = 1$. To evaluate the global conductivity of the system, the full set of bond conductances was mapped on a resistor network and the overall conductivity was calculated through numerical decimation of the resistor network [51, 60, 120]. The results for three different shell thicknesses ($\delta/D = 1.0$, $\delta/D = 0.5$, and $\delta/D = 0.1$) are displayed in Figure 4.17. Each symbol is the arithmetic mean of 100 realizations involving systems of

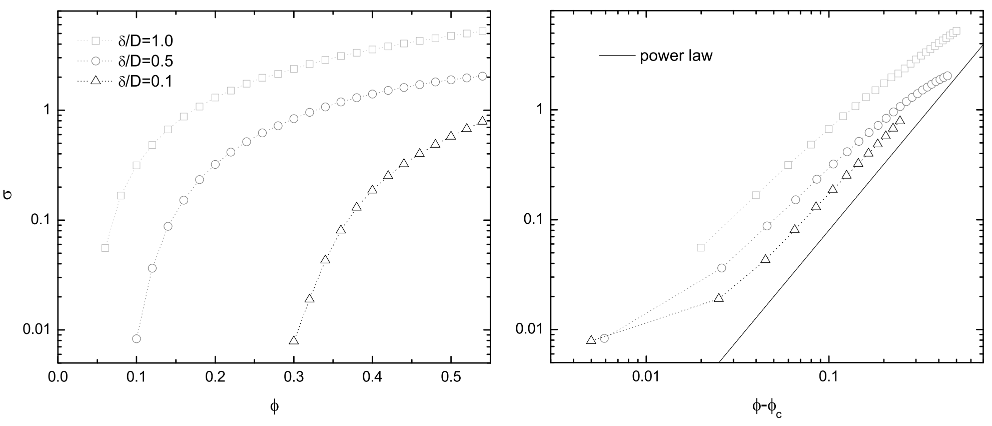

Figure 4.17: *Left*: Conductivity σ as a function of the volume fraction ϕ for hard spheres surrounded with a penetrable shell of thickness $\delta/2$. For connected spheres the bond conductance is $\varrho = 1$. *Right*: The same data together with the power law $\sigma \propto (\phi - \phi_c)^2$ (solid line) plotted as a function of $\phi - \phi_c$.

~ 900 spheres. To get a feeling of how these outcomes would compare with the prediction of the infinite system percolation power law $\sigma = \sigma_0(\phi - \phi_c)^t$ (with $t \simeq 2$), in the right panel of Figure 4.17 we displayed this latter and the numerical results as a function of $\phi - \phi_c$. As it is apparent, the simulation data show indeed a linear behavior with a slope close to two. However, near the percolation threshold ϕ_c, finite size effects become important and the results start to deviate. Also the slopes slightly below two are to be ascribed to finite size effects. On the other side, at sufficiently high values of ϕ the systems deviate from the power law behavior since we are now outside its regime of validity.

4.5 Conclusions

In the present chapter, dedicated to connectivity-based models, the geometrical percolation threshold in the continuum of random distributions of prolate and oblate hard spheroids surrounded with a penetrable shell of constant thickness $d = \delta/2$ has been investigated. Simulation results spanning a broad range of aspect-ratios (from $a/b = 1/200$ to $a/b = 100$) and cutoff distances (from $\delta/D = 0.007$ to $\delta/D = 4$) values have been reported for both random sequential addition and equilibrium systems and spanned the whole isotropic phase of the hard spheroid fluid. For sufficiently aspherical oblate spheroids, it is shown that random sequential addition results deviate only slightly from the equilibrium ones. It is then found that higher shape-anisotropy systems entail lower percolation thresholds, in agreement with the behavior observed experimentally in insulator-conductor composites where the conducting phase is constituted by fibrous or plate-like objects, such as nanotubes or graphite nanosheets. For a shell thickness of $\delta/D = 0.02$, the percolation threshold of aspect-ratio 100 fiber-like objects is more than 260 times lower that the one of spheres, while for oblate aspect-ratio 1/200 plate-like objects it is more than 36 times lower. Furthermore, the average number B_c of connected object at percolation was investigated and is found for oblate spheroids to be quasi-invariant with respect to the aspect-ratio, in contrast with the results for prolate objects. We then introduced a series of relations for the estimation of percolation critical quantities. Excluded volume quantities have been identified which allows to quickly infer the system percolation threshold for sufficiently large cutoff distance oblate spheroids and for high aspect-ratio prolate objects with a sufficiently thin shell. In addition, relations for high shape-anisotropy oblate spheroids and for spheres were also found. A full set of asymptotic relations for the estimation of the critical cutoff distance δ_c as a function of the volume fraction ϕ for sufficiently elongated prolate, for sufficiently flat oblate spheroids, as well as for spheres can be found in Equations (4.17), (4.18), and (4.19). Finally, we showed some results for a hard-core-penetrable-shell model which also includes conductivity and assumes a constant conductance between the connected pairs, and these show a behavior consistent with the percolation power law $\sigma = \sigma_0(\phi - \phi_c)^t$.

Chapter 5

Electron tunneling

We saw in Section 2.2.2 that the main inter-particle transport mechanism in composite materials near the insulator-conductor transition is considered to be quantum mechanical electron tunneling. Before implementing such mechanism in our numerical replications of the composites, we want in the present chapter to treat in some detail the formal derivation of an expression for the bond conductance. Historically, the tunneling formulation of the conductor-insulator-conductor junction which has been applied the most to composite materials is the WKB approximation-based one of Simmons [121]. This has been particularly effective for the inclusions of temperature effects and the fluctuation-induced tunneling of Sheng and co-workers [72, 73, 122]. However, the study of tunneling went through a renaissance just a few years after the publication of these works with the invention of the scanning tunneling microscope (STM) by Binnig and Rohrer [123] in 1981. Since for the STM the understanding of the spatial resolution was paramount, tunneling formulations which could account for it were introduced [124–126], and generally followed an approach due to Bardeen [127]. With the aid of such formulations, instead of the temperature dependence, we try then here to investigate the geometrical aspects of the tunneling between two filler particles modeled as two conductive spheres, something that was not reported before in the literature. This chapter is also somehow more pedagogical than the others, and for the reader not interested in the quantum-mechanical details of tunneling can be skipped without compromising significatively the understanding of the following of the present thesis.

5.1 Introduction to electron tunneling

One of the most striking features of the quantum mechanical laws that govern the dynamics of microscopic systems is the ability of particles to penetrate regions that would be classically forbidden to them, with the remarkable consequence that, if the forbidden region is of finite width, there is a certain probability of having the particles "tunneling" through it. This is a direct consequence of the wave nature of matter and is "in-built" in the Schrödinger equation. To illustrate this more concretely we start with the one-dimensional case with a rectangular potential barrier, a classic problem of introductory quantum mechanics. Let us consider the case of a potential which is zero everywhere except for a region of width w centered in $x = 0$, where it takes a value V_0 (see Fig. 5.1). An electron in such a system will obey the one-dimensional (time-independent) Schrödinger equation:

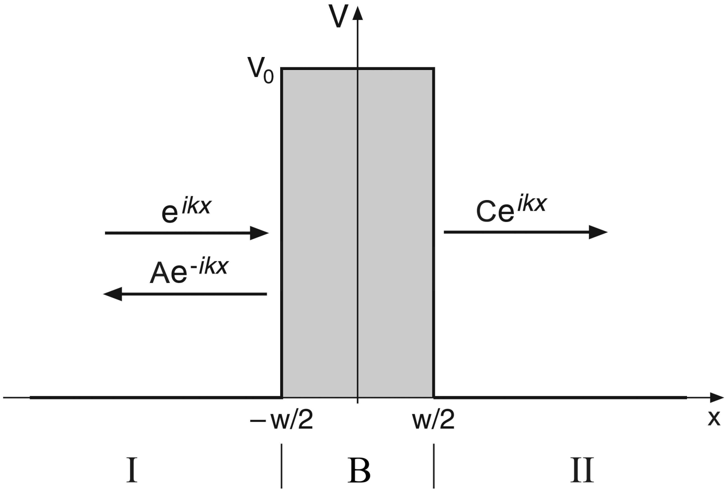

Figure 5.1: The one-dimensional rectangular barrier tunneling problem.

$$-\frac{\hbar^2}{2m}\frac{\mathrm{d}^2}{\mathrm{d}x^2}\psi(x) + V(x)\psi(x) = E\psi(x) \tag{5.1}$$

where m is the electron mass, $\hbar$ is Plank's constant divided by 2π, $V(x)$ is the potential and E the electron energy. In regions I and II, Equation (5.1) reduces to the free particle equation $-\frac{\hbar^2}{2m}\frac{\mathrm{d}^2\psi}{\mathrm{d}x^2} = E\psi$, while inside the barrier region B a constant potential is present and (5.1) can be written as $-\frac{\hbar^2}{2m}\frac{\mathrm{d}^2\psi}{\mathrm{d}x^2} = (E - V_0)\psi$. All these differential equations admit simple solutions, and for an electron initially in region I and propagating from left to right with energy E less than the barrier height V_0 (i.e. $E < V_0$), we will have

$$\psi = \begin{cases} \mathrm{e}^{ikx} + A\mathrm{e}^{-ikx} & \text{if } x < -w/2 \\ B\mathrm{e}^{\kappa x} + B'\mathrm{e}^{-\kappa x} & \text{if } -w/2 < x < w/2 \\ C\mathrm{e}^{ikx} & \text{if } x > w/2 \end{cases} \tag{5.2}$$

where A, B, B' and C are coefficients to be determined and where we have introduced

$$k \equiv \frac{\sqrt{2mE}}{\hbar} \tag{5.3}$$

$$\kappa \equiv \frac{\sqrt{2m(V_0 - E)}}{\hbar}. \tag{5.4}$$

Now, in order for (5.2) to be a solution of the full equation (5.1), we have to match the partial solutions at the barrier interfaces by imposing to ψ and to the derivative $\frac{\mathrm{d}\psi}{\mathrm{d}x}$ to be continuous in $x = -w/2$ and in $x = w/2$. This will in turn determine the coefficients A, B, B' and C. Once the coefficients have been determined, the tunneling probability D, i.e. the probability that an electron striking the barrier from the left will make it to the right follows immediately (see e.g. [128]):

$$D = |C|^2 = \frac{4k^2\kappa^2}{(k^2+\kappa^2)^2 \sinh^2(\kappa w) + 4k^2\kappa^2} \tag{5.5}$$

In the thick barrier limit $\kappa w \gg 1$, (5.5) reduces to

$$D \simeq \frac{4k^2\kappa^2}{(k^2+\kappa^2)^2} \mathrm{e}^{-2\kappa w} \qquad ; \qquad \kappa w \gg 1 \tag{5.6}$$

where we can appreciate the exponential decrease of the tunneling probability with the increase of the barrier width, a behavior common to most tunneling phenomena.
So, this simple example shows how a particle with an energy that in the macroscopic world would be insufficient to overcome a certain potential barrier can manage to pass through it. The wave-like behavior appears clearly if we consider that the solutions of (5.2) outside the barrier have the form of an incoming plane wave with amplitude 1 that is partially reflected with amplitude $|A|$ and partially transmitted with amplitude $|C|$.

5.2 The transfer-Hamiltonian formalism

The exact resolution of the tunneling problem carried out in the previous section is possible only for a few elementary cases and, for the remaining vast majority, approximation techniques are needed. We will then introduce a powerful approach to tunneling due to Bardeen [127], the transfer-Hamiltonian formalism, that has been widely applied to the modeling of the scanning tunneling microscope (see e.g. [124–126, 129–132]) and that is predisposed to include many-body effects. The transfer-Hamiltonian formalism exploits first-order time-dependent perturbation theory to evaluate the electron transfer rate between the two sides of the barrier, and was first applied to field ionization by Oppenheimer [133]. The outline will follow that of the excellent tutorial of Gottlieb and Wesoloski [134], while valuable resources have also been the classic book of Duke [66] and the beautiful introduction to the scanning tunneling microscope of Chen [126].

Let us start with the generic barrier problem, where two regions, I and II respectively, are separated by a potential barrier of arbitrary shape $V_B(\mathbf{r})$, see Figure 5.2. Given some electronic structure for region I and II, we are interested in the electron tunnel current between them. Since what we are looking for is an approximation route, a good place to start is to list the required simplifying assumptions. Although the need for these assumptions will become apparent only along the derivation, introducing them now gives immediately a clear idea of what we have to sacrifice. So, our working assumptions will be [134]:

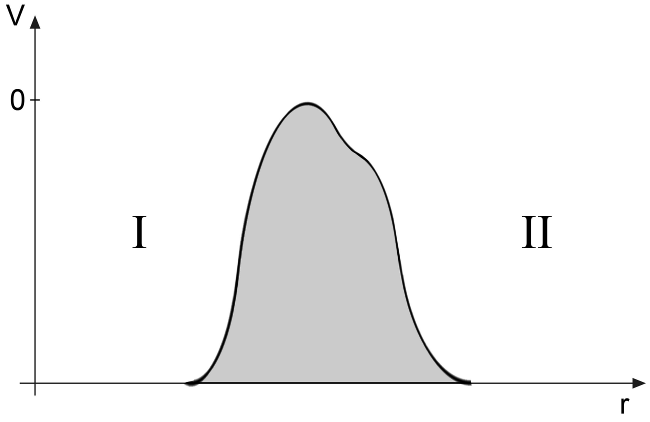

Figure 5.2: The generic potential barrier separating two regions, I and II.

- **A1** Tunneling is weak enough so that the first-order approximation of (5.26) is valid.
- **A2** The electron states of the two sides of the barrier, I and II, are nearly orthogonal.
- **A3** Electron-electron interactions can be ignored.
- **A4** Electron occupation probabilities for the two sides are independent from each other and do not change, despite the tunneling.
- **A5** The two sides are each in electrochemical equilibrium.

The decision to neglect electron-electron interaction (**A3**) implies that the electrons will be independently governed by the single-electron Hamiltonian of the full system

$$\hat{H}(\mathbf{r}) = -\frac{\hbar^2}{2m}\nabla^2 + V(\mathbf{r}) \tag{5.7}$$

and the corresponding time-dependent Schrödinger equation

$$\hat{H}(\mathbf{r})\Psi(\mathbf{r},t) = \left[-\frac{\hbar^2}{2m}\nabla^2 + V(\mathbf{r},t) \right] \Psi(\mathbf{r},t) = i\hbar\frac{\partial}{\partial t}\Psi(\mathbf{r},t) \tag{5.8}$$

where the potential $V(\mathbf{r})$ will include the barrier potential $V_B(\mathbf{r})$ and the region I and II potentials. However, as previously stated, the resolution of the Schrödinger equation of the full problem with (5.7) is generally too difficult. To circumvent this problem, in the transfer-Hamiltonian approach the barrier region is divided in two parts which are then associated to region I and II respectively, as to identify two "augmented" regions I and II to be treated independently. To do that, two new potentials $V_{\mathrm{I}}(\mathbf{r})$ and $V_{\mathrm{II}}(\mathbf{r})$ are constructed which have the same form of $V(\mathbf{r})$ in their respective regions up to the division boundary in the barrier and are zero elsewhere (this is somehow more similar to the modified Bardeen approach (MBA) of Chen [126] than the original formulation of Bardeen [127]). We note that the boundary between the two region can be drawn arbitrarily and so chosen as to suit at best the problem. An example is shown in Figure 5.3 for the barrier of Figure 5.2. We can then write the two separate single-electron Hamiltonians

$$\hat{H}_{\mathrm{I}}(\mathbf{r}) = -\frac{\hbar^2}{2m}\nabla^2 + V_{\mathrm{I}}(\mathbf{r}) \tag{5.9}$$

$$\hat{H}_{\mathrm{II}}(\mathbf{r}) = -\frac{\hbar^2}{2m}\nabla^2 + V_{\mathrm{II}}(\mathbf{r}) \tag{5.10}$$

and their respective Schrödinger equations for their eigenfunctions ψ and ϕ

$$\hat{H}_{\mathrm{I}}(\mathbf{r})\psi(\mathbf{r},t) = i\hbar\frac{\partial}{\partial t}\psi(\mathbf{r},t) \tag{5.11}$$

$$\hat{H}_{\mathrm{II}}(\mathbf{r})\phi(\mathbf{r},t) = i\hbar\frac{\partial}{\partial t}\phi(\mathbf{r},t). \tag{5.12}$$

which, in order for the transfer-Hamiltonian formalism to be of some help, have to be (considerably) easier to solve compared to the full problem. Fortunately, this is normally the case. Proceeding further, we may rewrite Equations (5.11) and (5.12) in the more compact and more general representation-independent form

$$\hat{H}_{\mathrm{I}}|\psi(t)\rangle = i\hbar\frac{\partial}{\partial t}|\psi(t)\rangle \tag{5.13}$$

$$\hat{H}_{\mathrm{II}}|\phi(t)\rangle = i\hbar\frac{\partial}{\partial t}|\phi(t)\rangle. \tag{5.14}$$

Since the potentials are time-independent, equations (5.13) and (5.14) admit stationary solutions labeled by their energies E_{I} and E_{II} and we will have

$$\hat{H}_{\mathrm{I}}|\psi_j\rangle = E_{\mathrm{I}j}|\psi_j\rangle \tag{5.15}$$

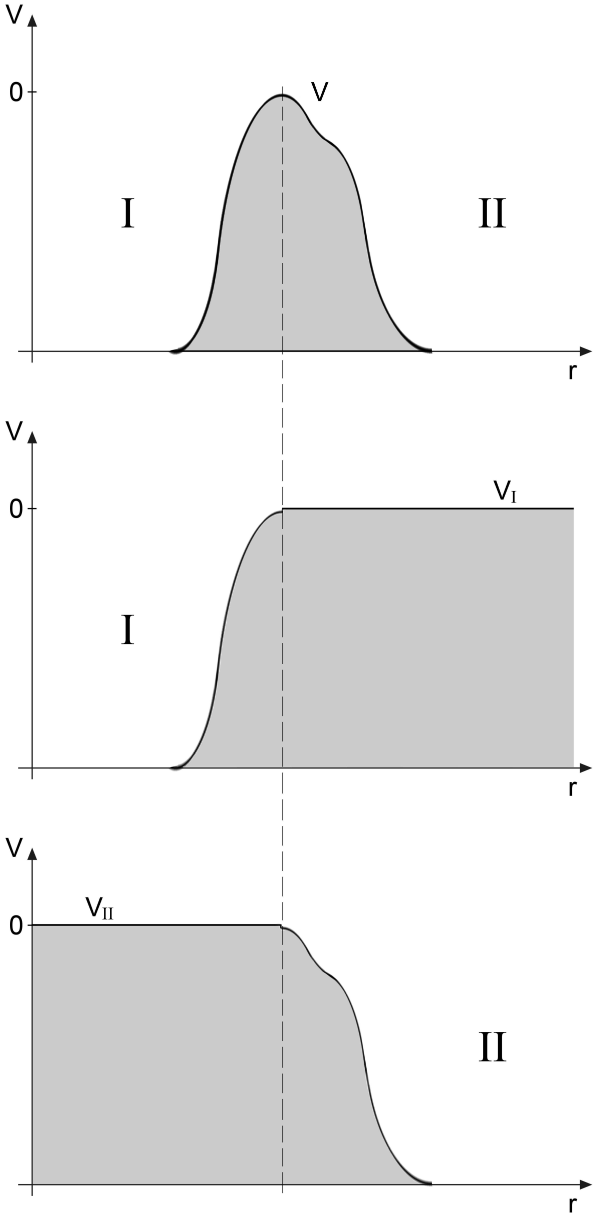

Figure 5.3: The potentials $V_{\mathrm{I}}(\mathbf{r})$ and $V_{\mathrm{II}}(\mathbf{r})$ for the construction of independent regions I and II.

$$\hat{H}_{\mathrm{II}}|\phi_k\rangle = E_{\mathrm{II}k}|\phi_k\rangle \tag{5.16}$$

and the time evolution of the states $|\psi\rangle$ and $|\phi\rangle$ will be given by

$$|\psi_j(t)\rangle = \mathrm{e}^{-\frac{iE_{\mathrm{I}j}}{\hbar}}|\psi_j\rangle \tag{5.17}$$

$$|\phi_k(t)\rangle = \mathrm{e}^{-\frac{iE_{\mathrm{II}k}}{\hbar}}|\phi_k\rangle. \tag{5.18}$$

Assumption **A2** requires the set of eigenstates $\{|\psi\rangle\}$ and $\{|\phi\rangle\}$ to be nearly orthogonal i.e. $\langle\psi_j|\phi_k\rangle \simeq 0\ \forall j,k$. This is not a trivial request, since the $\{|\psi\rangle\}$ and $\{|\phi\rangle\}$ are eigenstates of different Hamiltonians (for further details see e.g [66, 134, 135]).

5.2.1 Single-electron transition probabilities

Let us go back to the full system and consider an electron which initially, at $t = 0$, is in a region I state $|\psi_j\rangle$ with energy $E_{\mathrm{I}j}$. If region II would not have been present, the state would have evolved in time according to (5.17). If region II is present but its influence is weak, i.e. tunneling is weak, for t small enough we may have that the state $|\psi_j\rangle$ evolves into a state $|\tilde{\psi}_j(t)\rangle$ which is still close to $\mathrm{e}^{-\frac{iE_{\mathrm{I}j}}{\hbar}}|\psi_j\rangle$. Since the deviation from $|\psi_j(t)\rangle$ is due to the presence of region II, it is natural to try to quantify this deviation in terms of $\hat{H}_{\mathrm{II}}$ eigenstates $\{|\phi\rangle\}$. So, we can write

$$\begin{aligned}|\tilde{\psi}_j(t)\rangle &= \mathrm{e}^{-\frac{iE_{\mathrm{I}j}}{\hbar}}|\psi_j\rangle + |\tilde{\psi}_j(t)\rangle - \mathrm{e}^{-\frac{iE_{\mathrm{I}j}}{\hbar}}|\psi_j\rangle = \\ &\simeq \mathrm{e}^{-\frac{iE_{\mathrm{I}j}}{\hbar}}|\psi_j\rangle + \sum_k |\phi_k\rangle\langle\phi_k|\Big(|\tilde{\psi}_j(t)\rangle - \mathrm{e}^{-\frac{iE_{\mathrm{I}j}}{\hbar}}|\psi_j\rangle\Big) = \\ &= \mathrm{e}^{-\frac{iE_{\mathrm{I}j}}{\hbar}}|\psi_j\rangle + \sum_k\Big(\langle\phi_k|\tilde{\psi}_j(t)\rangle - \mathrm{e}^{-\frac{iE_{\mathrm{I}j}}{\hbar}}\langle\phi_k|\psi_j\rangle\Big)|\phi_k\rangle.\end{aligned} \tag{5.19}$$

If the states of region II would have formed a complete set and spanned the whole state space, we would have had $\sum_k |\phi_k\rangle\langle\phi_k| = \mathbf{1}$, where $\mathbf{1}$ is the identity operator, and the second step of Equation (5.19) would have implied an equality. However, this is not the case, and (5.19) is approximate. By identifying

$$a_{kj}(t) \equiv \langle\phi_k|\tilde{\psi}_j(t)\rangle - \mathrm{e}^{-\frac{iE_{\mathrm{I}j}}{\hbar}}\langle\phi_k|\psi_j\rangle \tag{5.20}$$

we can rewrite (5.19) as

$$|\tilde{\psi}_j(t)\rangle = \mathrm{e}^{-\frac{iE_{\mathrm{I}j}}{\hbar}}|\psi_j\rangle + \sum_k a_{kj}(t)|\phi_k\rangle. \tag{5.21}$$

The problem of knowing the evolution of the state $|\tilde{\psi}_j(t)\rangle$ reduces then (in approximate form) to the evaluation of the coefficients a_{kj}. For this purpose, we evaluate the Schrödinger equation for the full system (5.8) (in its representation-independent form) for $|\tilde{\psi}_j(t)\rangle$ (which is *not* an eigenstate of (5.8)). For the left hand side of (5.8) we can write

$$\hat{H}|\tilde{\psi}_j(t)\rangle = \mathrm{e}^{-\frac{iE_{\mathrm{I}j}}{\hbar}}\hat{H}|\psi_j\rangle + \sum_k a_{kj}(t)\hat{H}|\phi_k\rangle =$$

$$= \mathrm{e}^{-\frac{iE_{\mathrm{I}j}}{\hbar}}\left(\hat{H}_{\mathrm{I}} + \hat{H} - \hat{H}_{\mathrm{I}}\right)|\psi_j\rangle + \sum_k a_{kj}(t)\left(\hat{H}_{\mathrm{II}} + \hat{H} - \hat{H}_{\mathrm{II}}\right)|\phi_k\rangle =$$

$$= \mathrm{e}^{-\frac{iE_{\mathrm{I}j}}{\hbar}}E_{\mathrm{I}j}|\psi_j\rangle + \mathrm{e}^{-\frac{iE_{\mathrm{I}j}}{\hbar}}(\hat{H} - \hat{H}_{\mathrm{I}})|\psi_j\rangle + \sum_k a_{kj}(t)\left[E_{\mathrm{II}k} + (\hat{H} - \hat{H}_{\mathrm{II}})\right]|\phi_k\rangle \tag{5.22}$$

where we have obtained a form in terms of the $\hat{H} - \hat{H}_{\mathrm{I}}$ and $\hat{H} - \hat{H}_{\mathrm{II}}$ operators. For the right hand side we have

$$i\hbar\frac{\partial}{\partial t}|\tilde{\psi}_j(t)\rangle = E_{\mathrm{I}j}\mathrm{e}^{-\frac{iE_{\mathrm{I}j}}{\hbar}}|\psi_j\rangle + i\hbar\sum_k \frac{\partial a_{kj}(t)}{\partial t}|\phi_k\rangle. \tag{5.23}$$

Combining the two sides and simplifying the common $E_{\mathrm{I}j}\mathrm{e}^{-\frac{iE_{\mathrm{I}j}}{\hbar}}|\psi_j\rangle$ term we get

$$i\hbar\sum_k \frac{\partial a_{kj}(t)}{\partial t}|\phi_k\rangle = \mathrm{e}^{-\frac{iE_{\mathrm{I}j}}{\hbar}}(\hat{H} - \hat{H}_{\mathrm{I}})|\psi_j\rangle + \sum_k a_{kj}(t)\left[E_{\mathrm{II}k} + (\hat{H} - \hat{H}_{\mathrm{II}})\right]|\phi_k\rangle. \tag{5.24}$$

Multiplying now from the left by $\langle\phi_l|$ and using the orthonormality of the $\{|\phi\rangle\}$ e.g. $\langle\phi_j|\phi_k\rangle = \delta_{jk}$ we obtain a set of decoupled equations for the a's:

$$i\hbar\frac{\partial a_{lj}(t)}{\partial t} = \mathrm{e}^{-\frac{iE_{\mathrm{I}j}}{\hbar}}\langle\phi_l|\hat{H} - \hat{H}_{\mathrm{I}}|\psi_j\rangle + E_{\mathrm{II}l}a_{lj}(t) + \sum_k a_{kj}(t)\langle\phi_l|\hat{H} - \hat{H}_{\mathrm{II}}|\phi_k\rangle. \tag{5.25}$$

Now, the major obstacle to the resolution of Equation (5.25) is represented by the $a_{kj}(t)\langle\phi_l|\hat{H} - \hat{H}_{\mathrm{II}}|\phi_k\rangle$ terms. However, at $t = 0$ all the a's are zero by construction, since $|\tilde{\psi}_j(0)\rangle \equiv |\psi_j\rangle$, and it is here where we enforce **A1** and assume that the a's will remain small for some time (at least a few picoseconds) and approximate (5.25) as

$$i\hbar\frac{\partial a_{lj}(t)}{\partial t} \simeq \mathrm{e}^{-\frac{iE_{\mathrm{I}j}}{\hbar}}\langle\phi_l|\hat{H} - \hat{H}_{\mathrm{I}}|\psi_j\rangle + E_{\mathrm{II}l}a_{lj}(t), \tag{5.26}$$

where we have kept the $E_{\mathrm{II}l}a_{lj}(t)$ term although we assumed the a's to be small because (5.26) is solvable without neglecting it and a better approximation can be obtained. The solution for the differential equation (5.26), with the initial condition $a_{lj}(0) = 0$ is

$$a_{lj}(t) = \frac{\mathrm{e}^{-\frac{iE_{\mathrm{I}j}}{\hbar}} - \mathrm{e}^{-\frac{iE_{\mathrm{II}l}}{\hbar}}}{E_{\mathrm{I}j} - E_{\mathrm{II}l}}\langle\phi_l|\hat{H} - \hat{H}_{\mathrm{I}}|\psi_j\rangle \tag{5.27}$$

and we can take the square of the modulus of (5.27), getting easily

$$|a_{lj}(t)|^2 = \frac{4\sin^2\left[\frac{(E_{\mathrm{II}l}-E_{\mathrm{I}j})}{2\hbar}t\right]}{(E_{\mathrm{I}j}-E_{\mathrm{II}l})^2}|\langle\phi_l|\hat{H}-\hat{H}_{\mathrm{I}}|\psi_j\rangle|^2. \tag{5.28}$$

Having found an approximate expression for the a coefficients, we are now able to estimate $|\tilde{\psi}_j(t)\rangle$ from (5.21). Then, we can evaluate the probability that an electron initially in region I and in state $|\psi_j\rangle$ will have, at a later time, scattered into a (vacant) region II state $|\phi_l\rangle$ under the influence of the whole system Hamiltonian (5.7). This probability is represented by the transition amplitude $|\langle\phi_l|\tilde{\psi}_j(t)\rangle|^2$. Now, multiplying from the left (5.21) with $\langle\phi_l|$ we get (with $\langle\phi_j|\phi_k\rangle = \delta_{jk}$)

$$\langle\phi_l|\tilde{\psi}_j(t)\rangle = \mathrm{e}^{-\frac{iE_{\mathrm{I}j}}{\hbar}}\langle\phi_l|\psi_j\rangle + a_{lj}(t). \tag{5.29}$$

To take full advantage of our approximate expression for the a we have to further simplify this expression and thus we enforce the assumption **A2** of orthogonality between $\{|\phi\rangle\}$ and $\{|\psi\rangle\}$ states, obtaining $\langle\phi_l|\tilde{\psi}_j(t)\rangle \simeq a_{lj}(t)$ and so

$$|\langle\phi_l|\tilde{\psi}_j(t)\rangle|^2 \simeq |a_{lj}(t)|^2 = \frac{4\sin^2\left[\frac{(E_{\mathrm{II}l}-E_{\mathrm{I}j})}{2\hbar}t\right]}{(E_{\mathrm{I}j}-E_{\mathrm{II}l})^2}|\langle\phi_l|\hat{H}-\hat{H}_{\mathrm{I}}|\psi_j\rangle|^2. \tag{5.30}$$

If we consider the function $\frac{\sin^2(tx/2\hbar)}{x^2}$, this is a function with a strong peak at $x = 0$ and which becomes more peaked and narrower with larger t, tending eventually to a Dirac δ (see e.g. [136]). So, observing that the function has an area of $\pi t/2\hbar$ (see e.g. formula 3.821 (9.) of [137]) and approximating its main peak area with it, we have then in the large t limit (and in distributional sense)

$$\frac{\sin^2\left[\frac{(E_{\mathrm{II}l}-E_{\mathrm{I}j})}{2\hbar}t\right]}{(E_{\mathrm{I}j}-E_{\mathrm{II}l})^2} \qquad \longrightarrow \qquad \frac{\pi t}{2\hbar}\delta(E_{\mathrm{I}j}-E_{\mathrm{II}l}) \tag{5.31}$$

Now, if t is large enough for (5.31) to be valid while being at the same time small enough for **A1** and the approximation of (5.26) to be still holding (which is possible if it is in the order of a few picoseconds), we may write (5.30) as

$$|\langle\phi_l|\tilde{\psi}_j(t)\rangle|^2 \simeq \frac{2\pi t}{\hbar}|\langle\phi_l|\hat{H}-\hat{H}_{\mathrm{I}}|\psi_j\rangle|^2\delta(E_{\mathrm{I}j}-E_{\mathrm{II}l}). \tag{5.32}$$

This also shows that at “large” times the transition from region I states to region II states is significant only for states of similar (equal) energy.

From Equation (5.32) we can immediately obtain the *transition probability per unit time* from state $|\psi_j\rangle$ into a (vacant) region II state $|\phi_l\rangle$:

$$P_{j\to l} \equiv \frac{\mathrm{d}}{\mathrm{d}t}|\langle\phi_l|\tilde{\psi}_j(t)\rangle|^2 = \frac{2\pi}{\hbar}|\langle\phi_l|\hat{H}-\hat{H}_{\mathrm{I}}|\psi_j\rangle|^2\delta(E_{\mathrm{I}j}-E_{\mathrm{II}l}). \tag{5.33}$$

From (5.33) we can in turn obtain the *transition probability per unit time* from state $|\psi_j\rangle$ into the *full* set of (unoccupied) states of region II:

$$P_{j\to\mathrm{II}} = \frac{2\pi}{\hbar}\sum_l |\langle\phi_l|\hat{H}-\hat{H}_{\mathrm{I}}|\psi_j\rangle|^2\delta(E_{\mathrm{I}j}-E_{\mathrm{II}l}). \tag{5.34}$$

This has the classic form of the "golden rule" of ordinary time-dependent first-order perturbation theory, but differs from it in the fact that $|\psi_j\rangle$ and $|\phi_l\rangle$ are eigenstates of different Hamiltonians.
Let us now concentrate on the matrix element $\langle\phi_l|\hat{H}-\hat{H}_{\mathrm{I}}|\psi_j\rangle$, which we rename as M_{lj} and rewrite in the coordinate representation, i.e.

$$M_{lj} \equiv \langle\phi_l|\hat{H}-\hat{H}_{\mathrm{I}}|\psi_j\rangle = \int \mathrm{d}\mathbf{r}\ \phi_l^*(\mathbf{r})\Big(\hat{H}(\mathbf{r})-\hat{H}_{\mathrm{I}}(\mathbf{r})\Big)\psi_j(\mathbf{r}). \tag{5.35}$$

In this expression, the contributions to the integral will come only from region II, since by construction of $\hat{H}_{\mathrm{I}}$ we have that, in region I, $\hat{H}-\hat{H}_{\mathrm{I}}\equiv 0$. So

$$M_{lj} = \int_{\mathrm{II}} \mathrm{d}\mathbf{r}\ \phi_l^*(\mathbf{r})\Big(\hat{H}(\mathbf{r})-\hat{H}_{\mathrm{I}}(\mathbf{r})\Big)\psi_j(\mathbf{r}). \tag{5.36}$$

With the same reasoning of above, we will have $\hat{H}-\hat{H}_{\mathrm{II}}=0$ in region II, and nothing changes to the result of (5.36) if we subtract the auxiliary (null on region II) quantity $\psi_j(\mathbf{r})(\hat{H}(\mathbf{r})-\hat{H}_{\mathrm{II}}(\mathbf{r}))\phi_l^*(\mathbf{r})$. Then,

$$\begin{aligned}
M_{lj} &= \int_{\mathrm{II}} \mathrm{d}\mathbf{r}\ \Big[\phi_l^*(\mathbf{r})\Big(\hat{H}(\mathbf{r})-\hat{H}_{\mathrm{I}}(\mathbf{r})\Big)\psi_j(\mathbf{r}) - \psi_j(\mathbf{r})\Big(\hat{H}(\mathbf{r})-\hat{H}_{\mathrm{II}}(\mathbf{r})\Big)\phi_l^*(\mathbf{r})\Big] = \\
&= \int_{\mathrm{II}} \mathrm{d}\mathbf{r}\ \Big[\phi_l^*(\mathbf{r})\Big(\hat{H}(\mathbf{r})-E_{\mathrm{I}}\Big)\psi_j(\mathbf{r}) - \psi_j(\mathbf{r})\Big(\hat{H}(\mathbf{r})-E_{\mathrm{II}}\Big)\phi_l^*(\mathbf{r})\Big] = \\
&= \int_{\mathrm{II}} \mathrm{d}\mathbf{r}\ \Big[\phi_l^*(\mathbf{r})\Big(-\frac{\hbar^2}{2m}\nabla^2+V(\mathbf{r})-E_{\mathrm{I}}\Big)\psi_j(\mathbf{r}) \\
&\qquad -\psi_j(\mathbf{r})\Big(-\frac{\hbar^2}{2m}\nabla^2+V(\mathbf{r})-E_{\mathrm{II}}\Big)\phi_l^*(\mathbf{r})\Big] = \\
&= \int_{\mathrm{II}} \mathrm{d}\mathbf{r}\ \Big[\phi_l^*(\mathbf{r})\Big(-\frac{\hbar^2}{2m}\nabla^2-E_{\mathrm{I}}\Big)\psi_j(\mathbf{r})-\psi_j(\mathbf{r})\Big(-\frac{\hbar^2}{2m}\nabla^2-E_{\mathrm{II}}\Big)\phi_l^*(\mathbf{r})\Big].
\end{aligned} \tag{5.37}$$

Since with our approximations the transition probabilities are significant only for states of similar (equal) energy, we may assume $E_{\mathrm{I}j} = E_{\mathrm{III}l}$ also in (5.37), obtaining

$$M_{lj} \simeq -\frac{\hbar^2}{2m}\int_{\mathrm{II}} \mathrm{d}\mathbf{r}\, \Big(\phi_l^*(\mathbf{r})\nabla^2\psi_j(\mathbf{r}) - \psi_j(\mathbf{r})\nabla^2\phi_l^*(\mathbf{r})\Big) =$$

$$= -\frac{\hbar^2}{2m}\int_{\mathrm{II}} \mathrm{d}\mathbf{r}\, \boldsymbol{\nabla}\cdot\Big(\phi_l^*(\mathbf{r})\boldsymbol{\nabla}\psi_j(\mathbf{r}) - \psi_j(\mathbf{r})\boldsymbol{\nabla}\phi_l^*(\mathbf{r})\Big) \qquad (5.38)$$

which through the divergence theorem can be transformed in a surface integral calculated on the surface S dividing region I and II, obtaining finally

$$M_{lj} = -\frac{\hbar^2}{2m}\int_{S} \mathrm{d}\mathbf{S}\cdot\Big(\phi_l^*(\mathbf{r})\boldsymbol{\nabla}\psi_j(\mathbf{r}) - \psi_j(\mathbf{r})\boldsymbol{\nabla}\phi_l^*(\mathbf{r})\Big) \qquad (5.39)$$

where $\mathrm{d}\mathbf{S} = \mathrm{d}S\mathbf{n}$, and $\mathbf{n}$ is the unitary vector normal to S. We see that the above procedure has allowed us to obtain a form for M_{lj} which entails a modulus $|M_{lj}|$ which is symmetric under the exchange of region I states with region II states, in the sense that $|M_{lj}(\phi_l, \psi_j)| = |M_{jl}(\psi_j, \phi_l)|$. We note that since in the following the relevant quantity is indeed the modulus $|M_{lj}|$, we will sometimes for convenience invert the sign and the wavefunction order in (5.39).

With M_{lj} the transition probability (5.33) is rewritten as

$$P_{j\to l} \simeq \frac{2\pi}{\hbar}|M_{lj}|^2\delta(E_{\mathrm{I}j} - E_{\mathrm{III}l}). \qquad (5.40)$$

In this formulation of $P_{j\to l}$, the symmetry under the exchange of region I states with region II states is manifest. This implies that $P_{j\to l}$ can be interpreted dually as the total transition probability per unit time at which an electron in region II state $|\phi_l\rangle$ scatters into a given (vacant) region I state $|\psi_j\rangle$, i.e. $P_{j\to l} = P_{l\to j}$.

5.2.2 The transfer-Hamiltonian tunneling current

The transition probability $P_{j\to l}$ as written in Equations (5.33), (5.40) was always considered to be between an initially occupied state $|\psi_j\rangle$ and a state $|\phi_l\rangle$ (of region II) which was empty. However, in real conductors this is generally not the case and, on one side, a certain fraction of initial states will be empty and, on the other side, a certain fraction of "target" states in which tunneling is attempted will be occupied and thus unavailable owing to Pauli's exclusion principle. So, we have to take into account the occupation statistics of the electron states of our regions I and II. If we assume **A4** and **A5**, then the occupation probability of a state of energy E is given (at all times) by the Fermi-Dirac distribution:

$$f(E) = \frac{1}{\mathrm{e}^{\frac{E-\mu}{k_B T}} + 1} \qquad (5.41)$$

where μ is the chemical potential, k_B is Boltzmann's constant and T the system temperature. Obviously, the vacancy probability of the same state will be $1 - f(E)$. Then, the transition probability per unit time from region I state $|\psi_j\rangle$ to region II state $|\phi_l\rangle$ (5.40) will become

$$P^{FD}_{j\to l} = \frac{2\pi}{\hbar} f_{\mathrm{I}}(E_{\mathrm{I}j})\Big(1 - f_{\mathrm{II}}(E_{\mathrm{II}l})\Big)|M_{lj}|^2 \delta(E_{\mathrm{I}j} - E_{\mathrm{II}l}) \tag{5.42}$$

and, similarly, the transition probability per unit time from region II state $|\phi_l\rangle$ to region I state $|\psi_j\rangle$ is

$$P^{FD}_{l\to j} = \frac{2\pi}{\hbar} f_{\mathrm{II}}(E_{\mathrm{II}l})\Big(1 - f_{\mathrm{I}}(E_{\mathrm{I}j})\Big)|M_{lj}|^2 \delta(E_{\mathrm{I}j} - E_{\mathrm{II}l}). \tag{5.43}$$

By summing over all the region I and region II states we can obtain from (5.42) the *electron transfer rate* from region I to region II

$$P^{FD}_{I\to II} = \frac{2\pi}{\hbar} \sum_{lj} f_{\mathrm{I}}(E_{\mathrm{I}j})\Big(1 - f_{\mathrm{II}}(E_{\mathrm{II}l})\Big)|M_{lj}|^2 \delta(E_{\mathrm{I}j} - E_{\mathrm{II}l}) \tag{5.44}$$

and from (5.43) the electron transfer rate from region II to region I

$$P^{FD}_{II\to I} = \frac{2\pi}{\hbar} \sum_{lj} f_{\mathrm{II}}(E_{\mathrm{II}l})\Big(1 - f_{\mathrm{I}}(E_{\mathrm{I}j})\Big)|M_{lj}|^2 \delta(E_{\mathrm{I}j} - E_{\mathrm{II}l}). \tag{5.45}$$

The *total electron current* I between region I and II will then simply be the difference between forward transfer rate $P^{FD}_{I\to II}$ and the reverse transfer rate $P^{FD}_{II\to I}$ multiplied by the electron charge e. We can then write, with some index renaming

$$\begin{aligned} I = \frac{2\pi e}{\hbar} \sum_{jk} \Big[& f_{\mathrm{I}}(E_{\mathrm{I}j})\Big(1 - f_{\mathrm{II}}(E_{\mathrm{II}k})\Big) \\ & - f_{\mathrm{II}}(E_{\mathrm{II}k})\Big(1 - f_{\mathrm{I}}(E_{\mathrm{I}j})\Big)\Big] |M_{jk}|^2 \delta(E_{\mathrm{I}j} - E_{\mathrm{II}k}). \end{aligned} \tag{5.46}$$

If we assume the two regions I and II to be made of the same material (i.e. with the same chemical potential μ) and to be at the same temperature, then $f_{\mathrm{I}}(E) = f_{\mathrm{II}}(E) \equiv f(E)$ and, with this, (5.46) simplifies to

$$I = \frac{2\pi e}{\hbar} \sum_{jk} \Big(f(E_{\mathrm{I}j}) - f(E_{\mathrm{II}k})\Big)|M_{jk}|^2 \delta(E_{\mathrm{I}j} - E_{\mathrm{II}k}). \tag{5.47}$$

We note that, in the absence of an external applied potential, the current (5.47) will be, of course, zero. We note moreover that these expressions for the tunneling current have been explicitly derived in the framework of the non-interacting, single-particle approximation. A generalization to an expression including many-body effects may be obtained with the linear-response formalism [66], see also [42, 131, 135], but will not be used in the present discussion.

5.2.3 The tunneling current with an external potential and the low temperature -low voltage limit

Let us now consider the current between two similar conductors (5.47) in the case when an external potential difference is applied between them. Then, the introduction of the potential will create a shift in the energy levels of one side with respect to the other, as illustrated in Figure 5.4 for the case of a positive bias voltage V applied to conductor II. If we refer to the states energy with respect to the bottom of the conduction band we can drop the distinction between region I and II energies, and, with the notation of Figure 5.4, we will have $E_k = E_j + eV$. Then, the Dirac δ imposing the transitions to be within states of equal energy will take the form $\delta(E_j - E_k + eV)$ and the current will become

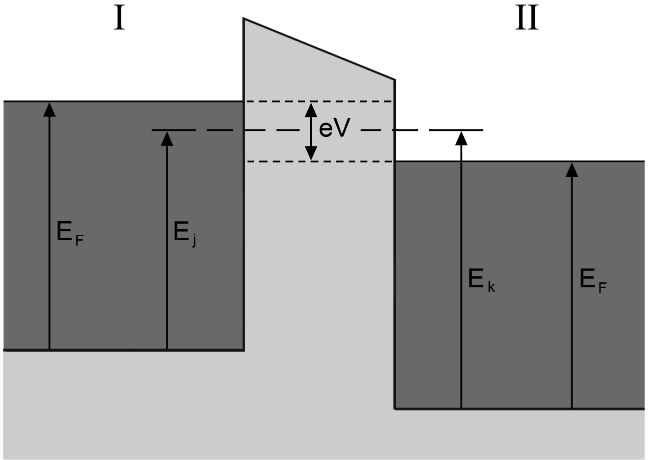

Figure 5.4: The tunneling problem between two identical conductive regions in the presence of an external positive bias potential V applied to region II.

$$I = \frac{2\pi e}{\hbar} \sum_{jk} \Big(f(E_j) - f(E_k) \Big) |M_{jk}|^2 \delta(E_j - E_k + eV). \tag{5.48}$$

A further simplification of this expression can be obtained by considering first the low temperature limit of (5.48). In this case, the Fermi-Dirac distribution (5.41) tends to a Heaviside step function i.e.

$$\lim_{T \to 0} f(E) = \theta(E_F - E) \tag{5.49}$$

where we have identified the customary Fermi energy:

$$E_F \equiv \lim_{T \to 0} \mu(T) \tag{5.50}$$

which is also shown in Figure 5.4.
In this limit, the tunneling current (5.48) becomes

$$I = \frac{2\pi e}{\hbar}\sum_{jk}\Big(\theta(E_F - E_j) - \theta(E_F - E_k)\Big)|M_{jk}|^2\delta(E_j - E_k + eV) =$$

$$= \frac{2\pi e}{\hbar}\sum_{jk}\Big(\theta(E_F - E_j) - \theta(E_F - E_j - eV)\Big)|M_{jk}|^2\delta(E_j - E_k + eV) \quad (5.51)$$

where we have used the constraint on the energies imposed by the δ to rewrite the argument of the second θ function. Now, we have that

$$\theta(E_F - E_j) - \theta(E_F - E_j - eV) = \left\{ \begin{array}{lcl} 1 & ; & E_F - eV < E_j < E_F \\ 0 & ; & \text{otherwise} \end{array} \right. \quad (5.52)$$

and on the other side we have the approximation of the δ [138]

$$a\delta(x) \simeq \left\{ \begin{array}{lcl} 1 & ; & -\frac{a}{2} < x < \frac{a}{2} \\ 0 & ; & \text{otherwise} \end{array} \right. \quad (5.53)$$

when a is small. This implies that for small eV i.e. in the low voltage limit we have $\theta(E_F - E_j) - \theta(E_F - E_j - eV) \simeq eV\delta(E_F - eV/2 - E_j)$, obtaining for (5.51)

$$I \simeq \frac{2\pi}{\hbar}e^2V\sum_{jk}|M_{jk}|^2\delta(E_F - \frac{eV}{2} - E_j)\delta(E_j - E_k + eV) =$$

$$= \frac{2\pi}{\hbar}e^2V\sum_{jk}|M_{jk}|^2\delta(E_F - \frac{eV}{2} - E_j)\delta(E_F + \frac{eV}{2} - E_k) =$$

$$\simeq \frac{2\pi}{\hbar}e^2V\sum_{jk}|M_{jk}|^2\delta(E_F - E_j)\delta(E_F - E_k) \quad (5.54)$$

where in the first passage we have used the constraint on the energies imposed by the first δ to rewrite the argument of the second δ, while in the second passage we have neglected the $eV/2$ terms.

Recapitulating, within the transfer-Hamiltonian formalism, the tunneling current between to similar conductors I and II with a positive bias voltage applied on II takes the form of (5.48)

$$I = \frac{2\pi e}{\hbar}\sum_{jk}\Big(f(E_j) - f(E_k)\Big)|M_{jk}|^2\delta(E_j - E_k + eV) \quad (5.55)$$

which in the low temperature -low bias limit reduces to (5.54)

$$I = \frac{2\pi}{\hbar} e^2 V \sum_{jk} |M_{jk}|^2 \delta(E_F - E_j)\delta(E_F - E_k) \tag{5.56}$$

which is a form that is widely used (see e.g. [124, 125, 130, 131]) The matrix element M_{jk} is given by (5.39)

$$M_{jk} = -\frac{\hbar^2}{2m}\int_S \mathrm{d}\mathbf{S} \cdot \left(\phi_j^*(\mathbf{r})\boldsymbol{\nabla}\psi_k(\mathbf{r}) - \psi_k(\mathbf{r})\boldsymbol{\nabla}\phi_j^*(\mathbf{r})\right) \tag{5.57}$$

where the ψ and ϕ are eigenfunctions of the separate region I and II Hamiltonians.

5.2.4 The one-dimensional rectangular barrier tunneling problem with the transfer-Hamiltonian formalism

As a first application of the transfer-Hamiltonian tunneling formalism we consider the one-dimensional rectangular barrier case treated in the introductory Section 5.1. So, we may proceed by constructing the eigenfunctions of the separate region I and II Hamiltonians, which will be the ones of a free electron encountering a potential step, as shown in Figure 5.5. The full system will still be governed by Equation (5.1). For the independent region I case, we will have two situations (see Figure 5.5): for $x < 0$ (5.1) reduces to the free particle equation $-\frac{\hbar^2}{2m}\frac{\mathrm{d}^2\psi_\mathrm{I}}{\mathrm{d}x^2} = E\psi_\mathrm{I}$, while inside the potential step i.e. for $x > 0$ a constant potential is present and (5.1) becomes $-\frac{\hbar^2}{2m}\frac{\mathrm{d}^2\psi_\mathrm{I}}{\mathrm{d}x^2} = (E - V_0)\psi_\mathrm{I}$. Again, these differential equations admit simple solutions, and for an electron initially in region I and propagating from left to right with energy E_I less than the step height V_0 (i.e. $E_\mathrm{I} < V_0$), we will have

$$\psi_\mathrm{I} = \begin{cases} \mathrm{e}^{ikx} + A\mathrm{e}^{-ikx} & \text{if } x < 0 \\ B\mathrm{e}^{-\kappa x} & \text{if } x > 0 \end{cases} \tag{5.58}$$

where A, B are coefficients to be determined and where, as in Section 5.1

$$k(E) = \frac{\sqrt{2mE}}{\hbar} \tag{5.59}$$

$$\kappa(E) = \frac{\sqrt{2m(V_0 - E)}}{\hbar}. \tag{5.60}$$

If we want (5.58) to be an eigenfunction of the full region I Hamiltonian, we have to match the partial solutions at the barrier interfaces by imposing to ψ and to the derivative $\frac{\mathrm{d}\psi}{\mathrm{d}x}$ to be continuous at $x = 0$. We have then the conditions on A and B:

$$\begin{cases} 1 + A = B \\ ik - ikA = -\kappa B \end{cases} \tag{5.61}$$

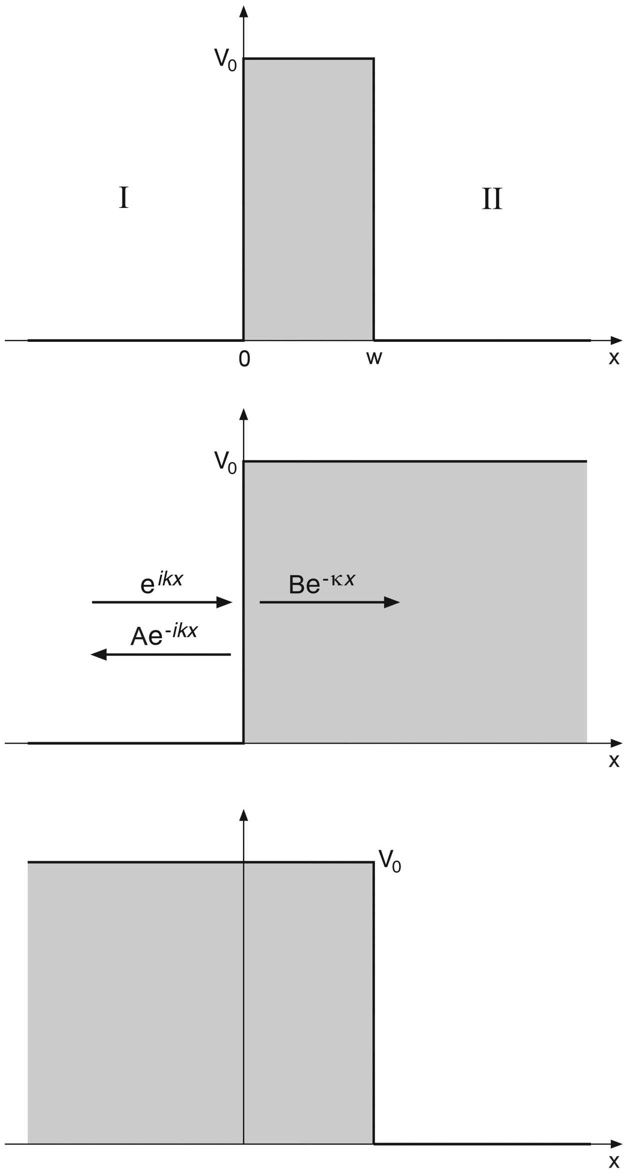

Figure 5.5: The region I and II potentials for the construction of independent Hamiltonians in the one-dimensional rectangular barrier case.

which implies immediately

$$B = \frac{2k}{k + i\kappa} \tag{5.62}$$

which in turn allows us to write the region I eigenfunction inside the potential step as

$$\psi_{\mathrm{I}}(k) = \frac{2k}{k+i\kappa}\mathrm{e}^{-\kappa x}. \tag{5.63}$$

With the same procedure we can easily obtain the independent region II (right-propagating) solution inside the potential step ending at $x = w$:

$$\psi_{\mathrm{II}}(k) = \frac{2k}{k+i\kappa}\mathrm{e}^{\kappa(x-w)}. \tag{5.64}$$

The matrix element M (5.57) calculated in the barrier is then, in its one-dimensional form,

$$M_{pq} = -\frac{\hbar^2}{2m}\left(\psi^*_{\mathrm{II}}(k_q)\frac{\mathrm{d}}{\mathrm{d}x}\psi_{\mathrm{I}}(k_p) - \psi_{\mathrm{I}}(k_p)\frac{\mathrm{d}}{\mathrm{d}x}\psi^*_{\mathrm{II}}(k_q)\right) =$$

$$= -\frac{\hbar^2}{2m}\frac{4k_pk_q(\kappa_p+\kappa_q)}{(k_p+i\kappa_p)(k_q-i\kappa_q)}\mathrm{e}^{-\kappa_p x+\kappa_q(x-w)} \tag{5.65}$$

from which it follows immediately

$$|M_{pq}|^2 = \frac{\hbar^4}{4m^2}\frac{16k_p^2k_q^2(\kappa_p+\kappa_q)^2}{(k_p^2+\kappa_p^2)(k_q^2+\kappa_q^2)}\mathrm{e}^{-2\kappa_p x+2\kappa_q(x-w)}. \tag{5.66}$$

Let us now consider first, for the sake of compactness, the simple case where region I is occupied with electrons with a given occupation probability $f(E)$ and II is completely empty i.e. all the states are available. Then, the tunneling current will be given by (5.46)-(5.47), and we may write

$$I_{\mathrm{I}\to\mathrm{II}} = \frac{2\pi e}{\hbar}\sum_{pq} f(E_p)|M_{pq}|^2\delta(E_p-E_q) =$$

$$= \frac{2\pi e}{\hbar}\sum_{pq}\int \mathrm{d}E_r\ \delta(E_r-E_p)\int \mathrm{d}E_s\ \delta(E_s-E_q)f(E_p)|M_{pq}|^2\delta(E_p-E_q) =$$

$$= \frac{2\pi e}{\hbar}\int \mathrm{d}E_r\sum_p \delta(E_r-E_p)\int \mathrm{d}E_s\sum_q \delta(E_s-E_q)f(E_r)|M_{rs}|^2\delta(E_r-E_s) =$$

$$= \frac{2\pi e}{\hbar}\int \mathrm{d}E_r\int \mathrm{d}E_s\ \rho(E_r)\rho(E_s)f(E_r)|M_{rs}|^2\delta(E_r-E_s) \tag{5.67}$$

where in the last passage we have introduced the independent particles density of states ρ, defined as (see e.g. [131])

$$\rho(E) \equiv \sum_k \delta(E_k-E) \tag{5.68}$$

which by construction of the present problem will be equal for both region I and II.

Now, for a one-dimensional free particles system the density of states takes the form

$$\rho^{1D}(E) = \frac{1}{\pi\hbar}\sqrt{\frac{m}{2E}} = \frac{m}{\pi\hbar^2}\frac{1}{k} \tag{5.69}$$

and observing also that by definition $k_r(E_s) = k_s$ and $k_s(E_r) = k_r$ (and similarly for the κ), we can write for (5.67)

$$\begin{aligned} I_{\mathrm{I}\to\mathrm{II}} = \frac{2\pi e}{\hbar}\int \mathrm{d}E_r \int \mathrm{d}E_s \, \frac{m^2}{\pi^2\hbar^4}\frac{1}{k_r k_s} f(E_r)|M_{pq}|^2\delta(E_r - E_s) = \\ = \frac{4e}{h}\int \mathrm{d}E_r \int \mathrm{d}E_s \; f(E_r)\frac{4k_r k_s(\kappa_r + \kappa_s)^2}{(k_r^2+\kappa_r^2)(k_s^2+\kappa_s^2)}\mathrm{e}^{-2\kappa_r x + 2\kappa_s(x-w)}\delta(E_r - E_s) = \\ = \frac{4e}{h}\int \mathrm{d}E_r \; f(E_r)\frac{4k_r^2\kappa_r^2}{(k_r^2+\kappa_r^2)^2}\mathrm{e}^{-2\kappa_r w}. \end{aligned} \tag{5.70}$$

With the same procedure as above one can easily obtain the current for the case of two similar one-dimensional conductors separated by a rectangular barrier and where a positive bias voltage V is applied on the right conductor (but does not change the shape of the barrier). The current will be given by (5.55) and we have

$$\begin{aligned} I = \frac{2\pi e}{\hbar}\sum_{pq}\Big(f(E_p) - f(E_q)\Big)|M_{pq}|^2\delta(E_p - E_q + eV) = \\ = \frac{4e}{h}\int \mathrm{d}E_p \Big(f(E_p) - f(E_p + eV)\Big)\frac{4k_p^2\kappa_p^2}{(k_p^2+\kappa_p^2)^2}\mathrm{e}^{-2\kappa_p w}. \end{aligned} \tag{5.71}$$

where for clarity we have kept the p subscript.

Now, by confronting the result (5.71) with the general tunneling expression of classic calculations of tunneling between two conductors like e.g. Simmons [121], Holm [139], Frenkel [140] (see also Chap. 7 of [66]) adapted to one dimension, we can identify

$$D_{TH} \equiv \frac{4k^2\kappa^2}{(k^2+\kappa^2)^2}\mathrm{e}^{-2\kappa w} \tag{5.72}$$

which, when compared to (5.6), shows us that for the one-dimensional rectangular barrier the transfer-Hamiltonian formalism reproduces the exact result in the thick barrier limit [66]. This has to be contrasted to the widely used (as in [121, 139]) semi-classical WKB approximation for D (see e.g. [128]) which, for the rectangular barrier, takes the simple form

$$D_{WKB} = \mathrm{e}^{-2\kappa w} \tag{5.73}$$

This is of more relevance if we consider that many three-dimensional calculation like e.g. [121,139,140] deal with planar junctions and introduce relations

where tunneling is calculated only along one direction.
However, we can observe that all three expressions for D (5.6), (5.72), and (5.73) have an exponential factor $\mathrm{e}^{-2\kappa w}$ that will dominate their behavior. Therefore, many discussions on tunneling stop short of the pre-factor quagmire and retain the relevant information i.e. the exponential dependence.

5.3 Electron tunneling between two conductive spheres

We want now to apply the theoretical apparatus of the transfer-Hamiltonian formalism to the case of our interest of tunneling between two identical conductive spheres of radius R embedded in an insulating medium, as shown in Figure 5.6. The most simple way to proceed is to assimilate the spheres to three-dimensional quantum wells (with barriers of finite height V_0). However, before investigating the full spherical quantum well solutions as independent sphere I and sphere II eigenfunctions, we further restrict ourselves to 0 angular momentum ($l = 0$) s-wave solutions, which are the dominating contribution when the radius of the spheres is small [124, 125]. These

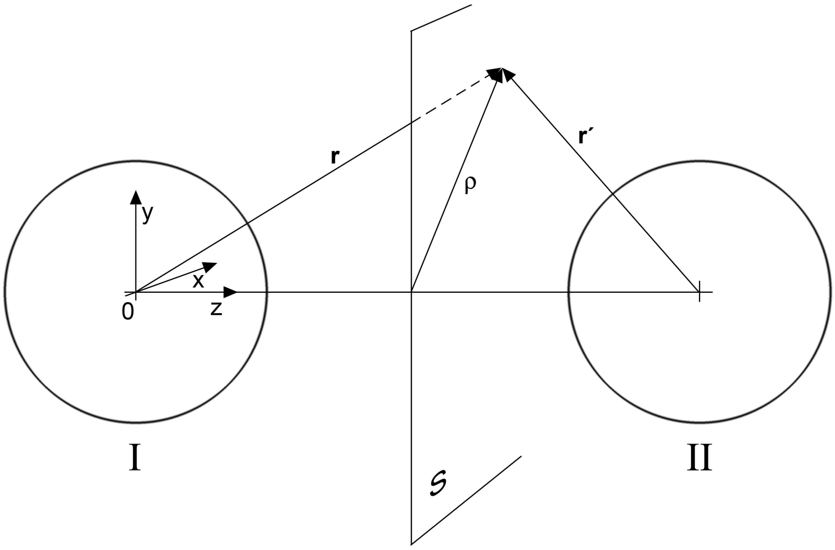

Figure 5.6: The tunneling between two spheres problem, shown with a part of the (infinite) integration surface S for the computation of the matrix element M. Sphere I is placed with its center in the origin, while sphere II is placed with its center on the z axis at distance z_0 from the origin.

solutions are, for a 3D quantum well of radius R [128]

$$\begin{cases} \psi_0(\mathbf{r}) = \frac{A}{r}\sin(kr) & \text{if } 0 < r < R \\ \psi(\mathbf{r}) = \frac{B}{r}\mathrm{e}^{-\kappa r} & \text{if } r > R \end{cases} \tag{5.74}$$

where $r = |\mathbf{r}|$ and where, as usual, $k = \frac{\sqrt{2mE}}{\hbar}$ and $\kappa = \frac{\sqrt{2m(V_0-E)}}{\hbar}$. The coefficients A and B have again to be determined by the matching conditions for ψ and $\frac{\mathrm{d}\psi}{\mathrm{d}x}$ at R. Of these, the first reads

$$\frac{A}{R}\sin kR = \frac{B}{R}\mathrm{e}^{-\kappa R} \tag{5.75}$$

i.e.

$$B = A\sin(kR)\mathrm{e}^{\kappa R} = \frac{A\sin(kR)}{R}R\mathrm{e}^{\kappa R} = \psi_0(R)R\mathrm{e}^{\kappa R} \tag{5.76}$$

and we can write our sphere I and sphere II eigenfunctions outside the well as

$$\psi_{\mathrm{I}}(\mathbf{r}) = \psi_0 R\mathrm{e}^{\kappa R}\,\frac{\mathrm{e}^{-\kappa|\mathbf{r}|}}{|\mathbf{r}|} \tag{5.77}$$

$$\psi_{\mathrm{II}}(\mathbf{r}) = \psi_0 R\mathrm{e}^{\kappa R}\,\frac{\mathrm{e}^{-\kappa|\mathbf{r}-\mathbf{r}_{0\mathrm{II}}|}}{|\mathbf{r}-\mathbf{r}_{0\mathrm{II}}|} \tag{5.78}$$

where in the second one we have introduced the vector for the sphere II center $\mathbf{r}_{0\mathrm{II}} = (0, 0, z_0)$ and where in both cases it is intended $\psi_0 = \psi_0(R)$. To calculate the matrix element M (5.57), a natural choice for the surface on which to evaluate the integral is a plane inside the barrier and normal to the z axis where the centers of the two spheres stay. For that purpose, we may exploit the 2D Fourier transform of a spherical wave (see e.g. [141]) for the case of an evanescent wave [124, 125, 130]

$$\frac{\mathrm{e}^{-\kappa|\mathbf{r}-\mathbf{r}_0|}}{|\mathbf{r}-\mathbf{r}_0|} = \frac{1}{2\pi}\int \mathrm{d}^2q\;\mathrm{e}^{i\mathbf{q}\cdot(\boldsymbol{\rho}-\boldsymbol{\rho}_0)}\;\frac{\mathrm{e}^{-|z-z_0|\sqrt{\kappa^2+q^2}}}{\sqrt{\kappa^2+q^2}} \tag{5.79}$$

where $\boldsymbol{\rho}$ is the projection on the xy plane of $\mathbf{r}$. With our choice of the spheres centers and with the integration surface in the positive z barrier region, the sphere I and II eigenfunctions outside the well are then rewritten in that region as

$$\psi_{\mathrm{I}}(\mathbf{r}) = \psi_0 R\mathrm{e}^{\kappa R}\,\frac{1}{2\pi}\int \mathrm{d}^2q\;\mathrm{e}^{i\mathbf{q}\cdot\boldsymbol{\rho}}\;\frac{\mathrm{e}^{-z\sqrt{\kappa^2+q^2}}}{\sqrt{\kappa^2+q^2}} \tag{5.80}$$

$$\psi_{\mathrm{II}}(\mathbf{r}) = \psi_0 R\mathrm{e}^{\kappa R}\,\frac{1}{2\pi}\int \mathrm{d}^2q\;\mathrm{e}^{i\mathbf{q}\cdot\boldsymbol{\rho}}\;\frac{\mathrm{e}^{(z-z_0)\sqrt{\kappa^2+q^2}}}{\sqrt{\kappa^2+q^2}}. \tag{5.81}$$

The matrix element M will have the usual form (5.57). Observing that with an integration surface S which is a plane parallel to the xy plane we have $\mathbf{n} = (0, 0, 1)$ and $\mathrm{d}S = \mathrm{d}^2\rho$, so that

$$\mathrm{d}\mathbf{S} \cdot \boldsymbol{\nabla} = \mathrm{d}^2\rho \, \mathbf{n} \cdot \boldsymbol{\nabla} = \mathrm{d}^2\rho \, \frac{\partial}{\partial z} \tag{5.82}$$

and with this,

$$\begin{aligned} \mathrm{d}\mathbf{S} \cdot \psi_{\mathrm{I}}^* \boldsymbol{\nabla} \psi_{\mathrm{II}} = \psi_{0k}^* \psi_{0k'} \, \frac{R^2 \mathrm{e}^{\kappa R + \kappa' R}}{(2\pi)^2} & \int \mathrm{d}^2 q \; \mathrm{e}^{i\mathbf{q}\cdot\boldsymbol{\rho}} \, \frac{\mathrm{e}^{-z\sqrt{\kappa^2+q^2}}}{\sqrt{\kappa^2+q^2}} \\ \times & \int \mathrm{d}^2 q' \; \mathrm{e}^{i\mathbf{q}'\cdot\boldsymbol{\rho}} \; \mathrm{e}^{(z-z_0)\sqrt{\kappa'^2+q'^2}} \end{aligned} \tag{5.83}$$

and

$$\begin{aligned} \mathrm{d}\mathbf{S} \cdot \psi_{\mathrm{II}} \boldsymbol{\nabla} \psi_{\mathrm{I}}^* = \psi_{0k}^* \psi_{0k'} \, \frac{R^2 \mathrm{e}^{\kappa R + \kappa' R}}{(2\pi)^2} & \int \mathrm{d}^2 q \; \mathrm{e}^{i\mathbf{q}\cdot\boldsymbol{\rho}} \; \mathrm{e}^{-z\sqrt{\kappa^2+q^2}} \\ \times(-1) & \int \mathrm{d}^2 q' \; \mathrm{e}^{i\mathbf{q}'\cdot\boldsymbol{\rho}} \, \frac{\mathrm{e}^{(z-z_0)\sqrt{\kappa'^2+q'^2}}}{\sqrt{\kappa'^2+q'^2}} \end{aligned} \tag{5.84}$$

so that we can write for M

$$\begin{aligned} M_{\kappa\kappa'} &= -\frac{\hbar^2}{2m} \int_S \mathrm{d}\mathbf{S} \cdot \Big(\psi_{\mathrm{I}}^*(\kappa, \mathbf{r}) \boldsymbol{\nabla} \psi_{\mathrm{II}}(\kappa', \mathbf{r}) - \psi_{\mathrm{II}}(\kappa', \mathbf{r}) \boldsymbol{\nabla} \psi_{\mathrm{I}}^*(\kappa, \mathbf{r}) \Big) = \\ &= -\frac{\hbar^2}{2m} \psi_{0k}^* \psi_{0k'} \, \frac{R^2 \mathrm{e}^{\kappa R + \kappa' R}}{(2\pi)^2} \int \mathrm{d}^2 q \int \mathrm{d}^2 q' \\ &\times \underbrace{\int \mathrm{d}^2\rho \; \mathrm{e}^{i\boldsymbol{\rho}\cdot(\mathbf{q}'-\mathbf{q})}}_{(2\pi)^2 \delta(\mathbf{q}'-\mathbf{q})} \; \mathrm{e}^{-z\sqrt{\kappa^2+q^2} + (z-z_0)\sqrt{\kappa'^2+q'^2}} \left(\frac{1}{\sqrt{\kappa^2+q^2}} + \frac{1}{\sqrt{\kappa'^2+q'^2}} \right) = \\ &= -\frac{\hbar^2}{2m} \psi_{0k}^* \psi_{0k'} \; R^2 \mathrm{e}^{\kappa R + \kappa' R} \int \mathrm{d}^2 q \; \mathrm{e}^{-z\sqrt{\kappa^2+q^2} + (z-z_0)\sqrt{\kappa'^2+q^2}} \\ &\qquad \times \left(\frac{1}{\sqrt{\kappa^2+q^2}} + \frac{1}{\sqrt{\kappa'^2+q^2}} \right). \end{aligned} \tag{5.85}$$

Let us now calculate the current between the spheres when a small positive bias voltage V is applied on sphere II. If we furthermore assume low temperatures, the tunneling current will be given by (5.56). In that expression, the two Dirac delta functions will impose on M $\kappa = \kappa' = \kappa(E_F)$ and we will have for it

$$M_{E_F} = -\frac{\hbar^2}{m} |\psi_0|^2 \; R^2 \mathrm{e}^{2\kappa R} \int \mathrm{d}^2 q \; \frac{\mathrm{e}^{-z_0\sqrt{\kappa^2+q^2}}}{\sqrt{\kappa^2+q^2}} =$$

$$= -\frac{\hbar^2}{m}|\psi_0|^2\ 2\pi R^2 \mathrm{e}^{2\kappa R}\ \frac{\mathrm{e}^{-\kappa z_0}}{z_0} \tag{5.86}$$

where we have used the fact that from (5.79) it follows

$$\frac{\mathrm{e}^{-\kappa z_0}}{z_0} = \frac{\mathrm{e}^{-\kappa|\mathbf{r}_{0\mathrm{II}}|}}{|\mathbf{r}_{0\mathrm{II}}|} = \frac{1}{2\pi}\int \mathrm{d}^2 q\ \frac{\mathrm{e}^{-z_0\sqrt{\kappa^2+q^2}}}{\sqrt{\kappa^2+q^2}}$$

If we introduce the minimal distance between the surfaces of the two spheres, $\mathfrak{d}$ (we do not use here the symbol δ used in the rest of this thesis to avoid confusion with the Dirac delta function), we have $z_0 = 2R + \mathfrak{d}$, so that M becomes

$$M_{E_F} = -\frac{2\pi\hbar^2}{m}|\psi_0|^2\ \frac{R^2 \mathrm{e}^{-\kappa\mathfrak{d}}}{2R+\mathfrak{d}}. \tag{5.87}$$

The tunneling current (5.56) is then

$$\begin{aligned} I &= \frac{2\pi}{\hbar} e^2 V \sum_{\kappa\kappa'} |M_{\kappa\kappa'}|^2 \delta(E_F - E_\kappa)\delta(E_F - E_{\kappa'}) = \\ &= \frac{2\pi}{\hbar} e^2 V |M_{E_F}|^2 \sum_{\kappa\kappa'} \delta(E_F - E_\kappa)\delta(E_F - E_{\kappa'}) = \\ &= V\ h^3\left(\frac{e}{m}\right)^2 |\psi_0|^4\ \frac{R^4 \mathrm{e}^{-2\kappa\mathfrak{d}}}{(2R+\mathfrak{d})^2} \sum_{\kappa\kappa'} \delta(E_F - E_\kappa)\delta(E_F - E_{\kappa'}) = \\ &= V\ h^3\left(\frac{e}{m}\right)^2 \rho_s^2(E_F)\ \frac{R^4 \mathrm{e}^{-2\kappa\mathfrak{d}}}{(2R+\mathfrak{d})^2} \end{aligned} \tag{5.88}$$

where, in a similar fashion to (5.68), we have introduced the surface density of states (at R and E_F) i.e. the charge per unit energy from states of the spheres surface and energy around E_F [124, 125]:

$$\rho_s(E_F) \equiv \sum_j |\psi_0(E_F)|^2 \delta(E_F - E_j). \tag{5.89}$$

Finally, from Ohm's law $I = \varrho V$ and (5.88) we have the tunneling conductance ϱ

$$\varrho = \ h^3\left(\frac{e}{m}\right)^2 \rho_s^2(E_F)\ \frac{R^4 \mathrm{e}^{-2\kappa\mathfrak{d}}}{(2R+\mathfrak{d})^2}. \tag{5.90}$$

In both (5.88) and (5.90) it is intended

$$\kappa = \kappa(E_F) = \frac{\sqrt{2m(V_0 - E_F)}}{\hbar} = \frac{\sqrt{2m\phi}}{\hbar} \tag{5.91}$$

where we have introduced the workfunction of the material of the spheres $\phi \equiv V_0 - E_F$.

5.3.1 The tunneling between two spherical wells including angular terms (and a more elegant way to do it)

We want now to investigate the contributions to the tunneling current between two identical spheres which are coming from the nonzero angular momentum solutions of the three-dimensional quantum well. The full solutions of the 3D well have the form (see e.g. [130, 132, 136])

$$\begin{cases} \psi_{0,nlm}(\mathbf{r}) = A_{nlm}\mathrm{i}_l(k_{nlm}r)Y_{nlm}(\theta,\varphi) & \text{if } 0<r<R \\ \psi_{nlm}(\mathbf{r}) = B_{nlm}\mathrm{k}_l(\kappa_{nlm}r)Y_{nlm}(\theta,\varphi) & \text{if } r>R \end{cases} \tag{5.92}$$

where l and m are the customary orbital and azimuthal quantum numbers labeling the solutions, while n labels, for a given l and m, the solutions of the continuity equations for the matching at $r = R$ [130]. i_l and k_l are the spherical modified Bessel functions of the first and second kind respectively, while Y_{lm} are spherical harmonics. θ is the elevation angle and φ the azimuthal angle of the spherical coordinate system. The A and B are, again, the constants to be determined by the matching conditions and normalization. Finally, in (5.92) it is intended $k_{nlm} = \frac{\sqrt{2mE_{nlm}}}{\hbar}$ and $\kappa_{nlm} = \frac{\sqrt{2m(V_0-E_{nlm})}}{\hbar}$.
Now, of these solutions, the major contribution will come from these with $m = 0$, since $m \neq 0$ functions have a node on the z axis [124, 125, 142]. Therefore, in the following we will only consider $m = 0$ solutions.
Dropping the n index (which labels solutions with identical functional form), and dropping furthermore all the indexes for the k and κ, the solutions outside the well up to $l = 2$ have the explicit form [130, 132, 143]

$$\begin{aligned}
&\psi_{00}(\mathbf{r}) = B_{00}\mathrm{k}_0(\kappa|\mathbf{r}-\mathbf{r}_0|)Y_{00}(\theta) = B_{00}\tfrac{\mathrm{e}^{-\kappa|\mathbf{r}-\mathbf{r}_0|}}{\kappa|\mathbf{r}-\mathbf{r}_0|} \qquad \text{s-wave solution}\\
&\psi_{10}(\mathbf{r}) = B_{10}\mathrm{k}_1(\kappa|\mathbf{r}-\mathbf{r}_0|)Y_{10}(\theta) = B_{10}\left[\tfrac{1}{\kappa|\mathbf{r}-\mathbf{r}_0|} + \tfrac{1}{(\kappa|\mathbf{r}-\mathbf{r}_0|)^2}\right]\mathrm{e}^{-\kappa|\mathbf{r}-\mathbf{r}_0|}\cos\theta\\
&\psi_{20}(\mathbf{r}) = B_{20}\mathrm{k}_2(\kappa|\mathbf{r}-\mathbf{r}_0|)Y_{20}(\theta) =\\
&\qquad = B_{20}\left[\tfrac{1}{\kappa|\mathbf{r}-\mathbf{r}_0|} + \tfrac{3}{(\kappa|\mathbf{r}-\mathbf{r}_0|)^2} + \tfrac{3}{(\kappa|\mathbf{r}-\mathbf{r}_0|)^3}\right]\mathrm{e}^{-\kappa|\mathbf{r}-\mathbf{r}_0|}(\cos^2\theta - \tfrac{1}{3})
\end{aligned} \tag{5.93}$$

where we have written the solutions in term of the distance from the well center $\mathbf{r} - \mathbf{r}_0$. Similarly to has been done for B for (5.77) and (5.78), we pose [130]

$$B_{l0} = \frac{\bar{\psi}_{0,l0}(R)}{\mathrm{k}_l(\kappa R)Y_{l0}} \tag{5.94}$$

where $\bar{\psi}_0$ is the root mean square of the ψ_0 solutions over the well surface

$$\bar{\psi}_{0,l0} = \left(\frac{1}{4\pi}\int \mathrm{d}\theta\ \sin\theta \int \mathrm{d}\varphi\ |\psi_{0,l0}(R,\theta,\varphi)|^2\right)^{1/2} \tag{5.95}$$

which is a quantity that at large radiuses is weakly dependent on l [124,125, 130].
To calculate the transition matrix element M, instead of using the 2D fourier decomposition route used for the s-wave case we will follow the elegant approach of Chen [126, 132]. Let us consider for that purpose the Schrödinger equation for the well outside the well i.e. in the classically forbidden region

$$(\nabla^2 - \kappa^2)\psi(\mathbf{r}) = 0. \tag{5.96}$$

This equation admits a Green function G defined by the differential distributional equation (written for a well centered at $\mathbf{r}_0$)

$$(\nabla^2 - \kappa^2)G(\mathbf{r} - \mathbf{r}_0) = -\delta(\mathbf{r} - \mathbf{r}_0) \tag{5.97}$$

whose solution which is regular at infinity is

$$G(\mathbf{r} - \mathbf{r}_0) = \frac{\mathrm{e}^{-\kappa|\mathbf{r}-\mathbf{r}_0|}}{4\pi|\mathbf{r} - \mathbf{r}_0|}. \tag{5.98}$$

By confronting this result with the solutions of (5.93) we can identify

$$G(\mathbf{r} - \mathbf{r}_0) = \frac{\kappa}{4\pi}\mathrm{k}_0(\kappa|\mathbf{r} - \mathbf{r}_0|) \tag{5.99}$$

and

$$\psi_{00}(\mathbf{r}) = B_{00}\frac{4\pi}{\kappa}G(\mathbf{r} - \mathbf{r}_0). \tag{5.100}$$

Interestingly, using the properties of the derivatives of the spherical modified Bessel functions we have also that [132]

$$\frac{\partial}{\partial z_0}G(\mathbf{r} - \mathbf{r}_0) = \frac{\kappa^2}{4\pi}\frac{z - z_0}{|\mathbf{r} - \mathbf{r}_0|}\mathrm{k}_1(\kappa|\mathbf{r} - \mathbf{r}_0|) = \frac{\kappa^2}{4\pi}\cos\theta\ \mathrm{k}_1(\kappa|\mathbf{r} - \mathbf{r}_0|) \tag{5.101}$$

which implies

$$\psi_{10}(\mathbf{r}) = B_{10}\frac{4\pi}{\kappa}\frac{\partial}{\kappa\partial z_0}G(\mathbf{r} - \mathbf{r}_0) \tag{5.102}$$

and, similarly,

$$\psi_{20}(\mathbf{r}) = B_{20}\frac{4\pi}{\kappa}\left(\frac{\partial^2}{\kappa^2\partial z_0^2}G(\mathbf{r} - \mathbf{r}_0) - \frac{1}{3}G(\mathbf{r} - \mathbf{r}_0)\right). \tag{5.103}$$

These expressions are immediate to verify with the explicit form of the k_l. Since we want to calculate the tunneling current in the low temperature -low bias limit (5.56), for all the ψ we will have $\kappa = \kappa(E_F)$. The matrix element M will then be

$$M_{E_F} = -\frac{\hbar^2}{2m}\int_S \mathrm{d}\mathbf{S}\cdot\Big(\psi_{\mathrm{II}}(\mathbf{r})\boldsymbol{\nabla}\psi_{\mathrm{I}}(\mathbf{r}) - \psi_{\mathrm{I}}(\mathbf{r})\boldsymbol{\nabla}\psi_{\mathrm{II}}(\mathbf{r})\Big) \tag{5.104}$$

where we have made explicit the fact that the ψ are real, and where the surface S is now a general surface separating spheres I and II. Let us consider first the case when ψ_{I} is an s-wave state. Then, from (5.100) it follows

$$M_{E_F} = B_{00}\frac{2\pi\hbar^2}{m\kappa}\int_S \mathrm{d}\mathbf{S}\cdot\Big(G(\mathbf{r}-\mathbf{r}_{0\mathrm{I}})\boldsymbol{\nabla}\psi_{\mathrm{II}}(\mathbf{r}) - \psi_{\mathrm{II}}(\mathbf{r})\boldsymbol{\nabla}G(\mathbf{r}-\mathbf{r}_{0\mathrm{I}})\Big) =$$

$$= B_{00}\frac{2\pi\hbar^2}{m\kappa}\int_{\mathrm{I}}\mathrm{d}\mathbf{r}\Big(G(\mathbf{r}-\mathbf{r}_{0\mathrm{I}})\nabla^2\psi_{\mathrm{II}}(\mathbf{r}) - \psi_{\mathrm{II}}(\mathbf{r})\nabla^2 G(\mathbf{r}-\mathbf{r}_{0\mathrm{I}})\Big) =$$

$$= B_{00}\frac{2\pi\hbar^2}{m\kappa}\int_{\mathrm{I}}\mathrm{d}\mathbf{r}\Big[G(\mathbf{r}-\mathbf{r}_{0\mathrm{I}})\kappa^2\psi_{\mathrm{II}}(\mathbf{r}) - \psi_{\mathrm{II}}(\mathbf{r})\Big(\kappa^2 G(\mathbf{r}-\mathbf{r}_{0\mathrm{I}}) - \delta(\mathbf{r}-\mathbf{r}_{0\mathrm{I}})\Big)\Big] =$$

$$= B_{00}\frac{2\pi\hbar^2}{m\kappa}\psi_{\mathrm{II}}(\mathbf{r}_{0\mathrm{I}}) \tag{5.105}$$

where in the first passage we have used the divergence theorem to re-convert the surface integral in a volume integral (this time on region I). In the second passage we have used: i) the fact that, in region I, the solutions of the spherical well II satisfy the Schrödinger equation for forbidden region (5.96), so that $\nabla^2\psi_{\mathrm{II}} = \kappa^2\psi_{\mathrm{II}}$ and, ii) the fact that G is solution of (5.97) to write $\nabla^2 G(\mathbf{r}) = \kappa^2 G(\mathbf{r}) - \delta(\mathbf{r})$.

Now, if we choose ψ_{II} to be also an s-wave solution, then (5.105) is equivalent to the result (5.87), as can be seen by substituting in (5.105) the form of ψ_{II} (5.78) and $B_{00} = \bar{\psi}_0(R)\kappa R e^{\kappa R}$ (and our choice of the sphere I center $\mathbf{r}_{0\mathrm{I}} = (0,0,0)$).

Besides of being elegant and compact, Chen's approach [132] allows to easily treat in the same fashion of what we have just done for the sphere I s-wave case also region I ψ_{10} and ψ_{20} states. For ψ_{10}, we have, with (5.102)

$$M_{E_F}[\psi_{\mathrm{I},10}] = \frac{\hbar^2}{2m}\int_S \mathrm{d}\mathbf{S}\cdot\Big(\psi_{\mathrm{I},10}(\mathbf{r})\boldsymbol{\nabla}\psi_{\mathrm{II}}(\mathbf{r}) - \psi_{\mathrm{II}}(\mathbf{r})\boldsymbol{\nabla}\psi_{\mathrm{I},10}(\mathbf{r})\Big) =$$

$$= B_{10}\frac{2\pi\hbar^2}{m\kappa}\int_S \mathrm{d}\mathbf{S}\cdot\Big(\frac{\partial}{\kappa\partial z_{0\mathrm{I}}}G(\mathbf{r}-\mathbf{r}_{0\mathrm{I}})\boldsymbol{\nabla}\psi_{\mathrm{II}}(\mathbf{r}) - \psi_{\mathrm{II}}(\mathbf{r})\boldsymbol{\nabla}\frac{\partial}{\kappa\partial z_{0\mathrm{I}}}G(\mathbf{r}-\mathbf{r}_{0\mathrm{I}})\Big) =$$

$$= B_{10}\frac{2\pi\hbar^2}{m\kappa}\frac{\partial}{\kappa\partial z_{0\mathrm{I}}}\int_S \mathrm{d}\mathbf{S}\cdot\Big(G(\mathbf{r}-\mathbf{r}_{0\mathrm{I}})\boldsymbol{\nabla}\psi_{\mathrm{II}}(\mathbf{r}) - \psi_{\mathrm{II}}(\mathbf{r})\boldsymbol{\nabla}G(\mathbf{r}-\mathbf{r}_{0\mathrm{I}})\Big) =$$

$$= B_{10}\frac{2\pi\hbar^2}{m\kappa}\frac{\partial}{\kappa\partial z_{0\mathrm{I}}}\psi_{\mathrm{II}}(\mathbf{r}_{0\mathrm{I}}) \tag{5.106}$$

where in the last passage we have used the result of (5.105).

In a similar way, with (5.103), we have for ψ_{20}

$$M_{E_F}[\psi_{\mathrm{I},20}] = B_{20}\frac{2\pi\hbar^2}{m\kappa}\Big(\frac{\partial^2}{\kappa^2\partial z_{0\mathrm{I}}^2}\psi_{\mathrm{II}}(\mathbf{r}_{0\mathrm{I}}) - \frac{1}{3}\psi_{\mathrm{II}}(\mathbf{r}_{0\mathrm{I}})\Big). \tag{5.107}$$

In all these expressions it is intended that in the ψ_{II} it is first posed $\mathbf{r} = \mathbf{r}_{0\mathrm{I}}$ with the generic $\mathbf{r}_{0\mathrm{I}}$ i.e. $\mathbf{r}_{0\mathrm{I}} = (x_{0\mathrm{I}}, y_{0\mathrm{I}}, z_{0\mathrm{I}})$, then the derivative with respect to $z_{0\mathrm{I}}$ is taken, and finally, the case-specific value of $\mathbf{r}_{0\mathrm{I}}$ is introduced.
Proceeding further, tunneling between ψ_{I} and ψ_{II} states will be significant only for states of (nearly) equal energies. The study of the energy levels of the 3D quantum well, which is bound the study of the solutions of the matching equations at $r = R$ (which in turn determine n), is difficult to be carried out exactly but can be managed numerically, as done in [130]. For the solutions up to $l = 2$ we have that the only non-direct tunneling "channel" is $\psi_{20} \leftrightarrow \psi_{00}$. So, in our specific case where the spheres are identical (i.e. $\psi_{l0} \rightarrow \psi_{l'0} = \psi_{l'0} \rightarrow \psi_{l0}$), we have to consider only four matrix elements, some of which are immediate to compute:

$$\begin{aligned}
&{\scriptstyle \psi_{00}\rightarrow\psi_{00}:} \quad M_{E_F} = B_{00}^2 \tfrac{2\pi\hbar^2}{m\kappa} \tfrac{\mathrm{e}^{-\kappa|\mathbf{r}_{0\mathrm{I}}-\mathbf{r}_{0\mathrm{II}}|}}{\kappa|\mathbf{r}_{0\mathrm{I}}-\mathbf{r}_{0\mathrm{II}}|} \\
&{\scriptstyle \psi_{10}\rightarrow\psi_{10}:} \quad M_{E_F} = B_{10}^2 \tfrac{2\pi\hbar^2}{m\kappa} \tfrac{\partial}{\kappa\partial z_{0\mathrm{I}}} \Bigg\{ \left[\tfrac{1}{\kappa|\mathbf{r}_{0\mathrm{I}}-\mathbf{r}_{0\mathrm{II}}|} + \tfrac{1}{(\kappa|\mathbf{r}_{0\mathrm{I}}-\mathbf{r}_{0\mathrm{II}}|)^2} \right] \\
&\qquad\qquad \times \mathrm{e}^{-\kappa|\mathbf{r}_{0\mathrm{I}}-\mathbf{r}_{0\mathrm{II}}|} \cos\theta \Bigg\} \\
&{\scriptstyle \psi_{20}\rightarrow\psi_{00}:} \quad M_{E_F} = B_{20} B_{00} \tfrac{2\pi\hbar^2}{m\kappa} \left[\tfrac{1}{\kappa|\mathbf{r}_{0\mathrm{I}}-\mathbf{r}_{0\mathrm{II}}|} + \tfrac{3}{(\kappa|\mathbf{r}_{0\mathrm{I}}-\mathbf{r}_{0\mathrm{II}}|)^2} + \tfrac{3}{(\kappa|\mathbf{r}_{0\mathrm{I}}-\mathbf{r}_{0\mathrm{II}}|)^3} \right] \\
&\qquad\qquad \times \mathrm{e}^{-\kappa|\mathbf{r}_{0\mathrm{I}}-\mathbf{r}_{0\mathrm{II}}|} (\cos^2\theta - \tfrac{1}{3}) \\
&{\scriptstyle \psi_{20}\rightarrow\psi_{20}:} \quad M_{E_F} = B_{20}^2 \tfrac{2\pi\hbar^2}{m\kappa} \left(\tfrac{\partial^2}{\kappa^2 \partial z_{0\mathrm{I}}^2} - \tfrac{1}{3} \right) \\
&\qquad\qquad \times \Bigg\{ \left[\tfrac{1}{\kappa|\mathbf{r}_{0\mathrm{I}}-\mathbf{r}_{0\mathrm{II}}|} + \tfrac{3}{(\kappa|\mathbf{r}_{0\mathrm{I}}-\mathbf{r}_{0\mathrm{II}}|)^2} + \tfrac{3}{(\kappa|\mathbf{r}_{0\mathrm{I}}-\mathbf{r}_{0\mathrm{II}}|)^3} \right] \\
&\qquad\qquad \times \mathrm{e}^{-\kappa|\mathbf{r}_{0\mathrm{I}}-\mathbf{r}_{0\mathrm{II}}|} (\cos^2\theta - \tfrac{1}{3}) \Bigg\}
\end{aligned} \tag{5.108}$$

where we have used the explicit expressions of (5.93). We also observe that in (5.108) we will have $\cos\theta = \frac{z_{0\mathrm{I}} - z_{0\mathrm{II}}}{|\mathbf{r}_{0\mathrm{I}} - \mathbf{r}_{0\mathrm{II}}|}$.
Without loss of generality, we can restrict the centers of the spheres to be bound on the z axis, and we can further choose sphere I to be always on the left of sphere II, i.e. $z_{0\mathrm{I}} < z_{0\mathrm{II}}$. Then, in the above expressions, $\cos\theta = -1$, and $|\mathbf{r}_{0\mathrm{I}} - \mathbf{r}_{0\mathrm{II}}| = z_{0\mathrm{II}} - z_{0\mathrm{I}}$. Furthermore, we may introduce, as done for (5.87), the minimal distance between the two spheres $\mathfrak{d}$, which implies $z_{0\mathrm{II}} - z_{0\mathrm{I}} = 2R + \mathfrak{d}$. With this, after having carried out the remaining

derivations, we can rewrite (5.108) as

$$\begin{aligned}
&{\scriptstyle \psi_{00}\to\psi_{00}:}\quad M_{E_F} = B_{00}^2\tfrac{2\pi\hbar^2}{m\kappa}\tfrac{\mathrm{e}^{-\kappa(2R+\mathfrak{d})}}{\kappa(2R+\mathfrak{d})}\\
&{\scriptstyle \psi_{10}\to\psi_{10}:}\quad M_{E_F} = -B_{10}^2\tfrac{2\pi\hbar^2}{m\kappa}\left\{\tfrac{1}{\kappa(2R+\mathfrak{d})}+\tfrac{2}{[\kappa(2R+\mathfrak{d})]^2}+\tfrac{2}{[\kappa(2R+\mathfrak{d})]^3}\right\}\mathrm{e}^{-\kappa(2R+\mathfrak{d})}\\
&{\scriptstyle \psi_{20}\to\psi_{00}:}\quad M_{E_F} = B_{20}B_{00}\tfrac{4\pi\hbar^2}{3m\kappa}\left\{\tfrac{1}{\kappa(2R+\mathfrak{d})}+\tfrac{3}{[\kappa(2R+\mathfrak{d})]^2}+\tfrac{3}{[\kappa(2R+\mathfrak{d})]^3}\right\}\mathrm{e}^{-\kappa(2R+\mathfrak{d})}\\
&{\scriptstyle \psi_{20}\to\psi_{20}:}\quad M_{E_F} = B_{20}^2\tfrac{4\pi\hbar^2}{9m\kappa}\left\{\tfrac{2}{\kappa(2R+\mathfrak{d})}+\tfrac{18}{[\kappa(2R+\mathfrak{d})]^2}+\right.\\
&\qquad\qquad\left.+\tfrac{54}{[\kappa(2R+\mathfrak{d})]^3}+\tfrac{108}{[\kappa(2R+\mathfrak{d})]^4}+\tfrac{108}{[\kappa(2R+\mathfrak{d})]^5}\right\}\mathrm{e}^{-\kappa(2R+\mathfrak{d})}
\end{aligned}\tag{5.109}$$

while, from (5.94) the B coefficients will have the explicit form

$$\begin{aligned}
B_{00}^2 &= \bar{\psi}_{0,00}^2\kappa^2R^2\mathrm{e}^{2\kappa R}\\
B_{10}^2 &= \bar{\psi}_{0,10}^2\tfrac{\kappa^4R^4}{(\kappa R+1)^2}\mathrm{e}^{2\kappa R}\\
B_{20}B_{00} &= \bar{\psi}_{0,20}\bar{\psi}_{0,00}\tfrac{3\kappa^4R^4}{2[(\kappa R)^2+3\kappa R+3]}\mathrm{e}^{2\kappa R}\\
B_{20}^2 &= \bar{\psi}_{0,20}^2\tfrac{9\kappa^6R^6}{4[(\kappa R)^2+3\kappa R+3]^2}\mathrm{e}^{2\kappa R}
\end{aligned}\tag{5.110}$$

If we now consider the large radius limit $\kappa R \gg 1$ for (5.109) with (5.110), we can see that in all the cases there will be a dominating term of the form $\frac{R^2\mathrm{e}^{-\kappa\mathfrak{d}}}{2R+\mathfrak{d}}$ i.e.

$$M_{E_F} \simeq \frac{2\pi\hbar^2}{m}\bar{\psi}_{0,l0}\bar{\psi}_{0,l'0}\frac{R^2\mathrm{e}^{-\kappa\mathfrak{d}}}{2R+\mathfrak{d}} \qquad ; \qquad \kappa R \gg 1, \quad \forall\, l,l' \leq 2 \tag{5.111}$$

which is identical in form to the s-wave contribution (5.87). Observing the above procedure, and considering the properties of the 3D quantum well solutions, it is easy to verify that (5.111) will be valid for all combinations of l and l' smaller than 2 and not only for the four cases treated explicitly. Equation (5.111) implies finally that, in the large radius limit, the tunneling current will be given by (5.88) also for tunneling channels different that the s-wave one, at least for $l \leq 2$.

5.4 Some concluding remarks on tunneling

In this chapter, we have introduced quantum mechanical electron tunneling in the framework of the transfer-Hamiltonian formalism [66, 127, 134]. We then applied this formalism to the exactly solvable case of a one-dimensional rectangular potential barrier and, subsequently, to the case of two conductive spheres represented by three-dimensional quantum wells.

The two spheres case, which we assimilate to two filler particles embedded in the insulating matrix, shows that in the large radius limit (and in the low temperature, low bias limit), the tunneling current will be made up by contributions of the form of (5.88) i.e.

$$I \propto V\, h^3 \left(\frac{e}{m}\right)^2 \rho_s^2(E_F)\, \frac{R^4 \mathrm{e}^{-2\kappa\mathfrak{d}}}{(2R+\mathfrak{d})^2} \tag{5.112}$$

which implies an inter-particle conductance

$$\varrho \propto h^3 \left(\frac{e}{m}\right)^2 \rho_s^2(E_F)\, \frac{R^4 \mathrm{e}^{-2\kappa\mathfrak{d}}}{(2R+\mathfrak{d})^2}. \tag{5.113}$$

The large radius approximation is valid when $\kappa R \gg 1$. Now, κ is the inverse of the characteristic tunneling distance ξ

$$\kappa = \frac{1}{\xi} \tag{5.114}$$

and ξ is typically in the order of the nanometer, which implies that the large radius limit is holding down to fillers with a diameter in the order of hundred nanometers.

Finally, as the treatment of the one-dimensional rectangular barrier example has shown, different approaches to tunneling can lead to results for the tunneling current which differ in the details. However, we may appreciate the fact that there was always a dominating exponential term of the form $\mathrm{e}^{-\kappa w}$ where w is a distance representing the spacing between the two regions between which tunneling is occurring, while the different formulations led to slightly different expressions for the pre-factor but with a much weaker w dependence than the exponential term. This exponential term is then the fundamental quantity to retain, and we will in the following use for ϱ the simplified form we already introduced in Chapter 2, Equation (2.3):

$$\varrho = \varrho_0\, \mathrm{e}^{-\frac{\mathfrak{d}}{\xi}} \tag{5.115}$$

where we consider ϱ_0 as a constant. Finally, these results are expected to hold also for non-spherical geometries provided that the characteristic particle dimensions are large enough.

Chapter 6

Tunneling-based formulation of conductivity in nanocomposites

Although electrically conductive polymer nanocomposites, such as carbon nanotubes or graphene sheets dispersed in a polymer matrix, are intensively investigated for their unique properties and potential technological applications, a fundamental understanding of the filler effects on conductivity is still lacking. As made explicit in Chapter 2, for composites with nanometric inclusions, there is an incompatibility between the currently employed connectivity-based percolation models and the tunneling inter-particle transport mechanism which is expected to become manifest in this class of materials. In the present chapter, we are going to introduce a model which explicitly considers the microscopic filler features and replicates the composites as random distributions of particles interconnected via electron tunneling. By exploiting the critical path method, we are able to obtain simple formulas, applicable to most nanocomposites, which allow to infer the overall composite conductivity starting from few parameters like filler volume fraction, size, and aspect-ratio. The validity of our formulation is assessed by reinterpreting existing experimental results and by extracting the characteristic tunneling length, which is mostly found within its expected value range. Since in the framework of the model we propose, the insulator-conductor transition is interpreted as a crossover between a conductivity dominated by the matrix and one dominated by the filler particles tunneling network, we finally illustrate one example extracted from the literature which gives support, and allows to gain insight into, the crossover interpretation.

6.1 The global tunneling network model

When including conductive fillers into a polymer matrix in order to obtain electrically conductive composites, a central issue is to control overall conductivity σ of the resulting materials through the volume fraction ϕ, the shape of the conducting fillers, their dispersion in the polymer matrix, and the local inter-particle electrical connectedness. Understanding how these local properties affect the composite conductivity is therefore the ultimate goal of any theoretical investigation of such composites. In the case of composites with a polymeric matrix, we saw in Chapter 2 that the conducting particles are separated from each other by a thin polymeric layer and that the conduction between the fillers is originating from quantum mechanical tunneling processes. However, although a description in term of connectivity-based percolation models applicable to macroscopic filler system may exist, when considering nanofibers, nanosheets and nanospheres, which have one or more characteristic dimensions that are comparable with the typical distances of tunneling, these models become inadequate. In particular, with nanocomposites the detailed behavior of tunneling is expected to take an explicit role in $\sigma(\phi)$ [144] and such a processes do not entail the presence of any abrupt interaction cutoff, a fundamental ingredient for most percolation formulations. On the other side, we could infer that also a model based on tunneling with no percolative behavior may be suited to describe the experimentally observed insulator-conductor transition. Consequently, in the present work we address this issue by assuming that the conducting fillers form a network of globally connected sites via tunneling processes without any detectable cutoff, i.e. a global tunneling network (GTN).

6.2 Conductivity simulations of nanocomposites

In line with what was done in the previous chapters, to model the conductor-insulator composite morphology, we treated the conducting fillers as identical impenetrable objects dispersed in a continuous insulating medium, with no interactions between the conducting and insulating phases. Again, to describe filler particle shapes varying from rod-like (nanotubes) to plate-like (graphene), we considered impenetrable spheroids (ellipsoids of revolution) ranging from the extreme prolate ($a/b \gg 1$) to the extreme oblate limit ($a/b \ll 1$), where a and b are as usual the spheroid polar and equatorial semi-axes respectively. In considering the overall conductivity arising in such composites, we assumed the spheroids of our distributions to be perfectly conductive and attributed to each spheroid pair i, j a tunneling conductance of the form (2.3), (5.115)

$$\varrho^{ij} = \varrho_0 \exp\left(-\frac{2\delta^{ij}}{\xi}\right). \tag{6.1}$$

Regarding the minimal distance between the two spheroid surfaces δ^{ij}, for spheres ($a/b = 1$) it is simply the center-to-center distance minus twice the radius of the two spheres, while for the general case ($a/b \neq 1$), δ^{ij} depends also on the relative orientation of the spheroids and can be obtained from the numerical procedure described in Section 3.2.4. The pre-factor ϱ_0, which we treated as constant and set equal to unity, contains, as we saw in Chapter 5, other minor dependencies on δ^{ij} and on the geometry of the fillers arising from the tunneling conductance. Nevertheless, its specific value may vary for different composites. We also note that in writing equation (6.1) we disregarded particle charging effects, random energy potentials, and Coulomb interactions between the particles [145–148]. At constant room temperature, which is the case considered here, and if the particles are identical and sufficiently large to limit the particle charging energy to a few meV, these contributions play a minor role compared to the tunneling term.

To evaluate the global conductivity of the system, the full set of bond conductances given by equation (6.1) was mapped on a resistor network and the overall conductivity is calculated through a numerical decimation procedure [51,60,120]. The decimation is an exact transformation easily deducible from the laws of Kirchhoff, and consists in removing sequentially all nodes from the system, and replacing them by additive resistances (for further details see appendix B of Ref. [51]). To reduce computational times of the decimation procedure to manageable limits, an artificial maximum distance was introduced in order to reject negligibly small bond conductances. It is important to note that this artifice is not in conflict with the rationale of the GTN model, since the cutoff it implies neglects conductances which are completely irrelevant for the global system conductivity. We chose the maximum distance to be generally fixed and equal to four times the spheroid major axis (i.e. a in the prolate case and b in the oblate case), which is equivalent to reject inter-particle conductances below e^{-60} for $\xi/D = 1/15$ case (and considerably less for smaller ξ values). For high aspect-ratios and high densities the distance, however, had to be reduced further. Moreover, since the maximum distance implies in turn an artificial geometrical percolation threshold of the system, again for high aspect-ratios, at low volume fractions the distance had to be increased to avoid its effect. By comparing the results with the ones obtained with significantly larger maximum distances we verified their effect to be undetectable.

Now, due to the exponential dependence of equation (6.1), the distribution of the calculated conductivities was approximately of log-normal form. Moreover, this distribution tended to the average of the logarithm as the

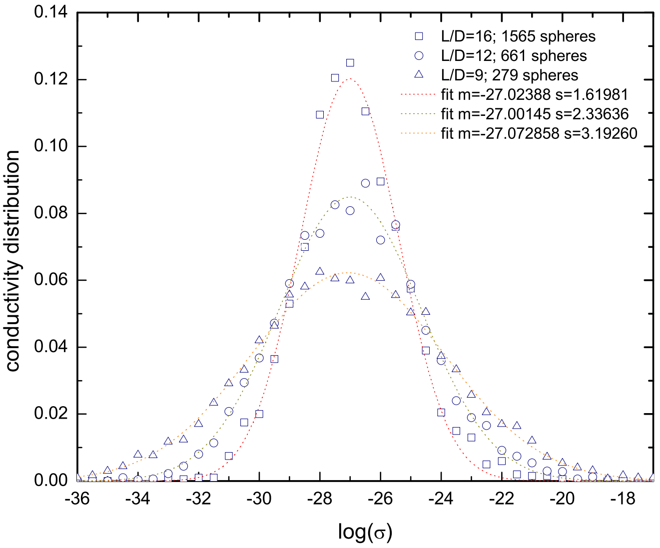

Figure 6.1: Distributions of conductivities of simulated sphere systems as a function of the cubic simulation cell size (defined by its side length to sphere diameter ratio L/D). Simulation parameters are: $D = 1.0$, $\xi/D = 1/150$, $\varrho_0 = 1$, $\phi = 0.2$. For $L/D = 16$ the replication number was 2000, for $L/D = 12$ 6000 and for $L/D = 9$ 5000. To appreciate the log-normal behavior, the results are plotted as a function of the logarithm of the conductivity and gaussian fits of the data are also shown.

particle number was increased and showed no significant drifts under such scaling. Figure 6.1 shows the distribution of the single simulation run conductivity outcome as a function of the system size (i.e. the particle number) for the case of spheres. The average of the logarithm of single run conductivity outcomes is then the quantity we considered in the following. We performed simulation for five different spheroid systems with $a/b = 1$ (spheres), 2, 1/2, 1/10, and 10 with eight different characteristic tunneling lengths ($\xi/D = 1/15$, 1/25, 1/50, 1/100, 1/150, 1/250, 1/500, and 1/1000). Each concentration step involved 300 realizations for $a/b = 1$, 2, 1/2, 1/10, and 200 realizations for $a/b = 10$. The particle number was fixed around $900 - 1000$. We report the so-obtained conductivity σ values (symbols) as function of the volume fraction ϕ for spheres in Figure 6.2 and for prolate spheroids with aspect-ratio $a/b = 10$ in Figure 6.3 for different values of ξ/D, where $D = 2\max(a, b)$. The strong reduction of σ for decreasing ϕ is a direct consequence of the fact that as ϕ is reduced, the inter-particle distances get larger, leading in turn to a reduction of the local tunneling conductances (6.1). Furthermore, as shown in the left panel of Figure 6.4, such reduction

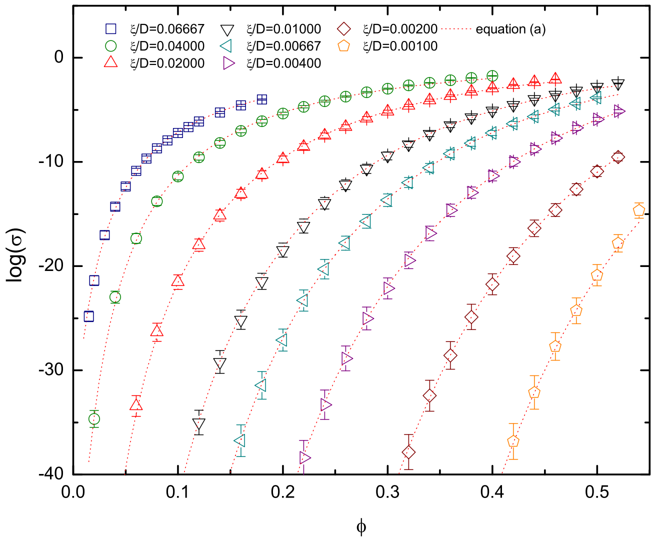

Figure 6.2: Volume fraction ϕ dependence of the tunneling conductivity σ for a system of hard spheres ($a/b = 1$) with different characteristic tunneling distances ξ/D with $D = 2r$. (a) results from equation (6.2) (with $\sigma_0 = 0.115$) are displayed by dotted lines.

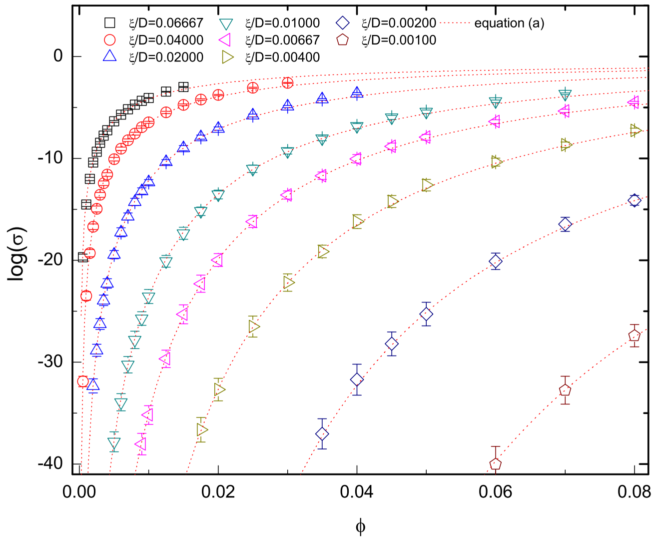

Figure 6.3: Volume fraction ϕ dependence of the tunneling conductivity σ for a system of aspect-ratio $a/b = 10$ hard prolate spheroids with different characteristic tunneling distances ξ/D with $D = 2a$. (a) results from equation (6.2) (with $\sigma_0 = 0.179$) are displayed by dotted lines.

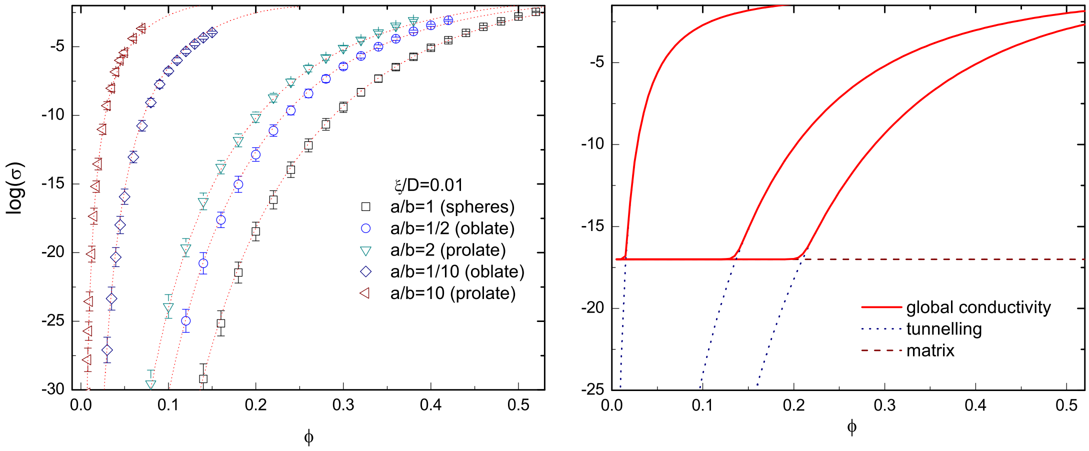

Figure 6.4: *Left*: Tunneling conductivity in a system of hard spheroids with different aspect-ratios a/b for the same ξ/D, with $D = 2\max(a,b)$. Dotted lines: results from equation (6.2) with $\sigma_0 = 0.124$ for $a/b = 2$, $\sigma_0 = 0.099$ for $a/b = 1/2$, and $\sigma_0 = 0.351$ for $a/b = 1/10$. *Right*: schematic illustration of the tunneling conductivity crossover for the cases $a/b = 1$, $a/b = 2$, and $a/b = 10$.

depends strongly on the shape of the conducting fillers. Specifically, as the shape-anisotropy of the particles is enhanced, the composite conductivity drops for much lower values of ϕ for fixed ξ. However, in real composites, we have to take into account the polymer matrix whose intrinsic conductivity σ_m, which falls typically in the range $\sigma_m \simeq 10^{-13} \div 10^{-18}$ S/cm, prevents an indefinite drop of σ. This can be modeled as a contribution in parallel to the tunneling conductivity, giving an overall conductivity $\sigma_{tot} = \sigma_m + \sigma$ which is plotted with a thick red line in the right panel of Figure 6.4. To introduce σ_m with our unit-less results, we observed that most experimental conductivity versus ϕ curves (like the ones of Figures 2.4, 2.4 of Chapter 2) have high density data which settle around 0.1-10 S/cm, so that we may estimate an unit-less $\sigma_m \simeq 10^{-13} \div 10^{-18}$. Now, if we identify ϕ_c with the volume fraction at which $\sigma \simeq \sigma_m$, then fillers with larger shape anisotropy entail lower values of ϕ_c, consistently with what is commonly observed. This also implies that a model of the composite conductivity based on the tunneling contribution of equation (6.1) alone will be representative only if ϕ is sufficiently larger than ϕ_c to consider the effect of σ_m negligible. However, the right panel of Figure 6.4 also shows us how the GTN model can account for, and reproduce the typical sigmoidal curves of the experimental σ versus ϕ plots, as the ones of e.g. Figures 2.4 and 2.5. From this perspective, it is also clear how ϕ_c will not represent anymore a percolation threshold but rather a crossover point where the conductivity contribution due to the tunneling network overtakes that due to the intrinsic matrix conductivity and becomes dominant.

6.3 Critical path approximation of the conductivity

We are now going to show that the strong dependence of $\sigma(\phi)$ on a/b and ξ of Figures 6.2-6.4 can be reproduced by the critical path (CP) method [149,150] applied to our system of impenetrable spheroids. For the tunneling conductances of equation (6.1), this method amounts to keep only the subset of conductances ϱ^{ij} having $\delta^{ij} \leq \delta_c$, where δ_c, which in turn defines the characteristic conductance $\varrho_c = \varrho_0 \exp(-2\delta_c/\xi)$, is the largest among the δ^{ij} distances such that the so-defined subnetwork forms a conducting cluster spanning the sample. Next, by assigning ϱ_c to all the (larger) conductances of the subnetwork, a CP approximation for σ is

$$\sigma \simeq \sigma_0 \exp\left[-\frac{2\delta_c(\phi, a, b)}{\xi}\right], \tag{6.2}$$

where σ_0 is a pre-factor proportional to ϱ_0. The significance of equation (6.2) is that it reduces the conductivity of a distribution of hard objects electrically connected by tunneling to the computation of the geometrical “critical" distance δ_c, which we considered in Section 4.3.2.

The first application of the CP approximation to numerical simulations of tunneling interconnected systems goes back to the classic work of Seager and Pike [151] which dealt with random distribution of point-like particles to account for hopping conductivity in amorphous semiconductors. Using the critical distance result for point particles (4.23) in Equation (6.2) we obtain the Seager and Pike conductivity estimation:

$$\sigma \simeq \sigma_0 \exp\left(-\frac{3.5\,\rho^{-1/3}}{\xi}\right), \tag{6.3}$$

where, as usual, ρ is the particle number density.

In order to illustrate the efficacy of the CP method also for the general hard particle case, we calculated Equation (6.2) with the same parameters of the conductivity simulations by using the results for δ_c of Section 4.3.2. As it can be appreciated from Figures 6.2-6.4, where the predictions of (6.2) are plotted as dotted lines, we obtain excellent agreement with the outcomes of the full numerical decimation of the resistor network.

Now, in Section 4.3.2 we obtained simple relations for the evaluation of δ_c in the case of sufficiently elongated prolate or sufficiently flat oblate spheroids, and of spheres. This means that we can formulate explicit relations between σ and the shapes and concentration of the conducting fillers which allow to evaluate quickly and precisely the tunneling conductivity of random distributions of prolate, oblate and spherical objects for $\sigma > \sigma_m$. By substituting equations (4.17),(4.18) and (4.19) into (6.2) we obtain

$$\sigma \simeq \sigma_0 \exp\left[-\frac{2D}{\xi}\frac{\gamma(b/a)^2}{\phi}\right] \quad \text{for prolates,} \tag{6.4}$$

$$\sigma \simeq \sigma_0 \exp\left\{-\frac{2D}{\xi}\left[\frac{0.15(a/b)}{\phi}\right]^{4/3}\right\} \quad \text{for oblates,} \tag{6.5}$$

$$\sigma \simeq \sigma_0 \exp\left[-\frac{2D}{\xi}\frac{1.65(1-\phi)^3}{12\phi(2-\phi)}\right] \quad \text{for spheres,} \tag{6.6}$$

where in Equation (6.4) it is $\gamma = 0.4$ for spheroids and $\gamma = 0.6$ for spherocylinders. The conditions on the validity of these relations will be the same as those for Equations (4.17),(4.18) and (4.19), i.e. the above equations will hold when $(b/a)^2 \lesssim \phi \lesssim 0.03$ for prolate objects, $\phi \gtrsim a/b$ and $a/b < 0.1$ for oblate spheroids, and $\phi \gtrsim 0.1$ for spheres. We note in passing that for the case of prolate objects, a relation of more general validity than Equation (6.4) can be obtained by substituting Equation (4.12) into Equation (6.2).

6.4 Re-interpretation of conductivity experimental results

Let us now show how the above outlined GTN formalism may be used to re-interpret the experimental data on the conductivity of different nanocomposites that can be found in the literature. In the left panel of Figure 6.5 we report measured data of $\ln(\sigma)$ versus ϕ for polymer composites filled with graphene sheets [29], Pd nanospheres [10], Cu nanofibers [31], and nanotubes [152]. Equation (6.2) implies that the same data can be more profitably re-plotted as a function of δ_c, instead of ϕ. Indeed, from

$$\ln(\sigma) = -\frac{2}{\xi}\delta_c + \ln(\sigma_0), \tag{6.7}$$

a linear behavior with slope $-2/\xi$ is expected, independently of the specific value of σ_0, which allows for a direct evaluation of the characteristic tunneling distance ξ. The exact value of ξ is a much investigated topic [153], and is expected to be between a fraction of nm and a few nm [69,150,151,153,154]. By using the values of D and a/b provided in refs. [10, 29, 31, 152] and our formulas for δ_c, we find indeed an approximately linear dependence on δ_c (right panel of Figure 6.5), from which we extract $\xi \simeq 9.22$ nm for graphene, 1.50 nm for the nanospheres, 5.90 nm for the nanofibers, and 1.64 nm for the nanotubes.

We further applied this procedure to several published data on polymer-based composites with fillers having a/b ranging from $\sim 10^{-3}$ up to $\sim 10^3$ and

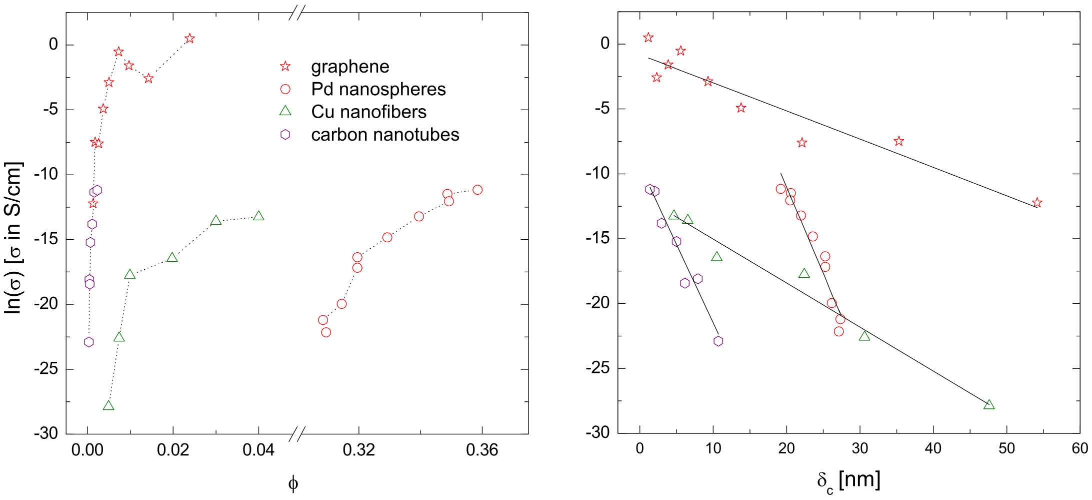

Figure 6.5: *Left*: Natural logarithm of the sample conductivity σ as a function of the volume fraction ϕ for different polymer nanocomposites: Graphene-polystyrene [29], Pd nanospheres-polystyrene [10], Cu nanofibers-polystyrene [31], and single-wall carbon nanotubes-epoxy [152]. When, for a given concentration, more then one value of σ was given (as in Refs [31, 152]), the average of $\ln \sigma$ was considered. *Right*: the same data re-plotted as function of the corresponding critical distance δ_c. Solid lines are fits to equation (6.7).

the detailed fits to equation (6.7) can be found in Appendix B. The results are collected in Figure 6.6, showing that most of the so-obtained values of the tunneling length ξ are comprised between ~ 0.1 nm and ~ 10 nm. This is a striking result considering the number of factors that make a real composite deviate from an idealized model. Most notably, as we saw in Chapter 2, fillers may have non-uniform size, aspect-ratio, and geometry, they may be oriented, bent and/or coiled, and interactions with the polymer may lead to agglomeration, segregation, and sedimentation. Furthermore, composite processing can alter the properties of the pristine fillers, e.g. nanotube or nanofiber breaking (which may explain the downward drift of ξ for high aspect-ratios in Figure 6.6) or graphite nanosheet exfoliation (which may explain the upward shift of ξ for the graphite data). In principle, deviations from ideality can be included in the present formalism by evaluating their effect on δ_c [117]. It is however interesting to notice that all these factors have often competing effects in raising or lowering the composite conductivity, and Figure 6.6 suggests that in average they compensate each other to some

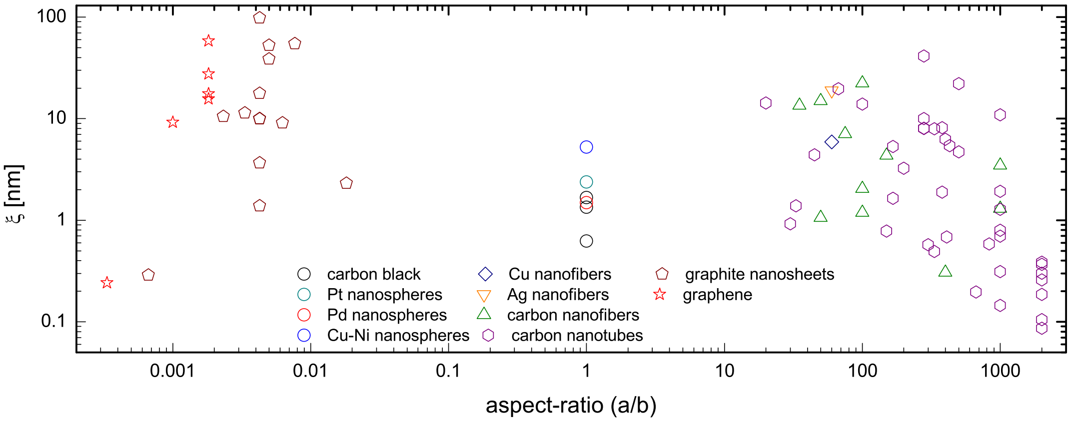

Figure 6.6: Characteristic tunneling distance ξ values for different polymer nanocomposites as extracted by means of equation (6.7).

extent, allowing tunneling conduction to emerge strongly from $\sigma(\phi)$ as a visible characteristic of nanocomposites. Considering in further detail the distribution of the values of ξ, we plot in Figure 6.7 the histograms of these for the case of prolate and oblate nanofillers. We can appreciate how the distribution for plate-like objects is somehow shifted upwards with respect to the one for fibrous systems. However, it has also to be considered that the former counts a smaller number of results. The average values are $\xi = 2.09^{+2.60}_{-1.16}$ nm for prolates, $\xi = 9.84^{+12.52}_{-5.51}$ nm for oblates, and $2.01^{+0.31}_{-0.27}$ nm for spheres.

It should then be noticed that, in spite of the rather narrow distribution of the extracted ξ values reported in Figure 6.6, the values of the pre-factor σ_0 obtained from the fits are widely dispersed. This is of course due to the fact that, besides intrinsic variations of the tunneling pre-factor conductance for different composites, interpolating the data to $\delta_c = 0$ leads to a large variance of σ_0 even for minute changes of the slope. The dispersion of the values of σ_0 is apparent in Figure 6.8, which shows the various results for prolate and oblate fillers as a function of the aspect-ratio. The spherical filler cases fluctuated more wildly, and are not displayed in Figure 6.8. Finally, we did not notice any significant correlation between the extracted ξ and σ_0 values, as it can be seen from Figure 6.9.

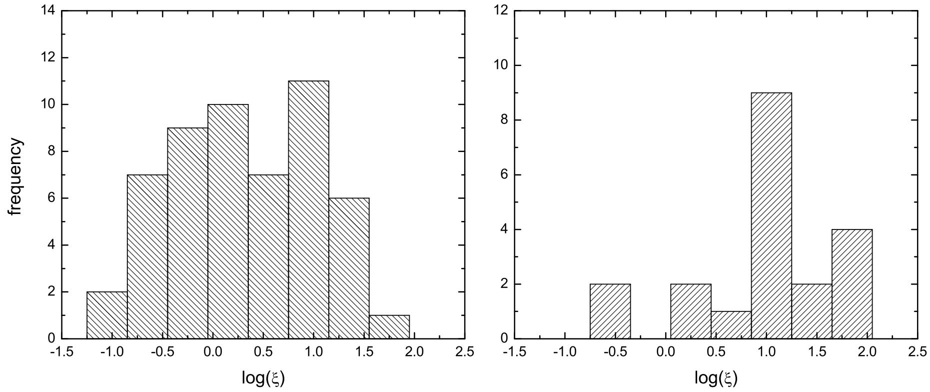

Figure 6.7: *Left*: Histogram of the characteristic tunneling distance ξ values for prolate nanofillers displayed in Figure 6.6. *Right*: The same for oblate nanofillers.

6.5 A closer look at the crossover

We now want to consider in further detail the crossover region where the contribution to the conductivity due to electron tunneling between the filler particles overtakes that due to the matrix. A first step in that direction is to assess which conduction mechanism is responsible for the intrinsic conductivity of the pristine polymer. Conductivity in these materials can be either electronic or ionic, but in polymers with chemically saturated structures (like e.g. polyethylene or polypropylene), where the backbone of the polymer chain involves only sigma bonds, it is generally ascribed to accidental ions [4]. However, the direct identification of the charge carriers is a quite complex issue, since the conductivities of saturated polymers are so low that their measure becomes ridden with difficulties. For instance, the initial current detected in a measure may be dominated by displacement currents originating from the polarization of the material and dipole reorientation. This can be a very slow process, lasting long enough to be comparable with the drift characteristics of the measurement equipment [4]. Nevertheless, in both cases of an intrinsic matrix conductivity due to ionic impurities or to displacement currents, we have that these are separated conduction paths from the electronic one due to the tunneling network, allowing thus to be treated in parallel. This implies in turn that a description of conductivity in terms of a crossover between two contributions is fully consistent, since these contributions come from independent conduction paths, and the total system conductivity is indeed $\sigma_{tot} = \sigma_m + \sigma$. From the inversion of Equations (6.4) and (6.5) it is then easy to obtain expressions for the critical crossover volume fraction ϕ_c at which $\sigma = \sigma_m$ for prolate and oblate fillers

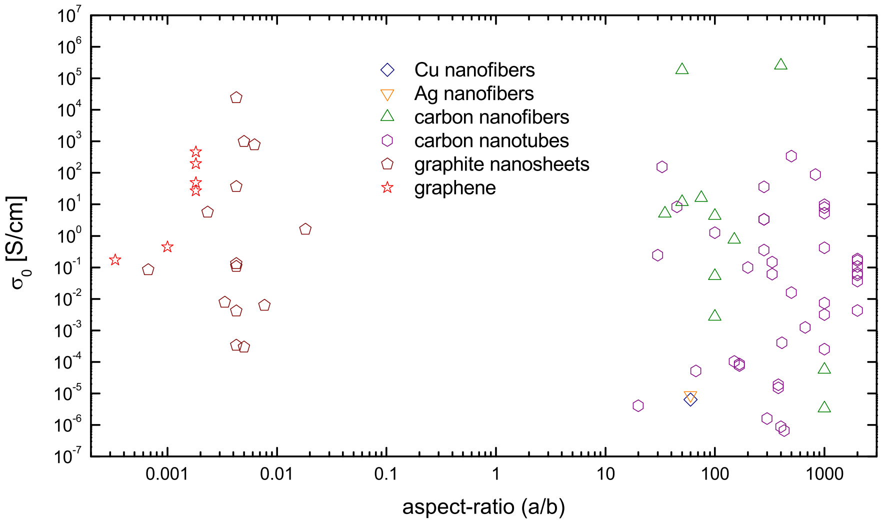

Figure 6.8: σ_0 values for different polymer nanofiber, nanotube, nanosheet and graphene composites as extracted by means of equation (6.7).

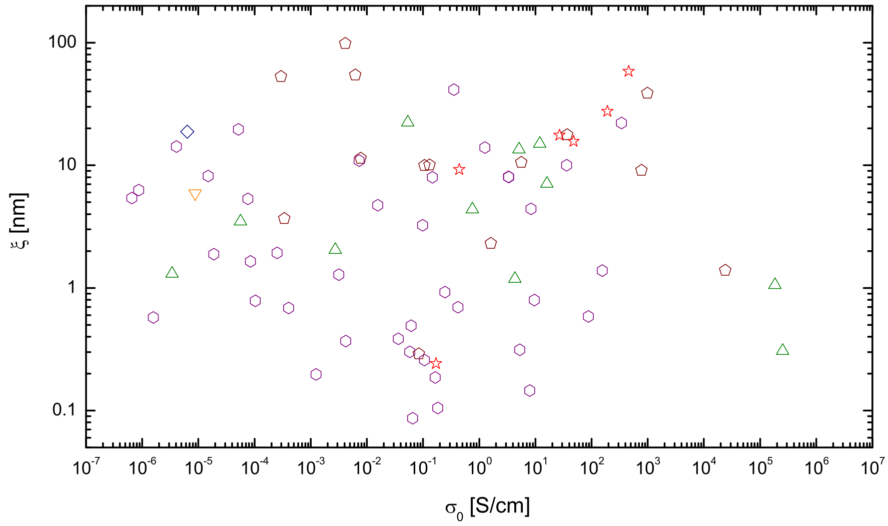

Figure 6.9: Correlation between the extracted ξ and σ_0 values for different polymer nanofiber, nanotube, nanosheet and graphene composites. Symbols as in Figure 6.8.

with sufficiently high shape-anisotropy:

$$\phi_c = \frac{2D}{\xi}\frac{\gamma(b/a)^2}{\ln(\sigma_0/\sigma_m)} \qquad \text{for prolates,} \tag{6.8}$$

$$\phi_c = 0.15(a/b)\left[\frac{2D}{\xi}\frac{1}{\ln(\sigma_0/\sigma_m)}\right]^{3/4} \qquad \text{for oblates.} \tag{6.9}$$

These expressions show naturally the same aspect-ratio dependence as the corresponding geometrical percolation critical densities, as it can be appreciated by comparing with Equation (4.4) (prolates) or with the inverse of Equation (4.15) (oblates).

Now, the crossover interpretation also implies that if, by some means, we could alter the matrix intrinsic conductivity i.e. raise it or lower it, we would see a corresponding shift in the crossover point but have the curve where tunneling is dominant unchanged. One mean to achieve that could be to increase (or decrease) the concentration of the ionic carriers within the polymer. Polymers having high ionic conductivities are fundamental for electrochemical devices such as fuel cells or lithium-ion batteries [4], but are rarely combined with conductive fillers to obtain also electronic conductivity, since this latter is unwanted for these applications. However, we managed to find an example where a conductive polymer composite with also high ionic conductivity was studied as a material for humidity sensors [155]. This consisted of carbon black dispersed in a Poly(4-vinylpyridine) matrix which was quaternized in order to obtain a polyelectrolyte. Since the absorbed water molecules interact with the polyelectrolyte and facilitate the ionic dissociation, higher humidity implies a higher ionic conductivity. We thus redraw Figure 4 of Ref. [155] in terms of sample conductance as a function of carbon black content for different humidity levels in Figure 6.10. Consistently with our assumptions, we can see how with the increase of the humidity the matrix intrinsic conductivity is indeed shifted upwards, while the results leading to a higher conductivity owing to the carbon black remain basically constant until matrix conductivity overtakes them (a slight downward shift comes from the fact that water absorption leads to swelling of the composite and thus to enhanced inter-particle distances). Then, this simple re-interpretation of a result with completely different objectives gives quite a support to the crossover interpretation. It is also interesting to note that the explanations the authors of Ref. [155] propose to account for their finding are in fact equivalent to the global tunneling network/crossover model.

6.6 Conclusions

When considering the electrical conductivity of composite materials with fillers having at least one of their characteristic dimensions in the nanometer

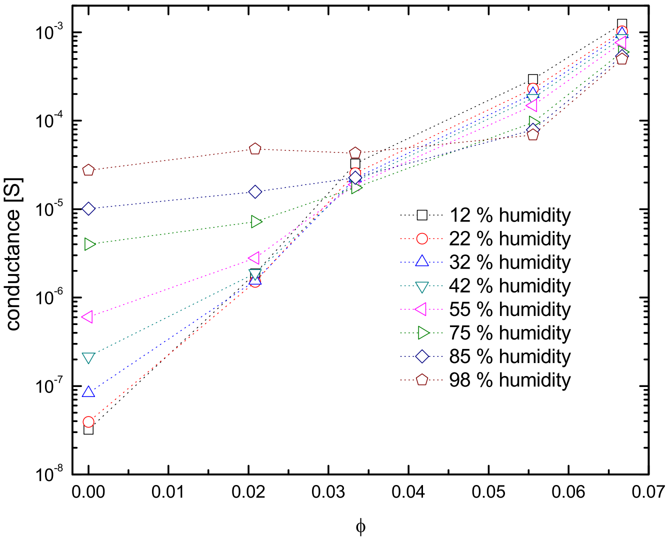

Figure 6.10: Conductance versus ϕ dependence for a carbon black-quaternized Poly(4-vinylpyridine) composite for different humidities. Adapted from Ref. [155].

range, the features of inter-particle quantum tunneling have to be explicitly included. In this chapter, we have evaluated numerically the conductivity σ resulting from electron tunneling in dispersions of impenetrable spheroidal particles for different aspect-ratios, and have shown that the resulting conductivity can be re-obtained by generalizing the critical path method of refs. [149, 150]. We have identified simple formulas for σ valid in several regimes of interest, and applicable to dispersions of nanotubes, nanofibers, nanosheets, and nanospheres. Furthermore, to validate our formulation, we have analyzed published conductivity data for several composites with different particle fillers (nanofibers, nanotubes, nanosheets, and nanospheres), and extracted from the experimental data the corresponding values of the tunneling length ξ. Remarkably, most of the extracted ξ values fall within its expected range, showing that tunneling is a manifest characteristic of the conductivity of polymer nanocomposites. The above outlined procedures can be likewise used as guidelines to tailor the electrical properties of real composites, and can be generalized to include filler size and aspect-ratio polydispersity and interactions with the polymer. Finally, we considered a result from the literature which gives additional support to the crossover interpretation of the insulator-conductor transition which is entailed by the above global tunneling network model.

Chapter 7

A microscopic interpretation of electrical conductivity of graphite polymer composites

This chapter presents a more in-depth analysis of the specific case of conductive graphite/polymer composites. Conventional graphite fillers have typically sizes (length and thickness) up to several microns and do not qualify as nanoparticles. This implies that the global tunneling network model may not be optimally suited for the description of these materials (see Section 8.1.1 for further details). However, we will see how a critical path analysis can again be invoked to account for the observed electrical properties of graphite-loaded polymers. For that purpose, we will present various optical micrographs of the materials which evidence a large amount of sub-micrometric debris, and a model of conductivity driven by this debris is proposed. Finally, a highly anisotropic graphite type is considered and 3D reconstructions of X-ray tomography images of it compounded with polypropylene are shown, allowing us to gain further insights into the complex morphology of real composites.

7.1 Conventional graphite polymer composites

7.1.1 Phenomenological results and comparison with existing models

Commonly to most random insulator-conductor mixtures, graphite-polymer composites undergo a quite abrupt transition of the overall conductivity once a sufficient volume fraction ϕ of the conductive phase is reached. Graphite as a conductive filler takes generally the form of a powder composed of roughly ellipsoidal-shaped particles with sizes varying from few microns up

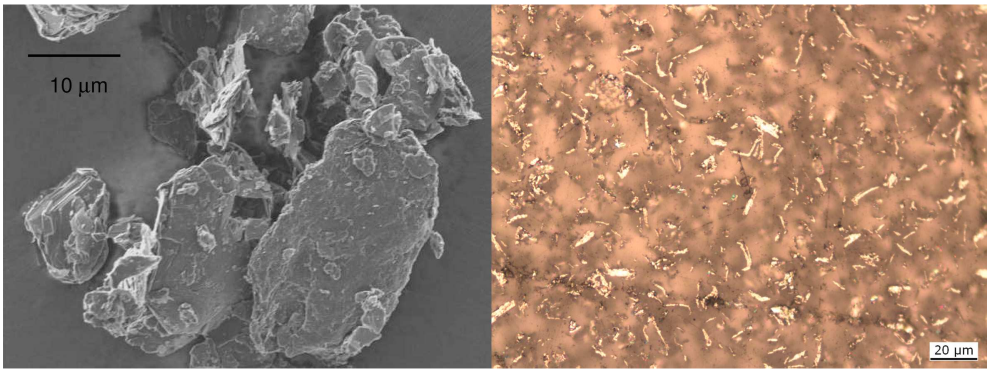

Figure 7.1: Left: TIMCAL T44 graphite. Right: TIMCAL KS15 graphite in an epoxy matrix. The volume fraction is $\phi = 0.1$.

to hundreds of microns [80]. An example is displayed in the left panel of Figure 7.1. During compounding with the polymer, the graphite particles are more or less homogeneously dispersed in the matrix. An example of such composites is shown in the right panel of Figure 7.1. Let us now consider some experimental results of overall composite conductivity as a function of the graphite volume fraction which are displayed in Figure 7.2. Graphite types are all standard products of TIMCAL Graphite and Carbon SA of Bodio, Switzerland. It immediately appears clear how heavily the experimental conditions can influence the results. Different polymer types (i.e. low density polyethylene (LDPE), polypropylene (PP), and epoxy), as well as different compounding, moulding and measurement setups lead to consistent variations of the conductivity of composites containing identical (or similar) graphite types (KS and T graphite types with the same numbers have very similar particle size distributions and particle morphologies). This poses a daunting challenge to the design of a model for the direct estimation of conductivity as a a function of the filler dependencies. Nevertheless, Figure 7.2 gives us an important piece of information, and namely that different graphite types, characterized by different average particle sizes and aspect-ratios, lead to very similar conductivities when investigated by different research groups. This is generally in contrast with what would be expected from both the hard-core-penetrable-shell model of Chapter 4 and global tunneling network model of Chapter 6. To substantiate this statement, let us start with the hard-core-penetrable-shell model. We report in Figure 7.3 the critical percolation volume fraction ϕ_c as a function of the cutoff distance (i.e. twice the penetrable shell thickness) to major particle dimension ratio δ/D for oblate spheroids (this figure contains some additional result not shown in Chapter 4). Oblate spheroids replicate quite effectively the average shape of graphite particles. It is then clear that, for a given cutoff distance δ, larger particles (i.e. with larger D) will imply a higher value for

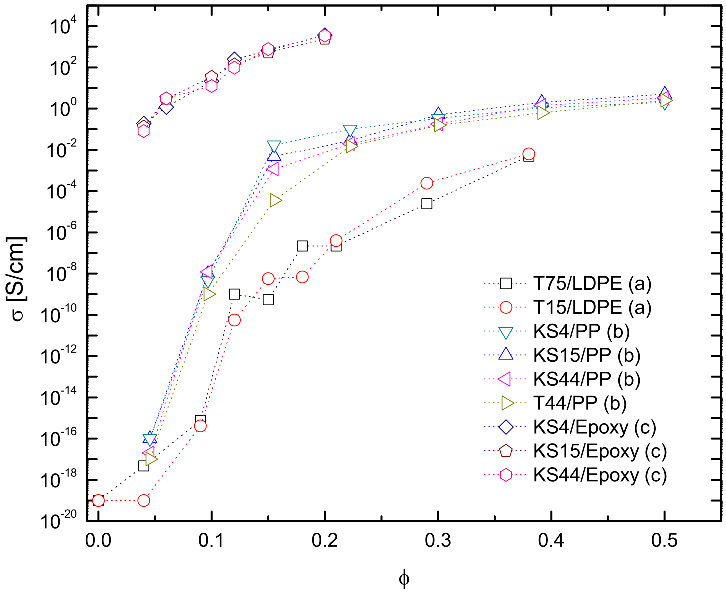

Figure 7.2: Overall conductivity of different graphite polymer composites as a function of the filler volume fraction ϕ. (a) low density polyethylene (LDPE) matrix, from Refs. [23, 156] pressure molding, (b) polypropylene matrix, from TIMCAL, extrusion compounding and injection molding, (c) epoxy matrix, from LPM-EPFL, screen printing.

ϕ_c. However, this could be partially compensated by a simultaneous increase of the aspect-ratio, but that would require quite a coincidence. Let us proceed now with the global tunneling network model. Again, if we consider Figures 6.2-6.4 of Chapter 6, it can be appreciated how, for a given value of ξ, the dependence of the bulk conductivity on the particle size D is strong. The contemporary reduction of the aspect-ratio argument holds again but, again, is unlikely.

7.1.2 The debris model

To tackle the discrepancy between the independence from the graphite type of Figure 7.2 and what would be expected from the models, we first performed optical microscopy analysis on the composite samples prepared with metallographic techniques. For that purpose the composite samples were embedded in a cold-polymerizing methyl methacrylate-based resin in cylindrical molds that were successively surface polished with a Presi (Grenoble, France) Mecapol P230 polishing machine. Images of the polished surfaces were taken with a Leica Microsystems (Wetzlar, Germany) DM LM reflected light microscope combined with a Leica Microsystems DFC 280 camera. Figure 7.4

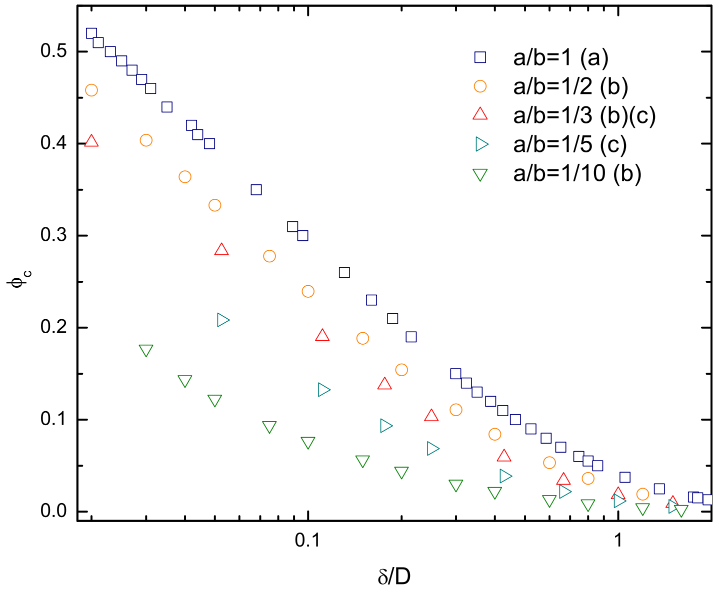

Figure 7.3: Critical volume fraction ϕ_c as a function of the cutoff distance to particle major dimension ratio δ_c/D (D=2b) for oblate spheroids with different aspect-ratios a/b. (a) data from Ref. [59], (b) equilibrium results, (c) random sequential addition results.

	KS44	KS15	KS4
Average particle largest size [μm]:	23.3	8.5	3.1
Average aspect-ratio (a/b):	5.7	3.7	2.6

Table 7.1: Geometrical characteristics of three KS graphite types from optical micrographs analysis.

shows examples for three KS graphite types. The geometrical characteristics of three KS graphite types obtained from the analysis of the micrographs are reported in Table 7.1.

Now, from the composites images we can see that, besides the main particles, there is a considerable amount of sub-micron debris (which was verified not to come from the sample surface polishing). Moreover, the amount of debris seems to be roughly constant in all the three different composites. It is then sensible to assume that these small particles will play a role in the overall conductivity. In the light of these observations, we may construct a simple model which takes into account the presence of the debris. For this purpose, we first introduce the following working assumptions:

1. All the systems are fundamentally bi-disperse in graphite particle sizes

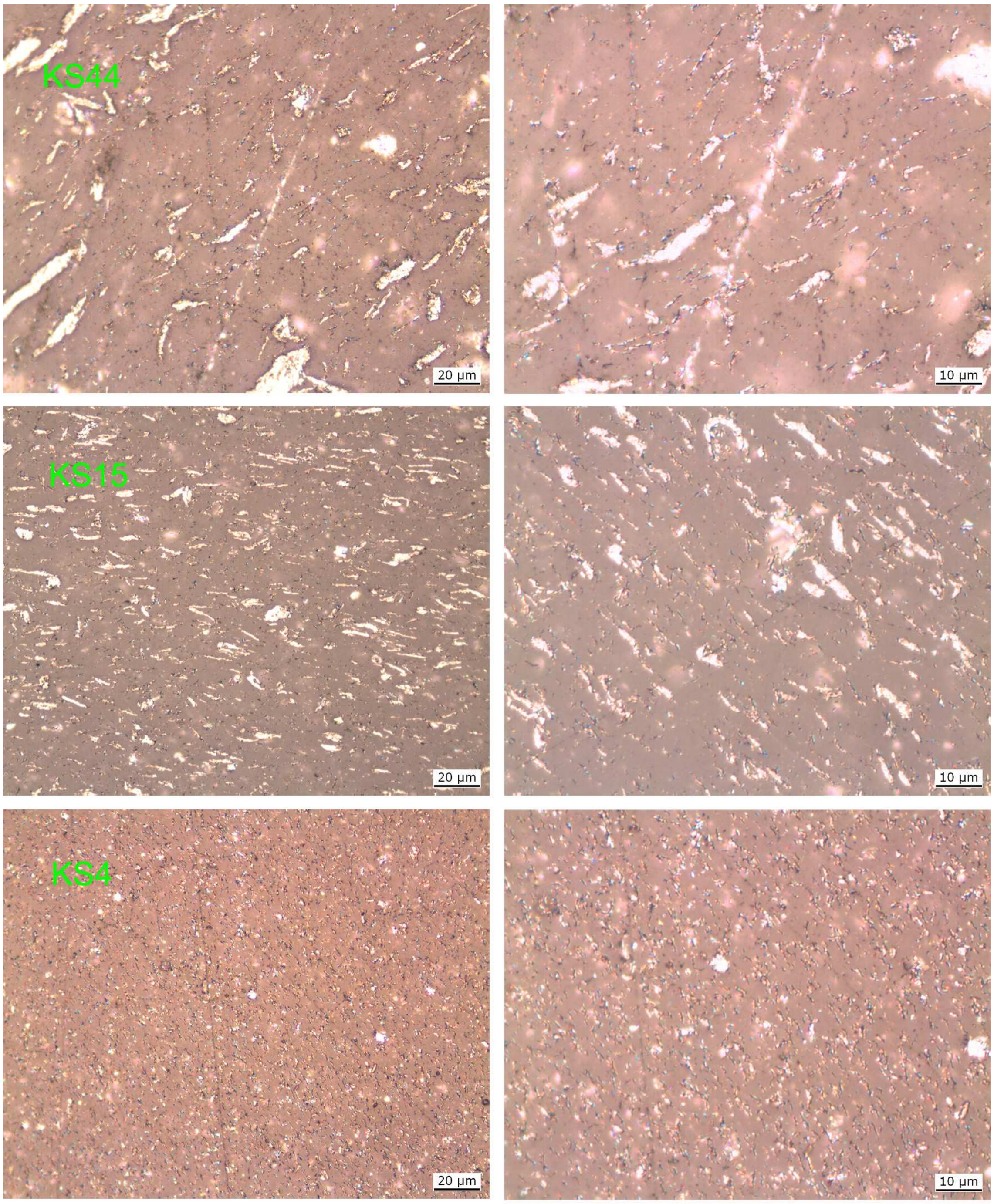

Figure 7.4: Optical micrographs of KS44, KS15, and KS4 graphite types in a PP matrix, extruded and injection molded. The volume fraction is $\phi = 0.1$. Notice the orientation effects typical of injection molding.

i.e. there are two coexisting families of (roughly) equally sized particles, one of which sees considerably larger members and which will thus dominate the volume fraction. The other represents the debris and we assume its contribution to the total volume fraction negligible.

2. The debris particle number is dependent only upon the overall graphite volume fraction and not on the larger graphite particle number i.e. at same volume fraction the debris particle number is independent from the graphite type.
3. The average debris particle size is independent from the larger graphite particle size i.e. is independent from the graphite type.

From assumption 1. and 2. we can write a relation for the debris number density ρ_d as a function of the overall volume fraction ϕ. If the number of debris particles is bounded linearly to the overall volume fraction, we have:

$$\rho_d = \lambda \frac{\phi}{1-\phi} \tag{7.1}$$

where λ is a proportionality constant. Let us concentrate ourselves on the debris-polymer matrix system. This is most simply assimilated to a conducting point-like particles distribution in an insulating matrix. Then, its conductivity σ may be estimated quite precisely with the critical path analysis of Seager and Pike [151] introduced in the previous chapter (see Equation (6.3)),

$$\sigma \simeq \sigma_0 \exp\left(-\frac{3.5\,\rho^{-1/3}}{\xi}\right) \tag{7.2}$$

where ρ is the particle number density, and σ_0 a proportionality constant. Proceeding further, we can now use equation (7.2) together with equation (7.1) to write the conductivity of the debris-polymer matrix system as a function of the overall volume fraction as:

$$\sigma \simeq \sigma_0 \exp\left[-\frac{\alpha}{\xi}\left(\frac{\phi}{1-\phi}\right)^{-1/3}\right] + \sigma_m \tag{7.3}$$

where α is a constant (equal to $3.5\,\lambda^{-1/3}$) and where we have introduced the intrinsic conductivity of the polymer matrix σ_m. We can then consider the debris-polymer matrix system as an “effective” matrix in which the large graphite particles are dispersed in. Electrical connectivity of the large particles will be governed by the current flow through the effective matrix and we model it with cylindrical channels connecting the particles along their shortest distance line. Furthermore, we consider these channels terminated at both extremes by semi-spheres approximating the particles surfaces, as illustrated in Figure 7.5. This allows us to write the conductance ϱ between

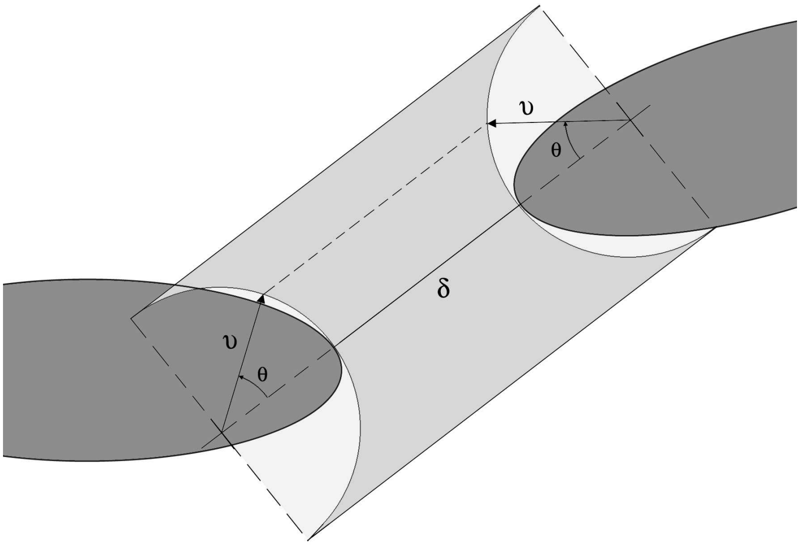

Figure 7.5: Schematic illustration of the inter-particle conduction channel geometry.

two particles as

$$\begin{aligned} \varrho = \sigma 2\pi\upsilon \int_0^{\frac{\pi}{2}} \mathrm{d}\theta \, \frac{\sin\theta\cos\theta}{\delta + 2\upsilon(1-\cos\theta)} &= \\ = \sigma\frac{\pi}{2}\upsilon\left[\left(\frac{\delta}{\upsilon}+2\right)\ln\left(\frac{2\upsilon}{\delta}+1\right)-2\right] & \end{aligned} \tag{7.4}$$

where υ is the radius of the semi-spheres and δ the minimal distance between the particles. Combining with (7.3) we can rewrite this relation as

$$\varrho = \frac{\pi}{2}\upsilon\left\{\sigma_m + \sigma_0 \exp\left[-\frac{\alpha}{\xi}\left(\frac{\phi}{1-\phi}\right)^{-1/3}\right]\right\}\left[\left(\frac{\delta}{\upsilon}+2\right)\ln\left(\frac{2\upsilon}{\delta}+1\right)-2\right] \tag{7.5}$$

Now, we can test this model by evaluating the bulk conductivity under these assumptions via simulations with the same algorithms used for the results of Chapter 6 but with an inter-particle conductance of the form of (7.5). We carried out these simulations for oblate spheroid systems having the geometrical parameters of the three graphite types of Table 7.1. Figure 7.6 reports the results obtained with $\sigma_m = 10^{-16}$ S/cm, $\upsilon = b$, $\xi/\alpha = 0.046$, and $\sigma_0 = 10^{12}$ S, together with the results for the corresponding polypropylene results of Figure 7.2. Every run involved ~ 500

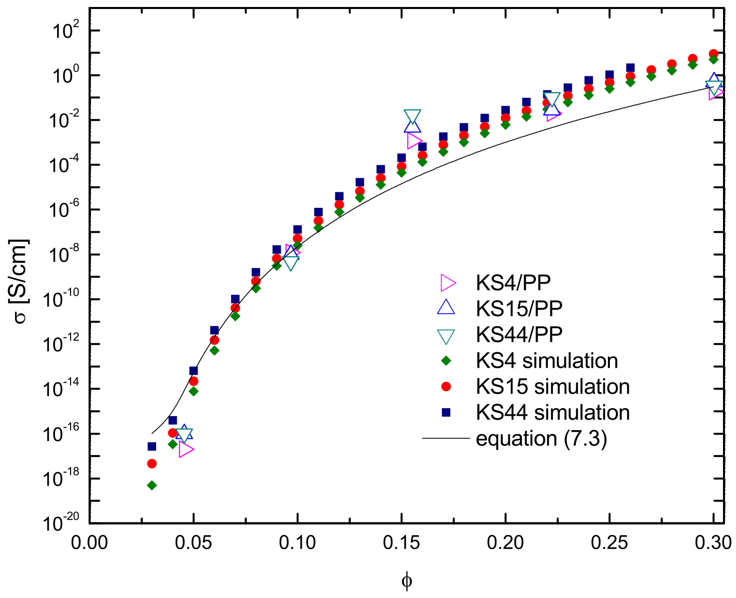

Figure 7.6: Conductivity of simulated KS systems with the debris model. Solid line is Equation (7.3).

particles, and the result for every concentration was the arithmetic mean of four replications. As we can see, the model reproduces quite well the trend of the experimental data, and, more importantly, shows no dependence on the particle size or aspect-ratio. The latter is also the relevant information to retain since, by considering again Figure 7.2, it appears clear that quite different values of σ_0 and ξ/α would be required to reproduce the results of different composites. This results indicates that in a bi-disperse system with one species considerably larger than the other (and where the smaller species is in a sufficient number), the smaller particles may dominate the bulk composite conductivity. A further confirmation of this interpretation comes from the classic effective conductivity estimations of heterogeneous media of Kim and Torquato [157–159]. For that purpose, let us consider a system of impenetrable conducting spheres (the filler) randomly distributed in a three-dimensional continuous medium (the matrix) with consistently lower conductivity than the spheres. Then, we can evaluate the effective conductivity of our matrix-filler system. Since by assumption the spheres possess an intrinsic conductivity which is several orders of magnitude greater than that of the matrix we may consider them as superconductive for all practical purposes. Following the results of Refs. [157–159], we can then write the effective conductivity σ_e of our system as [159]:

$$\sigma_e = \sigma_m \left[\frac{1 + 2\phi - 2(1-\phi)\zeta}{1 - \phi - 2(1-\phi)\zeta} \right] \tag{7.6}$$

where σ_m is the intrinsic conductivity of the matrix (in our case the debris-matrix conductivity (7.3)), ϕ the spheres volume fraction and ζ a microstructural parameter which has the approximate expression [94]

$$\zeta = 0.21068\phi - 0.04693\phi^2. \tag{7.7}$$

σ_e is then a monotonously growing function of the volume fraction reaching a roughly fivefold increase in the overall conductivity as ϕ reaches the metastable region of the hard sphere fluid at around $\phi = 0.49$. We note that the above result (7.6) is independent from the filler particles size provided that they are much smaller than the system under consideration (as to guarantee homogeneity). This shows that the intrinsic conductivity of the larger particles (which are not electrically interconnected by other means like e.g. tunneling) has a minor influence on the overall conductivity. As a final test of this interpretation, the conductivity of the debris-matrix system alone given by Equation (7.3) calculated for the same values of σ_m, σ_0 and ξ/α used for the numerical simulations is reported with a solid line in Figure 7.6 and shows a good agreement with the numerical outcomes.

In conclusion, the above analysis hints that the electrical properties of graphite-polymer composites may be dominated by the debris (with average particle sizes considerably smaller than the main filler particles) which is unavoidably present in the graphite powders. This would justify the observed independence from the different graphite types.

7.2 High aspect-ratio graphite polymer composites

It is a well established fact that conductive fillers possessing higher shape anisotropy lead to similar conductivities at considerably lower volume fractions. As seen in the previous chapters, fibrous systems like for instance carbon fibers, nanofibers and nanotubes are one widely known example [26,27]. Graphite-derived high shape-anisotropy fillers like graphite nanosheets [28] and the ultimate one-atom thick graphene sheets [29] have also recently become quite investigated conductive additives. For these nanometric fillers, which have at least one physical dimension comparable to the characteristic tunneling distance, we have shown in Chapter 6 that the tunneling model proves to be quite effective. We will in the following briefly consider the case of the TIMCAL BNB90 graphite, which is obtained from expanded

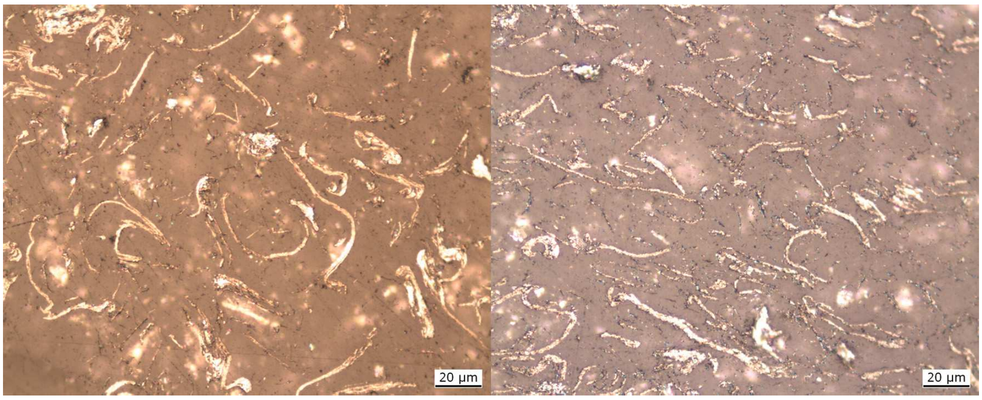

Figure 7.7: BNB90 graphite in an epoxy matrix (left, $\phi = 0.04$), and a polypropylene matrix (right, $\phi = 0.1$)

graphite [160]. In Figure 7.7 we show two examples of BNB90 compounded with epoxy and polypropylene. We furthermore present in Figures 7.8-7.10 three views of a 3D reconstruction based on X-ray tomography phase contrast images of a BNB90-polypropylene composite. Tomography was performed at the European Synchrotron Radiation Facility of Grenoble, France. The 3D reconstruction was carried out with the software Avizo 5 of Mercury Computer Systems, Chelmsford, USA. The reconstruction size is 140x140x70 μm. To have a clearer view of the large particles, the debris was not included in the reconstruction.

From these images we see that the BNB90 filler particles have generally the shape of thin more or less crumbled sheets, quite different from conventional graphite. These high shape-anisotropy sheets are, as opposed to graphite nanosheets and graphene, quite large, in the order of several tens of microns with a thickness around the micron, and not really qualify as nanofillers. Nevertheless, they enable the same enhancement of conductivity at a given volume fraction. This is illustrated in Figure 7.11, together with the conventional graphite results of Figure 7.2. Observing again the micrographs of Figure 7.7, we see that, also for BNB90 composites, large amounts of sub-micrometric debris are present. Then, from the debris model we would expect that these composites would also show a behavior akin to the conventional graphite types, since, in that description, the large particles play only a minor role. However, in that model we omitted the direct interactions between the large particles, which for conventional micrometric graphite types would occur only at higher volume fractions. This is not the case for high shape-anisotropy fillers like BNB90, and we assume that the performances of this graphite type already at very low volume fractions come from direct contact of the large filler particles.

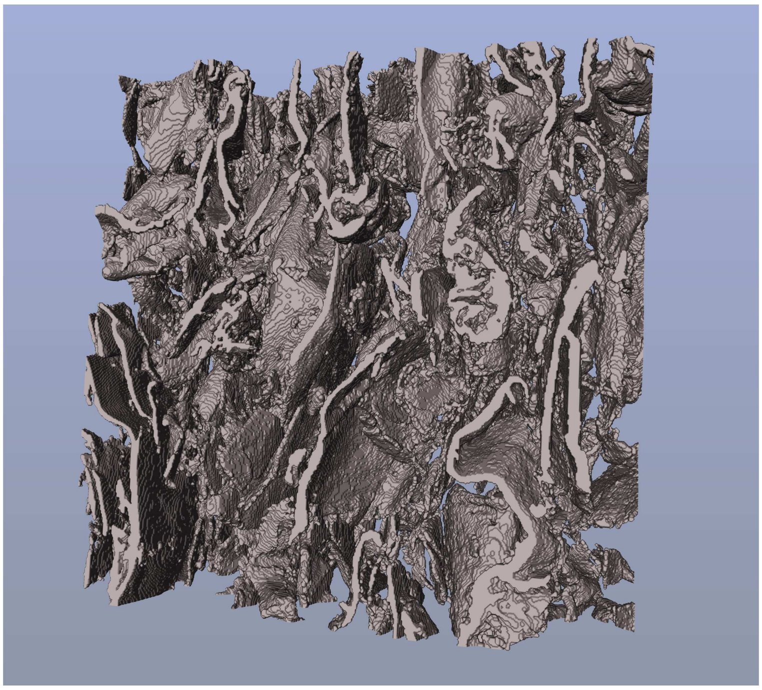

Figure 7.8: 3D reconstruction of X-ray tomography phase contrast images of a BNB90-polypropylene composite.

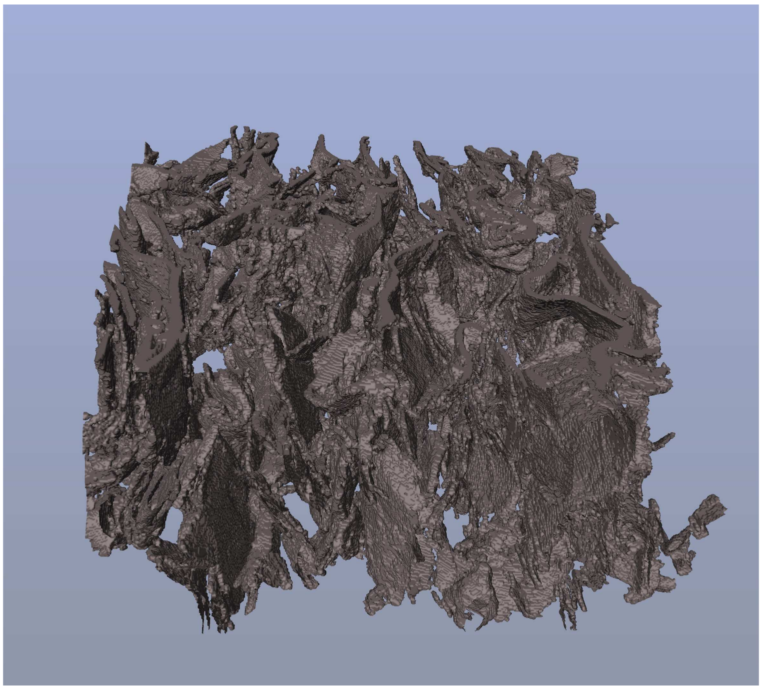

Figure 7.9: 3D reconstruction of a BNB90-polypropylene composite (cont.).

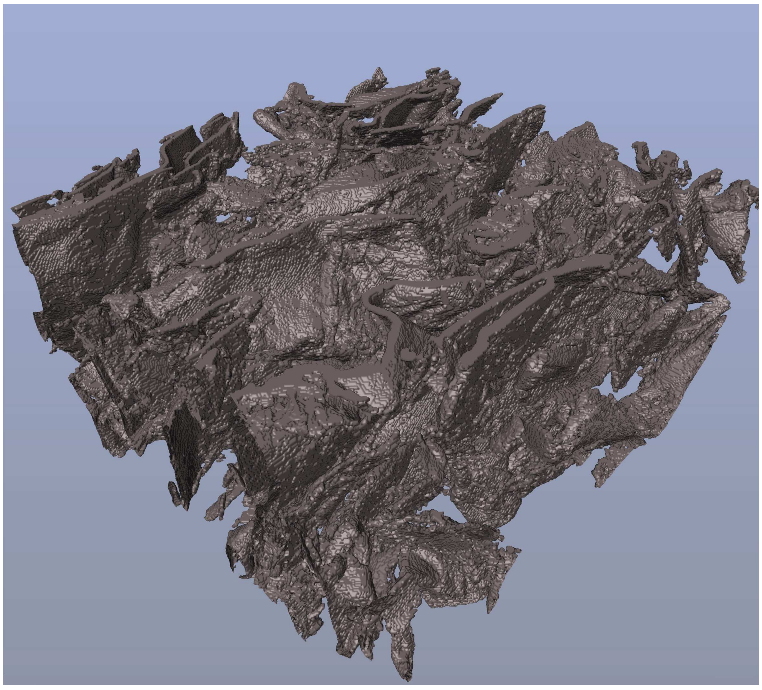

Figure 7.10: 3D reconstruction of a BNB90-polypropylene composite (cont.).

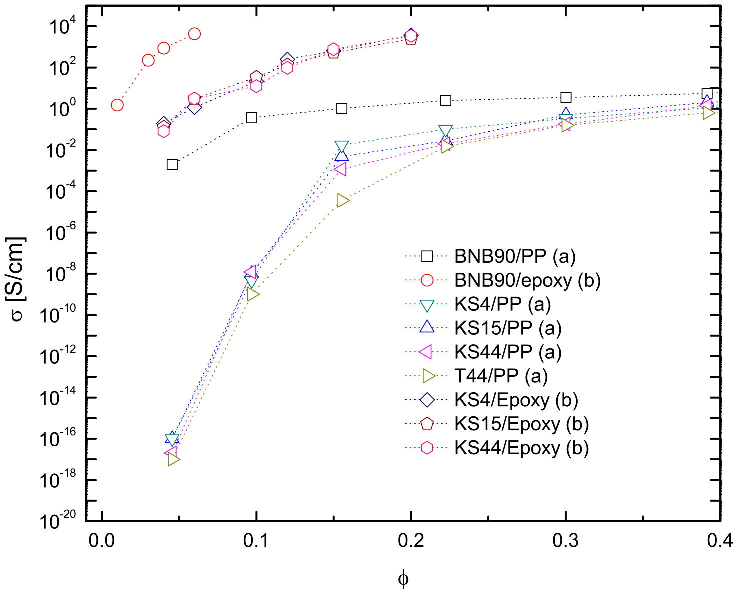

Figure 7.11: Overall conductivity of BNB90 and conventional graphite polymer composites as a function of the filler volume fraction ϕ. (a) from TIMCAL, extrusion molding and injection molding, (b) from LPM-EPFL, screen printing.

7.3 Conclusion

In this chapter, we have considered in further detail the specific case of conductive graphite-polymer composites. Optical imaging of these materials allowed us to introduce a formulation of conductivity driven by the large quantities of debris that is found in the composites. This model, which is able to account for the experimentally observed independence from the filler (main) particle size of the conductivity of graphite-loaded polymers, is again based on the critical path method [149,150] in the form introduced by Seager and Pike [151]. We finally considered a high shape-anisotropy graphite type whose 3D images obtained through X-ray tomography showed how complex the morphology of a real composite can get.

Chapter 8

Concluding remarks and open questions

The emerging field of nanotechnology has profoundly transformed materials science. The manifest quantum nature of the phenomena at the nanometer scale has opened up new and fruitful connections between materials engineering, chemistry and theoretical physics. Electrically conductive nanocomposites, which incorporate nanometric fillers such as carbon nanofibers, nanotubes or graphene sheets in a generally polymeric matrix to achieve improved global conductivity, are part of this new research domain. However, the models used so far to describe their electrical properties are in fact the same used for larger filler particle conventional conductive polymer composites. In particular, the mainstream interpretation goes through percolation theory and identifies the insulator-conductor transition commonly observed in these materials with the formation of a cluster of electrically connected filler particles which spans the sample. Nevertheless, percolation models require generally a sharp cutoff of the interaction between the particles in order to be applicable. This is at odds with quantum mechanical electron tunneling, which is held as the major transport mechanism in conductor-filled polymers, and which entails no abrupt cutoff. For macroscopic fillers, the percolation picture is still adequate, since these have typical dimensions orders of magnitude larger than the characteristic distances of tunneling. This ceases to be true for nanoparticles, which have at least one dimension comparable the typical lengths of tunneling, and where this latter is expected to take an explicit role in the volume fraction dependence of the composite conductivity. The main aim of this work was then to try to formulate a description of polymer composites containing nanometric fillers which can account for the experimentally observed conductivity versus volume fraction results and thus to at least partially resolve the dichotomy between tunneling and percolation.

The investigation route we followed relied strongly on numerical replications of the composite microscopic morphology, and an important part of the research involved the construction of a simulation algorithm able to model the broad range of filler particle shapes. With this routine, the filler particles were assimilated to equally-sized impenetrable ellipsoids of revolution (spheroids) of given aspect-ratio and the dispersions mimicked as random isotropic distributions of these objects.

Connectivity-based percolation models were then investigated with a special focus on the effect of the filler aspect-ratio, an aspect which for hard particles was not yet fully covered in the literature. Connectivity between the hard spheroids was introduced in the form of a penetrable shell of constant thickness, and two particles were considered connected if their shells overlapped. Simulations spanned an unprecedented broad range of aspect-ratios (from a/b=1/200 to a/b=100) and shell thicknesses, and the widely reported trend that fillers with higher shape-anisotropy entail a lower percolation threshold was found confirmed, also for the not yet reported case of hard oblate objects. Then, a series of relations which allow to estimate the percolation critical quantities quite precisely have been introduced, and turned out to play a major role in the models proposed in the present thesis.

As an intermediate step towards the implementation of quantum mechanical electron tunneling as transport mechanism between the fillers of our numerical replications of the composites, tunneling was studied from a more formal point of view. As opposed to previous investigations of tunneling in composite materials which were mainly concerned with the temperature dependence, we concentrated here on the geometrical aspects by studying tunneling between two conductive spheres with the powerful transfer-Hamiltonian formalism of Bardeen. We also confronted different approaches for the calculation of the simple one-dimensional barrier problem and observed that they lead to different results, but all with a dominating exponential term of the same form, which is the fundamental quantity to retain.

A model which explicitly includes tunneling conduction between the filler particles was then introduced, and conductivity simulations involving perfectly conducting hard spheroid distributions forming a network of globally connected objects via tunneling were carried out for prolate, oblate, and spherical systems. It was evidenced that at the same volume fraction, inclusions with higher shape-anisotropy give rise to higher conductivities with respect to lower shape-anisotropy ones, as found experimentally. By exploiting the critical path method, we showed that the computation of the conductivity of the tunneling system can be reduced to the computation of the percolation critical distance, a considerably easier quantity to calculate. Furthermore, simple relations have been derived which allow to infer with high accuracy the overall conductivity of systems containing sufficiently elongated, sufficiently flat and spherical fillers. The validity of the formulation for nanocomposites was assessed by extracting from a large number of literature experimental results on nanotube, nanofiber, nanosheet, and nanosphere -polymer composites the characteristic tunneling distance, and finding it mostly within its expected value range. We also showed how the global tunneling network model could reproduce the experimentally observed sigmoidal-shaped conductivity versus volume fraction curves when the finite conductivity of the polymer matrix was taken into account. Within this formulation, the insulator-conductor transition was interpreted as a crossover between a regime where the intrinsic conductivity of the matrix is dominant to one where the conductivity contribution due to the tunneling network is dominant. The analysis of a result published for different purposes gave support to this interpretation.

Finally, we considered in more detail the specific case of graphite-polymer composites. In these materials, although the main contribution to the filler volume fraction comes from generally relatively large (i.e. micrometric) graphite particles, a consistent amount of debris with dimensions below the micron was also found. We proposed a simple model, based again on the critical path analysis, which was able to reproduce the observed independence from the main particle size of these composites. 2D optical imaging and 3D computer tomography imaging of the composites were also presented.

In conclusion, our approach has been to model conductive polymer nanocomposites with the aid of numerical re-creations which explicitly considered the main microscopic filler features and which included a realistic interparticle conduction mechanism in the form of electron tunneling. These numerical investigations have been coupled with theoretical formulations in order to be able to identify some simple formulas which allow the evaluation of the composite conductivity without the need to pass through simulation campaigns. Our formulation allowed us in fact to reproduce the experimentally observed conductivity versus volume fraction behavior of nanocomposites without the need to invoke percolation theory. However, somehow ironically, percolation results still play an important role in our model as auxiliary quantities for the conductivity evaluation formulas.

8.1 Open questions

A thesis unavoidably has an ending, but this is (hopefully) not true for the research stream in which it is placed. Some facts may have been understood, but many other remain out there, unanswered. So, the aim of this last section is to make explicit a few of these open questions, hoping that some willing reader will eventually embark on the quest for their answer.

8.1.1 The large particle limit I

In the present thesis we introduced the global tunneling network model of conductivity in nanocomposites, where there is no abrupt cutoff of the electrical connectivity between the filler particles. On the other side, percolation models based on a sharp on-off connectivity are an effective description of composites whose fillers are considerably larger than the typical distances of tunneling. Now, since tunneling is decaying continuously with the particle separation, it is not trivial to identify where and owing to which effect the transition between the two regimes takes place. In a perfectly ideal equilibrium system, the global tunneling network model would be valid at any scale. However, if we consider that the deviations from ideality of a system are correlated to its characteristic dimensions and scale with them, we can guess that in the large particle limit, these deviations will totally mask the continuous nature of the tunneling decay. In other words, minute deviations from the equilibrium positions which for nanometric particles are smaller or comparable with the characteristic tunneling lengths may happen to be of sufficient magnitude to induce a sort of abrupt cutoff behavior in the case of large particles. Percolation would so be induced by these system deviations. Nevertheless, these qualitative argumentations remain quite tentative and a consistent substantiation would be needed.

8.1.2 The large particle limit II

It is then interesting to consider the large particle limit from an experimental point of view. In Figure 8.1 we report a collection of experimental critical (crossover) volume fractions ϕ_c for conductive polymer composites containing spherical fillers. These were either taken directly (when reported) or extrapolated from the experimental curves of Refs. [8, 10, 11, 13–18, 20, 21, 24, 32, 35, 38, 39, 47, 70, 161–171]. In Figure 8.1, a distinction is made between the cases where the sphericity of the fillers could be clearly assessed and the ones where the fillers where more irregular or of unknown shape. We note also that because the estimated ϕ_c were sometimes rounded off, there are three cases of superposed results.

Now, the advantage of spherical (or quasi-spherical) systems is that shape-anisotropy effects and orientation effects are absent. The main deviations from perfectly isotropic mono-disperse systems come thus from non-uniform particle sizes and non-isotropic position distributions (e.g. agglomeration, segregation, and sedimentation). To evaluate the deviations of the reported results, we plotted in Figure 8.1 also the crossover predictions of the global tunneling network model, which can be obtained from Equation 6.2 of Chapter 6 by putting $\sigma = \sigma_m$, with σ_m the matrix intrinsic conductivity, and inverting for ϕ, in a similar fashion with what has been done for Equations (6.8) and (6.9). We reported three cases, all with $\sigma_m = 10^{-15}$ S/cm, $\sigma_0 = 1$ S/cm and three characteristic tunneling distances: $\xi = 2.5$, 5.0, and 10.0 nm. It is quite remarkable that almost every result for particles larger than 1 μm is at a lower volume fraction than expected, sometimes consistently so. This is also something that has nothing to do with the specific model we used, since to reproduce these experimental thresholds also the (isotropic) hard-

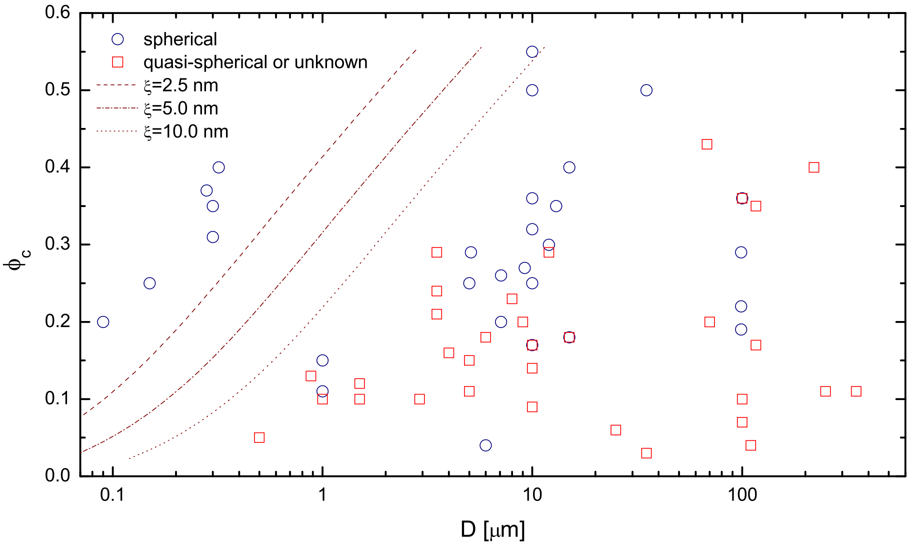

Figure 8.1: Critical (crossover) volume fraction as a function of the particle diameter for various spherical and quasi-spherical fillers in a polymer matrix. The crossover predictions of Equation (6.2) with $\sigma_m = 10^{-15}$ S/cm, $\sigma_0 = 1$ S/cm and $\xi = 2.5$, 5.0, and 10.0 nm. Results from Refs. [8, 10, 11, 13–18, 20, 21, 24, 32, 35, 38, 39, 47, 70, 161–171].

core-soft-shell percolation model would require shells which are too large to be compatible with any known inter-particle conduction channel. Another interesting observation is that the often reported fact that smaller particles imply a lower ϕ_c is less clear cut.

From our point of view, these lower than expected threshold values are imputable to segregation effects, but, again, this assumption needs to be substantiated. It would then be interesting to carry out a series of experiments with composites prepared with mono-disperse spheres. Equally-sized silver-coated glass microspheres are available, albeit expensive. The spatial position of the spheres in the composites could then be reconstructed from 2D images with stereology [172], allowing for a quantitative evaluation of the degree of deviation from isotropy.

8.1.3 Investigations of the crossover

In Section 6.5 we saw how, by changing the concentration of ionic species, the matrix intrinsic conductivity could be varied, leading to a shift of the crossover point where the the tunneling conductivity becomes dominant. To shed light on the nature of the crossover, further experiments in that direction could be carried out. One possibility is to fabricate, as done in

Ref. [155], a composite containing a conductive filler embedded in a polyelectrolyte matrix. Polyelectrolytes are polymers having at least one ionizable group per monomer unit and, in the ionized state, one type of ion remains attached to the polymer structure while the other species can be displaced through an applied field [4]. A fundamental aspect is that in these materials the ionic conductivity is strongly dependent on the water content, thus offering an easy way to tune their conductivity. Examples of polyelectrolytes include those based on perfluorinated polymers, the most known of which is Nafion® (widely used in PEM fuel cells) and sulphonated poly(etheretherketone) (PEEK) [4]. Another polymer family offering high ionic conductivity are solid polymer electrolytes, which are composed of alkali metal salts dissolved in e.g. in polyethylene oxide (PEO) [4], and which are used as electrolytes for lithium ion batteries. Other possibilities to shift the matrix intrinsic conductivity could exploit the effect of temperature, but may need to take into account its effect on the tunneling conductances.

Investigations of the crossover region could also be interesting in the case of matrices having an intrinsic electronic conductivity. In this situation the conduction paths due to the tunneling network and to the matrix are not anymore independent and an unified description would be needed.

8.1.4 Polydisperse systems

A final interesting investigation direction is one which considers the effect of non-uniform filler particle size, which is a very common situation. In the course of the present work, a version of the simulation algorithm which was able to generate distributions of spherical hard particles with a log-normal diameter distribution was constructed and preliminary investigations of the conductivity (under tunneling inter-particle transport mechanism) as a function of the deviation from mono-dispersion were carried out. These evidenced the expected fact that at a given volume fraction more polydisperse systems lead to lower conductivities. However, the deviations we considered were quite limited, since the computation times grew enormously with their increase. The debris model of Chapter 7 also showed us how, under given assumptions, a strongly bi-disperse system can lead to quite different results.

A thorough study of the effect of the particle size distribution and its functional form on both the geometrical percolation of the hard-core-soft-shell model, and on the conductivity of the global tunneling network model would surely improve our understanding of conductive polymer composites.

Appendix A

Evaluation of excluded volume quantities

A.1 Excluded volume quantities for oblate spheroids with explicit angle dependence

We first report in the following the derivation of the excluded volume of two oblate spheroids, the excluded volume of two oblate spheroids surrounded with a shell of constant thickness and their angular averages. We follow a route due to the pioneering work of Isihara [173] which is somehow more laborious than the one used by the same author [174] and the authors of [175] to derive the widely used Isihara-Ogston-Winzor spheroid excluded volume formula. The advantage is that it is possible to obtain, albeit in a series expansion form, the excluded quantities with their full angle dependence. The average on the spheroid angle distribution function is performed in a second time and can be easily extended to non-isotropic cases. Let us consider the case of two identical oblate spheroids of polar (minor) semi-axis a and equatorial (major) semi-axis b in contact as illustrated in Fig. A.1.

The geometrical quantities H and K, which represent the distances from the spheroid centers to the tangent plane to the two spheroids in the contact point, may be written as

$$H(\alpha) = b\sqrt{1-\epsilon^2\cos^2\alpha}, \tag{A.1}$$

$$K(\alpha') = b\sqrt{1-\epsilon^2\cos^2\alpha'}, \tag{A.2}$$

where ϵ represents the *eccentricity* (for oblate spheroids)

$$\epsilon \equiv \sqrt{1-\frac{a^2}{b^2}}. \tag{A.3}$$

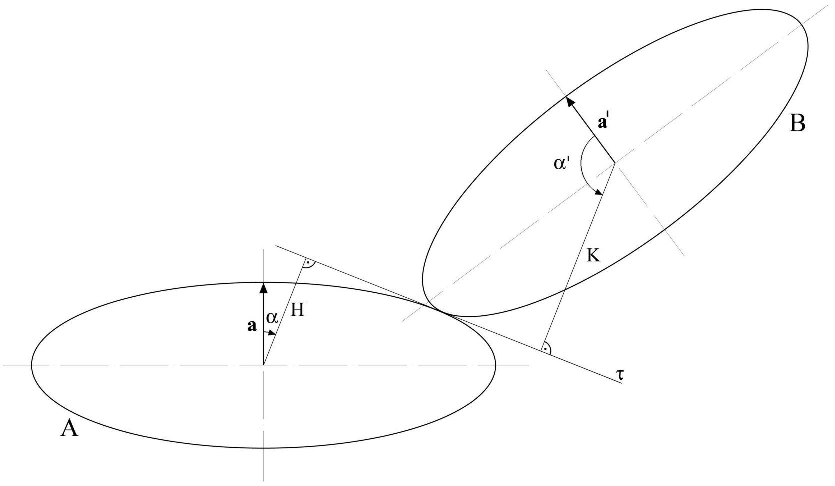

Figure A.1: Two identical oblate spheroids in contact (2D representation).

Furthermore, we have

$$\begin{aligned}\cos^2\alpha' &= [\sin\varphi\sin\alpha(\cos\theta cos\beta + \sin\theta\sin\beta) + \cos\varphi\cos\alpha]^2\\ &= [\sin\varphi\sin\alpha\cos(\beta-\theta) + \cos\varphi\cos\alpha]^2,\end{aligned} \tag{A.4}$$

where θ and φ are the angles which define the rotation that transforms the symmetry axis vector $\mathbf{a}$ of spheroid A in the one of B, $\mathbf{a}'$.

We can then write the excluded volume of two identical spheroids, or more generally two identical ovaloids, as [173, 174]:

$$V_{ex} = 2V + \int K(H,H)\mathrm{d}\omega = 2V + \int_0^{2\pi}\mathrm{d}\beta\int_0^{\pi}\mathrm{d}\alpha\sin\alpha K(H,H), \tag{A.5}$$

where $\mathrm{d}\omega$ is the infinitesimal surface element of the unit sphere centered in the origin which, by using the reference frame choice of fig. A.1, takes the form

$$\mathrm{d}\omega = \sin\alpha\mathrm{d}\alpha\mathrm{d}\beta. \tag{A.6}$$

Furthermore, in Eq. (A.5) we have introduced the differential operator on the unit sphere which for two equal scalar quantities F takes the form

$$(F,F) \equiv 2\left\{\left(\frac{\partial^2 F}{\partial\alpha^2}+F\right)\left(\frac{1}{\sin^2\alpha}\frac{\partial^2 F}{\partial\beta^2}+\frac{\cos\alpha}{\sin\alpha}\frac{\partial F}{\partial\alpha}+F\right)-\left[\frac{\partial}{\partial\alpha}\left(\frac{1}{\sin\alpha}\frac{\partial F}{\partial\beta}\right)\right]^2\right\}, \tag{A.7}$$

while V is the volume of the spheroid.

With the explicit form of H, Eq. (A.1), K, Eq. (A.2), and relation (A.4) we can write for the excluded volume (A.5) in the case of the two spheroids the integral form:

$$V_{ex}(\theta,\varphi) = 2V + 2b^3(1-\epsilon^2)\int_0^{2\pi} \mathrm{d}\beta \int_0^{\pi} \mathrm{d}\alpha \sin\alpha \frac{\sqrt{1-\epsilon^2\cos^2\alpha'}}{(1-\epsilon^2\cos^2\alpha)^2}$$

$$= 2V+2b^3(1-\epsilon^2)\underbrace{\int_0^{2\pi} \mathrm{d}\beta \int_0^{\pi} \mathrm{d}\alpha \sin\alpha \frac{\sqrt{1-\epsilon^2(\sin\varphi\sin\alpha\cos\beta+\cos\varphi\cos\alpha)^2}}{(1-\epsilon^2\cos^2\alpha)^2}}_{I}, \tag{A.8}$$

where we have used the fact that

$$\int_0^{2\pi} \mathrm{d}\beta \sqrt{1-\epsilon^2[\sin\varphi\sin\alpha\cos{(\beta-\theta)}+\cos\varphi\cos\alpha]^2}$$

$$= \int_0^{2\pi} \mathrm{d}\beta \sqrt{1-\epsilon^2(\sin\varphi\sin\alpha\cos\beta+\cos\varphi\cos\alpha)^2}, \tag{A.9}$$

because of the 2π periodicity of the integrand and which means that V_{ex} is θ-independent.

We now may expand the $1-\epsilon^2(\sin\varphi\sin\alpha\cos\beta+\cos\varphi\cos\alpha)^2$ square root:

$$\sqrt{1-\epsilon^2(\sin\varphi\sin\alpha\cos\beta+\cos\varphi\cos\alpha)^2}$$

$$= 1 - \frac{1}{2\sqrt{\pi}}\sum_{k=1}^{\infty}\Gamma(k-\frac{1}{2})\frac{\epsilon^{2k}}{k!}(\sin\varphi\sin\alpha\cos\beta+\cos\varphi\cos\alpha)^{2k}$$

$$= 1 - \frac{1}{2\sqrt{\pi}}\sum_{k=1}^{\infty}\Gamma(k-\frac{1}{2})\frac{\epsilon^{2k}}{k!}\sum_{i=0}^{k}\binom{k}{i}(\sin\varphi\sin\alpha\cos\beta)^{2i}(\cos\varphi\cos\alpha)^{2k-2i}. \tag{A.10}$$

Substituting this in integral I of (A.8) and integrating in β in the first resulting term we obtain:

$$\begin{aligned} I =& 2\pi\int_0^{\pi}\mathrm{d}\alpha\frac{\sin\alpha}{(1-\epsilon^2\cos^2\alpha)^2} \\ & - \frac{1}{2\sqrt{\pi}}\sum_{k=1}^{\infty}\Gamma(k-\frac{1}{2})\frac{\epsilon^{2k}}{k!}\sum_{i=0}^{k}\binom{k}{i}\sin^{2i}\varphi\cos^{2k-2i}\varphi \\ & \times\int_0^{2\pi}\mathrm{d}\beta\cos^{2i}\beta\int_0^{\pi}\mathrm{d}\alpha\frac{\sin^{2i+1}\alpha\cos^{2k-2i}\alpha}{(1-\epsilon^2\cos^2\alpha)^2}. \end{aligned} \tag{A.11}$$

The integration follows then with the aid of formulas 2.153 (3.), 3.682, 3.681 (1.) of Ref. [137] obtaining with (A.8) the expression for the *excluded volume of two identical oblate spheroids*:

$$V_{ex}(\varphi) = 2V + 2b^3(1-\epsilon^2)\Bigg[4\pi F(2,\tfrac{1}{2},\tfrac{3}{2},\epsilon^2)$$

$$-\sqrt{\pi}\sum_{k=1}^{\infty}\Gamma(k-\frac{1}{2})\epsilon^{2k}\sum_{i=0}^{k}\frac{\sin^{2i}\varphi\cos^{2k-2i}\varphi}{2^{i}(k-i)!(i!)^{2}}B(i+1\,,\tfrac{2k-2i+1}{2})F(2\,,\tfrac{2k-2i+1}{2}\,,\tfrac{2k+3}{2}\,,\epsilon^{2})\Bigg]. \tag{A.12}$$

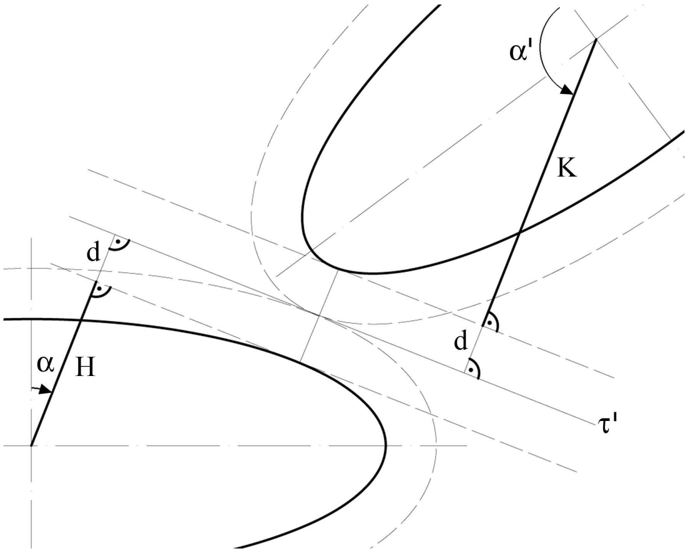

Figure A.2: Two oblate spheroids surrounded with shells of constant thickness which are in contact (2D representation).

Let us now consider the situation depicted in fig. A.2 which represent two (identical) spheroids surrounded with a shell of constant thickness d ($d = \delta/2$). We are again interested in evaluating the excluded volume of these objects which, because of the constant shell offset, will not be anymore ellipsoids. Nevertheless, we see that in this case we can again construct geometrical quantities like H and K of the two spheroids of Fig. A.1 and that these, which we will call H' and K', are parallel to the old H and K respectively. Then it follows:

$$H'(\alpha) = H(\alpha) + d \tag{A.13}$$

$$K'(\alpha') = K(\alpha') + d, \tag{A.14}$$

and H and K will be given by (A.1) and (A.2). Now, also in this case expression (A.5) holds true and, observing that the volume of an ovaloid may be written as [173, 174]

$$V = \frac{1}{6}\int G(G, G)\mathrm{d}\omega, \tag{A.15}$$

where G is a geometric quantity constructed like H, K, H', K', we are able to write for the excluded volume of the two spheroids with shell:

$$\begin{aligned}
V_{exd} &= 2V' + \int K'(H', H')\mathrm{d}\omega \\
&= V_{ex} + \frac{4d}{3}\underbrace{\int (H, H)\mathrm{d}\omega}_{I_1} + \underbrace{2d\int\left(\frac{H}{3} + \frac{4d}{3}\right)\left(\frac{\partial^2 H}{\partial\alpha^2} + \frac{\cos\alpha}{\sin\alpha}\frac{\partial H}{\partial\alpha} + 2H + d\right)\mathrm{d}\omega}_{I_2} \\
&\quad \underbrace{+ 2d\int K\left(\frac{\partial^2 H}{\partial\alpha^2} + \frac{\cos\alpha}{\sin\alpha}\frac{\partial H}{\partial\alpha} + 2H + d\right)\mathrm{d}\omega}_{I_3},
\end{aligned} \tag{A.16}$$

and V_{ex} is the excluded volume of the two spheroids (A.12).

Integrals I_1 and I_2 are straightforward and may be solved with the aid of formulas 3.682, 2.583 (3.), 2.584 (3.) and 2.584 (39.) of [137]:

$$I_1 = 2b^2(1-\epsilon^2)\int_0^{2\pi}\mathrm{d}\beta\int_0^{\pi}\mathrm{d}\alpha\frac{\sin\alpha}{(1-\epsilon^2\cos^2\alpha)^2} = 8\pi b^2(1-\epsilon^2)F(2, \tfrac{1}{2}, \tfrac{3}{2}, \epsilon^2), \tag{A.17}$$

$$\begin{aligned}
I_2 = &\int_0^{2\pi}\mathrm{d}\beta\int_0^{\pi}\mathrm{d}\alpha\sin\alpha\left(\frac{b\sqrt{1-\epsilon^2\cos^2\alpha}}{3} + \frac{4d}{3}\right) \\
&\times\left[\frac{b}{\sqrt{1-\epsilon^2\cos^2\alpha}} + \frac{b(1-\epsilon^2)}{(1-\epsilon^2\cos^2\alpha)^{\frac{3}{2}}} + d\right] \\
= &\frac{4\pi}{3}(b^2+4d^2) + 6\pi bd\left(\sqrt{1-\epsilon^2} + \frac{\arcsin\epsilon}{\epsilon}\right) + \frac{4\pi}{3}b^2(1-\epsilon^2)\frac{\operatorname{arctanh}\epsilon}{\epsilon}.
\end{aligned} \tag{A.18}$$

Regarding I_3 we have, using Eq. (A.2), Eq. (A.4) and Eq. (A.9):

$$\begin{aligned}
I_3 = &b\int_0^{2\pi}\mathrm{d}\beta\int_0^{\pi}\mathrm{d}\alpha\sin\alpha\sqrt{1-\epsilon^2(\sin\varphi\sin\alpha\cos\beta+\cos\varphi\cos\alpha)^2} \\
&\times\left[\frac{b}{\sqrt{1-\epsilon^2\cos^2\alpha}} + \frac{b(1-\epsilon^2)}{(1-\epsilon^2\cos^2\alpha)^{\frac{3}{2}}} + d\right],
\end{aligned} \tag{A.19}$$

and we can again expand the $1-\epsilon^2(\sin\varphi\sin\alpha\cos\beta+\cos\varphi\cos\alpha)^2$ square root obtaining

$$\begin{aligned}
I_3 =& b\int_0^{2\pi}\mathrm{d}\beta\int_0^{\pi}\mathrm{d}\alpha\sin\alpha\bigg[\frac{b}{\sqrt{1-\epsilon^2\cos^2\alpha}}+\frac{b(1-\epsilon^2)}{(1-\epsilon^2\cos^2\alpha)^{\frac{3}{2}}}+d\bigg]\\
&-\frac{b}{2\sqrt{\pi}}\sum_{k=1}^{\infty}\Gamma(k-\frac{1}{2})\frac{\epsilon^{2k}}{k!}\sum_{i=0}^{k}\binom{k}{i}\sin^{2i}\varphi\cos^{2k-2i}\varphi\int_0^{2\pi}\mathrm{d}\beta\cos^{2i}\beta\\
&\times\Bigg[b\int_0^{\pi}\mathrm{d}\alpha\frac{\sin^{2i+1}\alpha\cos^{2k-2i}\alpha}{\sqrt{1-\epsilon^2\cos^2\alpha}}+b(1-\epsilon^2)\int_0^{\pi}\mathrm{d}\alpha\frac{\sin^{2i+1}\alpha\cos^{2k-2i}\alpha}{(1-\epsilon^2\cos^2\alpha)^{\frac{3}{2}}}\\
&+d\int_0^{\pi}\mathrm{d}\alpha\sin^{2i+1}\alpha\cos^{2k-2i}\alpha\Bigg].
\end{aligned}\tag{A.20}$$

These integrals may be solved again with the use of the formulas 2.153 (3.), 3.682, 3.681 (1.), 2.583 (3.), 2.584 (39.) and 3.621 (5.) of [137], yielding

$$\begin{aligned}
I_3 =& 4\pi b\bigg(\frac{b\arcsin\epsilon}{\epsilon}+b\sqrt{1-\epsilon^2}+2d\bigg)\\
&-b\sqrt{\pi}\sum_{k=1}^{\infty}\Gamma(k-\frac{1}{2})\epsilon^{2k}\sum_{i=0}^{k}\frac{\sin^{2i}\varphi\cos^{2k-2i}\varphi}{2^i(k-i)!(i!)^2}\\
&\times B(i+1,\tfrac{2k-2i+1}{2})\Big[bF(\tfrac{1}{2},\tfrac{2k-2i+1}{2},\tfrac{2k+3}{2},\epsilon^2)+b(1-\epsilon^2)F(\tfrac{3}{2},\tfrac{2k-2i+1}{2},\tfrac{2k+3}{2},\epsilon^2)+d\Big].
\end{aligned}\tag{A.21}$$

We can then combine all these results together with property [176]

$$F(2,\tfrac{1}{2},\tfrac{3}{2},\epsilon^2)=\tfrac{1}{2}\bigg(\tfrac{1}{1-\epsilon^2}+\tfrac{\operatorname{arctanh}\epsilon}{\epsilon}\bigg)\tag{A.22}$$

and Eq. (A.16) to write the *excluded volume of two oblate spheroids surrounded with a shell of constant thickness* V_{exd}:

$$\begin{aligned}
V_{exd} =& V_{ex}+\frac{8\pi}{3}d(3b^2+4d^2+3bd)+4\pi bd(2b+3d)\bigg(\sqrt{1-\epsilon^2}+\frac{\arcsin\epsilon}{\epsilon}\bigg)\\
&+8\pi b^2d(1-\epsilon^2)\frac{\operatorname{arctanh}\epsilon}{\epsilon}-2bd\sqrt{\pi}\sum_{k=1}^{\infty}\Gamma(k-\frac{1}{2})\epsilon^{2k}\sum_{i=0}^{k}\frac{\sin^{2i}\varphi\cos^{2k-2i}\varphi}{2^i(k-i)!(i!)^2}\\
&\times B(i+1,\tfrac{2k-2i+1}{2})\Big[bF(\tfrac{1}{2},\tfrac{2k-2i+1}{2},\tfrac{2k+3}{2},\epsilon^2)+b(1-\epsilon^2)F(\tfrac{3}{2},\tfrac{2k-2i+1}{2},\tfrac{2k+3}{2},\epsilon^2)+d\Big].
\end{aligned}\tag{A.23}$$

We note that the above procedure allowed to obtain an expression for V_{exd} with an angular dependence only upon φ. However, the orientation of the surface enclosing this volume will be dependent also on θ, which is why it is needed e.g. in (5.110).

The above results can also be easily used to compute the *total volume of the spheroid with the shell* starting from Eq. (A.15) with Eq. (A.13):

$$V_d = V + \frac{d}{6}\int (H,H)\mathrm{d}\omega + \frac{d}{3}\int (H+d)\left(\frac{\partial^2 H}{\partial\alpha^2} + \frac{\cos\alpha}{\sin\alpha}\frac{\partial H}{\partial\alpha} + 2H + d\right)\mathrm{d}\omega, \tag{A.24}$$

which is very similar to the first part of Eq. (A.16) and can be integrated alike, obtaining

$$V_d = V + \frac{2\pi d}{3}\left[3b^2(1-\epsilon^2)\frac{\operatorname{arctanh}\epsilon}{\epsilon} + 3bd\left(\sqrt{1-\epsilon^2} + \frac{\arcsin\epsilon}{\epsilon}\right) + 3b^2 + 2d^2\right]. \tag{A.25}$$

We now want to calculate the averaged excluded volume starting from the angle distribution functions which arise in the spheroid distributions of the simulation algorithm. For axially symmetric objects the angle distribution function $\Phi(\varphi)$ is dependent only on the angle between the symmetry axes φ. In the case of an isotropic (or Poissonian) angle distribution, where any orientation is equally probable, it is easy to find

$$\Phi_{isotr.}(\varphi) = \frac{\sin\varphi}{4\pi}. \tag{A.26}$$

The averaged excluded volume of the two spheroids will then be

$$\langle V_{ex}\rangle_{isotr.} = \int_0^{2\pi}\mathrm{d}\theta \int_0^{\pi}\mathrm{d}\varphi\, \Phi_{isotr.}(\varphi)V_{ex}(\varphi) = \frac{1}{2}\int_0^{\pi}\mathrm{d}\varphi\, \sin\varphi V_{ex}(\varphi). \tag{A.27}$$

This easily leads with (A.12) and 3.621 (5.) of [137] to the *averaged excluded volume of two oblate spheroids*:

$$\begin{aligned}\langle V_{ex}\rangle &= 2V + 8\pi b^3(1-\epsilon^2)F(2, \tfrac{1}{2}, \tfrac{3}{2}, \epsilon^2)\\ &- \sqrt{\pi}b^3(1-\epsilon^2)\sum_{k=1}^{\infty}\Gamma(k-\frac{1}{2})\epsilon^{2k}\sum_{i=0}^{k}\frac{[B(i+1, \frac{2k-2i+1}{2})]^2}{2^i(k-i)!(i!)^2}F(2, \tfrac{2k-2i+1}{2}, \tfrac{2k+3}{2}, \epsilon^2),\end{aligned} \tag{A.28}$$

and with Eq. (A.23) and the same formula of [137] to the *averaged excluded volume of two oblate spheroids surrounded with a shell of constant thickness*:

$$\begin{aligned}\langle V_{exd}\rangle &= \langle V_{ex}\rangle + \frac{8\pi}{3}d(3b^2+4d^2+3bd) + 4\pi bd(2b+3d)\left(\sqrt{1-\epsilon^2} + \frac{\arcsin\epsilon}{\epsilon}\right)\\ &+ 8\pi b^2 d(1-\epsilon^2)\frac{\operatorname{arctanh}\epsilon}{\epsilon} - bd\sqrt{\pi}\sum_{k=1}^{\infty}\Gamma(k-\frac{1}{2})\epsilon^{2k}\sum_{i=0}^{k}\frac{[B(i+1, \frac{2k-2i+1}{2})]^2}{2^i(k-i)!(i!)^2}\\ &\times\left[bF(\tfrac{1}{2}, \tfrac{2k-2i+1}{2}, \tfrac{2k+3}{2}, \epsilon^2) + b(1-\epsilon^2)F(\tfrac{3}{2}, \tfrac{2k-2i+1}{2}, \tfrac{2k+3}{2}, \epsilon^2) + d\right].\end{aligned} \tag{A.29}$$

The quantities involved in Eq. (A.28) and Eq. (A.29) can then be easily evaluated with a mathematical software like Maple [176] .

The averaged excluded volume of the hard spheroids (A.28) is of course equivalent to the Isihara-Ogston-Winzor expression [174, 175]:

$$\langle V_{ex} \rangle_{I.O.W.} = \frac{4}{3}\pi a b^2 \left\{ 2 + \frac{3}{2} \left[1 + \frac{\arcsin \epsilon}{\epsilon\sqrt{1-\epsilon^2}} \right] \left[1 + \frac{(1-\epsilon^2)}{2\epsilon} \ln \left(\frac{1+\epsilon}{1-\epsilon} \right) \right] \right\}. \tag{A.30}$$

These expressions have then been successfully verified through simulation by generating a great number of randomly placed spheroids couples with fixed reciprocal orientation and seeing how many times their shells overlapped. The ratio of overlaps to the total trial number will then be equal to the ratio of the excluded volume to the volume of the simulation cell. As an example, we may consider the plot of such a comparison for $\langle V_{exd} \rangle$ (A.29) for the $\delta/D = 0.1765$ and $b = 0.5$ case, as shown in Fig. A.3. Convergence tests on the series were also performed.

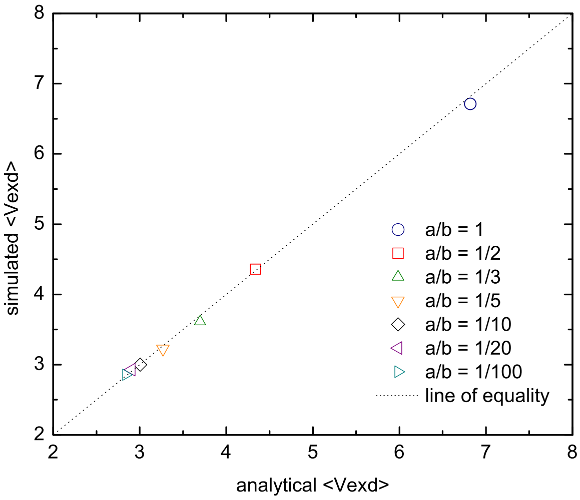

Figure A.3: Comparison between the analytical and simulated values of $\langle V_{exd} \rangle$ for the $\delta/D = 0.1765$ and $a = 0.5$ case and for different aspect-ratio oblate spheroids. Simulation data: L/D=40, trial placing number=10^7

It is finally interesting to observe that the ratio between $\langle V_{exd} \rangle$ and the spheroid volume V is roughly linearly dependent upon the spheroid aspect-ratio and that it slightly deviates from this behavior only close to the sphere case. The same holds true for the averaged excluded volume $\langle V_{ex} \rangle$, showing that interpreting the influence of the spheroid aspect-ratio as an excluded volume effect is a consistent approach.

A.2 General excluded volume expressions for spheroids with isotropic orientation distribution

In the previous section we explicitly derived excluded volume formulas for oblate ellipsoids of revolution (spheroids) and oblate ellipsoids of revolution with a shell of constant thickness. The derivation followed a route which allowed to obtain relations with full explicit orientation dependence albeit in an expanded form. However, another work of Isihara [174] allows to easily derive closed relations for the excluded volume of two spheroids with a shell of constant thickness if the mutual orientation of the spheroid symmetry axes follows that of an isotropic distribution. Given two spheroids with polar semi-axis a and equatorial semi-axis b, we will have that their *eccentricity* ϵ takes the form:

$$\epsilon = \sqrt{1-\frac{b^2}{a^2}} \qquad ; \qquad \text{Prolate}$$

$$\epsilon = \sqrt{1-\frac{a^2}{b^2}} \qquad ; \qquad \text{Oblate.} \tag{A.31}$$

If the mutual orientation of the spheroid symmetry axes follows that of the isotropic case, the averaged excluded volume of the two spheroids will take the form [174] (valid also for more general identical ovaloids)

$$\langle V_{ex} \rangle = 2V + \frac{MF}{2\pi} \tag{A.32}$$

where V is the spheroid volume and M and F are two quantities defined in the case of spheroids as [174]:

$$M = 2\pi a\left[1+\frac{(1-\epsilon^2)}{2\epsilon}\ln\left(\frac{1+\epsilon}{1-\epsilon}\right)\right] \qquad ; \qquad \text{Prolate}$$

$$M = 2\pi b\left(\sqrt{1-\epsilon^2}+\frac{\arcsin\epsilon}{\epsilon}\right) \qquad ; \qquad \text{Oblate} \tag{A.33}$$

and

$$F = 2\pi ab\left(\sqrt{1-\epsilon^2}+\frac{\arcsin\epsilon}{\epsilon}\right) \qquad ; \qquad \text{Prolate}$$

$$F = 2\pi b^2\left[1+\frac{(1-\epsilon^2)}{2\epsilon}\ln\left(\frac{1+\epsilon}{1-\epsilon}\right)\right] \qquad ; \qquad \text{Oblate.} \tag{A.34}$$

If we now consider the case of two spheroids coated with a shell of uniform thickness d ($d = \delta/2$), we will have that the averaged excluded volume of the spheroids plus shell will have again the form of (A.32):

$$\langle V_{exd} \rangle = 2V_d + \frac{M_d F_d}{2\pi} \tag{A.35}$$

and by constructing the quantities V_d, M_d, and F_d from their definition of Ref. [174] (see previous section for a similar calculation), one obtains:

$$\langle V_{exd}\rangle = \langle V_{ex}\rangle + 4dF + \frac{dM^2}{\pi} + 8d^2M + \frac{32\pi}{3}d^3 \tag{A.36}$$

while the volume of the spheroid plus shell can be written as:

$$V_d = V + dF + d^2M + \frac{4\pi}{3}d^3 \tag{A.37}$$

Now, if we consider the extreme cases, where $\epsilon \to 1$, we have

$$\begin{array}{lll} \text{Prolate } (\epsilon \to 1) & M = 2\pi a \quad , & F = \pi^2 ab \\ \text{Oblate } (\epsilon \to 1) & M = \pi^2 b \quad , & F = 2\pi b^2. \end{array} \tag{A.38}$$

Then, for the case of extreme (i.e. high aspect-ratio) prolate spheroids where we furthermore assume that $d/a \ll 1$, we will have from (A.36)

$$\langle V_{exd}\rangle \simeq \langle V_{ex}\rangle + 4\pi a^2 d = \langle V_{ex}\rangle + 4\pi a^3(\delta/D) \tag{A.39}$$

where, as usual, $D = 2\max(a,b) = 2a$.

A.3 Excluded volume quantities for spherocylinders

Spherocylinders are formed by cylinders of radius R and length H, capped by hemispheres of radius R, so that $a = R + H/2$ and $b = R$. Their volume is $V = (4/3)\pi R^3[1 + (3/4)(H/R)]$. The excluded volume for spherocylinders with isotropic orientation distribution was calculated in Ref. [105] and reads

$$\langle V_{ex}\rangle = \frac{32\pi}{3}R^3\left[1 + \frac{3}{4}(H/R) + \frac{3}{32}(H/R)^2\right]. \tag{A.40}$$

The excluded volume $\langle V_{exd}\rangle$ of spherocylinders with a shell of constant thickness $d = \delta/2$ will be:

$$\langle V_{exd}\rangle = \frac{32\pi}{3}(R+d)^3\left[1 + \frac{3}{4}\left(\frac{H}{R+d}\right) + \frac{3}{32}\left(\frac{H}{R+d}\right)^2\right]. \tag{A.41}$$

For the high aspect-ratio limit ($H/R \gg 1$), when $d/H \ll 1$, we will have

$$\langle V_{exd}\rangle \simeq \pi H^2(R+d)$$

$$\langle V_{exs}\rangle = \langle V_{exd}\rangle - \langle V_{ex}\rangle \simeq \pi H^2 d \tag{A.42}$$

Appendix B

Conductivity versus critical distance plots

We show in the following Figures B.1-B.9 the complete set of plots of the natural logarithm of the sample conductivity σ as a function of the geometrical percolation critical distance δ_c for different polymer nanocomposites, as used to obtain the ξ values of Figure 6.6 and the σ_0 vales of Figure 6.8 of Chapter 6. In collecting the published results of σ versus ϕ, we have considered only those works where a/b and $D = 2\max(a, b)$ were explicitly reported. In the cases of documented variations of these quantities, we used their arithmetic mean. The ϕ dependence of the original published data was then converted into a δ_c dependence as follows. For fibrous systems (nanofibers, nanotubes), the filler shape was assimilated to spherocylinders, while for nanosheet systems it was assimilated to oblate spheroids. For prolate fillers and $a/b > 10$, δ_c was obtained from Equation (4.17) when data were limited to $\phi < 0.01$. For the cases in which higher volume fractions were involved, we used the fit of the re-scaled results with $a/b > 10$ and penetrable shell with aspect-ratio greater than 5 of Equation (4.12). For spherical fillers, the values of δ_c were obtained from Equation (4.19) while for oblate fillers, the values for δ_c were obtained from Equation (4.18).

Since the model introduced in Chapter 6 is expected to be representative only if ϕ is sufficiently above ϕ_c to consider the effect of the insulating matrix negligible, for a given experimental curve, higher ϕ data were privileged, and lower density points sometimes omitted when deviating consistently from the main trend. The converted data were fitted to Equation (6.7) and the results of the fit are reported in Figures B.1-B.9 by solid lines. The results for $2/\xi$ and $\ln(\sigma_0)$ are also reported in the figures. As it may be appreciated from Figures B.1-B.9, in many instances the experimental data follow nicely a straight line, as predicted by Equation (6.7), while in others the data are rather scattered or deviate from linearity. In these latter cases, the fit to Equation (6.7) is meant to capture the main linear trend of $\ln(\sigma)$ as a function of δ_c.

Trionfi et al., Phys. Rev. Lett. 102, 116601 (2009)
CNF a/b=100 D=8000 nm

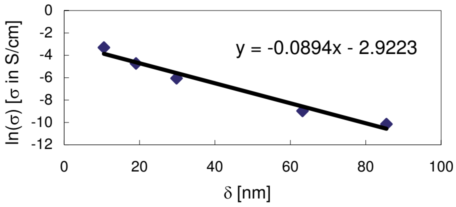

Arlen et al., Macromolecules 41, 8053 (2008)
CNF a/b=150 D=10000 nm

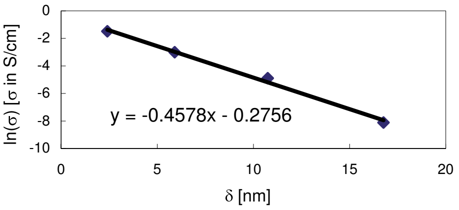

Hammel et al., Carbon 42, 1153 (2004)
CNF a/b=100 D=10000 nm

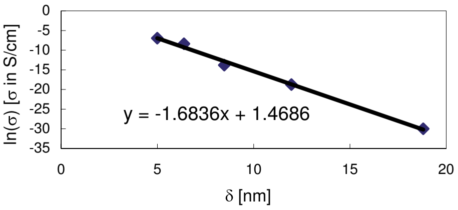

Hammel et al., Carbon 42, 1153 (2004)
CNF a/b=50 D=10000 nm

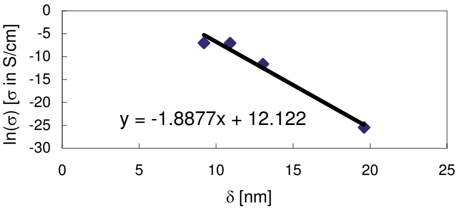

Hammel et al., Carbon 42, 1153 (2004)
CNF a/b=100 D=10000 nm

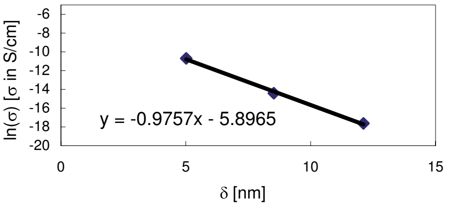

Gelves et al., Adv. Funct. Mater. 16, 2423 (2006)
Ag NF a/b=60 D=10000 nm

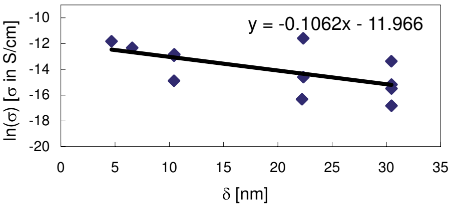

Gelves et al., Adv. Funct. Mater. 16, 2423 (2006)
Cu NF a/b=60 D=10000 nm

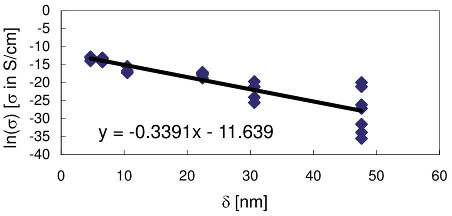

Zhang et al., J. Appl. Polym. Sci. 69, 1813 (1998)
CNF a/b=50 D=10000 nm

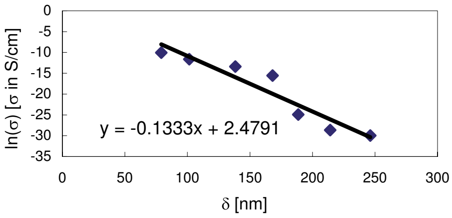

Finegan et al., J. Mater. Res. 16, 1668 (2001)
CNF a/b=35 D=7000 nm

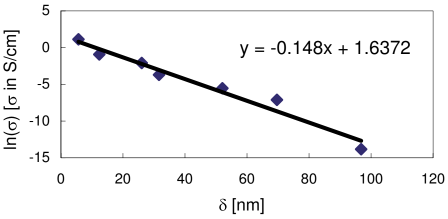

Finegan et al., J. Mater. Res. 16, 1668 (2001)
CNF a/b=75 D=15000 nm

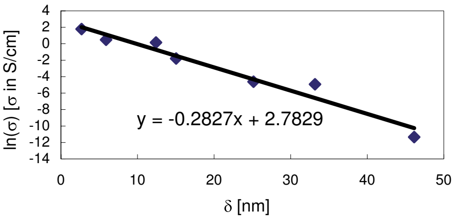

Figure B.1: plots of $\ln \sigma$ as a function of δ for different polymer-nanofiber composites.

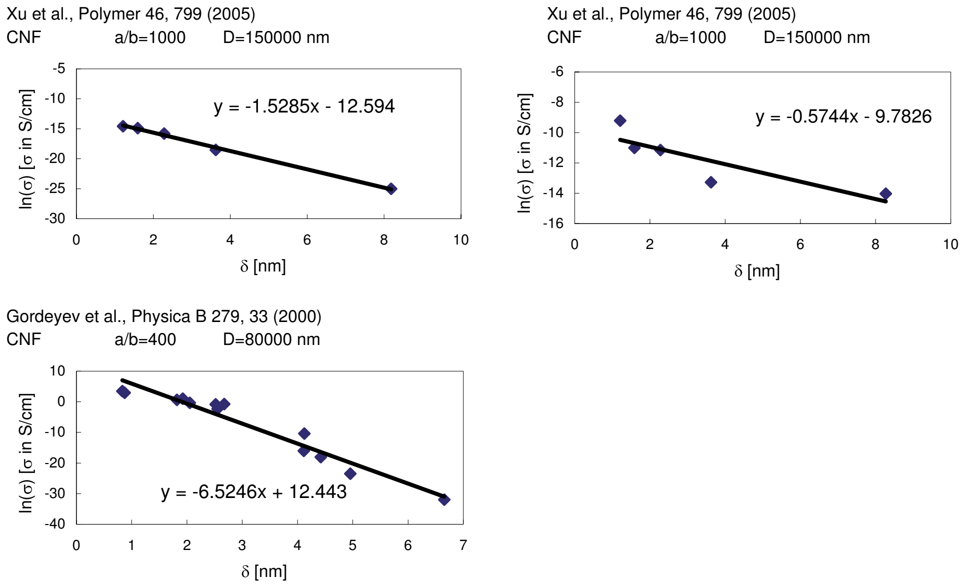

Figure B.2: plots of $\ln\sigma$ as a function of δ for different polymer-nanofiber composites (cont.)

Du et al., Phys. Rev. B 72, 121404 (2005)
a/b=45 D=300 nm

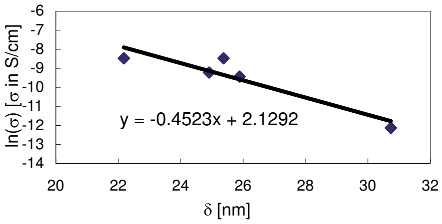

Xu et al., J. Phys. Chem. B 110, 12289 (2006)
a/b=150 D=3000 nm

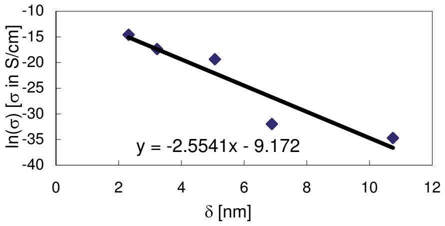

Ounaies et al., Compos. Sci. Technol. 63, 1637 (2003)
a/b=430 D=3000 nm

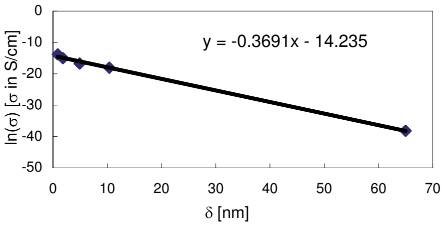

Shi et al., J. Polym. Res. (2008)
DOI 10.1007/s10965-008-9241-z
a/b=33 D=1000 nm

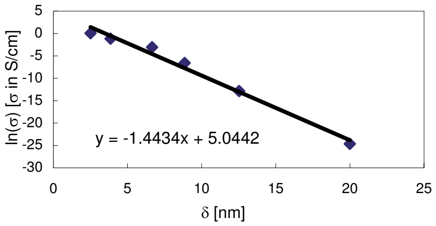

Bai et al., Comoposites A 34, 689 (2003)
a/b=333 D=50000 nm

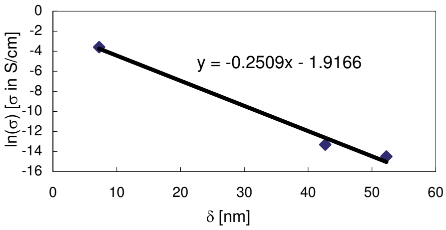

Bai et al., Comoposites A 34, 689 (2003)
a/b=67 D=10000 nm

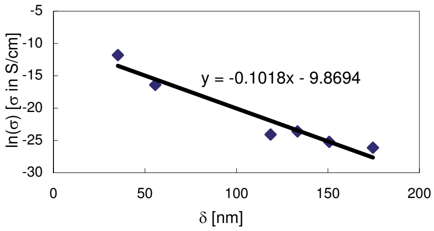

Bryning et al., Adv. Mater. 17, 1186 (2005)
a/b=380 D=516 nm

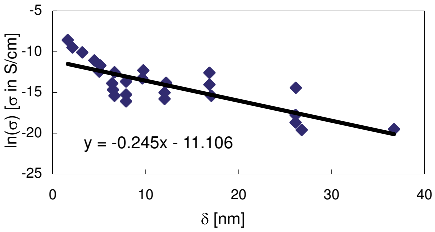

Bryning et al., Adv. Mater. 17, 1186 (2005)
a/b=380 D=516 nm

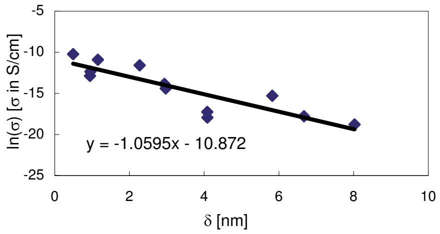

Bryning et al., Adv. Mater. 17, 1186 (2005)
a/b=167 D=150 nm

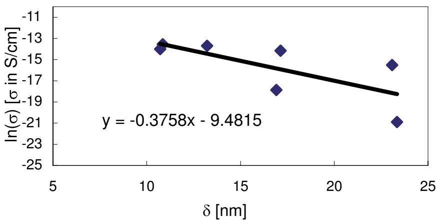

Bryning et al., Adv. Mater. 17, 1186 (2005)
a/b=167 D=150 nm

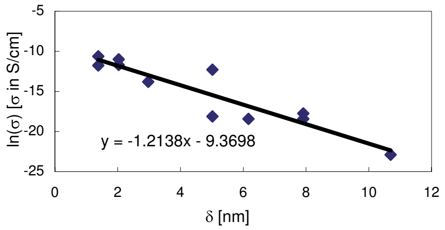

Figure B.3: plots of $\ln\sigma$ as a function of δ for different polymer-nanotube composites.

Chen et al., Nanotechnology 18, 415606 (2007)
a/b=100 D=7000 nm

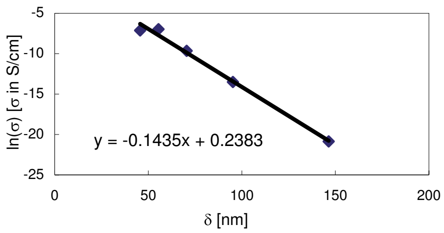

Chen et al., Nanotechnology 18, 415606 (2007)
a/b=1000 D=15000 nm

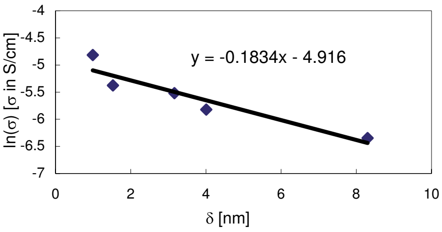

Cui et al., Carbon 41, 797 (2003)
a/b=20 D=1000 nm

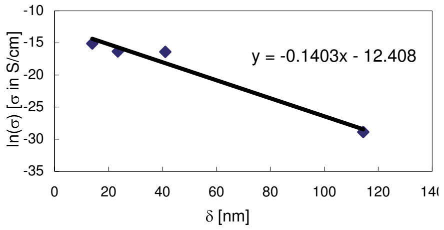

Gojny et al., Polymer 47, 2036 (2006)
a/b=1000 D=2000 nm

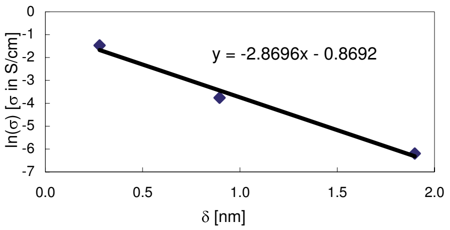

Gojny et al., Polymer 47, 2036 (2006)
a/b=1000 D=2800 nm

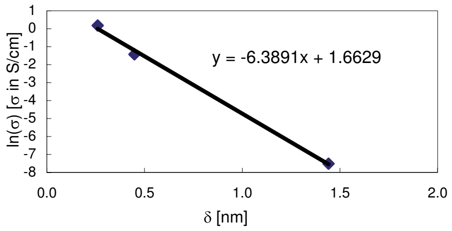

Gojny et al., Polymer 47, 2036 (2006)
a/b=1000 D=15000 nm

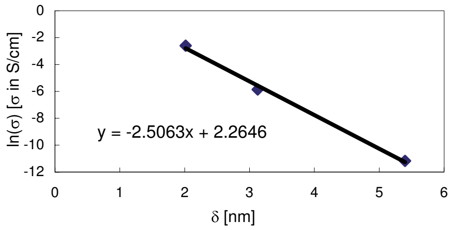

Hu et al., Polymer 47, 480 (2006)
a/b=667 D=10000 nm

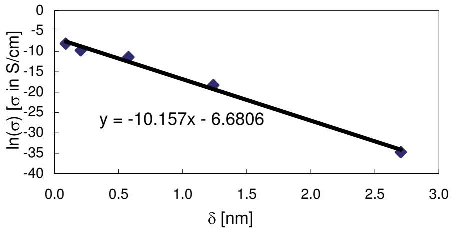

Jiang et al., Polymer 46, 7418 (2005)
a/b=1000 D=15000 nm

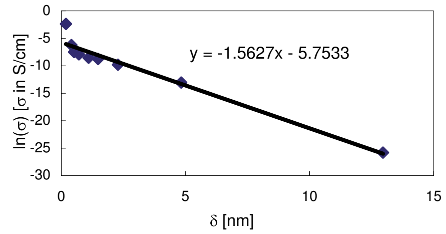

Jiang et al., Appl. Phys. Lett. 90, 042914 (2007)
a/b=410 D=12500 nm

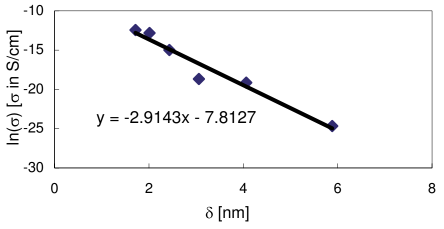

Kim et al., Carbon 43, 23 (2005)
a/b=2000 D=30000 nm

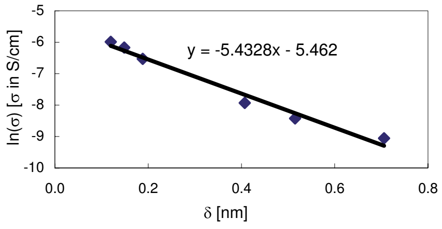

Figure B.4: plots of $\ln \sigma$ as a function of δ for different polymer-nanotube composites (cont.)

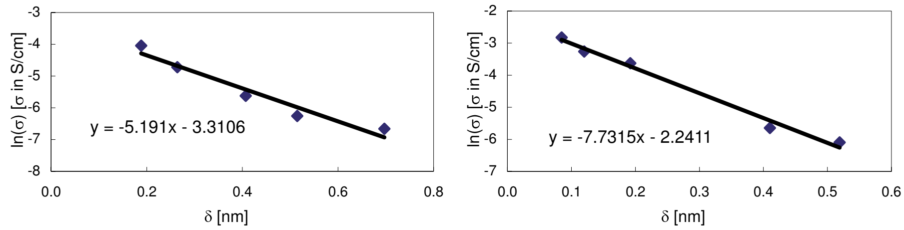
Kim et al., Carbon 43, 23 (2005)
a/b=2000 D=30000 nm

Kim et al., Carbon 43, 23 (2005)
a/b=2000 D=30000 nm

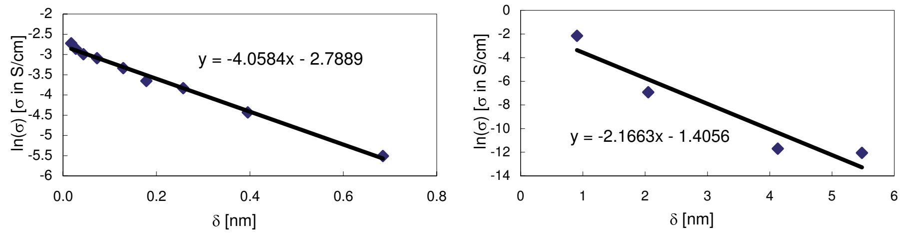
Konyushenko et al., Polymer 47, 5715 (2006)
a/b=333 D=10000 nm

Liu et al., JAP 101, 94106 (2007)
a/b=30 D=1250 nm

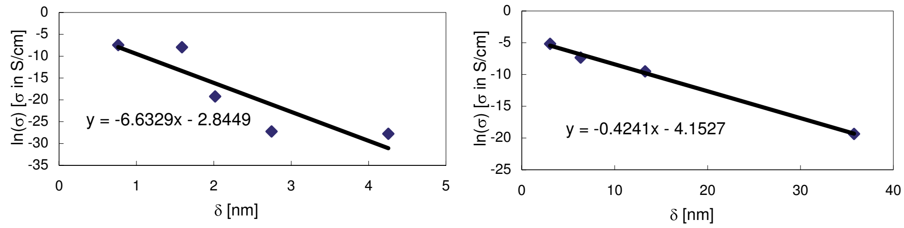
Li et al., Adv. Func. Mater. 17, 3207 (2007)
a/b=2000 D=30000 nm

Li et al., Adv. Func. Mater. 17, 3207 (2007)
a/b=500 D=7500 nm

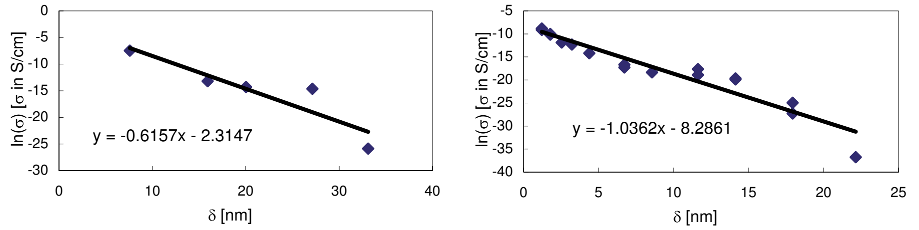
Li et al., Adv. Func. Mater. 17, 3207 (2007)
a/b=200 D=3000 nm

Mamunya et al., Compos. Sci. Technol. 68, 1981 (2008)
a/b=1000 D=15000 nm

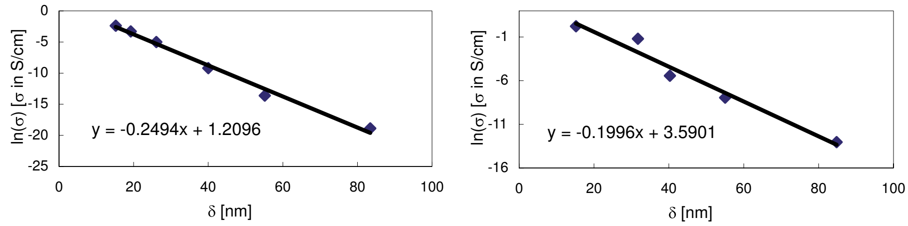
Myerczynska et al., J. Appl. Polym. Sci. 105, 158 (2007)
a/b=280 D=12500 nm

Myerczynska et al., J. Appl. Polym. Sci. 105, 158 (2007)
a/b=280 D=12500 nm

Figure B.5: plots of $\ln \sigma$ as a function of δ for different polymer-nanotube composites (cont.)

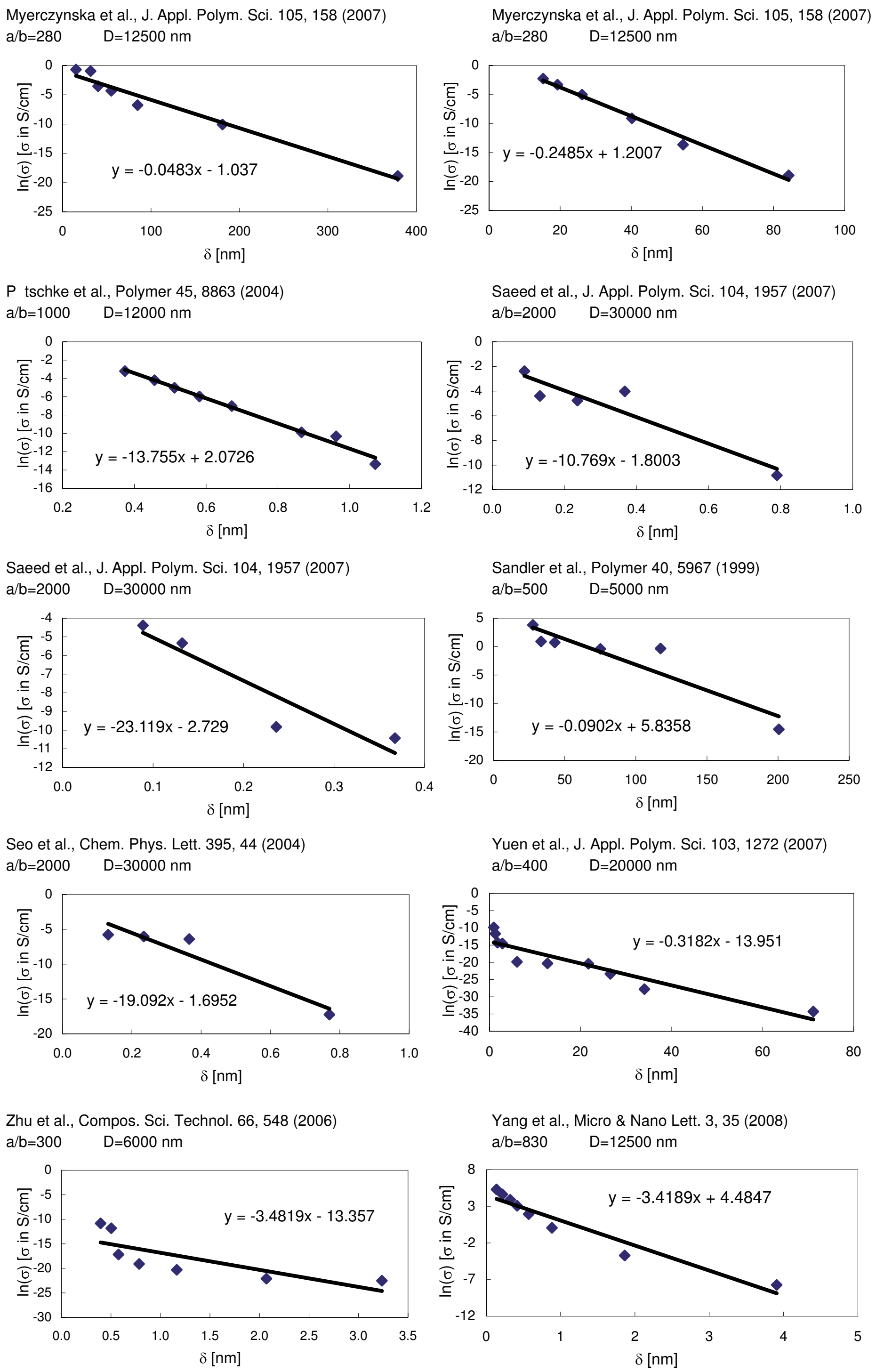

Myerczynska et al., J. Appl. Polym. Sci. 105, 158 (2007)
a/b=280 D=12500 nm

Myerczynska et al., J. Appl. Polym. Sci. 105, 158 (2007)
a/b=280 D=12500 nm

Pötschke et al., Polymer 45, 8863 (2004)
a/b=1000 D=12000 nm

Saeed et al., J. Appl. Polym. Sci. 104, 1957 (2007)
a/b=2000 D=30000 nm

Saeed et al., J. Appl. Polym. Sci. 104, 1957 (2007)
a/b=2000 D=30000 nm

Sandler et al., Polymer 40, 5967 (1999)
a/b=500 D=5000 nm

Seo et al., Chem. Phys. Lett. 395, 44 (2004)
a/b=2000 D=30000 nm

Yuen et al., J. Appl. Polym. Sci. 103, 1272 (2007)
a/b=400 D=20000 nm

Zhu et al., Compos. Sci. Technol. 66, 548 (2006)
a/b=300 D=6000 nm

Yang et al., Micro & Nano Lett. 3, 35 (2008)
a/b=830 D=12500 nm

Figure B.6: plots of $\ln\sigma$ as a function of δ for different polymer-nanotube composites (cont.)

Flandin et al., J. Appl. Polym. Sci. 76, 894 (2000)
CB D=300 nm

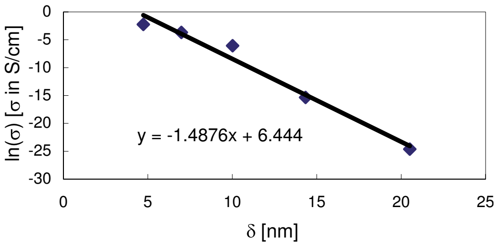

Nakamura et al., Jpn. J. Appl. Phys., Part I 36, 5163 (1997)
CB D=90 nm

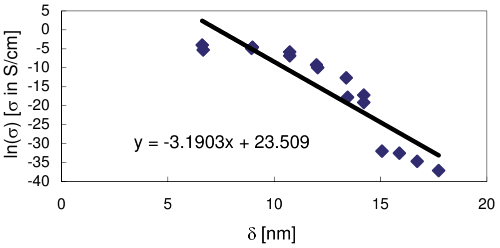

Rubin et al., Phys. Rev. B 59, 12196 (1997)
CB D=320 nm

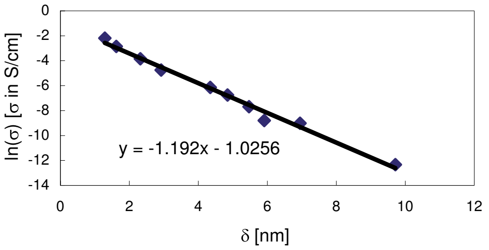

Kubat et al., Synthetic Met. 54, 187 (1993)
Pd D=300 nm

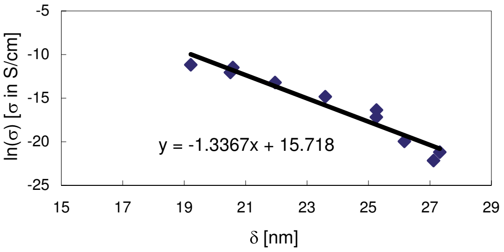

Mohanraj et al., Polym. Compos. (2007) DOI 10.1002/pc.20236
Ni-Cu D=70 nm

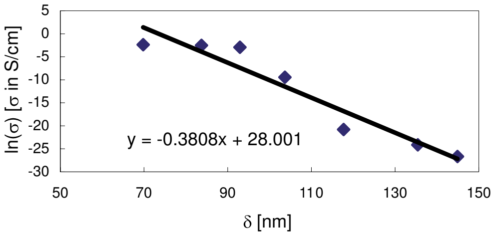

Untereker et al., Appl. Mater. Interfaces 1, 97 (2009)
Pt D=50 nm

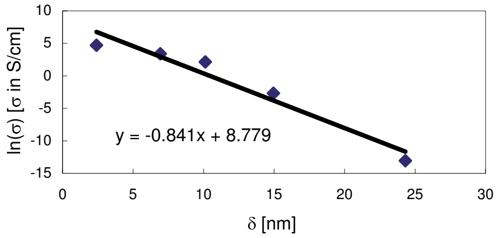

Figure B.7: plots of $\ln\sigma$ as a function of δ for different polymer-nanospheres composites

Weng et al., Polymer 46, 6250 (2005)
nano Gr a/b=1/235 D=12000 nm

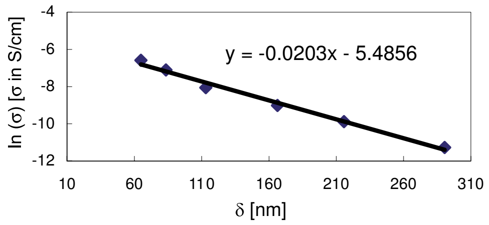

Lu et al., Mater. and Manufact. Proc. 21, 167 (2006)
nano Gr a/b=1/235 D=12000 nm

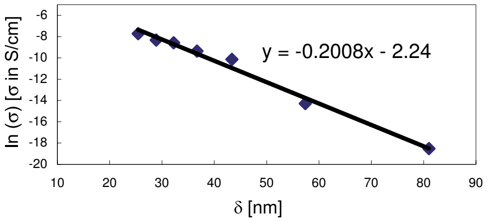

Stankovich et. al, Nature 442, 282 (2006)
Graphene a/b=1/1000 D=1000 nm

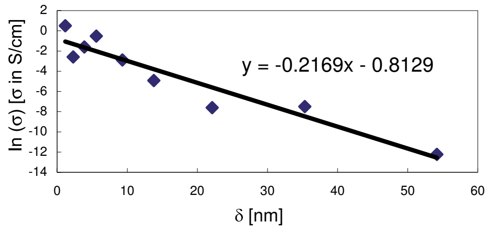

Chen et al., Polymer 44, 1781 (2003)
nano Gr a/b=1/235 D=12000 nm

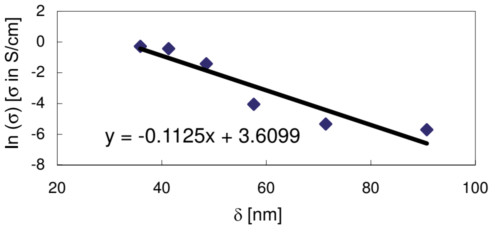

Celzard et al., Phys. Rev. B 53, 6209 (1996)
nano Gr a/b=1/200 D=10000 nm

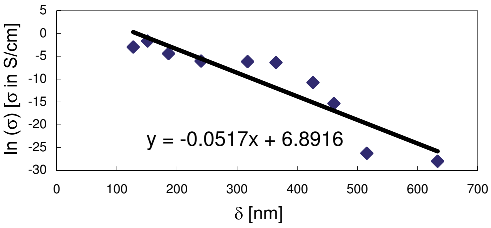

Celzard et al., Phys. Rev. B 53, 6209 (1996)
nano Gr a/b=1/200 D=10000 nm

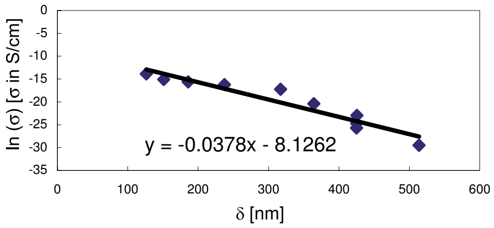

Liang et al., Carbon (2009) doi:10.1016/j.carbon.2008.12.038
Graphene a/b=1/3000 D=3000 nm

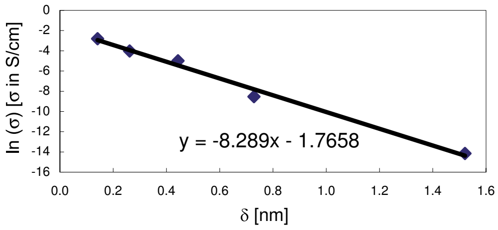

Lin et al., Synthetic Metals 159, 619 (2009)
nano Gr a/b=1/160 D=13000 nm

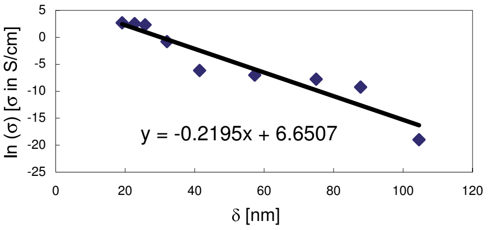

Liu et al., Adv. Funct. Mat. 18, 1518 (2008)
Graphene a/b=1/550 D=600 nm

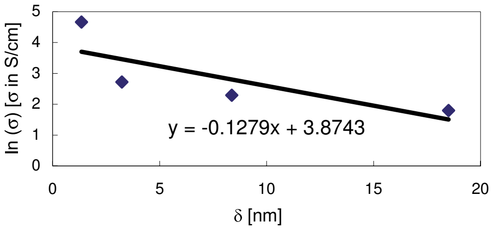

Liu et al., Adv. Funct. Mat. 18, 1518 (2008)
Graphene a/b=1/550 D=600 nm

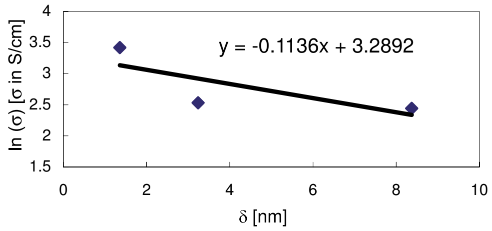

Figure B.8: plots of $\ln \sigma$ as a function of δ for different polymer-nanosheet composites

Liu et al., Adv. Funct. Mat. 18, 1518 (2008)
Graphene a/b=1/550 D=600 nm

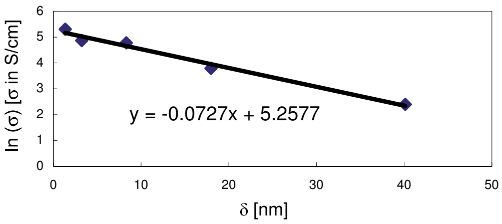

Liu et al., Adv. Funct. Mat. 18, 1518 (2008)
Graphene a/b=1/550 D=600 nm

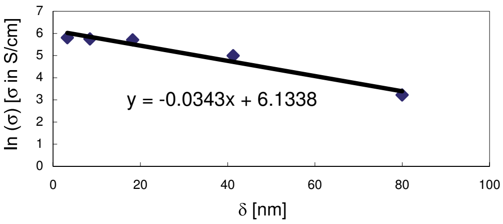

Wei et al., Carbon 47, 2290 (2009)
Graphen-like a/b=1/400 D=1500 nm

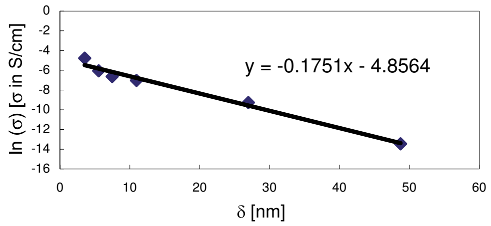

Wei et al., Carbon 47, 2290 (2009)
nano Gr a/b=1/130 D=4000 nm

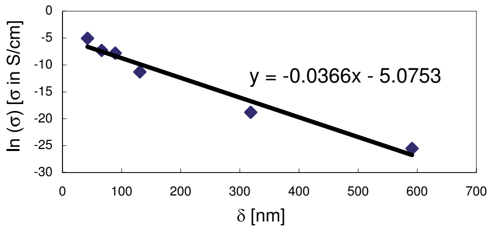

Lu et al., Adv. Funct. Mater. 15, 1358 (2005)
nano Gr a/b=1/235 D=12000 nm

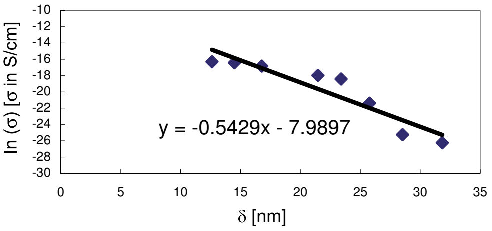

Fukushima et al., 17th Int. Conf. Amer. Soc. Compos.
nano Gr. a/b=1/430 D=13000 nm

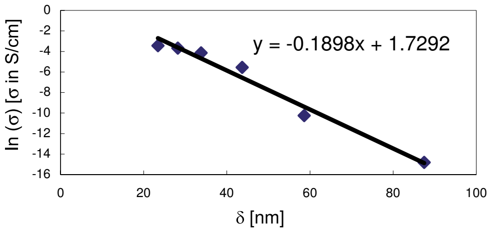

Fukushima et al., 17th Int. Conf. Amer. Soc. Compos.
nano Gr a/b=1/55 D=1100 nm

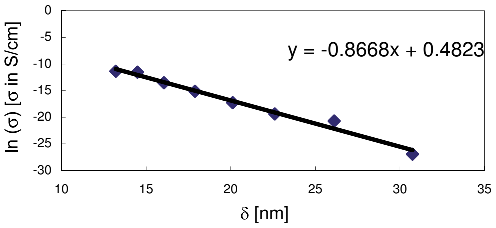

Chen et al., J. Appl. Polym. Sci. 103, 3470 (2007)
nano Gr a/b=1/235 D=12000 nm

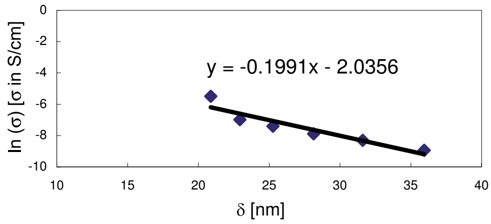

Chen et al., J. Appl. Polym. Sci. 103, 3470 (2007)
nano Gr a/b=1/235 D=12000 nm

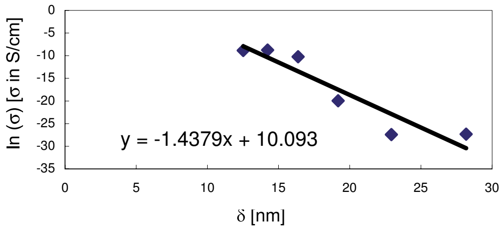

Kalaitzidou et al.,Compos. Sci. Technol. 67, 2045 (2007)
nano Gr a/b=1/1500 D=15000 nm

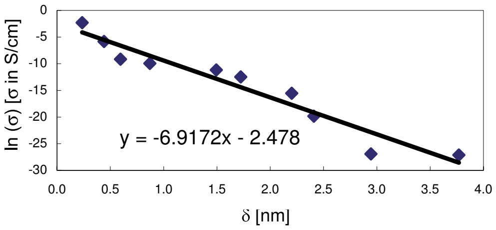

Figure B.9: plots of $\ln \sigma$ as a function of δ for different polymer-nanosheet composites (cont.)

Bibliography

[1] S. Kirkpatrick. Percolation and conduction. *Rev. Mod. Phys.*, 45:574–588, 1973.

[2] D. Stauffer and A. Aharony. *Introduction to percolation theory.* Taylor & Francis, London, 1992.

[3] G. W. Ehrenstein. *Polymeric materials.* Hanser, Munich, 2001.

[4] T. Blyte and D. Bloor. *Electrical properties of polymers.* Cambridge University Press, Cambridge, 2005.

[5] R. Strümpler and J. Glatz-Reichenbach. Conducting polymer composites. *J. Electroceram.*, 3:4:329–346, 1999.

[6] T. Sekitani, H. Nakajima, H. Maeda, T. Fukushima, T. Aida, K. Hata, and T. Someya. Stretchable active-matrix organic light-emitting diode display using printable elastic conductors. *Nature Mater.*, 8:494–499, 2009.

[7] G. Eda and M. Chhowalla. Graphene-based composite thin films for electronics. *Nano Lett.*, 9:814–818, 2009.

[8] J. Gurland. An estimate of contact and continuity of dispersions in opaque samples. *Trans. Met. Soc. AIME*, 212:642–646, 1966.

[9] X. Bourrat. Electrically conductive grades of carbon black: Structure and properties. *Carbon*, 31:287–302, 1993.

[10] J. Kubát, R. Kužel, I. Křivka, P. Bengtsson, J. Prokeš, and O. Stefan. New conductive polymeric systems. *Synthetic Met.*, 54:187–194, 1993.

[11] Y. Zweifel, C. J. G. Plummer, and H.-H. Kausch. A microscopic investigation of conducting filled composites. *J. Mater. Sci.*, 33:1715–1721, 1998.

[12] D. Untereker, S. Lyu, J. Schley, G. Martinez, and L. Lohstreter. Maximum conductivity of packed nanoparticles and their polymer composites. *Appl. Mater. Interf.*, 1:97–101, 2009.

[13] A. Maaroufi, K. Haboubi, A. El Amarti, and F. Carmona. Electrical resistivity of polymeric matrix loaded with nickel and cobalt powders. *J. Mater. Sci.*, 39:265–270, 2004.

[14] Y. P. Mamunya, V. V. Davidenko, and E. V. Lebedev. Percolation conductivity of polymer composites filled with dispersed conductive fillers. *Polym. Compos.*, 16:319–324, 1995.

[15] T. Ota, M. Fukushima, Y. Ishigure, H. Unuma, M. Takahashi, Y. Hikichi, and H. Suzuki. Control of percolation curve by filler particle shape in cu-sbr composites. *J. Mater. Sci.*, 16:1182–1183, 1997.

[16] G. Pinto, M. B. Maidana. Conducting polymer composites of zinc-filled nylon 6. *J. Appl. Polym. Sci*, 82:1449–1454, 2001.

[17] I.-G. Chen and W. B. Johnson. Alternating-current electrical properties of random metal-insulator composites. *J. Mater. Sci.*, 26:1565–1576, 1991.

[18] S. F. Wang and A. A. Ogale. Continuum space simulation and experimental characterisation of electrical percolation behavior of particulate composites. *Compos. Sci. Technol.*, 46:93–103, 1993.

[19] G. T. Mohanraj, P. K. Dey, T. K. Chaki, A. Chakraborty, and D. Khastgir. Effect of temperature, pressure, and composition on dc resistivity and ac conductivity of conductive styrene-butadiene rubber-particulate metal alloy nanocomposites. *Polym. Compos.*, 28:696–704, 2007.

[20] L. Nicodemo, L. Nicolais, G. Romeo, E. Scafora. Temperature effect on the electrical resistivity of metal/polymer composites. *Polym. Eng. Sci.*, 18:293–298, 1978.

[21] V. A. Sotskov. Electrical characteristics of insulator-conductor and insulator-semiconductor macrosystems. *Semiconductors*, 39:254–260, 2005.

[22] E. Sichel (ed.). *Carbon black polymer composites.* Marcel Dekker, New York, 1982.

[23] T. Ezquerra, M. Kulescza, C. Santa Cruz, and F. Baltà-Calleja. Charge transport in polyethylene-graphite composite materials. *Adv. Mater.*, 2:597, 1990.

[24] K. Nagata, H. Iwabuki, and H. Nigo. Effect of particle size of graphites on electrical conductivity of graphite/polymer composites. *Compos. Interf.*, 6:483–495, 1999.

[25] F. Carmona, P. Prudhon, and F. Barreau. Percolation in short fibres epoxy resin composites: conductivity behavior and finite size effects near threshold. *Solid State Commun.*, 51:255–257, 1984.

[26] M. H. Al-Saleh and U. Sundararaj. A review of vapor grown carbon nanofiber/polymer conductive composites. *Carbon*, 47:2–22, 2009.

[27] W. Bauhofer and J. Z. Kovacs. A review and analysis of electrical percolation in carbon nanotube polymer composites. *Compos. Sci. Technol.*, 69:1486–1498, 2009.

[28] A. Celzard, E. McRae, C. Deleuze, M. Dufort, G. Furdin, and J. F. Marêché. Critical concentration in percolating systems containing a high-aspect-ratio filler. *Phys. Rev. B*, 53:6209–6214, 1996.

[29] S. Stankovich, D. A. Dikin, G. H. B. Dommett, K. M. Kohlhaas, E. J. Zimney, E. A. Stach, R. D. Piner, S. T. Nguyen, and R. S. Ruoff. Graphene-based composite materials. *Nature*, 442:282–286, 2006.

[30] M. Weber and M. R. Kamal. Microstructure and volume resistivity of composites of isotactic polypropylene reinforced with electrically conductive fibers. *Polym. Compos.*, 18:726–740, 1997.

[31] G. A. Gelves, B. Lin, U. Sundararaj, and J. A. Haber. Low electrical percolation threshold of silver and copper nanowires in polystyrene composites. *Adv. Funct. Mater.*, 16:2423–2430, 2006.

[32] I. J. Youngs. Dielectric measurements and analysis for the design of conductor/insulator artificial dielectrics. *IEE Proc.-Sci. Meas. Technol.*, 147:202–208, 2000.

[33] M. S. Ahmad, A. M. Zihilif, E. Martuscelli, G. Ragosta, and E. Scafora. The electrical conductivity of polypropylene and nickel-coated carbon fiber composite. *Polym. Compos.*, 13:53–57, 1992.

[34] M. T. Korthschot and R. T. Woodhams. Electromagnetic interference shielding with nickel-coated mica. *Polym. Compos.*, 6:296–303, 1985.

[35] I. Novák, I. Krupa, and I. Chodák. Analysis of correlation between percolation concentration and leongation at break in filled electroconductive epoxy-based adhesives. *Eur. Polym. J.*, 39:585–592, 2003.

[36] J. Fournier, G. Boiteux, G. Seytre, and G. Marichy. Percolation network of polypyrrole in conductive polymer composites. *Synthetic Metals*, 84:839–840, 1997.

[37] N. Probst. Private communication. 2006.

[38] N. Probst, Ch. 8 of. *Carbon Black: Science and Technology, J. Donnet, R. Bansal, M. Wang (Ed).* Marcel Dekker, New York, 1993.

[39] L. Flandin, A. Chang, S. Nazarenko, A. Hiltner, and E. Baer. Effect of strain on the properties of an ethylene-octene elastomer with conductive carbon fillers. *J. Appl. Polym. Sci.*, 76:894–905, 1999.

[40] E. Hammel, X. Tang, M. Trampert, T. Schmitt, K. Mauthner, A. Eder, and P. Pötschke. Carbon nanofibers for composite applications. *Carbon*, 42:1153–1158, 2004.

[41] W. Lu, J. Weng, D. Wu, C. Wu, and G. Chen. Epoxy resin/graphite electrically conductive nanosheet nanocomposite. *Materials and Manufacturing Processes*, 21:167–171, 2006.

[42] G. Chen, X. Chen, H. Wang, and D. Wu. Dispersion of graphite nanosheets in polymer resins via masterbatch technique. *J. Appl. Polym. Sci.*, 103:3470–3475, 2007.

[43] F. Carmona, F. Barreau, P. Delhaes, and R. Canet. An experimental model for studying the effect of anisotropy on percolative conduction. *J. Physique Lett.*, 41:L–531–L–534, 1980.

[44] T. Wei, G. Luo, Z. Fan, C. Zheng, J. Yan, C. Yao, W. Li, and C. Zhang. Preparation of graphene nanosheet/polymer composites using in situ reduction-extractive dispersion. *Carbon*, 47:2290–2299, 2009.

[45] H. S. Göktürk, T. J. Fiske, D. M. Kalyon. Effects of particle shape and size distributions on the electrical and magnetic properties of nickel/polyethylene composites. *J. Appl. Polym. Sci.*, 50:1891–1901, 1993.

[46] A. Jillavenkatesa, S. J. Dapkunas, and L.-S. H. Lum. Particle size characterization. *NIST Recommended Practice Guide*, Special Pubblication 960-1, 2001.

[47] Y. P. Mamunya, V. V. Davydenko, P. Pissis, and E. V. Lebedev. Electrical and thermal conductivity of polymers filled with metal powders. *Eur. Polym. J.*, 38:1887–1897, 2002.

[48] Y. Agari, A. Ueda, and S. Nagai. Electrical and thermal conductivities of polyethylene composites filled with biaxial oriented short-cut carbon fibers. *J. Appl. Polym. Sci.*, 52:1223–1231, 1994.

[49] M. Karttunen, P. Ruuskanen, V. Pitkänen, and W. M. Albers. Electrically conductive metal polymer nanocomposites for electronics applications. *J. Electronic Materials*, 37:951–954, 2008.

[50] A. Malliaris and D. T. Turner. Influence of the particle size on the electrical resistivity of compacted mixtures of polymeric and metallic powders. *J. Appl. Phys.*, 42:614–618, 1971.

[51] N. Johner. On the origin of transport non-universality and piezoresistivity in segregated conductor-insulator composites and application to thick-film resistors. PhD thesis N°4351, EPFL, 2009.

[52] S. Feng, B. I. Halperin, and P. N. Sen. Transport properties of continuum systems near the percolation threshold. *Phys. Rev. B*, 35:197–214, 1987.

[53] A. Donev. Jammed packings of hard particles. PhD Thesis, Princeton University, 2006.

[54] A. L. R. Bug, S. A. Safran, G. S. Grest, and I. Webman. Do interactions raise or lower a percolation threshold ? *Phys. Rev. Lett.*, 55:1896–1899, 1985.

[55] I. Balberg and N. Binenbaum. Invariant properties of the percolation tresholds in the soft-core-hard-core transition. *Phys. Rev. A*, 35:5174–5177, 1987.

[56] S. B. Lee and T. J. Yoon. Determination of percolation thresholds for the correlated continuum percolation model. *J. Korean Phys. Soc.*, 33:612–616, 1998.

[57] S. Torquato. *Random Heterogeneous Materials: Microstructure and Macroscopic Properties.* Springer, New York, 2001.

[58] M. Rottereau, J. C. Gimel, T. Nicolai, and D. Durand. 3d monte carlo simulation of site-bond continuum percolation of spheres. *Eur. Phys. J. E*, 11:61–64, 2003.

[59] D. M. Heyes, M. Cass, and A. C. Brańka. Percolation threshold of hard-sphere fluids in between the soft-core and hard-core limits. *Molec. Phys.*, 104:3137–3146, 2006.

[60] N. Johner, C. Grimaldi, I. Balberg, and P. Ryser. Transport exponent in a three-dimensional continuum tunneling-percolation model. *Phys. Rev. B*, 77:174204, 2008.

[61] A. A. Ogale and S. F. Wang. Simulation of the percolation behavior of quasi- and transversely isotropic short-fiber composites with a continuum model. *Compos. Sci. Technol.*, 46:379–388, 1993.

[62] L. Berhan and A. M. Sastry. Modelling percolation in high-aspect-ratio fiber systems. i. soft-core versus hard-core models. *Phys. Rev. E*, 75:041120, 2007.

[63] T. Schilling, S. Jungblut, and M. A. Miller. Depletion-induced percolation in networks of nanorods. *Phys. Rev. Lett.*, 98:108303, 2007.

[64] S. Akagawa and T. Odagaki. Geometrical percolation of hard-core ellipsoids of revolution in the continuum. *Phys. Rev. E*, 76:051402, 2007.

[65] D. P. Bentz, J. T. G. Hwang, C. Hagwood, E. J. Garboczi, K. A. Snyder, N. Buenfeld, and K. L. Scrivener. Interfacial zone percolation in concrete: Effects of interfacial zone thickness and aggregate shape. *Mat. Res. Soc. Symp. Proc.*, 370:437–442, 1995.

[66] C. B. Duke. *Tunneling in solids.* Academic Press, New York, 1969.

[67] G. E. Pike and C. H. Seager. Electrical-properties and conduction mechanisms of ru-based thick-film (cermet) resistors. *J. Appl. Phys.*, 48:5152–5169, 1977.

[68] S. D. Sherman, L. M. Middleman, and S. M. Jacobs. Electron transport processes in conductor-filled polymers. *Polym. Eng. Sci.*, 23:36–46, 1983.

[69] I. Balberg. Tunneling and nonuniversal conductivity in composite materials. *Phys. Rev. Lett.*, 59:1305–1308, 1987.

[70] G. R. Ruschau, S. Yoshikawa, and R. E. Newnham. Resistivities of conductive composites. *J. Appl. Phys.*, 72:953–959, 1992.

[71] Y. Zweifel. Approche expérimentale des phénomènes microscopiques de la conduction électrique dans les polymères chargés. PhD thesis N°1482, EPFL, 1996.

[72] P. Sheng, E. K. Sichel, and J. I. Gittleman. Fluctuation-induced tunneling conduction in carbon-polyvinylchloride composites. *Phys. Rev. Lett.*, 40:1197–1200, 1978.

[73] E. K. Sichel, J. I. Gittleman, and P. Sheng. Transport properties of the composite material carbon-poly(vinyl chloride). *Phys. Rev. B*, 18:5712–5716, 1978.

[74] E. K. Sichel, J. I. Gittleman, and P. Sheng. Observation of fluctuation modulation of tunnel junctions by applied ac stress in carbon polyvinylchloride composites. *Phys. Rev. B*, 24:6131–6134, 1981.

[75] A. Celzard, E. McRae, G. Furdin, and J. F. Marêché. Conduction mechanisms in some graphite-polymer composites: The effect of a direct-current electric field. *J. Phys.: Condens. Matter*, 9:2225–2237, 1997.

[76] A. Celzard, E. McRae, J. F. arêché, G. Furdin, and B. Sundqvist. Conduction mechanisms in some graphite-polymer composites: Effects of temperature and hydrostatic pressure. *J. Appl. Phys.*, 83:1410–1419, 1998.

[77] S. Paschen, M. N. Bussac, L. Zuppiroli, E. Minder, and B. Hilti. Tunnel junctions in a polymer composite. *J. Appl. Phys.*, 78:3230–3237, 1995.

[78] C. Grimaldi and I. Balberg. Tunneling and nonuniversality in continuum percolation systems. *Phys. Rev. Lett.*, 96:066602, 2006.

[79] F. Lux. Models proposed to explain the electrical conductivity of mixtures made of conductive and insulating materials. *J. Mater. Sci.*, 28:285–301, 1993.

[80] M. L. Clingerman. Development and modelling of electrically conductive composite materials. PhD thesis, Michigan Technological University, 2001.

[81] J. Vieillard-Baron. Phase transition of the classical hard-ellipse system. *J. Chem. Phys.*, 56:4729–4744, 1972.

[82] J. W. Perram and M. S. Wertheim. Statistical mechanics of hard ellipsoids. i. overlap algorithm and the contact function. *J. Comp. Phys.*, 58:409–416, 1985.

[83] A. Donev, S. Torquato, and F. H. Stillinger. Neighbor list collision-driven molecular dynamics simulation for nonspherical hard particles. ii. applications to ellipses and ellipsoids. *J. Comp. Phys.*, 202:765–793, 2005.

[84] E. Rimon and S. P. Boyd. Obstacle collision detection using best ellipsoid fit. *J. Intell. Robotic Syst.*, 18:105–126, 1997.

[85] E. Rimon and S. P. Boyd. Efficient distance computation using best ellipsoid fit. *Tech. Rep. ISL, Stanford University*, pages 360–365, 1992.

[86] Computer code PALMYRA. MatSim GmbH, Zürich, 2005.

[87] Z. Néda, R. Florian, and Y. Brechet. Reconsideration of continuum percolation of isotropically oriented sticks in three dimensions. *Phys. Rev. E*, 59:3717–3719, 1999.

[88] Y. B. Yi and A. M. Sastry. Analytical approximation of the percolation threshold for overlapping ellipsoids of revolution. *Proc. R. Soc. London, Ser. A*, 460:2353–2380, 2004.

[89] M. Cosentino Lagomarsino, M. Dogterom, and M. Dijkstra. Isotropic-nematic transition of long, thin, hard spherocylinders confined in a quasi-two-dimensional planar geometry. *J. Chem. Phys.*, 119:3532–3540, 2003.

[90] J. D. Sherwood. Packing of spheroids in three-dimensional space by random sequential addition. *J. Phys. A: Math. Gen.*, 30:L839–L843, 1997.

[91] A. Donev, I. Cisse, D. Sachs, E. A. Variano, F. H. Stillinger, R. Connelly, S. Torquato, and P. M. Chaikin. Improving the density of jammed packings using ellipsoids. *Science*, 303:990–993, 2004.

[92] N. Metropolis, A. W. Rosenbluth, M. N. Rosenbluth, A. H. Teller, and E. Teller. Equation of state calculations by fast computing machines. *J. Chem. Phys.*, 21:1087–1092, 1953.

[93] D. Frenkel and B. M. Mulder. The hard ellipsoid-of-revolution fluid i. monte carlo simulations. *Molec. Phys.*, 55:1171–1192, 1985.

[94] C. A. Miller and S. Torquato. Effective conductivity of hard-sphere dispersions. *J. Appl. Phys.*, 68:5486–5493, 1990.

[95] C. De Michele, R. Schilling, and F. Sciortino. Dynamics of uniaxial hard ellipsoids. *Phys. Rev. Lett.*, 98:265702, 2007.

[96] S. B. Kharchenko, J. F. Douglas, J. Obrzut, E. A. Grulke, and K. B. Migler. Flow-induced properties of nanotube-filled polymer materials. *Nature Mater.*, 3:564–568, 2004.

[97] M. P. Allen and M. R. Wilson. Computer simulation of liquid crystals. *J. Comput. Aided Mol. Design*, 3:335–35, 1989.

[98] R. Eppenga and D. Frenkel. Monte carlo study of the isotropic and nematic phases of infinitely thin hard platelets. *Mol. Phys.*, 52:1303–1334, 1984.

[99] M. A. Bates and D. Frenkel. Nematic-isotropic transition in polydisperse systems of infinitely thin hard platelets. *J. Chem. Phys.*, 110:6553–6559, 1999.

[100] L. Onsager. The effects of shape on the interaction of colloidal particles. *Ann. N.Y. Acad. Sci.*, 51:627–657, 1949.

[101] H. N. W. Lekkerkerker, P. Coulon, R. Van Der Haegen, and R. Deblieck. On the isotropic liquid-crystal phase separation in a solution of rodlike particles of different lenghts. *J. Chem. Phys.*, 80:3427–3433, 1984.

[102] P. Bolhuis and D. Frenkel. Tracing the phase boundaries of hard spherocylinders. *J. Chem. Phys.*, 106:666–687, 1997.

[103] S. R. Williams, A. Philipse. Random packings of spheres and spherocylinders simulated by mechanical contraction. *Phys. Rev. E*, 67:051301, 2003.

[104] I. Balberg, N. Binenbaum, N. Wagner. Percolation thresholds in the three-dimensional sticks system. *Phys. Rev. Lett.*, 52:1465–1468, 1984.

[105] I. Balberg, C. Anderson, S. Alexander, N. Wagner. Excluded volume and its relation to the onset of percolation. *Phys. Rev. B*, 30:3933–3943, 1984.

[106] A.L.R. Bug, S.A. Safran, I. Webman. Continuum percolation of permeable objects. *Phys. Rev. B*, 33:4716–4724, 1986.

[107] L. Berhan, A.M. Sastry. Modeling percolation in high-aspect-ratio fiber systems. ii. the effect of waviness on the percolation onset. *Phys. Rev. E*, 75:041121, 2007.

[108] E. Charlaix, E. Guyon, N. Rivier. A criterion for percolation threshold in a random array of plates. *Solid State Commun.*, 50:999–1002, 1984.

[109] E. Charlaix. Percolation treshold of a random array of discs: a numerical simulation. *J. Phys. A: Math. Gen.*, 19:L533–L536, 1986.

[110] A. S. Skal, B. I. Shklovskii. Influence of the impurity concentration on the hopping conduction in semiconductors. *Sov. Phys. Semicond.*, 7:1058–1059, 1974.

[111] E.M. Sevick, P.A. Monson, J.M. Ottino. Clustering and percolation in assemblies of anisotropic particles: Perturbation theory and monte carlo simulation. *Phys. Rev. A*, 38:5376–5383, 1988.

[112] E.J. Garboczi, K.A. Snyder, J.F. Douglas, M.F. Thorpe. Geometrical percolation threshold of overlapping ellipsoids. *Phys. Rev. B*, 52:819–828, 1995.

[113] M. O. Saar, M. Manga. Continuum percolation for randomly oriented soft-core prisms. *Phys. Rev. E*, 65:056131, 2002.

[114] J. Hoshen, R. Kopelman. Percolation and cluster distribution i. cluster multiple labeling technique and critical concentration algorithm. *Phys. Rev. B*, 14:3438–3445, 1976.

[115] A. Al-Futaisi, T. W. Patzek. Extension of hoshen-kopelman algorithm to non-lattice environments. *Physica A*, 321:665–678, 2003.

[116] M. D. Rintoul, S. Torquato. Precise determination of the critical threshold and exponents in a three-dimensional continuum percolation model. *J. Phys. A: Math. Gen.*, 30:L585–L592, 1997.

[117] A. V. Kyrylyuk and P. van der Schoot. Continuum percolation of carbon nanotubes in polymeric and colloidal media. *Proc. Natl. Acad. Sci. USA*, 105:8221–8226, 2008.

[118] A. Trokhymchuk, I. Nezbeda, J. Jirsák, and D. Henderson. Hard-sphere radial distribution function again. *J. Chem. Phys.*, 123:024501, 2005.

[119] I. Balberg. "universal" percolation-threshold limits in the continuum. *Phys. Rev. B*, 31:4053–4055, 1985.

[120] R. Fogelholm. The conductivity of large percolation network samples. *J. Phys. C*, 13:L571–L574, 1980.

[121] J. G. Simmons. Generalized formula for the electric tunnel effect between similar electrodes separated by a thin insulating film. *J. Appl. Phys.*, 34:1793–1803, 1963.

[122] P. Sheng. Fluctuation-induced tunneling conduction in disordered materials. *Phys. Rev. B*, 21:2180–2195, 1980.

[123] G. Binnig and H. Rohrer. Scanning tunneling microscopy. *Helv. Phys. Acta*, 55:726–735, 1982.

[124] J. Tersoff and D. R. Hamann. Theory and application for the scanning tunneling microscope. *Phys. Rev. Lett.*, 50:1998–2001, 1983.

[125] J. Tersoff and D. R. Hamann. Theory of the scanning tunneling microscope. *Phys. Rev. B*, 31:805–813, 1985.

[126] C. J. Chen. Introduction to scanning tunneling microscopy. Oxford University Press, Oxford, 1993.

[127] J. Bardeen. Tunnelling from a many-particle point of view. *Phys. Rev. Lett.*, 6:57–59, 1961.

[128] L. Landau and L. Lifchitz. *Mécanique Quantique.* Éditions Mir, Moskow, 1973.

[129] N. D. Lang. Spectroscopy of single atoms in the scanning tunneling microscope. *Phys. Rev. B*, 34:5947–5950, 1986.

[130] M. S. Chung, T. E. Feuchtwang, and P. H. Cutler. Spherical tip model in the theory of the scanning tunneling microscope. *Surf. Sci.*, 187:559–568, 1987.

[131] T. E. Feuchtwang, and P. H. Cutler. The scanning tunneling microscope: Which sample characteristic does it prove ? *Physica Scripta*, 38:252–259, 1988.

[132] C. J. Chen. Tunneling matrix elements in three-dimensional space: The derivative rule and the sum rule. *Phys. Rev. B*, 42:8841–8857, 1990.

[133] J. R. Oppenheimer. Three notes on the quantum theory of aperiodic effects. *Phys. Rev.*, 31:66–81, 1928.

[134] A. D. Gottlieb and L. Wesoloski. Bardeen's tunnelling theroy as applied to the scanning tunnelling microscopy: A technical guide to the traditional interpretation. *Nanotechnology*, 17:R57–R65, 2006.

[135] T. E. Feuchtwang, and P. H. Cutler. Tunneling and scanning tunneling microscopy: A critical review. *Physica Scripta*, 35:132–140, 1987.

[136] G. Baym. *Lectures on Quantum Mechanics.* Benjamin/Cummings, Reading, 1969.

[137] I.S. Gradshteyn and I.M. Ryzhik. *Table of integrals, series, and products.* Academic Press, 2000.

[138] C. Cohen-Tannoudji, B. Diu, F. Laloë. *Quantum Mechanics.* Wiley, New York, 1977.

[139] R. Holm. The electric tunnel effect across thin insulator films in contacts. *J. Appl. Phys.*, 22:569–574, 1951.

[140] J. Frenkel. On the electrical resistance of contacts between solid conductors. *Phys. Rev.*, 36:1604–1618, 1930.

[141] N. Kato. Dynamical diffraction theory of waves in distorted crystals. i. general formulation and treatment for perfect crystals. *Acta. Cryst.*, 16:276–281, 1963.

[142] N. D. Lang. Vacuum tunneling current from an adsorbed atom. *Phys. Rev. Lett.*, 55:230–233, 1985.

[143] E. W. Weisstein. *MathWorld-A Wolfram Web Resource*, http://mathworld.wolfram.com, 2009.

[144] I. Balberg. Tunnelling and percolation in lattices and the continuum. *J. Phys. D: Appl. Phys.*, 42:064003, 2009.

[145] P. Sheng and J. Klafter. Hopping conductivity in granular disordered systems. *Phys. Rev. B*, 27:2583–2586, 1983.

[146] E. Cuevas, M. Ortuño, and J. Ruiz. Ground state of granular metals. *Phys. Rev. Lett.*, 71:1871–1874, 1993.

[147] T. Hu and B. I. Shklovskii, B. I. . Theory of hopping conductivity of a suspension of nanowires in an insulator. *Phys. Rev. B*, 74:054205, 2006.

[148] T. Hu and B. I. Shklovskii, B. I. . Hopping conductivity of a suspension of flexible wires in an insulator. *Phys. Rev. B*, 74:174201, 2006.

[149] V. Ambegaokar, B. I. Halperin, L. S. Langer. Hopping conductivity in disordered semiconductors. *Phys. Rev. B*, 4:2612–2620, 1971.

[150] B. I. Shklovskii and A. L. Efros. *Electronic properties of doped semiconductors*. Springer, Berlin, 1984.

[151] C. H. Seager and G. E. Pike. Percolation and conductivity: A computer study. ii. *Phys. Rev. B*, 10:1435–1446, 1974.

[152] M. B. Bryning, M. F. Islam, J. M. Kikkawa, and A. G. Yodh. Very low conductivity threshold in bulk isotropic single-walled carbon nanotube-epoxy composites. *Adv. Mater.*, 17:1186–1191, 2005.

[153] R. E. Holmlin, R. Haag, M. L. Chabinyc, R. F. Ismagilov, A. E. Cohen, A. Terfort, M. A. Rampi, and G. M. Whitesides. Electron transport through thin organic films in metal-insulator-metal junctions based on self-assembled monolayers. *J. Am. Chem. Soc.*, 123:5075–5085, 2001.

[154] J. M. Benoit, B. Corraze, and O. Chaurez. Localization, coulomb interactions, and electrical heating in single-wall carbon nanotubes/polymer composites. *Phys. Rev. B*, 65:241405(R), 2002.

[155] Y. Li, L. Hong, Y. Chen, H. Wang, X. Lu, and M. Yang. Poly(4-vinylpyridine)/carbon black composite as a humidity sensor. *Sens. Actuators, B Chem.*, 123:554–559, 2007.

[156] T. Ezquerra, M. Kulescza, and F. Baltà-Calleja. Electrical transport in polyethylene-graphite composite materials. *Synthetic Metals*, 41-43:915, 1991.

[157] I. C. Kim and S. Torquato. Effective conductivity of suspensions of hard spheres by brownian motion simulation. *J. Appl. Phys.*, 69:2280, 1991.

[158] I. C. Kim and S. Torquato. Determination of the effective conductivity of heterogeneous media by brownian motion simulation. *J. Appl. Phys.*, 68:3892, 1990.

[159] S. Torquato. Effective electrical conductivity of two-phase disordered composite media. *J. Appl. Phys.*, 58:3790, 1985.

[160] A. Celzard, M. Krzesiñska, D. Bégin, J. F. Marêché, S. Puricelli, and G. Furdin. Preparation, electrical and elastic properties of new anisotropic expanded graphite-based composites. *Carbon*, 40:557–566, 2002.

[161] S.-I. Lee, Y. Song, T. W. Noh, X.-D. Chen, and J. R. Gaines. Experimental observation of nonuniversal behavior of the conductivity exponent for three-dimensional continuum percolation systems. *Phys. Rev. B*, 34:6719–6724, 1986.

[162] C. Pierre, R. Deltour, J. A. A. J. Perenboom, and P. J. M. Van Bentum. Electrical-conduction mechanisms in polymer-copper-particle composites. i. temperature and high magnetic-field dependence of the conductivity. *Phys. Rev. B*, 42:3380–3385, 1990.

[163] A. Larena and G. Pinto. Electroconductive nylon 6 and copper composites. *Polym. Compos.*, 16:536–541, 1995.

[164] L. Karásek, B. Meissner, S. Asai, and M. Sumita. Percolation concept: polymer-filler gel formation, electrical conductivity and dynamic electrical properties of carbon-black-filled rubbers. *Polym. J.*, 28:121–126, 1996.

[165] S. Nakamura, K. Sato, G. Sawa, and K. Kitagawa. Percolation threshold of carbon nlack-polyethylene composites. *Jpn. J. Appl. Phys.*, 36:5163–5168, 1997.

[166] Y. N. Anisimov, L. P. Dobrova, and A. Y. Anisimov. Conducting and strenght properties of composites based on modified epoxy and oligoester resins filled with nickel. *Russian J. Appl. Chem.*, 71:819–822, 1998.

[167] Z. Rubin, S. A. Sunshine, M. B. Heaney, I. Bloom, and I. Balberg. Critical behavior of the electrical transport properties in a tunneling-percolation system. *Phys. Rev. B*, 59:12196–12199, 1999.

[168] Y. P. Mamunya, Y. V. Muzychenko, P. Pissis, E. V. Lebedev, and M. I. Shut. Percolation phenomena in polymers containing dispersed iron. *Polym. Eng. Sci.*, 42:90–100, 2002.

[169] A. Boudenne, L. Ibos, M. Fois, J.C. Majesté, and E. Géhin. Electrical and thermal behavior of polypropylene filled with copper particles. *Composites Part A*, 36:1545–1554, 2005.

[170] H. Horibe, T. Kamimura, and K. Yoshida. Electrical conductivity of polymer composites filled with metal. *Jpn. J. Appl. Phys.*, 44:4171–4175, 2005.

[171] I. Krupa, G. Miková, I. Novák, I. Janigová, Z. Nógellová, F. Lednický, and J. Prŏkes. Electrically conductive composites of polyethylene filled with polyamide particles coated with silver. *Eur. Polym. J.*, 43:2401–2413, 2007.

[172] J. Ohser and F. Mücklich. *Statistical analysis of microstructures in materials science.* Wiley, Chirchester, 2000.

[173] A. Isihara. Theory of anisotropic colloidal solutions. *J. Chem. Phys.*, 19:1142–1147, 1951.

[174] A. Isihara. Determination of molecular shape by osmotic measurement. *J. Chem. Phys.*, 18:1446–1449, 1950.

[175] A. G. Ogston, D. J. Winzor. Treatment of thermodynamic nonideality in equilibrium studies on associating solutes. *J. Phys. Chem.*, 79:2496–2500, 1975.

[176] Computer code MAPLE software (Waterloo Maple, Waterloo, 2006).

Family name: AMBROSETTI
First name: GIANLUCA
Place and date of birth: ZURICH, 10/08/1974
Nationality: SWISS
Address: VIA RONCHETTO 2, CH-6925 GENTILINO, SWITZERLAND
E-mail : GIANLUCA.AMBROSETTI@A3.EPFL.CH

CURRICULUM VITAE

PROFESSIONAL EXPERIENCES

Jan.2007-Dec.2009.................. Scientific project management of the Swiss Commission for Technology and Innovation (CTI) funded project “GraPoly” focused on the enhancement of conductive graphite-polymer nanocomposites. Project partners: TIMCAL Graphite and Carbon SA (Bodio Switzerland), the University of Applied Science of Southern Switzerland (SUPSI), and the Swiss Federal Institute of Technology Lausanne (EPFL).
Contributions compiled in a PhD thesis.

Sep.2007-Oct.2007.................. Preparation of the funding request for the Swiss Federal Office of Energy (SFOE) funded project “SolAir” focusing on innovative solar collectors for efficient and cost-effective solar thermal power generation. Project partners: ALE Airlight Energy SA (Biasca, Switzerland), SUPSI, and the Swiss Federal Institute of Technology Zurich (ETHZ). Awarded by SFOE grant No. 102327.

Sep.2006-Dec.2006................. Preparation of the funding request for project “GraPoly”. Awarded by grant CTI No. 8597.2 to the academic partners over a period of 2 ½ years.

Dec.2004-Aug.2006................. Technical director of the Radio Frequency Identification (RFID) division of Finser Packaging SA (Bioggio, Switzerland).
Responsible for bringing together all the technical know-how to become a system integrator of RFID solutions.

Jan.2004-Nov.2004.................. Realisation of a study comparing different alternative energies for road vehicles for the Chamber of Commerce, Industry and Crafts of the Canton Ticino (Lugano, Switzerland).
Financial and technical evaluation of a pilot project for hydrogen-fuelled vehicles.

EDUCATION

Feb.2007-Present…................. PhD student at the Swiss Federal Institute of Technology Lausanne (EPFL) under the direction of Prof. Peter Ryser and co-direction of Dr. Claudio Grimaldi. Thesis on physical models describing the electrical properties of polymer nanocomposite materials.

Sep.1997-Oct.2003.................. Master of Science in theoretical physics; University of Bologna, Italy.
Thesis on vacuum polarisation and charge loss of black holes with Prof. Roberto Balbinot.

Sep.1994-June1997................. Study of jazz soprano saxophone (Boston, USA, Lausanne, Switzerland and Paris, France).
Professional musician since 1997.

July 1994.................................. High school graduation from the Liceo di lugano 1, scientific high school degree (“Maturità” type C).

TRAINING

June 2009................................. Management of Technological Innovation (MiNT) course, EPFL, Lausanne, Switzerland.

Sep. 2004................................. Autumn School on Entrepreneurship for High-tech Start-ups; ALaRI/University of Lugano, Switzerland.

LANGUAGES

ITALIAN: native language	ENGLISH: excellent written/spoken
FRENCH: excellent written/spoken	GERMAN: good written/spoken

SOFTWARE

MS Office

LaTeX

Fortran programming

Adobe Photoshop

ACTIVITIES

As a musician, participation in various recordings and international festivals since 1997. Composition of soundtracks for theatre plays and shortcut movies.

PUBBLICATIONS

G. Ambrosetti, C. Grimaldi, I. Balberg, T. Maeder, A. Danani, and P. Ryser, “Solution of the tunneling-percolation problem in the nanocomposite regime”, Submitted for publication.

G. Ambrosetti, N. Johner, C. Grimaldi, T. Maeder, P. Ryser, and A. Danani, “Electron tunneling in insulator-conductor composites with spherical fillers”, J. Appl. Phys. 106, 016103 (2009)

G. Ambrosetti, N. Johner, C. Grimaldi, A. Danani, and P. Ryser, “Percolative properties of hard oblate ellipsoids of revolution with a soft shell”, Phys. Rev. E 78, 061126 (2008)

G. Ambrosetti, “Percorsi possibili per una mobilità sostenibile”, Study report, Chamber of Commerce, Industry and Crafts of the Canton Ticino (2005)

G. Ambrosetti, “Un approccio sostenibile alla mobilità individuale”, Scheda IFCAM No. 122 (2004)